

# Dielectric-sphere-based microsystem for optical super-resolution imaging

THÈSE N° 8767 (2018)

PRÉSENTÉE LE 10 AOÛT 2018

À LA FACULTÉ DES SCIENCES ET TECHNIQUES DE L'INGÉNIEUR  
LABORATOIRE DE MICROSYSTÈMES 2  
PROGRAMME DOCTORAL EN MICROSYSTÈMES ET MICROÉLECTRONIQUE

ÉCOLE POLYTECHNIQUE FÉDÉRALE DE LAUSANNE

POUR L'OBTENTION DU GRADE DE DOCTEUR ÈS SCIENCES

PAR

Gergely HUSZKA

acceptée sur proposition du jury:

Prof. L. G. Villanueva Torrijo, président du jury  
Prof. M. Gijs, directeur de thèse  
Prof. C. Gorecki, rapporteur  
Prof. H. Zappe, rapporteur  
Prof. O. Martin, rapporteur



ÉCOLE POLYTECHNIQUE  
FÉDÉRALE DE LAUSANNE

Suisse  
2018



# Acknowledgements

First and foremost, I would like to express my gratitude to my thesis supervisor, Professor Martin A. M. Gijs, for giving me the opportunity to conduct research in the Laboratory of Microsystems. I am grateful for his continuous support and helpful thoughts. He truly believed in this project and in my abilities to realize it. I could always ask for his guidance, which gave me a lot of encouragement, specially at times, when my fate in success was low. Without him, I would not have been able to complete my work.

I would like to thank to my thesis jury president, Prof. Guillermo Villanueva, who honoured me by accepting this duty. I helped him as a teaching assistant for several years and during this time he was always kind and helpful. I believe that he is a great scientist and teacher, therefore I feel privileged for his contribution. Furthermore, I would like to thank the other members of my thesis jury, Professor Martin Olivier, Professor Christophe Gorecki and Professor Hans Zappe for their review and evaluation of my work.

I would like to acknowledge the financial support of the Swiss National Science Foundation (Grant 200021-152948) and the EU ideas program (Grant ERC-2012-AdG-320404). Furthermore, I received a huge technical support from the Center of Micronanotechnology (CMi) and from the workshop of the Microtechnology Institute (ATPR). I would like to thank the specialists of both organisations, as their advices and practical help provided many key elements in my project.

I am thankful for all the discussions and helpful thoughts that I received from the colleagues, collaborators, co-authors and scientist, with whom I worked together in the last four years. I have learned a lot from them and they were always encouraging me to achieve more. I take the opportunity to express my special gratitude to Dr. Abdeljalil Sayah and Dr. Axel Hochstetter. They not only helped me with my scientific questions, but provided new perspectives in my carrier. I believe that these discussions helped me to develop a more complex view of the world and for this, I am truly grateful. Furthermore, I would like to thank to Dr. Arne Seitz, who gave me special insight into the field of optics and contributed to my publications.

I am grateful for all the support that I got from the administrative stuff of the Laboratory of Microsystems, of the Doctoral School and of EPFL, specially from Melis Martin, Marie Halm and Lucie Auberson.

I would like to thank all of my colleagues and friends, who helped me both in scientific questions and in enjoying the life in Lausanne. Thank you all for the nice discussions and

## Acknowledgements

---

leisure-time activities. I cannot really describe the amount of gratitude I have to Dr. Stefanie J. Krauth, who helped me with the German translation of the abstract of this work and who has the best scientific paper title ever, and to Roger Krenger who helped me integrating into the Swiss lifestyle and with whom we will have a fully established friendship only in about thirty years according to local standards. They helped me a lot both in my academic and everyday life and I can only hope that in some way I was able to return this.

Last, but not least I would like to thank to my family and friends who stayed in Hungary and continuously supported me on this journey. They made lots of huge efforts in order to help me, for which I am very grateful. Finally, I have to break my word, because I said many times that I will hide my favourite cooking recipe around page seventy, still, all the pages have scientific content. Despite of this, I hope, reading them will be joyful and they will inspire new thoughts that make the world a better place in the future.

*Lausanne, 16 July 2018*

Gergely Huszka

# Abstract

Well-established imaging techniques proved that features below the diffraction limit can be observed optically using so-called super-resolution microscopies, which overcome Abbe's resolution limit. In traditional far-field microscopy, the introduction of fluorescent samples and engineered light paths was key for this breakthrough. In parallel, near-field techniques with similar performance were developed, but they suffered from a limited field-of-view. The merge of the two approaches was already demonstrated ~15 years ago, when micrometer-sized dielectric objects positioned on a sample were found to be able to image the sample with super-resolution. By observing the sample through the micro-object with a classical optical microscope, the latter could capture a virtual image showing sub-diffraction details. Although this way the near-field information transfer into the far-field by the micro-object was proven and found to be key for enabling super-resolution imaging, the limited field-of-view, as determined by the size of the micro-object, remained an issue.

In this dissertation, a novel method is presented that provides a microscopy technique capable of achieving super-resolution without field-of-view restrictions. Based on previous studies, dielectric microspheres were chosen for this imaging technique. First, the working principle of these microspheres was explored by investigating both the illumination and the reflected light path. These findings provided a better understanding on the phenomena working behind microsphere-assisted imaging and allowed to create an engineering toolbox that can be used to design microsphere-based optical systems. This was followed by an investigation on microfabrication techniques, in order to create a microchip that can serve as a bridge between a single microsphere and the macro-sized-components of a classical optical microscope. The resulting chip was later embedded in a custom fixation system that allowed scanning of this microsphere over the sample, while keeping its position fixed compared to the microscope objective. The microscope mounted camera recorded pictures during the scan, which were used to generate a large field-of-view super-resolution image by stitching. After initial successes, the setup was improved in terms of robustness and application range. The new version allowed field-of-view in the millimetre range, while it could be operated in both oil- and water-immersion. Parallel imaging with an array of microspheres was also implemented, which further enhanced the imaging speed. The algorithmic background (including an automated scanning and image reconstruction protocol) of this microscopy method was developed in-house. Its validation showed superior performance compared to existing soft-

## Abstract

---

ware. Future developments (*e.g.* employment of 3D-printing for mass-production, imaging *in vivo* biological samples, metrology applications) are envisioned. The findings presented here may pave the road for an easy-to-use, generalized super-resolution imaging system.

**Keywords:** super-resolution, optical microscopy, photonic nanojet, dielectric microsphere, scanning microscopy, image processing, finite element method numerical simulation

# Zusammenfassung

Bereits etablierte Bildgebungsverfahren haben gezeigt, dass Probenmerkmale unterhalb der Lichtbeugungsgrenze mittels sogenannter superauflösender Mikroskopie, welche Abbe's Auflösungsgrenze überwindet, optisch beobachtet werden können. In der klassischen Fernfeldmikroskopie waren die Schlüsselereignisse für diesen Durchbruch die Einführung fluoreszierender Proben und kontrollierter Strahlengänge. Gleichzeitig wurden auch Nahfeldmethoden mit ähnlichen Leistungen vorgestellt, welche jedoch einen stark eingeschränkten Sichtbereich aufwiesen. Eine Verbindung dieser beider Methoden wurde bereits vor etwa 15 Jahren demonstriert, als auf einer Probe positionierte, dielektrische Objekte im Mikrometerbereich in der Lage waren die Probe superauflösend abzubilden. Indem die Proben mittels eines klassischen Mikroskopes durch das Mikroobjekt hindurch beobachtet wurden, konnte das Mikroskop eine virtuelle Abbildung mit Details unterhalb der Lichtbeugungsgrenze erstellen. Obwohl mit dieser Methode der Transfer von Nahfeldinformationen zu Fernfeldinformationen durch das Mikroobjekt bewiesen und als Schlüssel zur superauflösenden Mikroskopie erkannt wurde, blieb der limitierte Sichtbereich, welcher durch die Grösse des Mikroobjektes bestimmt wird, ein Problem.

In dieser Dissertation, stelle ich eine neue Mikroskopiermethode vor, welche es ermöglicht Superauflösung ohne Sichtfeldeinschränkung zu erreichen. Im Einklang mit früheren Studien, wurden dielektrische Mikrosphären für dieses Bildgebungsverfahren ausgewählt. In einem ersten Schritt wurde das Funktionsprinzip dieser Mikrosphären erforscht indem sowohl die Beleuchtung als auch der reflektierte Strahlengang untersucht wurde. Die Ergebnisse dieser Untersuchungen führen zu einem besseren Verständnis des Phänomens der Mikrosphären-unterstützten Bildgebung und ermöglichte es eine Entwicklungs-toolbox zu erstellen, welche zur Gestaltung Mikrosphären-basierter optischer Systeme herangezogen werden kann. Im nächsten Schritt folgte die Erforschung der Mikrofabrikationsprozesse mit dem Ziel einen Mikrochip herzustellen, welcher zur Überbrückung zwischen einer einzelnen Mikrosphäre und den Makrokomponenten des klassischen optischen Mikroskopes verwendet werden kann. Der resultierende Mikrochip wurde daraufhin in ein spezialangefertigtes Fixierungssystem eingebettet, welches das Scannen der Mikrosphäre über die gesamte Probe ermöglicht, während es dessen Position in Relation zum Objektiv fixiert. Eine auf dem Mikroskop fixierte Kamera zeichnet während des Scans Bilder auf, welche mittels Stitching zu einer Fernfeldabbildung vereint werden. Nach den ersten Erfolgen wurde die Konstruktion in Sachen Robustheit

## Zusammenfassung

---

und Anwendungsbereich weiter verbessert. Die neue Version ermöglichte einen Sichtbereich im Millimeterregime, welches sowohl in Öl- als auch in Wasserimmersion genutzt werden kann. Parallele Bildgebung mit mehreren Mikrosphären wurde ebenfalls implementiert, und beschleunigte die Bildgebung weiter. Der algorithmische Hintergrund (einschliesslich eines automatisierten Scanning- und Bildrekonstruierungsprotokolls) dieser Mikroskopiermethode wurde intern entwickelt. Die Validierung dessen zeigte eine verbesserte Leistung gegenüber erhältlicher Software. Weiterentwicklungen, (zum Beispiel die Verwendung von 3D Druckverfahren für die Massenproduktion, *in-vivo* Bildgebung für biologische Proben, metrologische Anwendungen etc.) sind möglich. Die hier vorgestellten Ergebnisse, können den Weg zu einfach anwendbaren, generell suprauflösenden Bildgebungssystemen ebnen.

**Stichwörter:** Superauflösung, optische Mikroskopie, dielektrische Mikrosphären, Rastermikroskopie, Bildverarbeitung, numerische Simulation mittels Finite-Elemente-Methode



# Contents

<b>Acknowledgements</b>	<b>iii</b>
<b>Abstract (English/Deutsch)</b>	<b>v</b>
<b>List of figures</b>	<b>xi</b>
<b>List of tables</b>	<b>xv</b>
<b>1 Introduction</b>	<b>1</b>
1.1 Thesis scope and outline . . . . .	1
<b>2 State-of-the-art of super-resolution optical imaging</b>	<b>3</b>
2.1 Far-field super-resolution techniques . . . . .	4
2.1.1 4Pi confocal fluorescence microscopy . . . . .	4
2.1.2 Stimulated-emission-depletion fluorescence microscopy . . . . .	5
2.1.3 Structured illumination microscopy . . . . .	8
2.1.4 Spatially modulated illumination microscopy . . . . .	10
2.1.5 Single molecule localization microscopy . . . . .	11
2.2 Near-field super-resolution techniques . . . . .	16
2.2.1 Photon tunneling microscopy . . . . .	16
2.2.2 Near-field scanning optical microscopy . . . . .	17
2.2.3 Tip enhanced near-field optical microscopy . . . . .	19
2.2.4 Photon scanning tunneling microscopy . . . . .	21
2.2.5 Near-field optical random mapping nanoscopy . . . . .	21
2.3 Micro-object-based super-resolution imaging . . . . .	22
2.3.1 Fixed micro-object-based techniques . . . . .	23
2.3.2 Scanning micro-object-based techniques . . . . .	36
<b>3 Principles governing micro-object-based imaging</b>	<b>43</b>
3.1 The illumination pathway . . . . .	44
3.2 The reflected light pathway . . . . .	54
<b>4 Microfabrication</b>	<b>63</b>
4.1 Microsphere array fabrication with self-assembly methods . . . . .	64
4.2 Initial microsphere array fabrication on wafer level . . . . .	66

## Contents

---

4.3	Chip for the single microsphere microsystem . . . . .	69
4.4	Chip for the microsphere array microsystem . . . . .	70
<b>5</b>	<b>The single microsphere microsystem</b>	<b>73</b>
5.1	Introduction . . . . .	73
5.2	Materials and methods . . . . .	75
5.3	Results and discussion . . . . .	76
<b>6</b>	<b>The microsphere array microsystem</b>	<b>87</b>
6.1	Introduction . . . . .	87
6.2	Materials and methods . . . . .	88
6.3	Results and discussion . . . . .	91
<b>7</b>	<b>Conclusion and outlook</b>	<b>99</b>
<b>A</b>	<b>Appendix</b>	<b>103</b>
A.1	Supplementary data for section 3.1 . . . . .	103
A.2	Supplementary data for section 3.2 . . . . .	110
A.3	Supplementary data for chapter 5 . . . . .	114
A.4	Copyright licenses . . . . .	116
	<b>Bibliography</b>	<b>121</b>
	<b>Acronyms</b>	<b>135</b>
	<b>Constants &amp; Symbols</b>	<b>137</b>
	<b>Curriculum Vitae</b>	<b>139</b>

# List of Figures

2.1	Schematic of the 4Pi confocal fluorescent microscope . . . . .	5
2.2	Principle of two-photon excitation fluorescent light microscopy . . . . .	6
2.3	Theoretical and instrumental background of stimulated-emission-depletion fluorescence microscopy . . . . .	7
2.4	Population probability and effective point spread function in ground-state-depletion fluorescence microscopy . . . . .	8
2.5	Concept of structured illumination microscopy . . . . .	9
2.6	Illumination pattern in spatially modulated illumination microscopy . . . . .	10
2.7	Principle and schematic of photoactivated localization microscopy . . . . .	13
2.8	The stochastic optical reconstruction microscopy . . . . .	14
2.9	Schematic of the photon tunneling microscopy . . . . .	16
2.10	Different imaging modes in near-field scanning optical microscopy . . . . .	17
2.11	Different illumination types in tip enhanced near-field optical microscopy . . . . .	20
2.12	Schematic of the near-field optical random mapping nanoscope . . . . .	22
2.13	First representation of the photonic nanojet . . . . .	24
2.14	The first observation of a photonic nanojet . . . . .	25
2.15	The (white-light) optical nanoscopy . . . . .	27
2.16	The effect of illumination on the photonic nanojet . . . . .	28
2.17	Super-resolution imaging with barium titanate glass microspheres . . . . .	30
2.18	Comparison of the imaging performance of a solid immersion lens against a microsphere . . . . .	32
2.19	Microsphere-based super-resolution imaging with a scanning laser confocal microscope . . . . .	33
2.20	Targets for characterizing the resolution . . . . .	36
2.21	The layout of the optical setup for scanning a microsphere over the sample surface with a micropipette . . . . .	36
2.22	Parallel wide-field imaging with uniform microspheres . . . . .	38
2.23	The microsphere-based scanning superlens microscopy . . . . .	39
2.24	Optical response in microsphere-based, atomic force microscopy assisted bright-field microscopy . . . . .	40
2.25	Parts of the superlensing microscope objective lens . . . . .	41
3.1	Mechanism of photonic nanojet generation . . . . .	45

## List of Figures

---

3.2	Numerical simulations of the light propagation through dielectric microspheres	46
3.3	Mechanism of imaging through a dielectric microsphere . . . . .	47
3.4	Analysis of the numerical simulation results . . . . .	47
3.5	Imaging of a grating nano-structure using different size microspheres . . . . .	48
3.6	Analysis of the magnification factor . . . . .	49
3.7	Experiments for the quantification of the resolution . . . . .	49
3.8	Measured data from the resolution quantification experiments . . . . .	50
3.9	Results of the resolution quantification experiments . . . . .	53
3.10	Analysis of the illumination profile in the imaging region of a microsphere . . .	55
3.11	Analysis of the illumination for barium titanate glass and soda-lime glass microspheres with various diameters . . . . .	56
3.12	Calculation of the enhanced-resolution zone created by the microsphere . . . .	58
3.13	Quantitative estimation of the resolution gain in presence of the microsphere .	59
3.14	Experimental confirmation of the predictions for different configurations . . .	60
3.15	Effect of the optical contrast and the microsphere size on the resolution gain .	61
4.1	Summary of the self-assembly-based microsphere-array-chip fabrication . . .	65
4.2	Comparison of the different patterning methods . . . . .	66
4.3	Process flow of the first glass-silicon-sandwich template chip . . . . .	67
4.4	The glass-silicon template chip . . . . .	68
4.5	Schematic of the fabrication process of the microsphere array chip . . . . .	71
4.6	Photographs of the fabricated microsphere array chip . . . . .	71
5.1	Principle of operation of the super-resolution scanning optical microscope . .	75
5.2	Image obtained after a single scan step and analysis of the super-resolution effect	77
5.3	Photograph of a 100 nm-wide line from a microscope calibration target . . . . .	78
5.4	Simulated electric fields of light propagation originating from a line pattern sample source placed at varying distances beneath a microsphere . . . . .	80
5.5	Analysis of the simulation results . . . . .	81
5.6	Scanning and image reconstruction . . . . .	82
5.7	Scanning and image reconstruction of a Blu-ray disk surface . . . . .	83
6.1	Operation principle of the improved imaging system . . . . .	89
6.2	The improved imaging setup . . . . .	90
6.3	Demonstration of the microsphere scanning process . . . . .	91
6.4	The dependency of the modulation on the radial distance . . . . .	92
6.5	Resolution analysis of the oil- and the water-immersion system in static imaging mode . . . . .	94
6.6	Resolution analysis of the oil-immersion imaging in dynamic mode . . . . .	95
6.7	Demonstration of large area imaging with super-resolution . . . . .	96
7.1	Future development plan of the scanning process . . . . .	100
7.2	Demonstration of the new scanning technique . . . . .	101

7.3 Demonstration of <i>in vivo</i> imaging . . . . .	102
A.1.1 Numerical study on photonic nanojet generation . . . . .	104
A.1.2 Comparison of the photonic nanojets generated by coherent and incoherent light sources . . . . .	105
A.1.3 Simulated intensity profiles at the waist of the photonic nanojet . . . . .	107
A.1.4 Evaluation of the simulated intensity profiles at the waist of the photonic nanojet	108
A.1.5 Fitting parameters . . . . .	109
A.2.1 Analysis of the illumination profile in the imaging region . . . . .	111
A.2.2 Analysis of the illumination profile in the imaging region II. . . . .	112
A.2.3 Notation for light path calculation . . . . .	113



# List of Tables

5.1	Performance evaluation of super-resolution imaging systems . . . . .	85
A.1.1	Computed values of the standard deviation for the illumination profiles . . .	108
A.3.1	Electric field simulation results for different lines-and-spaces patterns . . . .	115





# 1 Introduction

Classical optical microscopy is limited in resolution by Abbe's law, stating that no smaller features than half the wavelength of the illuminating light in free space, divided by the product of the refractive index and the angle at which the light can be captured by the microscope objective, can be observed. However, numerous microscopy systems were presented in the last decades, which proved resolution beyond Abbe's limit. The utilization of fluorescent samples and smart engineering of the illumination protocol allowed super-resolution (*i.e.* resolving features below the diffraction limit of the imaging system) for far-field microscope techniques. Parallel to this, optical near-field imaging systems were shown, offering excellent resolution but with a limited field-of-view. To overcome this issue, the latter methods implemented scanning protocols, but these increased the imaging time significantly. Furthermore, complex instrumentation was needed for most of them. Around 15 years ago, a new approach was born that was based on the near-field information transfer to the far-field, therefore enabling high resolution with low-cost far-field instrumentation and without the need of fluorescent samples. The technique was called micro-object-based super-resolution imaging, because its key element was to place a micrometer-sized rotational-symmetric object (typically a lens, cylinder or sphere) on top of the sample. As the object was in close contact with the surface of the sample, the former was able to collect and transfer the near-field information into the far-field, which resulted in a microscopy technique, in which a classical optical microscope could achieve super-resolution by observing the specimen through this object. However, an issue was that the field-of-view became limited by the dimension of this micro-object and its location could not be changed after the initial placement on the sample.

## 1.1 Thesis scope and outline

Here, a novel method is presented that aims to overcome these limitations and therefore creates the possibility of generalized, easy-to-use micro-object-based optical super-resolution imaging. Based on previous studies (chapter 2), we have chosen dielectric microspheres for this microscopy technique. To fully understand the operation principle of such microspheres, an extensive study was carried out, where both the illuminating and the reflected light path

was investigated (chapter 3). The former showed that the light gets confined as it travels through the microsphere and eventually focused into a tiny spot (called photonic nanojet) on the shadow-side of the sphere. It was demonstrated numerically and confirmed experimentally that the dimensions of this photonic nanojet play a significant role in the resolution and magnification of the imaging system, utilizing 2 to 20  $\mu\text{m}$  diameter dielectric glass spheres. However, because of practical considerations, bigger diameter spheres were more beneficial for implementing a more extended field-of-view. As for the bigger diameter microspheres (20 to 80  $\mu\text{m}$  in this study) ray tracing is enabled, the path of the reflected light could be studied analytically. These quantitative results provided information about the important factor of the optical contrast between the refraction index of the sphere and its surrounding medium. Furthermore, the effect of the size and material of the microsphere on the final resolution of the imaging system was also demonstrated. These predictions were later confirmed experimentally.

Based on the theoretical results, various microfabrication techniques were explored (chapter 4) to construct a microscopy method, where the field-of-view of a single microsphere could be extended by scanning. The first prototype of such a system was built and characterized and used a mechanical frame that held a glass template chip, on which a dielectric microsphere was fixed, in a steady position compared to the microscope objective of a classical optical microscope (chapter 5). Meanwhile, the sample was placed on a motorized stage that was scanned over a large area. During every step of the scan, an image was taken by the microscope-mounted camera and the thus obtained images were later reconstructed by an in-house written algorithm that generated the final, big field-of-view super-resolution image. This proof-of-concept device was then upgraded into a more robust system by enhancing both the microsphere-containing chip and the fixation system (chapter 6). Therefore, the latest version of the microsphere-based optical microscope could achieve super-resolution both in oil- and water-immersion, meanwhile providing a bigger field-of-view than the classical optical microscope's objective. The size of the imaged surface area had no intrinsic limitations, however scanning time scaled linearly with it. This increment was reduced by introducing an array of microspheres that could image in parallel. The presented image reconstruction algorithm also added a time factor, but the algorithm we developed was shown multiple times faster than existing stitching software.

The presented findings may be at the basis of a future generalized and affordable scanning super-resolution optical microscopy with huge potential in many research fields (*e.g.* life sciences, diagnostics, environmental monitoring, and robotics). We believe that our current results may help repositioning dielectric microsphere-based optical scanning super-resolution microscopy beyond the proof-of-concept stage towards a fully operational real-life application.

## 2 State-of-the-art of super-resolution optical imaging

*This chapter provides an overview of the state-of-the-art optical super-resolution techniques. In the first section, the far-field techniques are discussed that can be considered as the direct evolution of traditional optical microscopy, however, they mostly operate with fluorescent samples. In the second section, near-field techniques are presented that achieve super-resolution by maintaining a close distance to the sample, such that evanescent waves can be captured and processed. These methods typically involve some scanning procedure to be able to map a reasonably big area of the sample. Finally, in the third section, microobject-based techniques are showed. These represent a relatively new branch of this research field, as the pioneering works appeared only ~15 years ago. This section also discusses the basis and the motivation of this thesis.*

---

The basics of optics were already discovered by the ancient Greeks, who used simple lenses for focusing light [1]. In the Roman empire, magnifying glasses were already part of everyday life, as both Seneca (4 BCE - 65 CE) and Emperor Nero (37 CE - 68 CE) were reported to utilize them. Several centuries later, in 984 CE, the law of refraction, currently known as Snell's law, was already described by Ibn Sahl, who was a scientist at the court of Baghdad [2]. In the 17th century many famous scientist, including Thomas Harriot, Johannes Kepler, Willebrord Snellius and Rene Descartes rediscovered this law. In the same era, the first real optical microscope was built by Antonie van Leeuwenhoek, whose device achieved multiple fold magnification compared to prototypes created before his time. In the next 200 years, in the classical era of optical microscopy, instruments reached higher magnification, better resolution and already started to compensate aberrations. It was Ernst Karl Abbe, who laid down the basics of modern microscopy together with Otto Schott and Carl Zeiss at the end of the 19th century. Abbe's most significant contribution was the law named after him, which describes the relation between the diffraction limit (*i.e.* lowest detectable feature) ( $d$ ), the

wavelength of the light ( $\lambda$ ) and the numerical aperture ( $NA$ ).

$$d = \frac{\lambda}{2 \times NA} \quad (2.1)$$

This simple equation immediately showed the limit of optical microscopes and also the two possible development directions to overcome this restriction. To reach smaller  $d$ , either the wavelength must be smaller or the  $NA$  bigger. Various techniques achieving the latter or applying other methods to overcome this limitation will be discussed in the following sections. On the other hand, techniques involving wavelengths outside the visible light region will not be discussed here since the scope of this thesis focuses on optical methods.

### 2.1 Far-field super-resolution techniques

For more than a century it seemed that it is impossible to overcome the diffraction limit only by detecting the propagating waves emerging from a sample placed under the microscope (*i.e.* with far-field microscopy). Although sub-diffraction imaging was already possible by electron microscopy, or by near-field imaging, where information from the evanescent waves is extracted, the need to accomplish similar resolutions with far-field optical microscopy was still present. The motivation for this arrived from biology, because those samples needed to be investigated in-depth (*i.e.* not only at the surface), furthermore, *in vivo* imaging was also desired. The breakthrough came, when fluorescence-based super-resolution imaging techniques started to be developed in the beginning of the 1990s.

#### 2.1.1 4Pi confocal fluorescence microscopy

The patent of 4Pi microscopy was filed in 1990 [3] and the description was published in 1992 [4]. The significant improvement compared to confocal fluorescence microscopy (*CFM*) was to introduce two opposing microscope objective lenses for illumination and detection. A confocal system has an illumination and a detection intensity distribution which are described by the illumination- and detection-point spread function (*PSF*), respectively. Multiplying these two gives the confocal *PSF*, which determines the lateral and axial resolution of the system. Introducing a second microscope objective to such a system can increase the aperture of the system in two ways. Either the objectives generate coherent illumination wavefronts that constructively meet in the common focus or the collected fluorescent lights interfere constructively in the common point detector. This criteria enables three operation mode for the 4Pi microscope: Type A) illumination interference [5]; Type B) detection interference [6]; Type C) illumination and detection interference [4].

The first presented imaging setup of the 4Pi microscopy was mounted on an optical bench (see Figure 2.1). The light amplification by stimulated emission of radiation (*Laser*) light source was split towards the two objectives and the detected fluorescent signals were directed into the same photomultiplier. The sample was placed on a motorized stage that allowed 5 nm

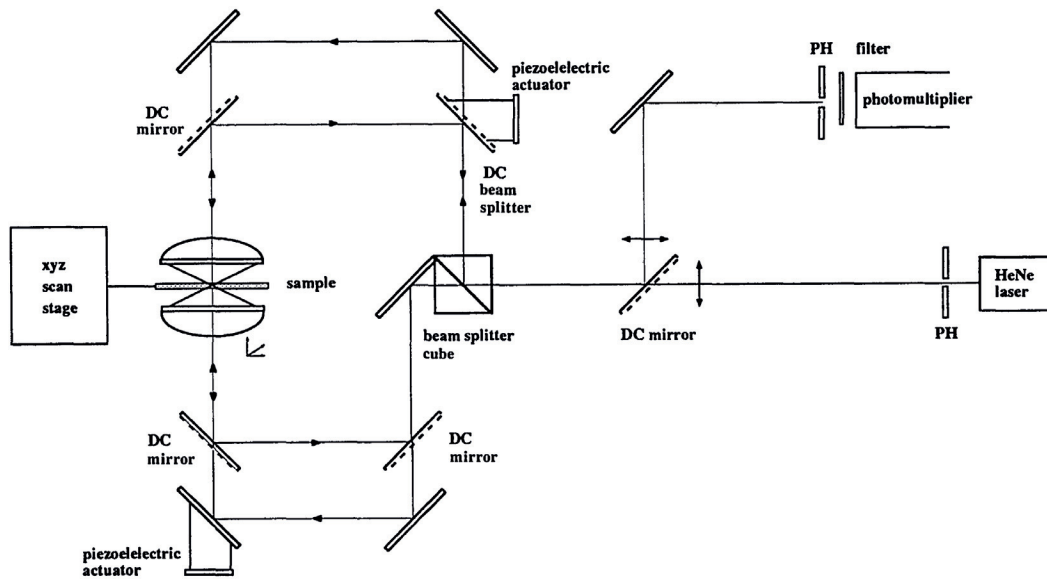


**Figure 2.1** – Schematic of the first 4Pi confocal fluorescent microscope, assembled in the European Molecular Biology Laboratory. Reproduced from [4].

steps over  $20\ \mu\text{m}$  distance for scanning. With this instrument a fourfold increment in the axial resolution was demonstrated, compared to the classical *CFM* setup, as the full width at half-maximum (*FWHM*) of the central peak was measured to be  $110\ \text{nm}$ . It was also shown that the instrument can operate in two-photon excitation mode which can further improve the achievable resolution [5]. A general advantage of the 4Pi microscope is that only half the light intensity is needed to expose the sample, therefore it gives better protection against out-of-focus bleaching. Furthermore, it can reach the same intensity and signal-to-noise ratio (*SNR*), as *CFM*, with smaller probe volume. The cost of these improvements is the expensive instrumentation as high-end objectives and other optical components (*e.g.* piezo-actuators, *Laser*, photomultiplier) are needed for the setup. It is also important to note that this microscopy system images fluorescent samples with scanning, which removes time-sensitive imaging from the application range and limits sample classes.

### 2.1.2 Stimulated-emission-depletion fluorescence microscopy

The introduction of 4Pi microscopy showed that Abbe's resolution limit can be overcome in axial direction, when imaging fluorescent samples. Achieving the same improvement in the lateral direction was shown only a few years later [7]. The technique was called two-photon excitation fluorescent light microscopy. The concept of this imaging setup was to place two point-like excitation sources laterally, to generate an overlap of their *PSF* in the focal plane of the imaging objective (Figure 2.2). It was shown that the *PSF* can be significantly narrower depending on the offset of the two light sources. A limitation of the offset positions is the appearing side lobe in the *PSF*. This would decrease the image quality, but can be suppressed with a point-like (*i.e.* confocal) detection as shown in Figure 2.2. Another issue is that as

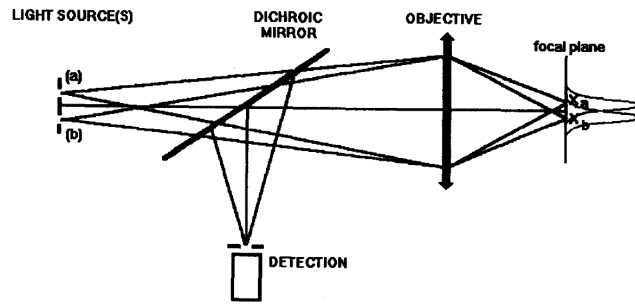


**Figure 2.2** – Schematic of the light paths in two-photon excitation fluorescent light microscope. Reproduced from [7].

the offset increases, the probability of the two-photon excitation decreases, as the overlap of their *PSF* becomes smaller and smaller. The offset between the excitation points can be achieved in two ways. Either two light sources with different wavelength are needed or a femtosecond *Laser* must be used. Due to the detector limitations mentioned earlier, high intensity illumination is needed for the imaging, however, this may damage biological samples, therefore, the latter illumination type is preferred. It was shown that with offsetting, the *PSF* can be reduced up to 59%, which corresponds to 75 nm lateral resolution considering visible light and conventional optics.

As an improvement of the two-photon excitation technique stimulated-emission-depletion (*STED*) fluorescence microscopy was developed [8]. It is known that the *PSF* determines the resolution of a scanning fluorescent microscope and that reducing its spatial extent is the key to improvement. A way of reduction, as presented in this imaging system, is to inhibit the fluorescence in the outer regions of the *PSF*. In order to understand how that is possible, the energy levels of a typical fluorophore have to be considered as shown in Figure 2.3.a. The  $L_0 \rightarrow L_1$  transition is induced by the point source (*i.e.* a *Laser* focused onto a pinhole). The  $L_1 \rightarrow L_2$  and  $L_3 \rightarrow L_0$  transitions are due to vibrational relaxation, meanwhile the  $L_2 \rightarrow L_3$  is the spontaneous emission that is three orders of magnitude faster, than the first two. This time difference allows the interaction that is the key element of *STED* technique. If a second *Laser* is introduced into the system, it is possible to artificially induce the  $L_2 \rightarrow L_3$  transition, therefore depleting the excited state before fluorescence takes place.

In practice this is achieved by placing a secondary (*STED*-) *Laser* next to the primary excitation *Laser* (Figure 2.3.b). The secondary beam is split into two and focused to the focal plane with a  $\pm 3 < \nu < 7$  optical unit offset. The optical unit  $\nu = 2\pi r NA / \lambda_{exc}$  where  $r$  is the distance from the focal point,  $NA$  is the numerical aperture of the objective lens and  $\lambda_{exc}$  is the excitation wavelength (*i.e.* the wavelength of the primary *Laser*). The depletion and the correlation resolution increment caused by these beams depends on their intensity values. Assuming  $\lambda = 600$  nm wavelength and  $1300 \text{ MW/cm}^2$  intensity for the *STED-Laser*, the *PSF* can be narrowed to reach a resolution increment of 3.4 and 4.5 times compared to *CFM* and conventional fluorescent microscope, respectively. Calculating for a dye that can be excited at  $\lambda = 490$  nm and its emission is at  $\lambda = 600$  nm, this means 50 nm lateral resolution using  $NA = 1.4$  objective and setting the *STED-Laser* to  $\Delta\nu = 3.9$  offset. Altering the dye emission wavelength to the

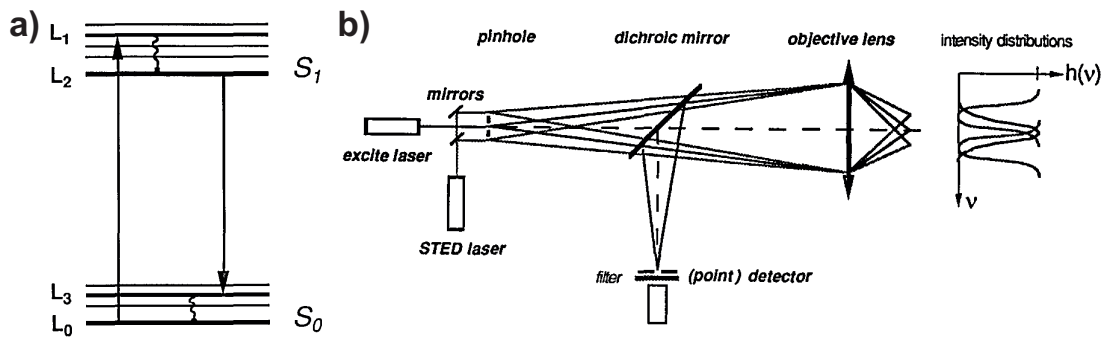


**Figure 2.3** – Theoretical and instrumental background of *STED* fluorescence microscopy. **a)** The possible energy levels of a typical fluorophore. **b)** Schematic of the light paths in *STED* fluorescence microscopy. Reproduced from [8].

low-end of the visible light spectrum (*i.e.* to 400 nm) would result in 35 nm resolution, which is deeply below the classical resolution limit. The price of such a big resolution enhancement ( $\sim 3$  times) is the signal strength which is only  $\sim 25\%$  of a conventional microscope's. Furthermore, the beam intensities are typically in the  $10^8$  to  $10^{10}$  W/cm<sup>2</sup> range, which is considerably big [9]. Despite of this, these results place this imaging method to one of the top ranks in far-field light microscopy techniques, since it has such a high lateral resolution, which is even comparable with near-field techniques. The development of this microscopy was awarded with the Nobel-price in chemistry in 2014 [10].

An improvement on further exploiting the resolution decreasing effect of the stimulated depletion, called ground-state-depletion (*GSD*) fluorescence microscopy, was reported in 1995 [11]. This concept showed how it is possible to achieve  $\sim 10$ -20 nm lateral resolution with low-power continuous-wave illumination. Because of the specific illumination type, the triplet state plays a significant role in the possible energy states of the fluorophore. As Figure 2.4.a shows, above 10 MW/cm<sup>2</sup> intensity, the ground state (marked as  $S_0$  in Figure 2.3.a) is depleted, as all the molecules are in singlet or triplet state. Calculating the *PSF* for different intensities show how much resolution gain can be achieved (Figure 2.4.b). In the case of 1 MW/cm<sup>2</sup> intensity, this enhancement is six-fold, compared to a classical scanning fluorescent microscope, but having a fluorophore with faster inter-system crossing time can increase this value to eleven-fold. The latter would mean 15 nm lateral resolution using  $NA=1.4$  objective and a fluorescent dye with  $\lambda_{exc}=400$  nm. To reach this intensity at the focal plane with the objective used for the previous calculation, only 1 mW illumination power is needed, which is not extraordinary from practical point-of-view. Technically there are no other factors that would hinder experimentation, as recording time can be comparable with a standard scanning *CFM* and the chemical environment can be adjusted to hinder photo-bleaching.

Despite of the clear concept, the realization of this microscopy technique was not pursued until 2007 [9]. The breakthrough happened by discovering conditions at which  $\mu$ s- and ms-long optical shelving is practical, with special attention to the chosen combinations of dyes and media. The other critical factor was the light intensity used for depletion. The resolution

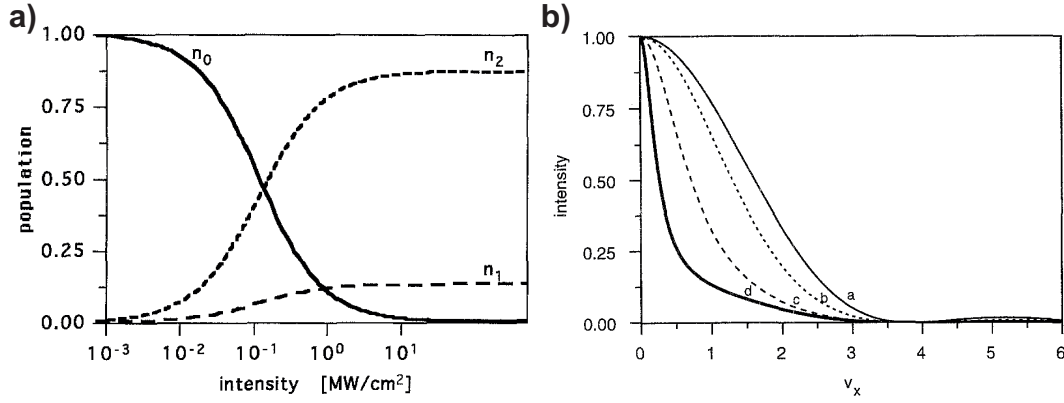


**Figure 2.4** – Population probability and effective point spread function in *GSD* fluorescence microscopy. **a)** The population probability of the ground state ( $n_0$ ), the first singlet state ( $n_1$ ) and the triplet state ( $n_2$ ) as a function of the excitation intensity. **b)** The effective *PSF* along the focal plane in the case of 0.01 (b), 0.1 (c) and 1 (d) MW/cm<sup>2</sup> intensity depletion beam (*GSD* technique), compared to a classical scanning fluorescent microscope (a). Reproduced from [11].

of *GSD* fluorescence microscopy is given by the following equation,

$$d \approx \frac{\lambda}{2 \times NA \sqrt{1 + \frac{I_D^{MAX}}{I_S}}} \quad (2.2)$$

where  $I_D^{MAX}$  is the depletion beam intensity and  $I_S$  is the saturation intensity at which half of the fluorescence is depleted. Equation 2.2 implies that the depletion beam intensity should be increased as high as possible to reach the lowest resolution, however, this would cause an imminent photo-bleaching. Therefore practically depletion intensity values are in the kW/cm<sup>2</sup> range. The low intensity normally means longer recording time, but this was compensated by a special image recording technique and processing algorithm. With such an illumination condition 50 nm - 90 nm lateral resolution was reached, depending on the shape of the depletion beam in the focal plane. Although these values were higher than the theoretical predictions presented in [11], further improvements in the imaging system showed that lateral resolution down to  $\approx 7,6$  nm can be reached with this microscopy technique [12]. The only disadvantage of the *GSD* fluorescent microscopy is the fluorescent dye that needs to be added to the sample and simultaneously has to be in a good combination with the surrounding medium in order to enable successful imaging.

### 2.1.3 Structured illumination microscopy

The structured illumination microscopy (*SIM*) was patented in 1995 [14], but its full description was presented only in 2000 [13]. The motivation behind this development was to be able to improve the lateral resolution, since existing *CFM*-based techniques suffered from a limitation set by the used pinhole sizes. To achieve smaller resolution, a smaller pinhole is



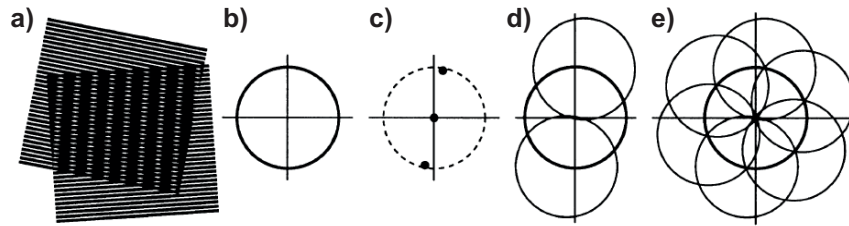


**Figure 2.5** – The concept behind *SIM*. **a)** Two fine patterns are superposed, generating Moiré fringes. **b)** The observable region of a conventional microscope in Fourier space. **c)** A sinusoidally striped illumination pattern that has three Fourier components, from which two is on the side and their position is limited by the same circle as in **b)**. **d)** Upon illumination, Moiré fringes will appear that represent information that changed position in the Fourier space. Therefore the observable region will be expanded with additional information, originating from the two offset regions. **e)** Repeating this method in sequence leads to recovering information from an area up to twice the size of the original observable region. This corresponds to twice the normal resolution. Reproduced from [13].

needed, but that discards much of the in-focus emission light together with the unwanted out-of-focus light. On the other hand, biological samples often produce a very weak signal, therefore, a larger pinhole is needed for their detection. However, by increasing the size of the pinhole, the resolution enhancement becomes minimal and eventually negligible.

The concept behind *SIM* can be explained by a simile with Moiré fringes. If two patterns with fine details are superposed multiplicatively, a third, coarser pattern will appear (Figure 2.5.a). If only one of the fine patterns and the superposed pattern is known, the other fine pattern can be calculated. Translating this idea to microscopy shows how imaging is performed. One of the fine patterns is the spatial distribution of the fluorescent dye, that needs to be imaged. The other fine pattern is the structured excitation light intensity. The superposed pattern is given by these two and can be observed with the microscope setup. Considering a conventional microscope with diffraction limit  $d_0$ , its resolution capabilities can be represent as a circle with radius  $1/d_0$  in Fourier space (Figure 2.5.b). Applying structured illumination to this system does not increase the radius, but makes it possible to involve information from outside it. As an example, a sinusoidal stripe pattern is considered (Figure 2.5.c). Such pattern has three non-zero points in Fourier space, from which two is in offset from the origin. Their position is determined by the direction and line spacing of the illumination pattern, but the distance from the origin cannot exceed the original radius. Upon imaging, Moiré fringes will appear that contain information -that would be impossible to get with a classical microscope,- from these offset regions (Figure 2.5.d). By repeating this operation with differently oriented patterns, it is possible to double the size of the observable region (Figure 2.5.e).

The instrumentation needed to construct *SIM* does not differ significantly from a confocal microscope. The main difference between the two is a diffraction grating that is used to generate high-contrast stripe pattern with feature size close to the resolution limit of the attached microscope objective. Furthermore, this grating has to be able to rotate for enabling the full imaging potential of the instrument. Experimental results showed that lateral resolution can be significantly improved with this technique. Meanwhile only 290 nm *FWHM* features were

## Chapter 2. State-of-the-art of super-resolution optical imaging

detected by a conventional microscope, *SIM* could improve that more than two-fold, down to 115 nm. Exposure times of 1-10 s were reported with an additional 30 s processing time. This included parameter fitting and did not use any *a priori* information. If these are used for the computation, the process could be speeded up to near real time, since the method is linear and deterministic.

An improved version of *SIM*, achieving 50 nm lateral resolution was reported in 2005 [15]. This advanced wide-field imaging technique was called saturated structured illumination microscopy (*SSIM*). The non-linearity arising from the saturation of the exciting light allowed to further decrease the resolution limit. To achieve this, long exposure times were needed, which made *in vivo* imaging difficult. For the same reason photostable and brightly labeled samples are obligatory in this method. It must be noted, that although scanning is not needed for *SSIM*, it still relies on image processing, which adds an extra time factor to the imaging.

### 2.1.4 Spatially modulated illumination microscopy

The first prototype of spatially modulated illumination (*SMI*) microscope was built C. Cremer's laboratory in Heidelberg in 1997 [16], [17]. It utilized interferometric illumination combined with optical sectioning to achieve high precision localization and resolution increment along the optical axis. The setup consisted of a coherent light source that was separated and lead into two objectives which were placed on the opposite side of the sample. The light was linearly polarized, collimated and interfered under an angle  $\nu$  (Figure 2.6). The convolution of the *PSF* of the resulted fringe pattern and the *PSF* of the object fluorochrome distribution resulted the image of the sample objects. For *3D* localization, scanning of the image planes was needed. Because of the special illumination pattern, the axial resolution was decreased to the half-distance ( $d/2$ ) between the wave fronts as shown in Figure 2.6. Such an improvement enabled localization with nanometer precision.

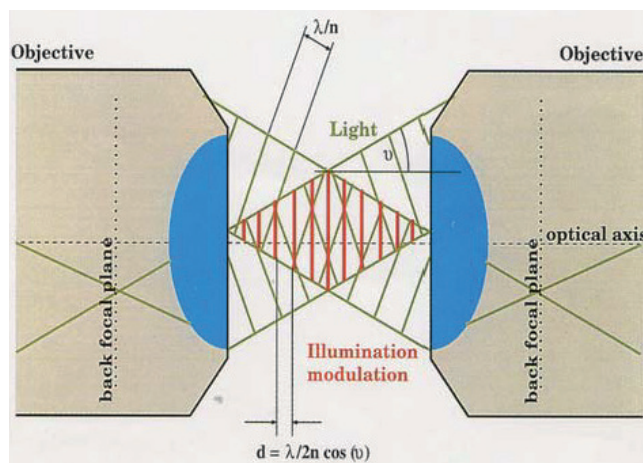


**Figure 2.6** – Illumination pattern in spatially modulated illumination microscopy. Reproduced from [18].

While the first prototype consisted of only one coherent light source, later developments applied a second one to allow the localization of different spectral signatures independently [18]. The key optical components were very similar in both cases. The light was divided evenly by a beam splitter and focused to the back focal plane of both objectives by two lenses. To control the length of one of the light paths a piezoelectric motor was placed between the beam splitter and the focusing lens. Another piezoelectric element was controlling the stage movement along the optical axis, which was needed for 3D scanning. All of the components were assembled on a thermally stabilized breadboard to conserve the stability of the illumination pattern during the image acquisition. For that, typical reported times were between 2-4 s per image plane. Therefore a sample volume of  $\sim 50 \mu\text{m} \times \sim 50 \mu\text{m} \times \sim 10 \mu\text{m}$  could be imaged in  $\sim 25$  min. Although imaging is not immediate, its accuracy is remarkable as both axial and lateral resolution was in the nanometer range [16]–[19].

A significant improvement was reported in 2008, when a full upright positioned imaging system was built on the bases of the *SMI* microscope prototype. The setup was upgraded to have three different wavelength coherent light sources and a white light emitting diode (*LED*) to reduce photo-bleaching during the initial search for the focal plane. Further additions like water-immersion objectives instead of oil-immersion ones, incubator chambers for cell cultures, air-flow and temperature control enabled near-real time observation of live cells. Finally, data acquisition speed was increased to reduce the imaging time to  $\sim 2$  s. It was also shown that this instrument can be operated both in "*SMI*" and "*2D* localization" mode. (Localization methods are detailed in section 2.1.5.) The former offers excellent axial resolution (44 nm diameter microspheres ( $\mu\text{S}$ -s) were imaged), meanwhile the latter has superior resolution in one image plane ( $\sim 15$  nm localization accuracy was demonstrated). The continuous improvement of the *SMI* microscopy placed this technique as one of the most complex and accurate light-based imaging techniques, but it still has one constrain, namely the need for fluorescent labelling, which cannot be avoided.

### 2.1.5 Single molecule localization microscopy

Single molecule localization microscopy (*SMLM*) hallmarks a branch of computational-based microscopy techniques that achieve super-resolution by precision distance and position measurements of individual emitters. The algorithmic basis behind these processes was established in 1997 [20], [21]. Originally, the algorithm was designed for high-precision distance measurement and for volume-conserving segmentation of fluorescent samples. Its accuracy was only given as an upper estimation of less than 60 nm, due to the unoptimized routine and experimental parameters. These results were obtained on a simulated data set and the evaluation took 3-10 min. Note, that at that time a 200 MHz clock frequency processor with 96 MB memory was used, which has multiple times less computational capacity than an entry-level consumer smartphone in 2018. Even under these conditions, the limitations of the method were already shown, namely, that there must be a minimal distance between the individual points, otherwise the algorithm can merge multiple objects. This indicates that dense populations must be separated with a method that generates different spectral signature

for the individual targets or for a sub-population of them. The concept was validated experimentally by measuring clusters of monodisperse quartz glass spheres [20] and pentacene molecules embedded in a *p*-terphenyl host crystal [22]. The former experiment achieved 15 nm lateral resolution in-plane and 55 nm out-of-plane, meanwhile the latter demonstrated 40 nm laterally and 100 nm axially. This technique was later referenced as spectral precision distance / spectral position determination microscopy (*SPDM*).

A new approach in localization microscopy was presented in 2005, when it was shown that super-resolution can be achieved with intermittent fluorescence of quantum dots and independent component analysis [23]. This type of analysis can separate the individual sources from the convoluted signals provided by the detectors (*i.e.* the pixels in the charge-coupled device (*CCD*)), if the following four criteria are met: (i) the individual fluctuations of the source must be statistically independent - quantum dots meet this condition; (ii) the probability distribution must be non-Gaussian - sampling in short time transforms the distribution into bimodal (*i.e.* on-off like); (iii) the convoluted detection signals, originating from the ensemble of sources, are linear combinations from the individual source signals and the latter need to be sufficiently apart, so that they are distinguishable at a given moment in time; (iv) the number of detectors is equal or greater than the number of sources - this would set a limit to the number of separable sources but can be increased with oversampling. The concept was experimentally proven as a set of 500 images of  $256 \times 256$  pixels size were taken and processed, showing finally the image of quantum dots with  $\sim 20$  nm lateral resolution in *2D*.

A further reflection of this idea is the photoactivated localization microscopy / fluorescence photoactivation localization microscopy (*PALM* / *FPALM*) [24], [25]. The two techniques were published only with a few months of difference from two different research groups, but the principle of them is the same and shown in Figure 2.7. Two *Lasers* are utilized for illuminating the sample, one for readout and one for activation. The latter one turns "on" with a brief pulse some of the fluorescently labelled targets in the sample, which are imaged and localized by the post-processing algorithm. Due to the imaging with the read-out *Laser*, these targets get photo-bleached with time and irreversibly turn into dark, meanwhile new targets are activated by a new pulse. This cycle is repeated until enough information is gathered to construct the final super-resolution image. The process can take up to several hours depending on the desired quality of the final result. In optimal conditions  $\sim 10$  nm lateral resolution was shown in fixed thin slices [24]. It was also demonstrated that this technique can be used *in vivo*, in this case  $\sim 40$  nm lateral resolution was achieved [26]. Although the resolution capabilities of this method are superb, the *PALM* / *FPALM* suffers from three major inconveniences: (i) it is sensitive to diffuse background, therefore its suppression is needed (*e.g.* by using total internal reflection fluorescence microscopy); (ii) usually thin samples are needed; (iii) acquisition times can be huge (up to 12 hours).

To overcome these issues, an improved method, called PALM with independently running acquisition (*PALMIRA*) was developed in 2007 [27]. The exposure time of a fast *CCD* camera was matched with the average on-time of a novel, reversibly switchable fluorescent protein. Since this protein could be switched on and excited at the same wavelength, one *Laser* light source was enough in the setup. Furthermore, because no synchronization was needed between the

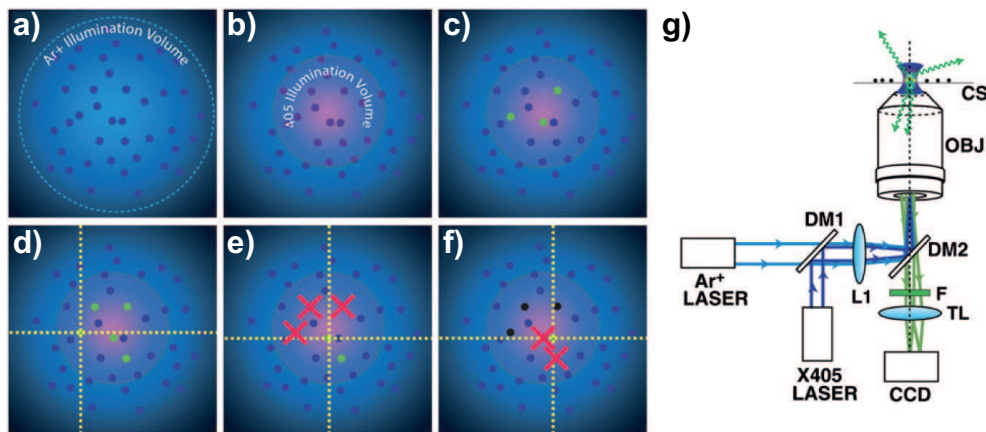


**Figure 2.7** – Principle and schematic of *PALM / FPALM*. Spatial illumination profile of **a)** the readout *Laser* ( $\text{Ar}^+$  ion *Laser*) and **b)** the activation *Laser* (405 nm diode *Laser*). Some of the fluorescently labeled samples are activated (green dots) within the illumination region **c)** and localized **d)**. **e)** As targets photo-bleach due to overexposure (red crosses), they become irreversibly dark, meanwhile new targets get activated **f)**. The process is repeated until sufficient amount of signal is detected for super-resolution imaging. **g)** Schematic of the microscope setup. Sample (CS) is illuminated with two *Lasers* through a focusing lens (L1) and two dichroic mirrors (DM1 and DM2). Emitted fluorescence from the sample arrives to the camera (CCD) through a filter (F) and focusing lens (TL). Reproduced from [25].

excitation and the readout, the data collection time could be significantly improved. This was possible, because during imaging a dynamic equilibrium was formed by these molecules, in which most of them were in the dark state and only a small fraction was activated in random times. This activation crosstalk, which was practically the  $\sim 0.2\%$  probability of on-state proteins at a time was the key component that enabled all of the aforementioned improvements. Due to the asynchronous 500 Hz camera frame rate, background suppression was not needed any more. Imaging experiments showed  $\sim 50$  nm lateral resolution with total acquisition time of  $\sim 2.5$  minutes including all image processing. However, these outstanding results were achieved at a cost of narrowing the possible sample classes to reversibly switchable fluorophores.

Parallel to *PALM / FPALM*, a very similar localization technique, stochastic optical reconstruction microscopy (*STORM*) was introduced in 2006 [28]. Its governing principle was based on switching fluorescent molecules on and off with two, different color *Lasers*, as it is shown in Figure 2.8. The cycling process started with turning all molecules into the dark state with a pulse generated by the red *Laser* ( $\lambda=633$  nm). This pulse did not permanently photo-bleached the molecules, but converted them into a photo-reversible non-fluorescent state [29]. Then a short pulse from the green *Laser* ( $\lambda=532$  nm) arrived that turned on (*i.e.* converted back to fluorescent state) a subset of the fluorophores in a way that the population density was low enough for accurate localization. After this pulse the red *Laser* served as excitation until the probes were turned off again. This cycle was repeated until sufficient amount of information was collected to construct the final image of the sample. It was also shown that the deoxyribonucleic acid (*DNA*) bound Cy5 switch can be turned on and off hundreds of times

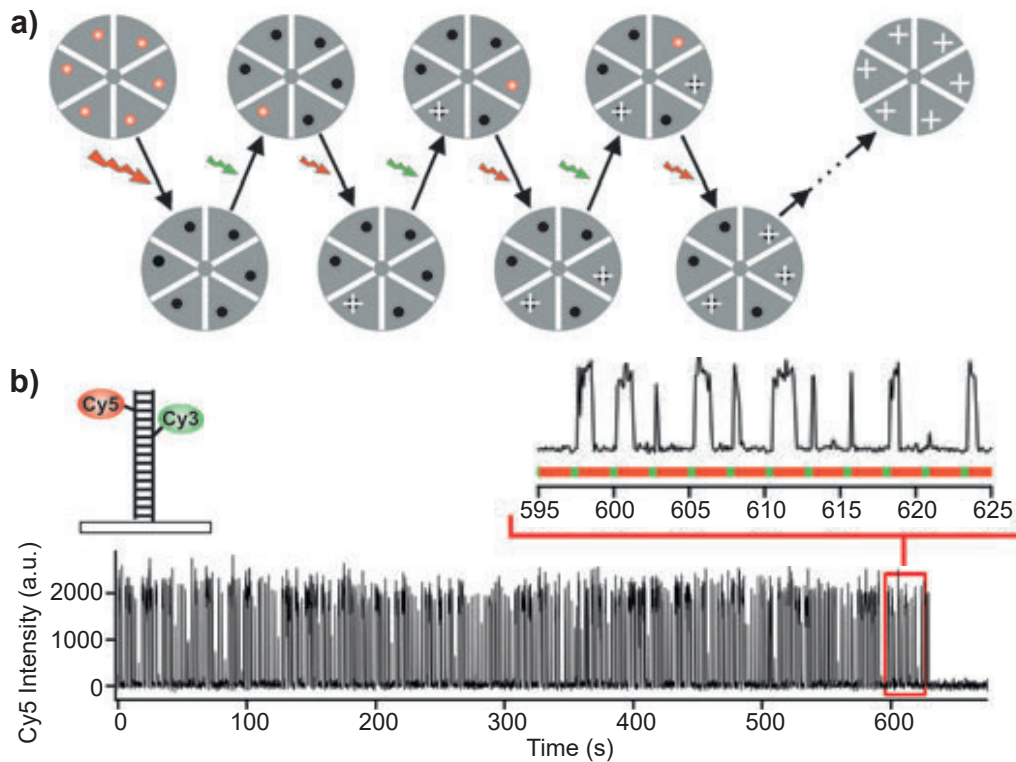


**Figure 2.8** – The stochastic optical reconstruction microscopy. **a)** The imaging principle. First, all fluorophores are switched to the dark state with a red *Laser*. Then, in every cycle a subset of the fluorophores are activated with a short pulse of a green *Laser*. The density of this subset is low enough for localization, as these molecules keep emitting fluorescence under red illumination until they are turned off. Over time, the full set can be imaged and the final image constructed. **b)** Demonstration of the lifetime of a DNA bound Cy5 switch. Bottom plot shows that the switch can be activated hundreds of cycles before permanent photo-bleaching. Inset shows the corresponding red and green *Laser* activation times, respectively. Reproduced from [28].

before permanent photo-bleaching occurs. For the same sample 20 nm lateral resolution was demonstrated.

Other variations for the *STORM* were reported two years later. Three different laboratories developed almost the same concept alongside. The new techniques were named direct *STORM* (*DSTORM*) [30], ground state depletion microscopy followed by individual molecule return (*GSDIM*) [31] and reversible photo-bleaching microscopy (*RPM*) [32], respectively. Instead of activation, these methods forced the fluorophores into their triplet state (or another metastable dark state) and recorded them as they slowly returned. Since the speed of this process could be regulated to be low enough for the earlier detailed localization processes, super-resolution imaging with lateral resolution of 20 - 30 nm was possible. Since multiple research groups were exploring this method, already at the time of first publications, a wide range of experimental imaging was demonstrated, including that of microtubules and actin filaments labelled with various Atto or Alexa dyes, showing the great imaging potential of this microscopy system. As for realization, imaging systems built on different approaches were

used, since this technique could be implemented in a single inverted microscope with special immersion (such as polyvinyl alcohol, mercaptoethanol or glucose oxidase) [31] or in a total internal reflection microscope with low *RI* media [32]. However, a common drawback of all *STORM*-based techniques is that they need to collect a huge amount of data to perform the image processing, therefore generating a single picture can take minutes.

It was also demonstrated that super-resolution can be reached not only by advanced instrumentation, but smart image processing too. A fine example of this is the super-resolution optical fluctuation imaging (*SOFI*), first presented in 2009 [33]. This method relies on the independent stochastic fluctuations of the emitters and needs three criteria to be fulfilled: (i) the fluorescent label has to be able to exhibit at least two optically distinguishable states; (ii) the switch between these states must be stochastic; (iii) the image should be acquired with pixels smaller than the diffraction limit. However, it was shown in a later publication that the third criteria can be overcome with an adjusted algorithm [34]. The principle of *SOFI* is based on the spatio-temporal evaluation of the optical signal by taking a series of pictures of the sample and subsequently calculating the temporal  $n^{\text{th}}$  order cumulant for each pixel. Plotting these yields a final picture with  $\sqrt{n}$  resolution increment. As experimental demonstration, 55 nm lateral resolution was achieved by calculating the 25th order while imaging quantum dots. Although this value is higher than other localization methods (shown earlier in this chapter), it is very important to see that no special electronics or acquisition schemes were needed. However, the first two criteria still remains a restriction that has to be kept in mind when applying this microscopy technique.

After a decade, the development of different localization microscopy techniques still did not slow down. Label-free version of *SPDM* was shown in 2011 [35]. It was demonstrated that cellular structures can be imaged with 20 nm resolution only by detecting the fluorescent signals emerging from within the cells. In the same year, a technique called binding-activated localization microscopy (*BALM*) was developed, utilizing the strong fluorescent signal, generated, when certain dyes bind to *DNA* [36]. Mapping these individual events allowed super-resolution imaging of bacteria with ~14 nm lateral resolution. Although these findings were widening the potential application fields of localization microscopies, they did not reach a significant breakthrough in terms of resolution, since sub-20 nm features were already imaged with the earliest localization techniques [20]. However, cryogenic optical localization in 3D (*COLD*) was shown recently, which enabled mapping multiple fluorescent site of a protein with Angstrom resolution [37]. For this microscopy technique, the sample had to be cooled down to 4,3 K. At this temperature, stochastic photo-blinking becomes way longer, its duration reaches above the second range. Atto647N type dye was used for demonstration with which binding sites could be imaged. Since the range of the measurements were in the Angstrom region, dimensions of the fluorescent label and its linker became a limiting factor of the accuracy. Nevertheless, this microscopy technique reached one of the highest resolution in optical imaging, although the needed temperature environment still remains a limiting factor.

## 2.2 Near-field super-resolution techniques

It is also possible to reach super-resolution without fluorescent labelling. For that, the information coded in the evanescent waves must be resolved (*i.e.* near-field imaging is needed). This can be done by placing a probe in the vicinity of the sample, where it can act as a transducer and transfer the information. However, such a tiny probe would typically limit the field-of-view (*FoV*). A logical solution is to implement a scanning technique, such as the well-established scanning tunneling microscopy (*STM*) [38] or atomic force microscopy (*AFM*) [39], and therefore combine their instrumentation with optical attachments to create a near-field optical imaging system.

### 2.2.1 Photon tunneling microscopy

The photon tunneling microscopy (*PTM*) was reported by J. M. Guerra in 1990 [40]. This instrument utilizes the so called photon tunneling effect, which determines how a photon behaves when it arrives from a medium with higher refractive index (*RI*) [ $n_1$ ] to one with lower *RI* [ $n_2$ ]. If the photon reaches the boundary at a critical angle [ $\sin^{-1}(n_2/n_1)$ ] or greater it will tunnel into the new medium and simultaneously generates an electric field there. But because no energy is transferred, total internal reflection will happen, therefore the generated field in the new medium will be evanescent. As such, it is exponentially decaying with the penetration depth, normal to the boundary. However, if a third medium with *RI* [ $n_3 > n_2$ ] is present, coupling will appear causing a complex interaction. This can cause an inverse and exponential change in the energy transfer, enabling to detect the topography of medium 3 (*i.e.* the vertical and spatial variation when the optical contrast is isotropic), as a modulation in the reflected light in medium 1. This mapping has a limit of the vertical resolution of the height variation, which is determined by the detector sensitivity on capturing the corresponding modulation intensities.

From the instrumentation point-of-view, the setup consists of an optical microscope with an

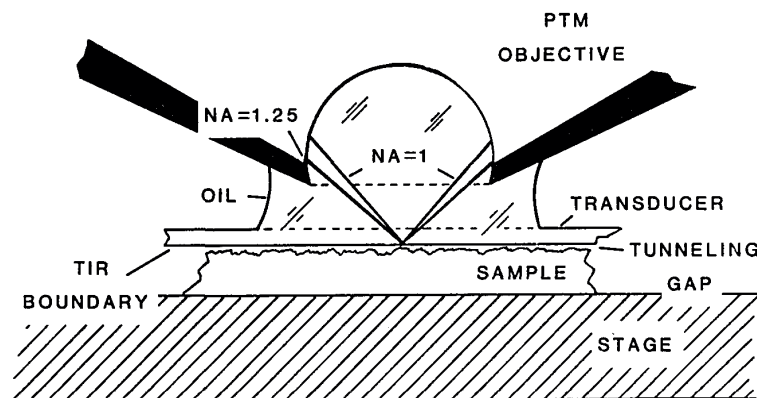


**Figure 2.9** – Detail from the schematic of the *PTM*, showing the relation between the microscope objective, the optical transducer and the sample. Reproduced from [40].



oil-immersion objective ( $NA=1.25$ ) and an optical transducer as is shown in Figure 2.9. The transducer is a cover glass which can be attached either to the objective with a special collar or to the motorized microscope stage. In the latter case a limiter protects the microscope objective from damage. The sample is placed on a motorized stage and it can be left at ambient atmospheric pressure and temperature. As for recording the image, a simple camera can be used for  $2D$  pictures and a three-axis oscilloscope for  $3D$  pictures.

It is possible to image dielectric, metallic and *in vivo* biological samples with this technique, however, for the two latter special conditions need to be fulfilled. Thus, the main advantage of this approach is to have real-time dielectric surface topography imaging, without scanning procedure. Reported lateral resolution was  $\sim 0.29\lambda$ , meanwhile without *PTM* the same setup achieved only  $0.4\lambda$ . Correspondingly, a vertical resolution of  $\sim 0.75\lambda$  was shown.

### 2.2.2 Near-field scanning optical microscopy

The near-field scanning optical microscopy (*NSOM*) (also known as scanning near-field optical microscopy) is a technique that forms a bridge between scanning probe imaging and optical microscopy. The development of such an imaging method was motivated by the fact that far-field techniques are limited in resolution, meanwhile electron microscopes and tip-based scanning methods (*e.g. STM, AFM*) are suffering from poor performance in terms of resolving spectral and dynamic properties. The first description of the experimental scheme of the *NSOM* dates back to 1928 [42]. This early concept contained already all the necessary components of this imaging method, unfortunately it was only realized more than 50 years later [43]–[47]. New fabrication techniques, namely, the microtechnology-based processes developed in that era, allowed to create a subwavelength optical aperture at the apex of a sharply pointed transparent tip that was coated with metal. Furthermore, control electronics were available to maintain a constant gap width of a few nanometers between the tip and the sample, which was needed for scanning. The scanning configuration could be established in multiple ways as is shown in Figure 2.10. In the classical, aperture-based mode, the sample is placed on a hemispherical substrate and only a small area of it is illuminated [48], [49]. The glass hemisphere acts a transducer and forwards the collected near-field information into the

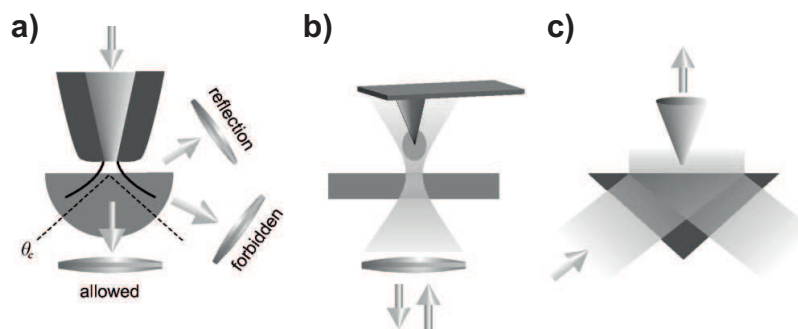


**Figure 2.10** – Different imaging modes in *NSOM*. **a)** Aperture-based imaging with angular resolved detection. **b)** Apertureless imaging. **c)** Scanning tunneling imaging mode. Reproduced from [41].

far-field, where the detectors are placed. Lateral resolutions between 10-100 nm were reported with this technique. In apertureless imaging mode (also known as tip enhanced near-field optical microscopy (*TENOM*)) an external far-field illumination is strongly confined at the tip, which allows lateral resolutions down to 1-20 nm, but the signal must be extracted from the background noise generated by the aforementioned external light source [50]–[57]. During the third imaging mode, an uncoated dielectric tip is used to collect the near-field information in direct vicinity of the sample. This method is also called scanning tunneling optical microscopy (*STOM*) [58] or photon scanning tunneling microscopy (*PSTM*) [59].

The instrumentation governing the aperture-based *NSOM* imaging is relative simple, it consists of a single *Laser* light source, piezo controllers for the tip, a motorized stage for sample positioning, optical elements to control the direction and the shape of the light and a detector. The most important parts of the setup are the microfabricated tip that determines the illumination reaching the sample and the objective that collects the light emerging from the sample. To maximize this collection, typically oil-immersion objectives with high *NA* (~1.4) are used. For tip fabrication two major methods were developed. The first approach is the so-called heating-and-pulling [60], [61]. This is based on local heating with a carbon dioxide (*CO*<sub>2</sub>) *Laser*, followed by a pulling of the glass fiber until the desired shape is reached. The advantage of this method is that it results in very smooth glass surfaces that are desired for effective metal evaporation. An important limitation of the process is the limited cone angle that is very difficult to increase above a certain level. The second approach is based on chemical etching with hydrofluoric acid (*HF*) [62], [63]. The tip is first dipped into the *HF* that is covered with an organic solvent, then it is slowly pulled out. The result is an easily reproducible process that yields tunable cone angles. In early attempts this procedure led to bad surface roughness quality of the glass walls, but further improvements in the method overcame this issue [64]. Finally, both processes end with the same step. Aluminium is evaporated from below the tip that is hold at an angle. This generates a shadowing effect at the tip and enables the self-aligned formation of the aperture.

The aperture of the tip has the highest influence on the performance of the imaging system. Its characteristic can be calculated with the Bethe-Bouwkamp model [65], [66], since it gives a good approximation on the transmission coefficient. The value of this coefficient decreases for small apertures (< 50 nm) drastically, which makes the imaging almost impossible. A theoretical compensation would be the increment of the input power, but this would damage the metal coating of the tip. A good compromise between minimizing the aperture size and the input power simultaneously, is to set the diameter of the former to 80-100 nm. At this condition the wavelength of the light becomes bigger than the opening on the tip, which results in an enhanced near-field power in the vicinity of the aperture. This plays a major role in the image formation, as was proven by several research papers [67]–[71]. These works also showed that scanning with constant gap between the tip and the sample is preferable due to the reduced number of artefact encounters.

The application range of the *NSOM* is widespread but restricted [41], [72]. This is due to the fact that this imaging method offers super-resolution, furthermore, all the contrast mechanisms (*e.g.* absorption, phase and fluorescence) can be transferred more or less directly from

conventional optical microscopy. However, compared to that a huge drawback is that only the surface of the samples can be imaged.

### 2.2.3 Tip enhanced near-field optical microscopy

The tip enhanced near-field optical microscopy (*TENOM*) is a special type of near-field optical techniques, where the *Laser* light source illuminates a metal tip that is scanned over the surface of the sample. Super-resolution can be achieved, because the tip locally excites the sample and extracts the emitted light in parallel. The original method was published in 1985 [73], and since then, it evolved into three main branches: (i) scattering-type microscopy; (ii) tip-enhanced nonlinear optical frequency generation and mixing; (iii) tip-enhanced microscopy. In the first case, the sample response is detected in the far-field at the frequency of the incident light [74], [75]. Special methods, like second-harmonic generation or four-wave mixing, belong to the second group [76]–[79]. The third branch utilizes locally enhanced fields to increase the spectroscopic response of the system [80]–[82]. The main governing phenomenon behind all the *TENOM*-based techniques is the field-enhancement that is generated at the metal tip. The three main contributors to this enhancement are the (i) electrostatic lightning-rod effect, (ii) surface plasmon resonances, and (iii) antenna resonances. All three of them can be tuned by adjusting the wavelength of the light, the shape, length and material of the tip and the surface features in the sub- or few-nanometer range. Furthermore, the field distribution and therefore the local enhancement also depends on the polarization of the light. Because of this, the exciting *Laser* beam needs to be polarized along the tip axis [83]. Besides continuous excitation, short pulses also can be used for this type of imaging. The research field specialized on designing nanooptical fields with this method is called ultrafast nanooptics [84]–[87].

Although the previously discussed electric field is generated at the end of the tip, the optical signal (*i.e.* the image contrast formed during the scanning of the sample) does not simply reflect the tip shape. This is due to the fact that *TENOM* is not an *AFM* with optical information. On the one hand, the enhanced field causes an enhanced excitation rate that is contributing to an increase in the excitation density generated by the light source. On the other hand, the same field promotes the radiative decay. The theoretical background of these phenomena can be described based on the Purcell effect and Fermi's golden rule in the weak coupling range [88], [89]. Based on this, it is possible to calculate the enhancement for both Raman scattering and fluorescence imaging modes. Since in the case of the former, the total signal depends on the product of the transition rates, the signal enhancement scales with the fourth power of the field enhancement, assuming that difference between the excitation and emission wavelength is small and field enhancement is not sensitive on these. As for fluorescence, the signal scales with the second power of the field, but it is also proportional to the ratio of the quantum yield of the tip and the sample. Because of the latter dependence, the most effective *TENOM* imaging was demonstrated with a sample of small quantum yield and high cycling rate [90], [91].

The main instrumentation components of *TENOM* are very similar to those used in *AFM* or *STM*. For controlling the sample - gap distance, the same method can be used. The tip

## Chapter 2. State-of-the-art of super-resolution optical imaging

fabrication also relies on the same basis, but besides custom designs, nowadays a wide variety of tips are already commercially available. Three types of illumination can be applied as shown in Figure 2.11. For non-transparent samples, on-axis illumination is better, since this allows high  $NA$  objectives for imaging. In such a system, both Raman spectra and traditional imaging components (*e.g.* visible or near-infrared light detectors) are allowed in parallel. For non-transparent samples, side illumination fits better, because the polarization requirement of the tip antenna can be easily fulfilled. An alternative method is to use parabolic mirror objectives. They do not exhibit chromatic aberrations and they can be used at all temperatures, but their alignment accuracy is crucial since only minor deviations lead to undesired focal fields and therefore reduced detection sensitivity.

A big issue concerning *TENOM* is originated from the far-field illumination. The major problem with it that it is also collected by the detector, therefore the near-field signal has to compete with it (*i.e.* it has to be enhanced to a level, where the *SNR* enables imaging). There are multiple techniques to reduce or eliminate the far-field background signal, one of them is the so-called tapping-mode imaging. This method induces an oscillatory movement of the tip, resulting in smaller and higher sample - gap distances. Using a demodulated optical signal and detection time tagging of the captured signals, even weak sources, like single fluorophores can be imaged. A different approach is to combine the aperture-based *NSOM* with *TENOM*. This results in the tip-on-aperture technique. Here, the evanescent waves created by the aperture are used for illumination for the tip-based imaging. A further advantage of this method is that the length of the tip can be fine tuned during fabrication, resulting a value that matches the antenna resonance, therefore realizing an extra enhancement. An alternative solution is to use surface plasmon propagation. This can be achieved through exciting a grating written into the tapered tip by focused ion beam. It is easy to see that, although *TENOM* can image with super-resolution [92], many restrictions must be met in order to enable this type of imaging.

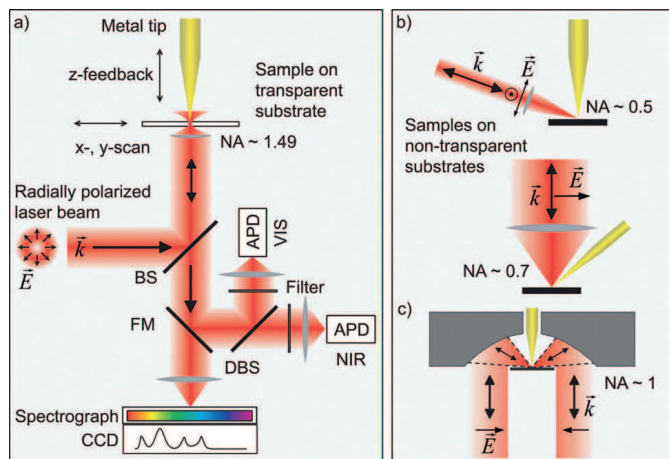


**Figure 2.11** – Different illumination types in *TENOM*. **a)** On-axis illumination for transparent samples with both Raman scattering (spectrograph and *CCD*) and photoluminescence (avalanche photodiodes - *APD* and visible - *VIS* or near infrared - *NIR* spectral range) detection. **b)** Side illumination for non-transparent samples. **c)** Imaging with a parabolic mirror and high  $NA$  aperture. Reproduced from [93].

### 2.2.4 Photon scanning tunneling microscopy

The photon scanning tunneling microscopy (*PSTM*) (also known as *STOM*) is the third branch of *NSOM* (see section 2.2.2) [59]. Its working principle is analogous to the *STM*. An optical fiber probe tip is scanned over the sample surface, controlled by a feedback circuit that prevents collision of the two. However, the difference between the two microscopy systems is that, in the case of *PSTM*, the tip collects evanescent waves. These waves originate from the surface of two media with different refraction indices (see section 2.2.1). When a medium with higher *RI* (in this case the tip of the optical fiber) is present in the second medium, sufficiently close to the border of the first two media, tunneling of the photons from the first to the third medium occur. Furthermore, the presence of a sample on the total internal reflection surface will modulate the evanescent wave forms, which modulation will manifest itself as spatial variation in the field intensity. This can be recorded by the scanning tip, resulting in topological information about the sample.

The instrumentation of the *PSTM* consists of a *Laser* light source, that is set at an angle at which total internal reflection occurs at the edge of the first medium. Piezo elements control the tip, just like in an *STM* setup. The tip might be coated, but it is not necessary for the operation. Shape and diameter of the aperture are critical for achieving super-resolution. Both of them can be tuned during the chemical etching process. The other end of the optical fiber is connected to a photomultiplier that serves as a detector during scanning. Acquired data must be processed by a computer in order to generate a gray-scale image of the sample.

Already during the first demonstration, *PSTM* achieved 200 nm lateral (with exciting wavelength  $\lambda=633$  nm) and 80 nm axial resolution, meanwhile the noise level reached ~16 nm peak-to-peak fluctuations. Although these results are not outstanding, it is important to note, that the theoretical resolution limit of this technique only depends on the effective sharpness of the tip. This statement was supported by a later-reported 10 nm lateral resolution [94].

### 2.2.5 Near-field optical random mapping nanoscopy

The near-field optical random mapping (*NORM*) nanoscopy was introduced in 2014 [95], and it combines the near-field acquisition with the far-field observation. The working principle behind this technique is to place objects in a scattering medium on the surface of the sample. Typically, these objects are nanoparticles. They can have different optical properties, such as transparency or reflectance, but their size must be smaller than the wavelength of the light. If this sole criteria is fulfilled, then it is possible to recover the near-field image from the far-field purely by determining the distribution of the scatterers (*i.e.* the nanoparticles). The method is very similar to the ones used for localization microscopies (see section 2.1.5). Since the particles moves stochastically due to the Brownian motion, their position can be determined with a much higher precision than the resolution of the far-field microscope objective. Additionally, the detected brightness of a single spot corresponds to the optical near-field intensity of the sample area below it. Therefore, observing the total sample area over time will provide information about all parts of the sample surface. However, a correction of the final

## Chapter 2. State-of-the-art of super-resolution optical imaging

image is needed, because the distance between the sample surface and the nanoparticles is not fixed. If the gap becomes too big, only low frequency spatial information will be transferred which will cause blurry picture. To dampen these lower frequencies, Fourier filtering can be applied on the final image.

To construct a *NORM* nanoscope, no special equipment is needed (see Figure 2.12). The base of the setup is a standard optical microscope with a low *NA* objective and a *CCD* camera. The recording speed of the camera (*i.e.* frames per second (*FPS*)) is the main factor that determines the image acquisition speed. Typical imaging times are between 1 - 10 min depending on the amount of pixels in the camera and its *FPS* rate. To improve the image quality dark-field illumination can be used that prevents non-scattered light from entering the objective. For successful imaging, a nanoparticle solution is also needed, as an example 120 nm titanium dioxide ( $TiO_2$ ) particles can be used, if the wavelength of the light is bigger than this dimension. In the same configuration, using 520 nm *LED* illumination,  $\sim 100$  nm lateral resolution was reported [95]. This is a considerable improvement, because the same objective ( $NA=0.4$ ) could only achieve  $\sim 650$  nm resolution without the *NORM* system. However, there are two restrictions that must be met to be able to use this microscopy technique. The sample must not be sensitive on the nanoparticle solution and it must not be time-dependent, since the imaging takes up to several minutes.

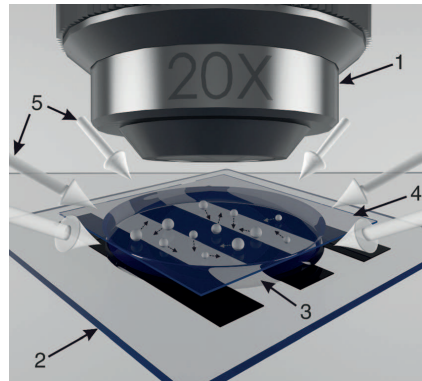


**Figure 2.12** – Schematic of the *NORM* nanoscope. 1: microscope objective; 2: sample; 3: nanoparticle suspension; 4: cover glass; 5: incident light by dark-field illumination. Reproduced from [95].

### 2.3 Micro-object-based super-resolution imaging

A new branch of super-resolution microscopy (*SRM*) started to emerge in 2004, when the first discovery of the photonic nanojet (*PNJ*) enhancement with the help of high *RI*, dielectric microobjects was published [96]. The *PNJ* is a very strong focused beam of the light generated on the shadow side of a microobject (*e.g.* cylinder, semi-sphere, sphere), when illuminated by a plane wave. The length of this focus is  $\sim 2\lambda$  at *FWHM*, while its width is  $\sim 0.5 \pm 0.2\lambda$  at *FWHM*, depending on the parameters of the surrounding. The main influencing factors are (i) the refractive index of the medium ( $n_{medium}$ ), (ii) the diameter of the focusing curvature of the

microobject / diameter of the microsphere ( $D$ ), (iii) the refractive index of the microsphere ( $n_{sphere}$ ) and (iv) the wavelength of the light ( $\lambda$ ). The exact mechanism of how these parameters influence the *PNJ* and how the *PNJ* enhances the resolution of the imaging, was studied extensively in the last decade and will be presented in the following chapters.

### 2.3.1 Fixed micro-object-based techniques

Imaging by a high *RI* lens, placed in vicinity of the sample, was demonstrated already in 1990 [97]. This technique was named solid immersion lens (*SIL*) microscopy, because the sample had to be in close contact with the lens hemisphere in order to increase resolution. An extra focus is created due to the geometrical shape of the lens that contributes to an effectively shorter wavelength and a decreased *FoV*, by a factor of  $\frac{1}{n_{SIL}}$  and to an increased magnification by a factor of  $n_{SIL}$ , where  $n_{SIL}$  is the *RI* of the *SIL*. However, to achieve this, the sample has to be in direct contact ( $\sim 0$  nm distance) with the lens. Theoretical calculations showed 15% increment in the width of the *PSF*, when this distance was increased to 100 nm. These calculations were made for  $n_{SIL} = 2.0$ ,  $\lambda = 546$  nm and a sample line-width of 100 nm. Experimental confirmation showed that this technique can be translated into practice, when a 100 nm lines-and-spaces pattern (*LSP*) was imaged.

The *LSP-s* are typical samples that are used to measure the spatial frequency response of an optical system. They consist of parallel, equidistant lines with a given width. The spacing distance between them is the same as the line-width, unless in uniquely specified cases. The lines and the spaces have big contrast difference, ideally, one part transmits the totally white, the other the totally black signal. Therefore, the intensity profile of this pattern is a rectangular function. To characterize the performance of an optical system in terms of contrast and resolution, its response can be measured and compared to this reference.

The advantages of the *SIL*-based system are its simple construction and the characteristic of its performance that depends almost entirely on the *RI* of the applied lens. However, to improve its performance,  $n_{SIL}$  has to be increased, which cannot be done infinitely due to material properties. Alternatively, the wavelength of the illumination can be decreased, but again, that is restricted by the spectrum of the visible light. Moreover, the *FoV* is also limited. This could be overcome by implementing a scanning procedure, as proposed by the authors [97], but that would disable the imaging of time-sensitive samples.

An alternative solution of using materials for lenses with negative *RI* was proposed in 2000 [98]. In this work a theoretical approach is shown to amplify the evanescent waves and transfer the information coded in them into the far-field. The major concern regarding this technique is that it is restricted to a certain frequency and to special materials of both the lens and the medium. Despite of the difficult realization, this work is an important milestone in the development of the microobject-based super-resolution imaging, as will be further detailed in chapter 3.

Discovery of the *PNJ* enhancement opened up a new development direction in microscopy [96]. It was shown by finite-difference time-domain (*FDTD*) numeric simulations, that dielec-

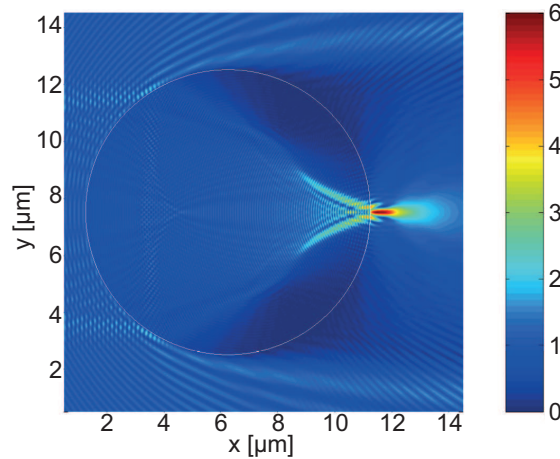


**Figure 2.13** – First representation of the *PNJ*. Result of a *FDTD* numerical modelling of a plane wave illuminating a dielectric  $\mu S$  from the left. Colors represent the electric field distribution.  $D=10 \mu\text{m}$ ,  $n_{\text{sphere}}=2.3275$ ,  $n_{\text{medium}}=1.33$ ,  $\lambda=300 \text{ nm}$ . Reproduced from [96].

tric  $\mu S$ -s can generate this special light focusing, when they are placed in a medium with tuned *RI* (Figure 2.13). More importantly, it was pointed out that, if a sample (*e.g.* nanoparticle) is placed in this *PNJ*, the generated backscattered light is increased multiple folds, therefore its detection became possible. This effect is the basis of the microobject-based super-resolution imaging. Further investigation using a generalized multiparticle Mie method showed, that the *PNJ* formation and the enhanced backscattering are also present in *3D* [99], [100]. These results started further investigations concerning the physical phenomena behind the light focusing and backscattering.

Already in 2005, the *PNJ* formation was precisely described by the combination of geometrical optics, Mie theory and angular spectrum analysis [101]. This theoretical investigation calculated the field structure with Mie theory, then resolved and translated the Mie solution into a Debye series. Finally, it obtained and analysed spatial characteristics of the *PNJ*. Results showed that the jet formation is possible because of a unique combination of (i) a peak in the angular spectrum, (ii) the finite content of the propagating spatial frequencies, (iii) a small but also finite content of the evanescent spatial frequencies and (iv) a special distribution of the phase. Furthermore, it confirmed the four main influencing components of the *PNJ*, detailed in the beginning of section 2.3. These findings were later supplemented by a study about the three dimensional spectral analysis of the *PNJ* [102]. Here, the contribution from all spatial frequencies was investigated. Based on the performed decomposition, it is clear, that mainly propagating waves are contributing, but the presence of the evanescent components close to the  $\mu S$  surface is crucial. Because the generation of the latter waves depends also on the *RI* mismatch on the border of the  $\mu S$  and the medium, changing any of those materials highly affects the shape and the strength (*i.e.* the field gradient) of the *PNJ*. These pioneering theoretical works gave an insight into the physics of  $\mu S$ -focused illumination light even before the first experimental confirmation of the phenomenon was published.

Parallel to these studies, the enhancement of the backscattered light was also investigated



### 2.3. Micro-object-based super-resolution imaging

[103]. The enhancement of the backscattering, originating from the *PNJ* illuminated nanoparticles, was characterized. It was shown, that the enhancement is due to a complex interaction between the  $\mu S$  and the imaged nanospheres, furthermore, the scaling factor is proportional to the third power of the size of the latter. This complex interaction can be considered as a feedback system. The nanoparticle is excited by the *PNJ* and therefore its scattering intensity is elevated proportionally to the intensity of the *PNJ* ( $\sim 2$  orders of magnitude in the investigated case). This causes a reradiation in the fields and changes the normal electromagnetic modes of the  $\mu S$ . As this process is constructive, it elevates the backscattering intensity further with around 4-9 additional orders. The highly elevated intensity is directly responsible for the enhanced imaging and enables super-resolution.

The experimental confirmation of the existence of the *PNJ* was demonstrated in 2008 [104]. Latex  $\mu S$ -s of 1, 3 and 5  $\mu m$  diameter were deposited on a cover glass in low concentration to avoid cross-scattering and they were imaged in air and water-immersion, respectively. To be able to map the shape of the expected *PNJ*, a laser scanning confocal microscope with an avalanche photodiode was used for acquisition. Collimated, unpolarized white light was applied to the sample, but a band pass filter (500-540 nm) was placed in front of the detector. Image stacks with 500 nm steps of focus were captured within  $\sim 400$  s, which was followed by data processing. Final pictures served as a proof for the existence of the *PNJ*-s (Figure 2.14). It was also demonstrated that multiple  $\mu S$ -s can produce *PNJ* simultaneously, without interference. Therefore, this study proved that  $\mu S$ -based *SRM* is a viable alternative microscopy technique.

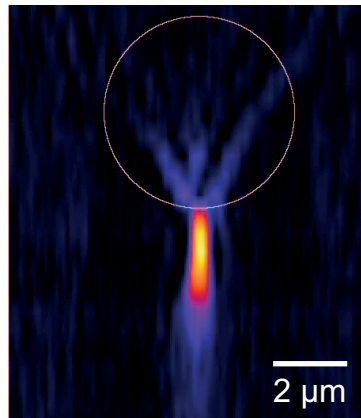


**Figure 2.14** – First observation of a *PNJ*. Constructed image of a *PNJ* formed at the shadow-side of a 5  $\mu m$  diameter microsphere ( $n_{sphere}=1.6$ ) in air, illuminated from the top. Reproduced from [104].

The research of *PNJ*-s and their application in microscopy techniques started to bloom around 2010. Numerous papers were published about the modification of the shape and the size of the *PNJ* [105]. As an example, it was shown by numerical experiments, that it is possible to confine the *PNJ* when illuminating the  $\mu S$  with a tightly focused Gaussian beam through a high *NA* objective [106]. The concluded cause of this shrinkage was the interference of the electric field and the collimation of the incident field, both caused by the  $\mu S$ . Although this model had

## Chapter 2. State-of-the-art of super-resolution optical imaging

---

some limitations (*e.g.* only dielectric materials were used and the resonance phenomenon was omitted), it showed the possible application of fluorescent signal detection. An alternative way of tuning the shape of the *PNJ* was demonstrated by constructing two-layer  $\mu\text{S}$ -s [107]. Calculations revealed, that the 'waist' (*i.e.* the width at *FWHM*) of the *PNJ* can remain smaller than the wavelength of the light independently from the diameter of the  $\mu\text{S}$  if the optical contrast (*i.e.* the ratio between  $n_{\text{sphere}}$  and  $n_{\text{medium}}$ ) is tuned optimally. However, since this tuning is restricted in the number of possible combinations (*e.g.* its upper boundary is  $\sim 1.7$ ), this sets a limitation on possible  $D$  values. Furthermore, considering a two-layer  $\mu\text{S}$  with precisely chosen refractive indices for both the core and the shell of it, it is possible either to significantly elongate the length of the *PNJ* or to highly increase its peak intensity. The former modification could be the basis of a nanometer-sized inhomogeneity detection technique [108].

Parallel to the computational studies, experimental approaches were also developed. It was shown that not only  $\mu\text{S}$ -s, but hemispheres are able to create a *PNJ* and that can be used for imaging [109], [110]. For demonstration, 0.05 - 3  $\mu\text{m}$  diameter hemispheres were grown and randomly placed on the sample surface. Imaging was performed in both orientation (*i.e.* with the flat and the curved surface of the hemisphere facing down). The magnifying effect and the resolution enhancement was measured on *LSP*-s. Published pictures confirmed a magnification factor of  $\sim 1.6$ . In contrast, the exact value of the resolution enhancement could not be easily determined, because the study focused more on the fabrication technology, than the quantification of the resolution enhancement. Despite of this, since the resolution limit ( $\sim 262$  nm, when calculating Abbe's limit) of the imaging system used for the experiment was very close to the pitch of the imaged *LSP*-s (220 - 250 nm), the achieved improvement could not be more than  $\sim 15\%$ . A more concerning issue about this microscopy technique originates from the fact that the *FoV* is limited by the diameter of the applied hemisphere and the location of this hemisphere is arbitrary and cannot be controlled. Therefore, in order to move it in any desired location, a manipulator system must be employed.

Utilizing the  $\mu\text{S}$ -s for single-molecule imaging was found to allow high-temperature imaging and to simultaneously improve photostability [111]. Coated  $\text{TiO}_2$  spheres ( $D=2\mu\text{m}$ ) were coupled to the sample by Cy3-labelled streptavidin for this experiment series. Results showed that the lifetime of the fluorophore before bleaching was increased in the presence of the  $\mu\text{S}$ , meanwhile molecular activity (*e.g.* *DNA* polymerase activity) could have been observed. A further advantage of this technique was the capability of allowing sample temperatures as high as  $70^\circ\text{C}$ .

One of the first reports demonstrating the true potential of the  $\mu\text{S}$ -based super-resolution imaging in the field of wide-field microscopy was published in 2011 [112]. In this study, silicon dioxide ( $\text{SiO}_2$ ) ( $2\mu\text{m} < D < 9\mu\text{m}$ ) were spread in a single layer over the surface of the sample and illuminated by white light ( $400\text{ nm} < \lambda < 700\text{ nm}$ , with peak at  $\lambda=600\text{ nm}$ ). The imaging system, called (white-light) optical nanoscopy (*ON*) could be operated both in transmission (Figure 2.15.a) and in reflection (Figure 2.15.b-d) mode. For acquisition, the objective was not focused to the sample-plane, but  $\sim D/2$  distance below. That is, where an enlarged virtual image of the sample is formed by the  $\mu\text{S}$ -s. This virtual image was recorded by a microscope-

### 2.3. Micro-object-based super-resolution imaging

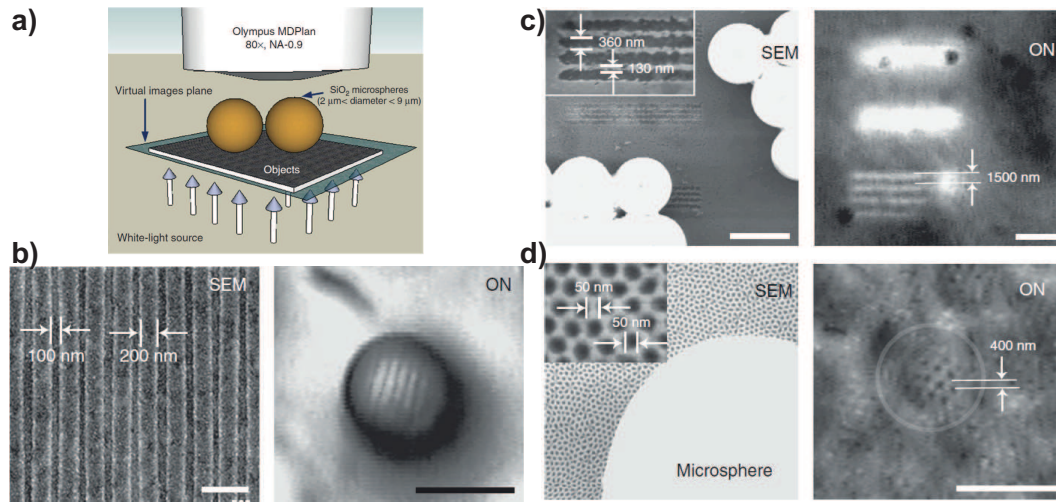


**Figure 2.15** – The *ON*. **a)** Schematic of the experimental configuration of the white-light nanoscope, operating in transmission mode. **b)** Parallel lines from the surface of a Blu-ray disc, as imaged by *SEM* (left) and the *ON* in reflection mode (right). The protective film was removed from the disc before imaging. Scale bar: 500 nm for *SEM* and 5 μm for *ON*. **c)** Image of a *LSP* with increased gaps, taken by *SEM* (left) and *ON* (right). The white, circular objects on the left are the *μS*-s, placed on the surface of the sample. Scale bars: 5 μm. **d)** Photograph of a gold-coated anodic aluminium oxide membrane, taken by *SEM* (left) and *ON* (right). Scale bars: 5 μm. Reproduced from [112].

mounted camera. The performance of the *ON* was evaluated by measuring multiple patterns using an objective with  $NA=0.9$ . This resulted in an Abbe's resolution limit of  $\sim 222$  nm. As reference, scanning electron microscopy (*SEM*) pictures were taken. First, the surface of a Blu-ray disc [113] without its protective film was imaged, and the *ON* could resolve its *LSP*. The pitch of this pattern was 300 nm that is above the resolution limit. A similar situation was presented next, when another *LSP* with 490 nm pitch was imaged. In the third case, a gold-coated anodic aluminium oxide membrane was investigated. This structure had a fishnet pattern with a pitch of  $\sim 100$  nm that is considerably below the diffraction limit. Still, the *ON* could resolve this pattern. However, the authors admitted, that the special surface (*i.e.* the gold coating) caused a near-field interaction that helped the resolution enhancement. Despite of that, super-resolution imaging was clearly demonstrated. More importantly, it was pointed out, that the performance of *μS*-based microscopy may depend on the sample.

In the same year, an extensive experimental study was carried out about the influence of the illumination on the *PNJ* [114]. A high-resolution interference microscope was employed to enable precise measurement of both the amplitude and the phase of the *PNJ*-s. As a general observation, it was stated, that the physical optics effects largely dominate the properties of the *PNJ*-s, therefore, their behaviour can be understood by applying conventional refractive optical arguments. First, the dependency from the wavelength of the light was confirmed by measuring the changes generated by switching the illumination between three *Lasers* with different wavelengths (Figure 2.16.a-c). It was found that the shape, the size and the position can be changed by varying  $\lambda$ , but the *PNJ* is always close to the surface of the *μS*. Important to

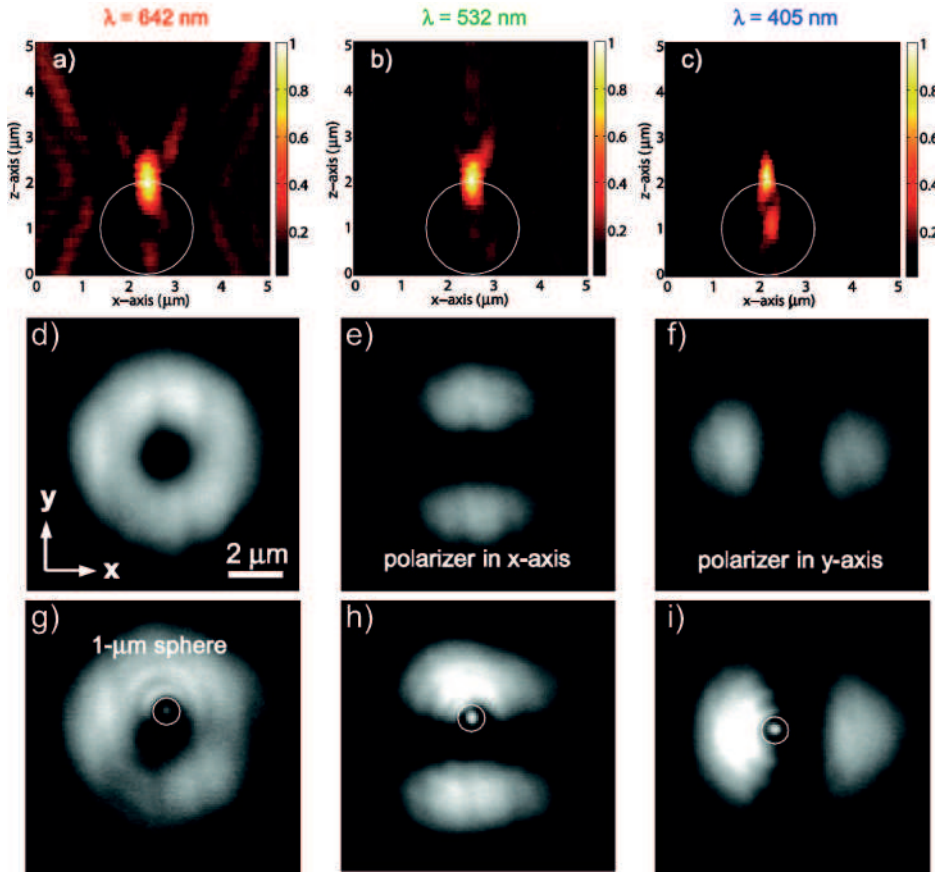


**Figure 2.16** – The effect of illumination on the *PNJ*. Illuminating a  $D=2\ \mu\text{m}$  glass ( $n_{\text{sphere}}=1.55$ )  $\mu\text{S}$  with three different wavelengths from below: **a)**  $\lambda=642\ \text{nm}$ , **b)**  $\lambda=532\ \text{nm}$ , **c)**  $\lambda=405\ \text{nm}$ . Grayscale *CCD* images of different illumination patterns (**d)** doughnut shape, **e)** x axis polarized half circles, **f)** y axis polarized half circles) with their corresponding *PNJ* shapes (**g)**–**i)** generated by  $D=1\ \mu\text{m}$  glass  $\mu\text{S}$ -s, respectively. Reproduced from [114].

note, that  $D=2\ \mu\text{m}$  glass spheres ( $n_{\text{sphere}}=1.55$ ) were measured. To adjust this position further away from the surface of the  $\mu\text{S}$ , spherical wavefronts of the illumination with various radii were proposed. These can relocate the *PNJ* up to several microns away, however, at a cost of slightly larger spot size. It was also demonstrated that it is possible to generate a two-spot *PNJ* by applying an off-axis Bessel-Gauss beam as illumination. In such a scenario, 200 nm distance between the two *PNJ* was observed with  $\lambda=642\ \text{nm}$ , which results in a spot size below the diffraction limit of the highest *NA* microscope objectives. To prove the first general statement of the study, other unique shapes (*e.g.* doughnut shape or two half-circles shape) were shown by applying different polarization-induced illumination beam shapes (Figure 2.16.d-i). Through this demonstration, it was proven that the *PNJ* is an optical phenomenon that can be also fine-tuned for wide range of applications by adjusting the properties of the illumination. A similar study was conducted also on glass *SIL*-s [115]. Here,  $\text{SiO}_2$  hemispheres ( $D=2\ \mu\text{m}$ ) were microfabricated and characterized. The measurement method was matching the one, described in the previous paragraph. Results showed that spot size reduction was also present

### 2.3. Micro-object-based super-resolution imaging

when illuminating hemispheres and its extent was in good agreement with the theoretical value calculated for  $SiO_2$   $\mu S$ -s. Furthermore, a  $\sim 50\%$  peak intensity increment was measured, compared to the illumination without the *SIL*. Transmission loss through the hemispheres was also investigated and found to be  $\sim 17\%$ , which was categorized as a sufficiently small value for applications (e.g. optical trapping). An indirect conclusion of this work was to show that the illumination pattern can be transferred to the *PNJ*-s independently from the shape of the microobject transducer [116]. As an alternative to glass lenses, polymer hemisphere fabrication was demonstrated in the same year [117]. The main advantage of using photocurable polymer droplets was the easy shape control. During the process, the lenses were created on a poly(dimethylsiloxane) (*PDMS*) stamp that was used to transfer the droplets to the final substrate. The only constrain regarding the target material was its surface roughness, which had to be moderate. A further advantage of the technique was the option for stamp-geometry-dependent, high-density array fabrication. However, the need of further material optimization was reported in order to be able to generate high contact angle lenses on various surfaces.

At the dawn of microobject-based *SRM*, only  $\mu S$ -s and hemispheres smaller than  $10\mu m$  were considered for imaging. However, it is possible to use spheres up to  $200\mu m$  for super-resolution imaging, as was shown in 2012 [118]. Barium titanate glass (*BTG*)  $\mu S$ -s ( $2\mu m < D < 200\mu m$ ,  $n_{sphere} \sim 1.9-2.1$ ) were immersed in water ( $n_{medium}=1.33$ ) and isopropyl alcohol (*IPA*) ( $n_{medium}=1.37$ ), respectively, for demonstration. The microscope used for acquisition was equipped with a  $100\times$ ,  $NA=0.9$  objective. Illumination originating from a halogen light source was filtered to  $550\pm 10$  nm. The imaged sample consisted of an array of gold cylinder pairs with  $120$  nm diameter each and the same distance between the members of a pair. The height of each cylinder was  $30$  nm, composed from  $2$  nm of chromium and  $28$  nm of gold. The  $\mu S$ -s were placed randomly on the sample and covered with *IPA*. Then a  $\mu S$  was found that was located directly above a pair of the gold cylinders. For imaging, the microscope objective was focused to the virtual image plane, located  $\sim D/2$  below the sample plane. Resulting images and their analysis for various  $\mu S$  diameters are shown on Figure 2.17. Plotting the intensity along the marked measurement lines showed, that the signals generated by the two cylinders can be separated. Control images revealed, that these patterns cannot be resolved solely by the microscope objective. Calculating the resolution improvement showed that originally this was  $d=306\pm 6$  nm, while the  $\mu S$ -s resolved a pitch of  $240$  nm. The latter can be calculated somewhat smaller considering the *FWHM* instead of the peak-to-peak distance. However, as it was mentioned earlier [112], the near-field interactions between the gold surface and the  $\mu S$  might further improve the imaging resolution, therefore the presented increment is sample-dependent. Measuring  $\mu S$ -s with various diameter showed, that increasing  $D$  increases linearly the *FoV*. However, the biggest magnification was not found with the smallest  $\mu S$  but when  $6\mu m < D < 10\mu m$ . This work successfully presented the possible application of  $\mu S$ -s bigger than  $10\mu m$  diameter for imaging. Repeating the experiments with water-immersion also proved the applicability of the method for imaging biological samples.

By the time of 2013, the field of  $\mu S$ -based *SRM* was widely expanded and three main directions of development became distinguishable: (i) further exploring the *PNJ*; (ii) demonstrating the imaging capabilities of various  $\mu S$ -s; (iii) finding new solutions to extend the *FoV* of  $\mu S$ -based

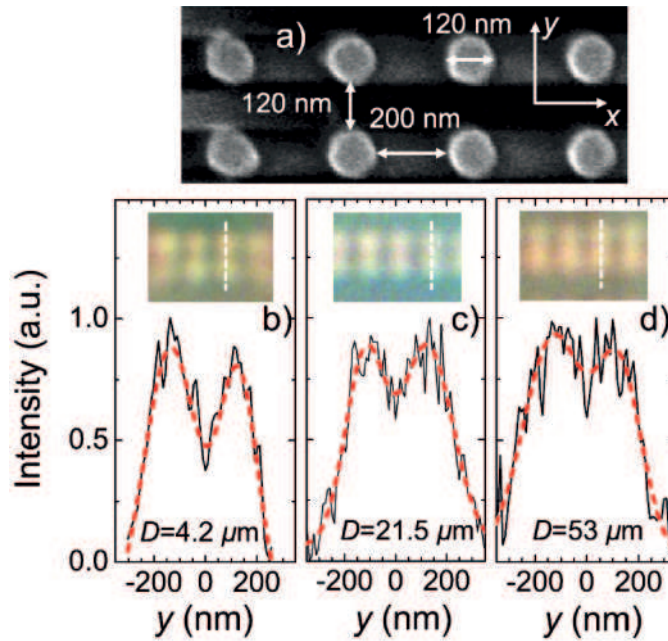


**Figure 2.17** – Super-resolution imaging with *BTG*  $\mu S$ -s. **a)** *SEM* picture of gold nano-cylinders, serving as the sample to be imaged. Pictures taken through **b)**  $D=4.2 \mu\text{m}$ , **c)**  $D=21.5 \mu\text{m}$ , **d)**  $D=53 \mu\text{m}$  *BTG*  $\mu S$ -s, with their intensity profiles along the marked measurement lines, respectively. Black lines correspond to raw data, while red dashed-lines represent a Gaussian fit of the intensity plots. Reproduced from [118].

imaging systems. Meanwhile various results from the first two development types are presented in the following paragraphs, the third direction is detailed in section 2.3.2.

Since larger diameter  $\mu S$ -s were already investigated and their *PNJ* creating abilities recognized, the research spotlight turned towards smaller spheres, particularly, to the case, when  $D$  becomes comparable to  $\lambda$  [119]. It was shown theoretically, that high *RI*  $\mu S$ -s at Mie resonances can significantly increase the field around them (*i.e.* generate a strong *PNJ*). The model explicitly showed a non-monotonic dependence of the resolution on the wavelength, confirming the enhancement due to the resonances. This special feature could be exploited while imaging broadband point emitters such as dye molecules or fluorophores. However, several practical problems were raised in connection with this technique. Mainly, it is particularly difficult to handle such small  $\mu S$ -s. This could hinder experimentation, as without precise positioning the desired part of the sample cannot be imaged directly. Moreover, the created *PNJ*-s are very close (in the range of  $\lambda$ ) to the  $\mu S$  surfaces. This latter issue was overcome by introducing two-layer  $\mu S$ -s that could project *PNJ*-s up to  $\sim 4\lambda$  distance [120]. The special composition of such gold- $\text{SiO}_2$   $\mu S$ -s allowed working distances comparable to the regular ones ( $10 \mu\text{m} < D$ ). The long-*PNJ* projecting property of the core-shell type  $\mu S$ -s were also exploited for bigger diameters [121]. When illuminating a  $D=5\lambda$ , two-layer  $\mu S$  ( $n_{\text{sphere}}=1.6028$  and  $n_{\text{sphere}}=1.8445$  for the inner and the outer layer, respectively), the measured length of the generated *PNJ* was  $\sim 22\lambda$ . For comparison, a single layer  $\mu S$  ( $n_{\text{sphere}}=1.377$ ) with the same diameter could achieve only  $\sim 9\lambda$  length. In both cases, the illumination wavelength and the refractive index of the

medium was kept the same. A further iteration on this technique was shown when the core of the two-layer structure was removed and the generated hollow structure was filled with liquid [122]. This theoretical investigation showed, that by fine-tuning the refractive indices of the medium and the liquid within the  $\mu S$ , the *PNJ* can be elongated over  $100\lambda$  distances.

Parallel to the investigations on the double layer  $\mu S$ -s, other unconventional geometries were investigated for their potential applicability on *PNJ* generation. One of them was a study on elliptical particles [123], and simulations predicted, that *PNJ*-s still could emerge. These results gave an additional degree of freedom for designing optical systems utilizing *PNJ*-s. Another theoretical study on various geometries focused on the influence of the surface roughness [124]. Three cases were modelled: (i) a completely smooth surface, (ii) a surface with regular pattern and (iii) a surface with random pattern. Interestingly, the first two  $\mu S$ -s could produce *PNJ*-s both in air and in water medium, meanwhile the one with the random roughness could only generate it in air. These results showed, that although the surface roughness is an important parameter, the refractive index of the medium may have a bigger impact on the final formation of the *PNJ*. As an extensive review showed in 2017 [125], the *PNJ* became a well-recognized phenomenon in optics. By that time, almost all the influencing parameters, structures and geometries were investigated theoretically and most of them also confirmed experimentally. Knowledge about these influencing factors gave the researchers a relatively large freedom in designing optical systems, however no conclusive design principle was laid down so far that would allow the accurate prediction of the final performance of a microobject-based microscopy system in terms of achievable resolution gain (see chapter 3 for further investigation of this topic).

The second development direction focused on demonstrating the imaging capabilities of various  $\mu S$ -s in multiple conditions. A study showing a possible way to increase the *FoV* of a  $\mu S$ -based microscopy system was shown in 2013 [126]. Their method consisted of observing the sample in air, through big diameter (30, 50 and 100  $\mu\text{m}$ ) polystyrene  $\mu S$ -s ( $n_{\text{sphere}}=1.59$ ) that were placed on the top of it. For the image acquisition, a halogen light source and a  $50\times$ ,  $NA=0.75$  objective was used. Pictures, taken from two different samples were shown. One of them was the surface of a Blu-ray disc (without the protection film), while the other was a quartz plate with gold nanopatterns. The 300 nm pitches (180 nm lines with 120 nm spaces) of the Blu-ray disc were resolvable in the presence of all the differently-sized  $\mu S$ -s. The same results were obtained when the 150 nm gold nanoparticles with 600 nm spacing on the quartz plate were imaged. Since the authors did not mention any applied filtering, the resolution of the microscope without the  $\mu S$ -s could only be estimated. Considering the lower end of the visible light spectrum ( $\lambda=400$  nm), possible limits are  $\sim 267$  nm according to Abbe's law or  $\sim 325$  nm according to Rayleigh criterion. Based on these assumptions, the achieved extra resolution is minimal in the case of the Blu-ray disc imaging. As for the gold nanoparticles, there the gold surface adds an uncertainty factor in the estimation of the purely  $\mu S$ -based enhancement. Moreover, the huge pitch (compared to the diffraction limited feature size) further reduces the detection limit.

It was demonstrated in the same year, that water-immersion imaging in a similar configuration is possible. The *BTG*  $\mu S$ -s ( $D=100$   $\mu\text{m}$ ,  $n_{\text{sphere}}=1.9$ ) were placed on the sample, which was a

## Chapter 2. State-of-the-art of super-resolution optical imaging

cluster of adenoviruses in the presented case. The typical size of such a virus is  $\sim 75\text{-}100\text{ nm}$ . Indeed, analysis of the intensity values on the recorded images showed, that the individual viruses were resolved. Therefore, it was proven that biological samples can be imaged with  $\mu\text{S}$ -based *SRM*.

A study, comparing the performance of the *SIL*-s with the  $\mu\text{S}$ -s showed superior performance of the latter [127]. This was concluded after the same sample (gold nanocylinders with 100 nm diameter and 160 nm pitch) was imaged by the two different methods under the same conditions (see Figure 2.18). In both cases a  $20\times$ ,  $NA=0.6$  objective with  $\lambda=405\text{ nm}$  illumination was used. The refractive indices were almost identical ( $n_{\text{sphere}} \sim 1.9$  for the *BTG*  $\mu\text{S}$  and  $n_{\text{SIL}} \sim 2$  for the *SIL*), but the diameter of the  $\mu\text{S}$  was five times bigger ( $D=10\text{ }\mu\text{m}$ ) than the diameter of the *SIL* ( $D_{\text{SIL}}=2\text{ }\mu\text{m}$ ). Other parameters (e.g. magnification factor) were also investigated, which showed, that both in terms of resolution and magnification, the  $\mu\text{S}$ -s can provide higher performance. These findings induced further research on potential  $\mu\text{S}$ -based microscopy applications.

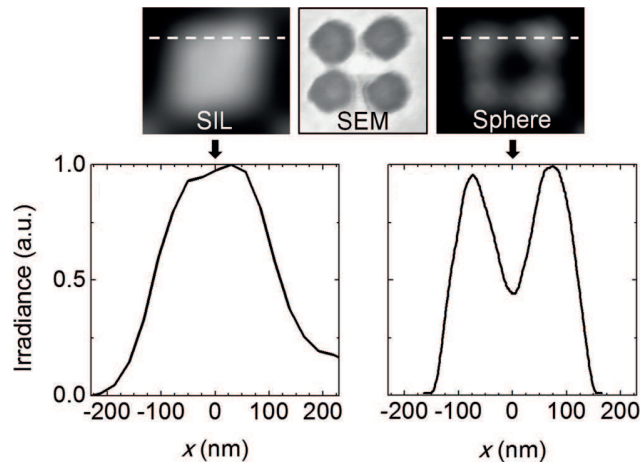


**Figure 2.18** – Comparison of the imaging performance of a *SIL* against a  $\mu\text{S}$ . The same nanopattern (center, *SEM* image) was imaged by a *SIL* (left) and by a  $\mu\text{S}$  (right). Corresponding analysis of the detected signals along the measurement lines are plotted below, respectively. Reproduced from [127].

It was also shown that  $\mu\text{S}$ -s can also be combined with scanning laser confocal microscopes [128]. To merge the two technologies, researchers followed a very simple method. They placed the  $\mu\text{S}$ -s at random locations on the top of the sample by mixing them into a solution and then pouring it on the surface. After evaporating the liquid component, the sample was imaged by the confocal microscope utilizing a *Laser* light source with  $\lambda=408\text{ nm}$ . In this demonstration (Figure 2.19), an anodic aluminium oxide template with 25 nm holes and 50 nm pitches was used. To be able to measure the resolution enhancement produced exclusively by the  $\mu\text{S}$ -s (fused silica with  $D=2.5, 5, 7.5\text{ }\mu\text{m}$ ,  $n_{\text{sphere}}=1.47$  and polystyrene  $D=5\text{ }\mu\text{m}$ ,  $n_{\text{sphere}}=1.62$ ), the surface was not coated with gold. Acquired photographs showed, that the sample patterns were resolved. Unfortunately, the authors did not provide any intensity or modulation measurement data for these experiments, therefore comparison with other methods and exact



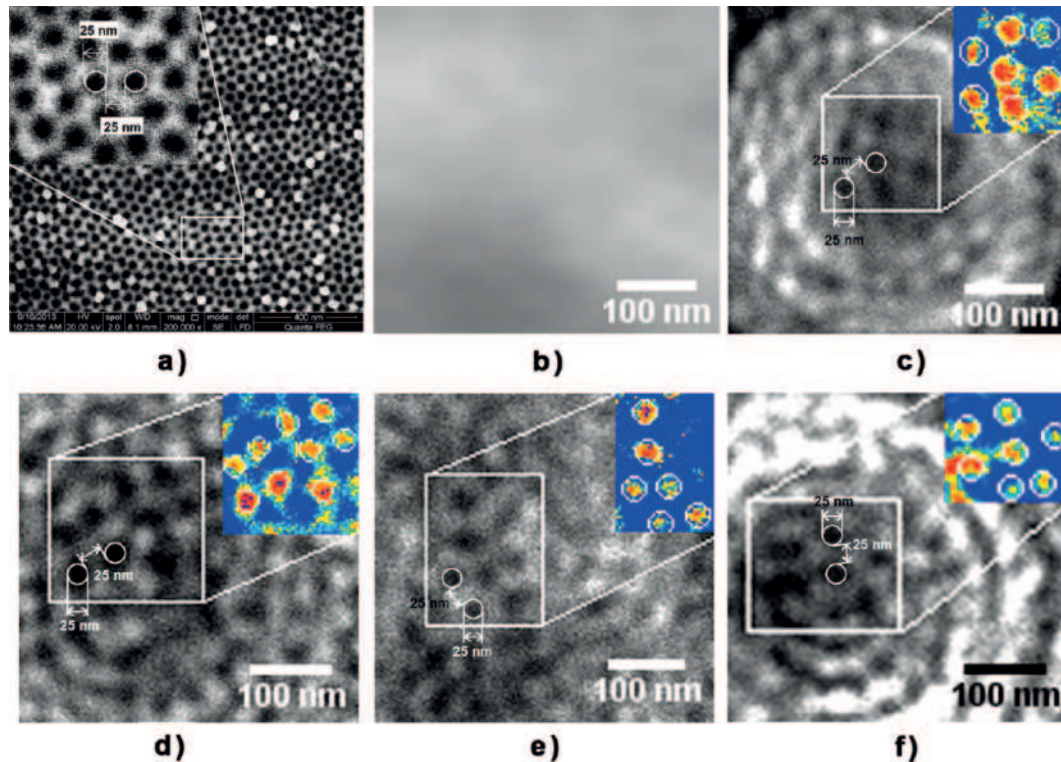


**Figure 2.19** –  $\mu S$ -based super-resolution imaging with a scanning *Laser* confocal microscope. Images of an anodic aluminium oxide template with 25 nm holes and pitches imaged by **a)** a SEM **b)** a scanning *Laser* confocal microscope in combination with **c)** 5  $\mu\text{m}$  fused silica  $\mu S$ , **d)** 2.5  $\mu\text{m}$  fused silica  $\mu S$ , **e)** 7.5  $\mu\text{m}$  fused silica  $\mu S$  and **f)** 5  $\mu\text{m}$  polystyrene  $\mu S$ . Insets show the corresponding pseudocolor images. Reproduced from [128].

resolution calculations are difficult to make. Moreover, it is important to note, that these impressively low-dimensional features were imaged with a *Laser* light source that provides increased illumination power and reflected light intensity. Another non-negligible factor is the confocal setup that by itself provides an increased resolution compared to a classical optical microscope due to the engineered *PSF*.

Following the idea of potential applications of high-*RI*  $\mu S$ -s [118], biological sample imaging with a similar setup was demonstrated in 2014 [129]. Here, super-resolved features of sub-cellular organelles and biomolecules were shown both in water- and oil-immersion with  $40\times$ ,  $NA=0.8$  and  $63\times$ ,  $NA=1.4$  objectives, respectively. Proving the imaging capabilities of  $D=60\mu\text{m}$  *BTG*  $\mu S$ -s in these conditions confirmed their applicability for life science-related microscopy. These findings were reproduced in the following year, when the same  $\mu S$ -s were embedded in *PDMS* and used for imaging various biological samples including mouse kidney tissues, proteins and human glioblastoma cells in both wide-field and fluorescent mode [130]–[132]. The advantage of the elastomer fixation was that the fabrication process could be done independent of the experiments. Furthermore, since no immersion liquid was needed, inverted microscopes could be used too and the potential effect of evaporation of the immersion medium was avoided. However, as it was pointed out in a follow-up paper [133], two issues

may hinder this kind of experimental approach. The *FoV* is limited by the diameter of the  $\mu S$  despite of the thin-film approach. Various techniques overcoming this issue, including the one shown in [133] will be presented in section 2.3.2. The other concern is the practical handling of the *PDMS* films as they can be difficult to peel off from the substrate depending on their thickness. To help the experimentation, the placement of a transparent tape on the substrate was proposed. The tape could reduce the surface energy and the Young's modulus effectively, therefore enabled the peeling without damaging the film. The thickness of the *PDMS* layer was regulated during the spin-coating of the uncured polymer. Measurements for *PDMS* films with  $\sim 3$ - $100 \mu m$  thickness showed its effect on both the achieved magnification and the *FoV*. The former was found to be decreasing when layer-thickness was increased, while the latter had a maximum at  $\sim 10 \mu m$  thickness. These values were found for *BTG*  $\mu S$ -s with  $D=15$  and  $20 \mu m$ . In those cases, when the diameter of the sphere was higher than the *PDMS*-layer, the surface of the  $\mu S$  was covered evenly with the given thickness of *PDMS*.

Besides for biological applications, the  $\mu S$ -based *SRM* could be also applied in the field of metrology [134]. Since diffraction-limited feature sizes are common in modern electronics, a general need for observation and optical investigation was raised. The most common method for imaging is currently the *SEM*. However, its instrumentation is expensive, sensitive on vibrations and its not optimal for imaging non-conductive samples. Both of these issues could be avoided by imaging with dielectric  $\mu S$ -s. In the presented paper,  $D=60 \mu m$  *BTG*  $\mu S$ -s were proposed for imaging. As a demonstration, a silicon template with *LSP*-s was observed. It had  $220 \text{ nm}$  pitch with non-equal line and space widths, since the lines were  $120 \text{ nm}$  wide. The microscope they used for these experiments was equipped with a halogen light source ( $400 \text{ nm} < \lambda < 750 \text{ nm}$ ) and a  $63\times$ ,  $NA=1.4$  objective. This resulted in a diffraction limit of  $d=174 \text{ nm}$  (Rayleigh criterion) or  $d=143 \text{ nm}$  (Abbe's law). The authors claimed to resolve this pattern with the help of the  $\mu S$ -s, but not with the microscope alone. This causes a contradiction, because the pitch of the *LSP* was  $220 \text{ nm}$ , therefore the microscope also should have been able to resolve it. Unfortunately, no measured intensity data or modulation supporting the images were published, therefore the cause of the difference is not obvious. However, it is possible that without the extra  $\sim 2.8$  magnification factor produced by the  $\mu S$ -s (measured data), the microscope-mounted camera was not able to map the structure properly, due to its pixel-size limitation, causing too small modulation in the final image for the human eye to detect (see chapter 6 for further investigations on this issue).

A novel approach on microobject-based *SRM* was reported in 2016 [135]. By assembling  $15 \text{ nm}$   $TiO_2$  nanoparticles, a *3D* dielectric metamaterial was constructed. This could be placed on various samples for imaging, similarly to a *SIL*. The metamaterial could create an array of illumination spots on the sample surface (like a  $\mu S$ ) and simultaneously could couple the near-field information into the far-field. To demonstrate this effect, various geometrical patterns from a semiconductor wafer with gold-coated feature sizes down to  $45 \text{ nm}$  were imaged. The main optical components besides the metamaterial-*SIL* consisted of a classical optical microscope with  $100\times$ ,  $NA=0.8$  objective and a *CCD* camera. The sample was imaged in three illumination conditions: white light (full visible spectrum), green light ( $\lambda \sim 540 \text{ nm}$ ) and blue light ( $\lambda \sim 470 \text{ nm}$ ). The pattern was recognizable in all cases, however, no intensity or modula-

### 2.3. Micro-object-based super-resolution imaging

---

tion analysis was provided with respect to the photographs. Although this system provides one of the best resolutions within the microobject-based *SRM* techniques, again, the smallest detectable features were demonstrated on a gold-coated surface that induces uncertainty in the performance analysis. Moreover, the preparation and handling of the assembled  $TiO_2$  spheres were not so straightforward as other previously shown  $\mu S$ -based methods.

Another microscopy system demonstrating super-resolution imaging was reported in the same year [136]. Here, *BTG*  $\mu S$ -s were placed in a commercial white light interferometer. The unique choice of hosting environment enabled to construct three-dimensional (*3D*) images when scanning the sample with the help of a piezoelectric translator. Results showed, that the same topography resolution could be achieved as with an *AFM*, but because in the x-y plane the *FoV* was extended by the  $\mu S$ , the scanning time could be significantly reduced. The lateral resolution of the system was determined by the water-immersed  $\mu S$ . Various silicon-based samples were imaged and diffraction-limited features were resolved. The authors claimed 50 nm lateral and 10 nm axial resolution, however the former was stated based on detecting a feature with that size and a much greater pitch. As they concluded in their work, the main advantage of this *3D* super-resolution technique is the reduced scanning time compared to an *AFM*.

Many  $\mu S$ -based imaging techniques were shown in this section with various approaches and results. But as it was pointed out, the main issue with most of them is that their resolution measurement method is arbitrary. Although claims of the fundamental limit of  $\mu S$ -based *SRM* was shown [137], the race to demonstrate lower and lower resolutions continued. In this process, samples with gold-coated surfaces, *LSP*-s with non-equal widths, random geometric patterns with one feature that only in one dimension satisfies the resolution claim and various illumination sources (*e.g.* coherent, incoherent, filtered, non-filtered) were used. This variety makes it very difficult to compare the results and to determine what is the real limitation of each presented technique. To call attention to this issue, standardizing the measurement processes was proposed [138], [139]. The key elements of an accurate description would be the following: (i) clear description of *a priori* knowledge, including illumination-type, -wavelength, -filtering and other major components of the optical system (*e.g.* the type of objective) and post-processing steps; (ii) imaging Siemens start targets (Figure 2.20.a) or *LSP*-s with various orientation and equal widths (Figure 2.20.b); (iii) considering substrates, such as gold-coated surfaces or fluorescent samples as special cases, and not deducing general conclusions from these measurements. As for wide-field systems, presenting data from different locations within the *FoV* would be advised. Evaluating new imaging systems based on these principles would benefit the whole community, because it would clarify the exact performances of the proposed methods.

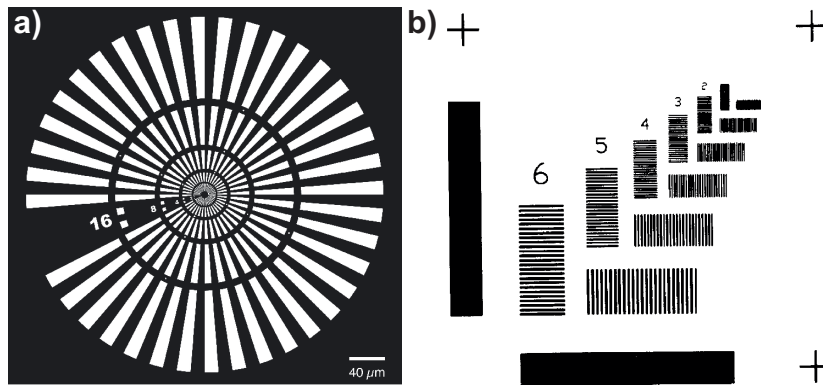


**Figure 2.20** – Targets for characterizing the resolution. **a)** The Siemens star target for coherent microscopy resolution measurement. **b)** Bar targets with different orientations and widths to determine the resolution of an incoherent microscopy system. Reproduced from a) [139], b) [138].

### 2.3.2 Scanning micro-object-based techniques

As was mentioned in the previous section, one realized already in the early works of  $\mu S$ -based SRM that the *FoV* is a main limiting factor of these techniques. It was also shown previously, that this scales with the diameter of the  $\mu S$ , but the size increment leads to a reduced resolution enhancement. Therefore, other approaches had to be found to overcome this issue. One of the first solutions was presented in 2013 [140]. A micromanipulator was integrated into the imaging system that could hold and move the  $\mu S$  in any desired position (Figure 2.21). This glass rod was mounted on a 3D translational stage and had a movement accuracy of  $\sim 20$  nm. Alternatively, it could be fixed, in which case, the sample had to be placed on a motorized microscope stage. The latter solution provided higher accuracy during movements, therefore it was preferred for the imaging experiments. The  $\mu S$ -s were attached to the glass rod with either air suction or an optical glue. During imaging the shaft did not influence the super-resolution capabilities of the  $\mu S$ , because the attachment point was out of the optical

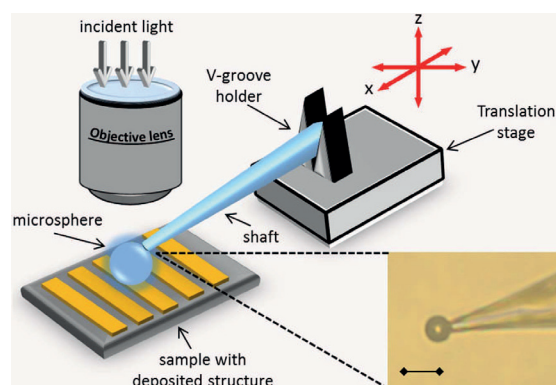


**Figure 2.21** – The layout of the optical setup for scanning a  $\mu S$  over the sample surface with a micropipette. Inset shows a photograph of a  $\mu S$ , attached to the micropipette. Reproduced from [140].

### 2.3. Micro-object-based super-resolution imaging

---

path, as was also confirmed by the numerical simulations. The smallest feature (a gap between 500 nm-wide gold structures) detected by the system was  $\sim 73$  nm. This was achieved with silica  $\mu S$ -s ( $6.1 \pm 0.6$  nm) observed by a  $50\times$ ,  $NA=0.55$  objective in air under white light illumination. The positioning technique was found robust, as no sphere was lost or unwillingly deposited during the experiments. This concept was reintroduced two years later [141], when the ethanol-immersed version of it was demonstrated. The added liquid reduced the friction between the glass-probe-actuated  $\mu S$  and the sample surface. It also acted as a "glue" and ensured good contact between the two objects. Furthermore, a post-processing method was shown, proposing a mosaic-like image stitching to construct a bigger *FoV* final picture. However, experimentally only a small increment was demonstrated, as the six acquired images of the sample surface,  $2\ \mu\text{m} \times 2\ \mu\text{m}$  each, were merged into a final picture showing an area of  $5\ \mu\text{m} \times 3\ \mu\text{m}$ . The cause of the shrinkage was in the overlapping, that was used for the stitching.

A novel, extended *FoV* imaging setup was shown in 2014, when fluorescence correlation microscopy was realized with an array of self-assembled  $\mu S$ -s [142]. To fabricate such an array, latex  $\mu S$ -s ( $D=2\ \mu\text{m}$ ,  $n_{\text{sphere}}=1.59$ ) were diluted in water and dispersed on a microscope cover glass. As the water evaporated, the spheres formed a single-layer hexagonal lattice. Then a chamber was formed by covering the chip with another cover glass.  $30\ \mu\text{m}$  spacers ensured a constant gap between the two of them. Afterwards, the formed chamber was filled with a solution containing fluorescent dyes. The sample was illuminated by a  $\lambda=633$  nm *Laser* and was observed with a  $10\times$ ,  $NA=0.3$  objective. Results showed, that each  $\mu S$  created a *PNJ* and each of those could contribute to the global detection volume. This led to an increased detection volume of several tens of femtoliters, while the fluorescent excitation and collection efficiency could be preserved. Furthermore, the diffusion time of a single molecule to cross an analysis spot (*i.e.* a *PNJ*) was reduced, therefore photobleaching could be significantly decreased. Demonstrations showed, that various parameters could be assessed with this technique, including fluorescence brightness, photo-physical blinking, diffusion coefficient and relative hydrodynamic radius. This approach to *SRM* showed, that imaging with parallel  $\mu S$ -s is possible, if the diameter uniformity is sufficiently high.

These findings were confirmed, when a study showed parallel imaging in wide-field microscopy [133]. The fabrication process described in this work was already shown in the previous section. However, in the last section of the paper, an experiment with multiple  $\mu S$ -s was presented. Uniform *BTG*  $\mu S$ -s ( $D=20\ \mu\text{m}$ ) were closely packed in a  $7.4\ \mu\text{m}$  thin *PDMS* film. When an image of the sample was acquired through all of them simultaneously, the generated virtual image was present under all of the  $\mu S$ -s that were placed in the *FoV* of the microscope objective (Figure 2.22.a). It was also shown, that already a couple of  $\mu\text{m}$  difference in the diameter forbids this kind of acquisition, since the *FoV* of the microscope objective along the *z* axis is limited (Figure 2.22.b). Since the commercially available  $\mu S$ -s typically have bigger deviation than that (*e.g.* the *BTG* spheres supplied by Cospheric, CA, USA), the difficulty of large array fabrication was pointed out. Eventually, this set a strict limiting factor on the maximally achievable *FoV*. As a consequence, research was focused on imaging methods, where the extended *FoV* is achieved by scanning a  $\mu S$  over the sample.

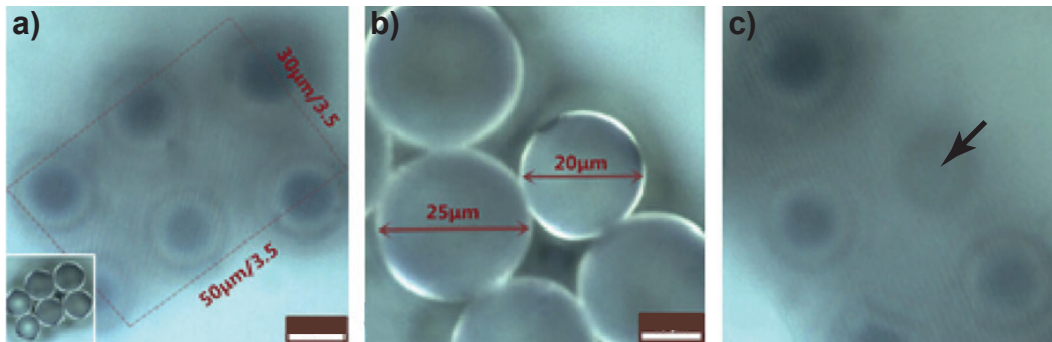


**Figure 2.22** – Parallel wide-field imaging with uniform  $\mu S$ -s. **a)** Virtual image of a *LSP* generated by six *BTG*  $\mu S$ -s simultaneously. The *FoV* of the  $\mu S$ -s is overlapping due to their close-distance positions. Scale bar  $10\ \mu m$ . **b)** Photograph of *BTG*  $\mu S$ -s with different diameters placed on the top of the sample. Scale bar  $10\ \mu m$ . **c)** Virtual image generated by the  $\mu S$ -s from **b)**. The arrow points to the lack of virtual image formation in the imaged plane by the  $\mu S$  with a smaller diameter. Reproduced from [133].

Chemically powered, autonomous microrobots were introduced to perform such a scanning in 2016 [143]. The concept, called swimming microrobot optical nanoscopy (*SMON*), utilized high *RI*  $\mu S$ -s swimming in a media and imaging the sample "on-the-fly". This could be achieved by selectively coating one side of the  $\mu S$  (polystyrene ( $n_{sphere}=1.59$ ) or  $TiO_2$  ( $n_{sphere}=2.1$ ),  $D=2-20\ \mu m$ ) with a thin Ti/Ni/Pt (2/5/5 nm) layer. This metallic tri-layer served as the "engine" of the microrobot, because it generated a local oxygen gradient through the asymmetric Pt-catalyzed decomposition of the hydrogen peroxide fuel. The fuel was mixed in the aqueous solution that served as the media for imaging. The swimming direction of the  $\mu S$  could be controlled remotely by an external magnet that interacted with the deposited Ni layer. Imaging was demonstrated with various *in silico* samples with feature sizes down to 20 nm. However, all of these patterns had huge pitches (up to  $2\ \mu m$ ), from which instead of the resolution limit, only the detection limit of the system could be determined. Another interesting aspect of the work was the image post-processing that allowed to stitch the acquired photographs, therefore map the sample along any desired path. These algorithms also allowed the stitching from parallel sources, enabling scanning with multiple swimming  $\mu S$ -s at the same time. Beside wide-field microscopy, the authors also demonstrated fluorescent imaging of biological samples, however, this was limited due to the toxic nature of the fuel mixed into the immersion medium. The fuel concentration determined the speed of the  $\mu S$ , typically in the range of 5 -  $35\ \mu m/s$ . The authors envisioned several possible directions of development for *SMON*, including large area parallel scanning with self-assembled  $\mu S$ -array and real-time, high-resolution imaging of soft biological samples with less toxic fuels such as glucose or urea. Since the trajectory of the scanning is not restricted, computer-controlled scanning along special patterns or features (*e.g.* tracking of a neuron) also could be realised in the future. An alternative solution for actuation, presented in the same year, was to combine a dielectric  $\mu S$  with an *AFM* [144]. Since the *AFM* instrumentation was a well-proven concept for precise and fine motions, it was a perfect candidate to overcome the *FoV* limitation of a single  $\mu S$ . The technique was called  $\mu S$ -based scanning superlens microscopy (*SSUM*) (Figure 2.23.a).

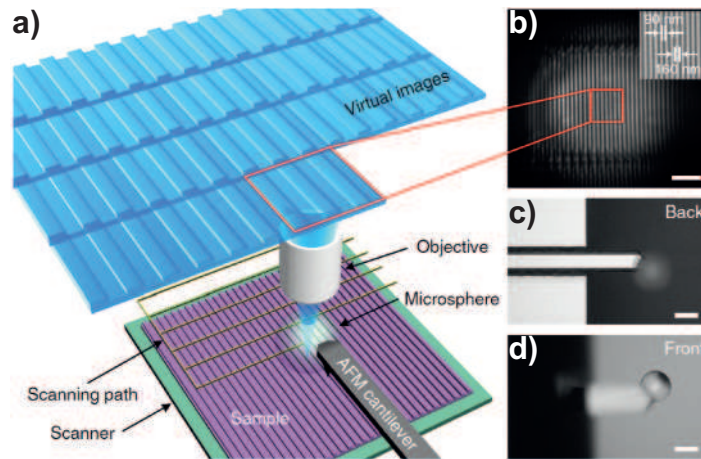


**Figure 2.23** – The  $\mu S$ -based SSUM. **a)** Schematic of the  $\mu S$ -based SSUM, showing the scanning initiated by the AFM instrumentation and the imaging conducted by the dielectric  $\mu S$ . **b)** Super-resolution virtual image generated by the imaging system as shown in a). Inset shows the SEM image of the sample. Scale bar  $2\ \mu\text{m}$ . **c), d)** Photograph of the AFM cantilever attached  $\mu S$  from the back and the front, respectively. Scale bars  $50\ \mu\text{m}$ . Reproduced from [144].

Experimentally, the two components were assembled by fixing a BTG  $\mu S$  to the end of an AFM cantilever with the help of Norland Optical Adhesive (NOA) 63 ultraviolet (UV) curable glue. As it is shown in Figure 2.23.c-d, the attachment point of the cantilever was on the side of the  $\mu S$ , therefore the optical path was not blocked. The imaging was done purely by an optical microscope, observing the sample through the  $\mu S$ , while the AFM was responsible only for the positioning.

Two operating modes were tested, contact scanning and constant-height scanning, both originating from the AFM instrumentation. In the former, the  $\mu S$  was always in direct contact with the sample. To enable this mode, three criteria had to be fulfilled: (i)  $D$  had to be greater than the tip height of the AFM probe, or a probe without a tip had to be used; (ii)  $D$  and the spring constant of the cantilever had to be adjusted to avoid vibrations during scanning, practically,  $D < 80\ \mu\text{m}$  had to be used; (iii) as mentioned earlier, the attachment point of the cantilever had to be on the side of the  $\mu S$ , in a way that the light path remained clear. Further consideration for  $D$  was to find a balance between the resolution and the FoV. The trade-off here was that the FoV scales with  $D$ , but the smaller  $\mu S$ -s could achieve better resolution. For the demonstration of imaging in this scanning mode, a  $D=57\ \mu\text{m}$  BTG  $\mu S$  was used to image LSP-s (Figure 2.23.b). The smallest pitch shown in this paper was  $250\ \text{nm}$ , but individual features down to  $40\ \text{nm}$  were also resolved.

In the second scanning mode, the challenge was to establish a height, where the  $\mu S$  was still close enough for capturing the evanescent waves. Both theoretical calculations and experiments showed, that this value should be maximum  $\sim 0.65\text{-}0.8\ \mu\text{m}$  for a  $D=60\ \mu\text{m}$   $\mu S$  under white-light illumination. This imaging mode was found to be particularly useful when imaging biological samples (e.g. cells), because they usually have bigger height variance than *in silico* samples and with this scanning mode, damaging of the sample can be avoided. The authors also showed

## Chapter 2. State-of-the-art super-resolution optical imaging

various image processing software packages that could perform the post-processing (*i.e.* the stitching) of the acquired images. These used automated algorithms to match the individual image tiles, which produced fine results, however, the process could be very time consuming for mapping large areas. Unfortunately, due to the huge variety in experimental parameters through the demonstrated images (*e.g.* unfiltered halogen light source, various  $\mu S$  diameters, samples containing non-comparable geometrical patterns), it is difficult to determine the exact resolution of the presented system. Although the super-resolution imaging capability was proven, the biggest drawback of this concept is the operation of the *AFM* instrumentation that is sensitive on vibrations and compared to previously shown methods, complex to handle. A very similar imaging method was shown in the following year [145]. In that case, the  $\mu S$  was attached to an *AFM* cantilever with electrostatic forces instead of the optical glue. This could be achieved by fabricating a  $3.5\ \mu m$  hole in the cantilever by focused ion beam lithography. This hole allowed the imaging to operate both in transmission and reflectance mode and kept the  $D=4.6\ \mu m$  silica  $\mu S$  fixed. Due to this connection method, it was also possible to release the  $\mu S$  on the sample and picking it up after imaging, however, the authors pointed out that the imaging was not hindered by the presence of the cantilever. They also emphasized the inconsistency in previously published resolution measurement methods and therefore fabricated equally spaced *LSP-s* with pitches between 100 - 1000 nm. These patterns were then imaged with and without the presence of the  $\mu S$ -s with  $\lambda=405\ \text{nm}$  illumination in transmission mode (Figure 2.24.a-b). Results showed, that  $\mu S$ -assisted imaging could resolve higher spatial frequencies than the  $50\times$ ,  $NA=0.5$  objective alone. Analysing the intensity values across the *LSP-s*, allowed the authors to calculate the frequency response (*i.e.* the modulation transfer function (*MTF*)) of both systems (Figure 2.24.c). The calculated data indicated that the  $\mu S$ -

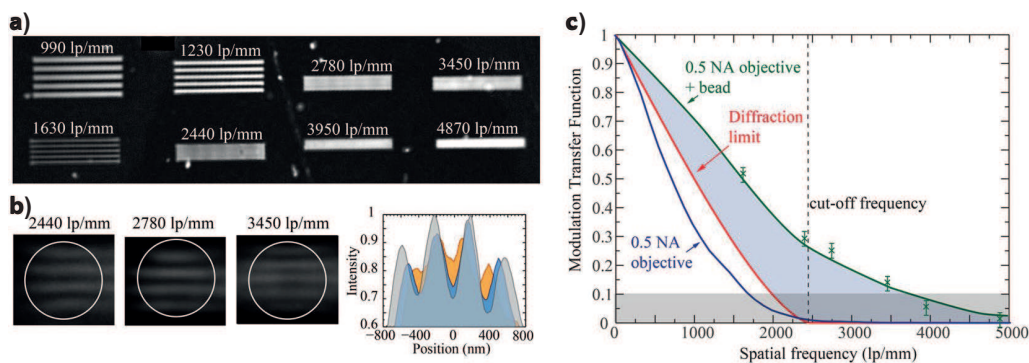


**Figure 2.24** – Optical response in  $\mu S$ -based, *AFM* assisted brightfield microscopy. **a)** Photograph of *LSP-s* with various pitches (with their values given as line-pairs/mm), taken with a  $50\times$ ,  $NA=0.5$  objective without the presence of a  $\mu S$ . **b)** Details of the same pattern observed through a  $\mu S$  with the corresponding intensity profiles along a vertical measurement line (not shown) on the right. **c)** Frequency response of the imaging system with and without a  $\mu S$ . The blue and the red lines show the measured and the theoretical values produced by the objective alone, respectively. The green line shows the measured values with the  $\mu S$ . The gray area indicates the minimum modulation difference needed for resolving the features according to Rayleigh criteria. The cut-off frequency was calculated based on the Abbe's limit of a system with  $NA=0.5$ . The highlighted area between the red and the green lines is the resolution gain achieved by the  $\mu S$ . Reproduced from [145].



### 2.3. Micro-object-based super-resolution imaging

assisted system could produce higher modulation for low spatial frequencies and allowed the information transfer of higher ones that otherwise would be lost. A considerable conclusion was given at the end of this work, demonstrating that despite the  $\mu S$ -assisted system could improve the achievable resolution for a low  $NA$  imaging system, its absolute performance was not better than the one of the commercially available best  $NA$  objective for the given medium. Further investigation on this topic is shown in section 3.2.

Recently, a new implementation of thin-film-embedded  $\mu S$ -s was shown [146]. To enable scanning, a custom adaptor was designed that synchronized the position of the so-called superlens and the microscope objective (Figure 2.25). The superlens was fabricated in a previously demonstrated way [133]:  $BTG \mu S$ -s with diameters between 3 - 80  $\mu m$  were fixed randomly in a  $PDMS$  layer. After curing the  $PDMS$ , the superlens was glued to the bottom of the plastic adaptor that was prepared by 3D printing. Due to carefully designed dimensions, the adaptor could be moved along the  $z$  axis, therefore it could be positioned in a way that the microscope objective could focus on the virtual image plane generated by the sample upon being observed through the  $\mu S$ -s.

To evaluate the static imaging performance of this system, two samples were imaged. First, the surface of a Blu-ray disc was observed with a 100 $\times$ ,  $NA=0.9$  objective under unfiltered white-light illumination ( $400 \text{ nm} < \lambda < 700 \text{ nm}$ ). Both  $D=22 \mu m$  and  $D=67 \mu m$   $BTG \mu S$ -s could resolve the features on the surface of the Blu-ray disc. These results did not show much improvement in the achieved resolution, as the pitch of the  $LSP$  on the disc surface was 300 nm while the microscope's Abbe-resolution-limit without the  $\mu S$ -s was between 222 nm and 389 nm depending on the wavelength of the light. The second sample was a cluster of adenoviruses that consisted of 90-100 nm individual elements. These were detected by a  $D=70 \mu m$  sphere, but from this result, the general resolution limit of the imaging system could not be deducted. Demonstrating the scanning mode of the setup was not a straightforward operation, as the  $PDMS$  superlens caused such a big friction on the sample that imaging biological objects became impossible. *In silico* structures were possible to image only when a special lubricant (WD40) was applied. Finally, extended  $FoV$  images were made, where a custom stitching algo-

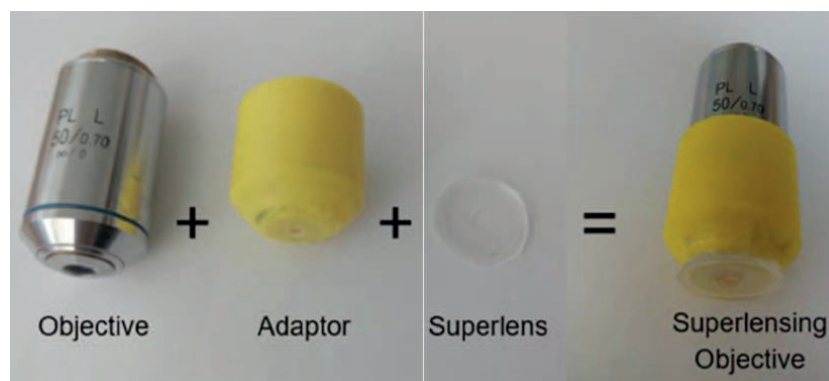


**Figure 2.25** – Parts of the superlensing microscope objective lens. A conventional microscope objective is integrated with  $PDMS$  thin-film-embedded  $BTG \mu S$ -s (called superlens) through a 3D-printed plastic adaptor. Reproduced from [146].

## Chapter 2. State-of-the-art of super-resolution optical imaging

---

rithm was demonstrated. This worked in a sequential way and it calculated the optimal offset between adjacent extracted regions, based on maximizing the normalized cross correlation. Final images were also smoothed by alpha blending. The end results showed good image quality, but the time consumption of this process was not discussed.

As conclusion for the presented  $\mu S$ -based *SRM* techniques, the advantages of these systems in terms of cost-effective alternatives to more complex super-resolution methods clearly can be seen. However, because of the variety of measurement methods and arbitrary definitions used in the publications, comparison of the achieved resolutions is not straightforward. Furthermore, the extension of the *FoV* is still an unresolved issue, as pioneering works only started to appear recently. In the following chapters of this thesis, some of the concerns discussed earlier will be addressed and alternative solutions for  $\mu S$ -based *SRM* will be provided.

## 3 Principles governing micro-object-based imaging

*This chapter presents the theoretical studies that we did in order to understand the physical phenomena behind microsphere-based super-resolution imaging. In the first section, the photonic nanojet is investigated. This unique light-focusing effect is created by the microsphere and it plays a significant role in imaging when the diameter of the microsphere is sufficiently small. In the second section, the path of the reflected light is investigated as this describes quantitatively the resolution enhancement generated by bigger diameter microspheres that are typically used in microscopy applications. Our results provide a theoretical toolbox that can help the engineers in designing microsphere-assisted super-resolution optical systems.*

---

This chapter was adapted from the following publications:

- Section 3.1: H. Yang, R. Trouillon, **G. Huszka**, and M. A. M. Gijs, “Super-resolution imaging of a dielectric microsphere is governed by the waist of its photonic nanojet”, Nano Letters, pp. 4862–4870, 2016.  
*My contribution:* I conducted the numerical study of the light propagation, fabricated the grating structure presented in Figure 3.7 and contributed to the data analysis and to the manuscript.
- Section 3.2: D. Migliozi, M. A. M. Gijs and **G. Huszka**, “Microsphere-mediated optical contrast tuning for designing imaging systems with adjustable resolution gain”, Scientific Reports, submitted  
*My contribution:* I initiated the study, did the numerical simulations of the photonic nanojet, analysed the data generated by both the simulations and the models, did the experimental confirmation, quantified its results and contributed to the manuscript.

As the number of  $\mu S$ -based super-resolution imaging applications were growing, the exact understanding of the physical phenomena behind them became an urgent issue. Therefore, we decided that an extensive investigation should be carried out. Based on the pioneering studies in this field (section 2.3.1), the focus of attention was turned towards the special light-focusing condition (*i.e.* the *PNJ*) that was generated by the  $\mu S$ . Our investigation regarding the

formation and the influence of this special optical phenomenon will be detailed in section 3.1. However, as the research was shifted towards microscopy applications, the diameter ( $D$ ) of the  $\mu S$ -s that we studied became larger. This was inevitable in order to make handling feasible and to increase the possible  $FoV$ . Besides this, numerous studies showed that  $\mu S$ -based imaging is sample-dependent. To observe, how these new conditions affect the performance of  $\mu S$ -based  $SRM$ , a new study was carried out, in which the focus of investigation was placed on the path of the reflected light, originating from the sample and traveling towards the microscope objective (section 3.2).

### 3.1 The illumination pathway

Conventional optical microscopes are limited by the diffraction limit and can resolve features of around half of the wavelength of illumination, as they are only capable of transmitting the propagating wave components emanating from the illuminated object [147]. The evanescent components that carry the fine information about the object, decay exponentially in a medium with positive permittivity and permeability. Therefore, they are lost before reaching the image plane. Several efforts have been pursued to overcome the diffraction limit as it was shown in section 2.1 and 2.2. However, the applications of these methods have been limited in part due to their sophisticated engineering designs or pretreatment steps. Alternatively, it has been demonstrated in section 2.3 that the use of various microobjects and especially dielectric  $\mu S$ -s on top of the objects can achieve near-field focusing and magnification, which in turn results in the capability to resolve features beyond the diffraction limit. The super-resolution capability of  $\mu S$ -s was found to be linked to two factors: (i) the  $\mu S$  performs as a solid-immersion lens and provides local enhancement of the  $NA$ ; (ii) the development of the  $PNJ$  [129], [134]. Even though it was suggested that the latter is essential to the super-resolution imaging capability of a  $\mu S$ , the exact link remained unclear. Therefore, we decided to study, in a quantitative way, the role of the  $PNJ$  for super-resolution imaging.

First a systematic numerical study of the light propagation through  $\mu S$ -s of different size using the finite element method ( $FEM$ ) was performed. This allowed characterizing the  $PNJ$  at the rear-surface of a  $\mu S$  and relating the theoretical magnification factor of a  $\mu S$  to the light focusing capability of the  $PNJ$ . Second, we performed an experimental study in which a systematic series of  $BTG$   $\mu S$ -s with diameter ( $D$ ) from 3 to 21  $\mu m$  were used to image linear test nanostructures that were immersed in water. The experimental magnification factor and the  $PSF$  that is analytically determined from the images allowed evaluating the resolution of the optical system, which was shown to directly correlate with the calculated properties of a  $\mu S$ 's  $PNJ$ .

As schematically illustrated in Figure 3.1, when a  $\mu S$  is illuminated by a propagating light beam from the far-field, the light is mostly refracted on its frontal surface at small incident angle and reflected at higher incident angle, the limiting angle between the two regions given approximately by the Brewster angle of the optical interface. When the size of the  $\mu S$  is much bigger than the illumination wavelength, it is a good approximation to use ray optics to explain

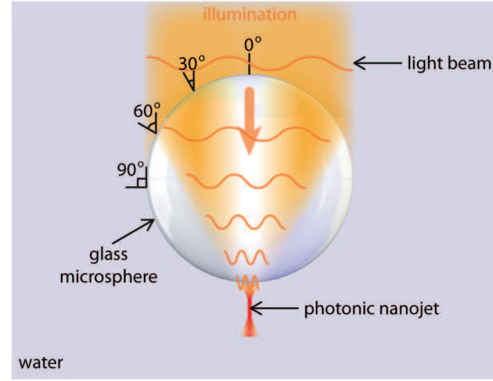


**Figure 3.1** – Mechanism of *PNJ* generation. Focusing of a plane wave light beam into a *PNJ* at the rear surface of a free-standing  $\mu S$ . At the front surface of the  $\mu S$ , the light is refracted at low incidence angle, while at higher incidence angle it gets mostly reflected.

how the light that is incident on the top-surface of the  $\mu S$  propagates. The refracted light propagates through the  $\mu S$  and generates a *PNJ* near the rear-surface of it (details described in Appendix A.1). A *FEM* study of the light wave propagation through a *BTG*  $\mu S$  ( $n_{sphere}=1.92$ ), with  $D$  ranging from 2 to 20  $\mu m$  in surrounding water medium ( $n_{medium}=1.33$ ) was performed in COMSOL Multiphysics software. The scalar equation 3.1 was used to study transverse electric waves in a two-dimensional (*2D*) model.

$$\nabla \times (\mu_r^{-1} \nabla \times E) - \left( \epsilon_r - \frac{j\kappa}{\omega\epsilon_0} \right) k_0^2 E = 0 \quad (3.1)$$

where  $\mu_r$  is the relative permeability,  $\epsilon_r$  is the relative permittivity,  $\epsilon_0$  is the vacuum permittivity,  $\kappa$  is the electric conductivity,  $\omega$  is the angular frequency,  $E$  is the electric field and  $k_0$  is the free-space wave number. The numerical simulations were carried out in *2D*, although for the currently investigated microsphere it would have been possible to construct a *3D* model. However, if  $D$  would be increased for further investigations (section 3.2), the needed computational power would exceed our resources and therefore would prohibit the comparison between studies. Furthermore, although this way we simulated an infinite *2D* cylinder instead of a *3D*  $\mu S$ , this simplified model captures the essential physical effects associated with our true *3D* system. In this model, the scattering boundary condition was used at all exterior boundaries, and the continuity boundary condition was used at material interfaces. A light source with  $\lambda=600$  nm and the same width as the diameter of the  $\mu S$  was set away from the front-surface of the  $\mu S$ -s. The wavelength was chosen to correspond to the peak of the halogen lamp that was used as the white-light illumination source in the experiments. After meshing of the model, the element size was  $\sim 22$  nm, that equalled  $1/30$  of the wavelength, which was sufficiently small to obtain a precise solution. In order to calculate the electric field, a line-source was placed at the edge of the model area. The initial values of the field along this line were set to zero in both *x*- and *y*-direction (*i.e.* in the plane of the model), while it had a positive value in the *z*-direction (*i.e.* out of plane). This generated a wave in the *y*-direction, corresponding to the illumination direction. After the model was solved, the light intensity distribution was

obtained by multiplying the electric field by its complex conjugate.

$\mu S$ -s with  $2\ \mu\text{m} < D < 20\ \mu\text{m}$  were analysed and Figure 3.2 shows the light intensity distributions near a 6, 2 and  $16\ \mu\text{m}$   $\mu S$ , respectively. When  $D=6\ \mu\text{m}$  (Figure 3.2.a), the *PNJ* directly emerged from the  $\mu S$  surface. When decreasing  $D$ , the focal point of the *PNJ* moved into the  $\mu S$ , as seen for the simulation result of a  $D=2\ \mu\text{m}$   $\mu S$  (Figure 3.2.b). For  $D > 6\ \mu\text{m}$ , the external focal point of the *PNJ* moved away from the rear-surface of the  $\mu S$ . As an example, Figure 3.2.c shows the simulation result obtained for a  $D=16\ \mu\text{m}$   $\mu S$ . To quantitatively study how light is focused by the  $\mu S$  into the *PNJ*, we determined from the model calculation (i) the linear region, where substantial refracted light enters the  $\mu S$  at its front surface, referred to as  $l_1$  in Figure 3.2, (ii) the width of the exiting beam at the rear surface is denoted as  $l_2$  and (iii) waist of the photonic nanojet (*i.e.* the full width at half-maximum of the photonic nanojet laterally at the peak intensity axially) marked as  $w$ . It should be noted that the light source in the *FEM* study was actually coherent, while the light source that was used later in conventional optical microscopy was incoherent. The comparison on the light intensity distribution in the *PNJ* under coherent and incoherent illumination is further discussed in the Appendix A.1. The study showed that the intensity profile along  $w$  does not significantly change, when using either an incoherent or a coherent light source, indicating that a coherent light-based simulation can provide sufficient information to study the resolution of our imaging system. The imaging mechanism of a dielectric  $\mu S$  is schematically illustrated in Figure 3.3. When the focused light that exits the  $\mu S$  illuminates the sample object (in this case a *LSP* with line width  $L$ ), no *PNJ* is generated but instead the reflected light follows a reflection-symmetric optical path, while evanescent waves that contain the high spatial-frequency information on the object are converted into propagating waves within the  $\mu S$  (Appendix A.1). The latter mechanism is only activated, when the distance  $h$  is small enough (of order of  $\lambda$ ). In the meanwhile, a magnified virtual image is generated in the far-field with magnification factor  $M$ . The imaging capability of the  $\mu S$  directly correlates with the formation of the focused *PNJ* as obtained from the numerical study, as the same optical paths are involved. Figures 3.4.a and

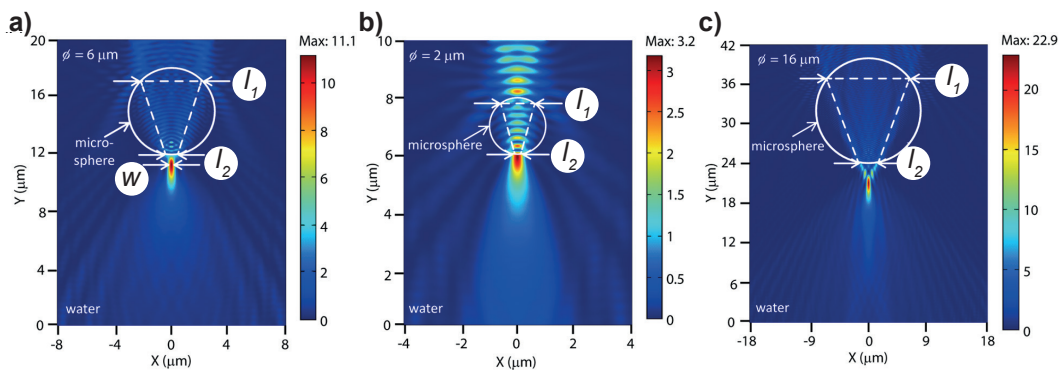


**Figure 3.2** – Numerical simulations of the light propagation through dielectric microspheres. **a)** *FEM* simulation of a plane-wave illuminated,  $D=6\ \mu\text{m}$  *BTG*  $\mu S$  in water. The linear region where substantial refracted light enters the  $\mu S$  at its front surface is referred to as  $l_1$ , while the width of the exiting beam at the rear surface is denoted as  $l_2$ ; the waist of the *PNJ* is referred to as  $w$ . **b), c)** Same as a) for  $D=2$  and  $16\ \mu\text{m}$   $\mu S$ -s, respectively.

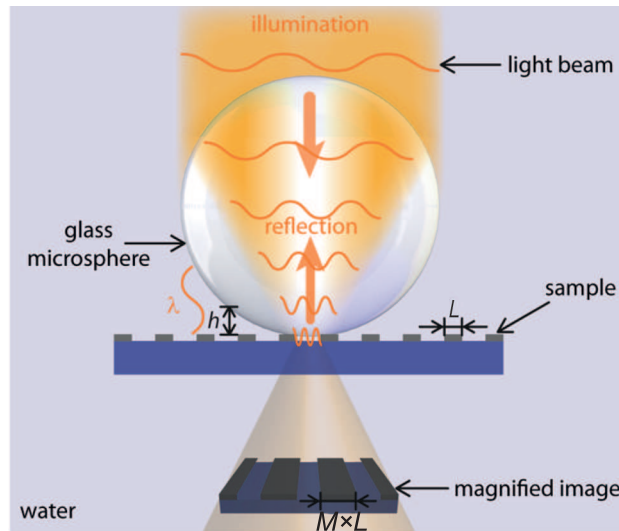


**Figure 3.3** – Mechanism of imaging through a dielectric  $\mu S$ . When a  $\mu S$  is positioned on a grating structure with line width  $L$  and illuminated from the front, the light reflected by the grating allows detecting a virtual image with magnification factor  $M$ . When the distance  $h$  between the  $\mu S$  and the grating is small enough (of order of  $\lambda$ ), the near-field evanescent wave carrying the fine details of the grating can become propagating in the high  $RI$   $\mu S$ , and later in the medium where it is to be collected by the microscope objective.

3.4.b show the calculated light focusing capability of a  $\mu S$ , expressed by the ratio  $l_1/l_2$ , and  $w/\lambda$  as a function of  $D$ , respectively. A bigger  $l_1/l_2$  indicates a better light focusing by the  $\mu S$  and corresponds to a smaller  $w$ . According to our simulations, the  $\mu S$  with  $D=6\mu m$  showed the best light focusing capability and smallest  $w$ .

To experimentally study the super-resolution imaging effect, a *LSP* with  $L=120$  nm and pitch of 220 nm (from Pelco, USA, see Figure 3.5.a), immersed in water, was used as test sample, to be imaged with transparent *BTG*  $\mu S$ -s that were loosely positioned on top of it. A conventional

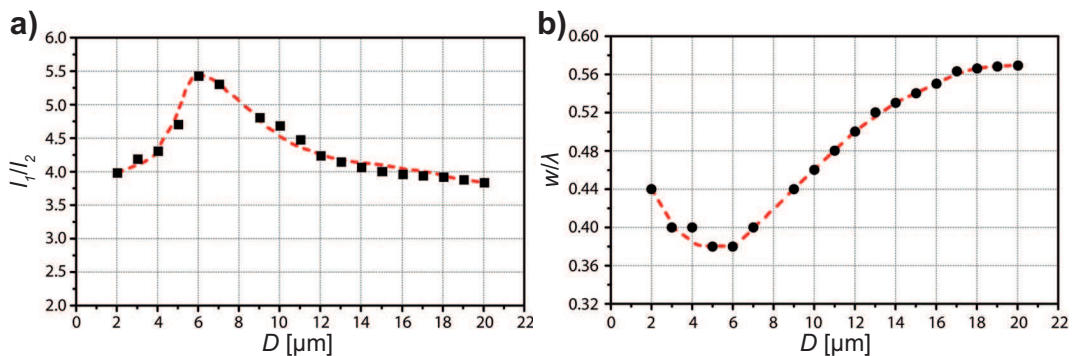


**Figure 3.4** – Analysis of the numerical simulation results. **a)** The light focusing capability of a  $\mu S$ , expressed by the ratio  $l_1/l_2$ , as a function of  $D$ . The dots mark the calculated values, while the red dotted line is a guide to the eye. **b)** The normalized waist of the *PNJ* ( $w/\lambda$ ), as a function of  $D$ . The dots were obtained from the simulation, while the red dotted line is a guide to the eye.

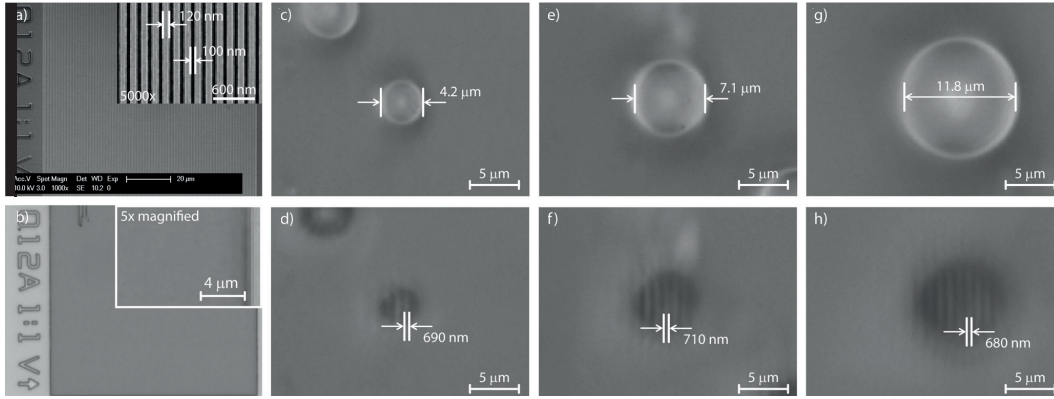


**Figure 3.5** – Imaging of a grating nano-structure (*LSP*) using different size  $\mu S$ -s and a water-immersion objective. **a)** SEM image of the *LSP* with  $L=120$  nm and  $P=220$  nm. **b)** Optical microscopy image of the nano-structure taken by a  $40\times$ ,  $NA=0.8$  water-immersion objective. The insert is a  $5\times$  magnified image, clearly showing that conventional microscopy cannot resolve the nano-structures with this feature size. **c-h)** Optical microscopy images obtained by positioning on the *LSP*  $\mu S$ -s with sizes of c),d)  $4.2\ \mu\text{m}$ , e),f)  $7.1\ \mu\text{m}$ , and g),h)  $11.8\ \mu\text{m}$ , respectively. The images of c),e),g) are focused on the  $\mu S'$  center plane, while the corresponding images d),f),h) are focused on the virtual image plane, showing that the *LSP* is imaged with a different magnification factor  $M$  for  $\mu S$ -s of different sizes.

reflection microscope (Zeiss Axioplan microscope) equipped with a CCD camera (AxioCam MRm camera) and a  $40\times$ ,  $NA=0.8$ , water-immersion objective was used to take images (all equipment from Carl Zeiss, Germany). A halogen lamp was used as the white-light illumination source with a wide-band spectrum, which is from  $\sim 400$  nm to  $700$  nm and the peak appears at  $\sim \lambda=600$  nm (data obtained from Zeiss). Figure 3.5.b is a microscopy image of the gratings taken by the  $40\times$  objective along, the inset is a  $5\times$  magnified image, clearly showing that the conventional optical microscope could not resolve the nanopatterns with a feature size of  $\sim 100$  nm. Indeed, even for the lowest wavelength of the illumination spectrum (*i.e.*  $\lambda=400$  nm), Abbe's law determines  $\sim 250$  nm diffraction limit that is bigger, than the pitch of the *LSP*. However, when a  $\mu S$  was placed on top of the nanoobjects, the diffraction-limited features became observable. Figures 3.5.c,e,g show  $\mu S$ -s with  $D=4.2$ ,  $7.1$  and  $11.8\ \mu\text{m}$  positioned on the sample, respectively. The focal plane of the microscope coincides with the plane of maximum sphere diameter, hence, on these pictures, the *LSP* is out-of-focus. When the focal plane of the microscope was set to the image plane of the  $\mu S$ -s, the virtual images appeared and could be captured by the camera. They are shown in Figures 3.5.d,f,h, corresponding to the  $\mu S$ -s of Figures 3.5.c,e,g, respectively. Compared to the size of the objects, the feature sizes of the *LSP* in the images are clearly magnified. As already schematically illustrated in Figure 3.3, comparing the size of the object with that of the image allowed determining  $M$ . Plotting these values against  $D$  showed that that the biggest magnification can be obtained by a  $D \approx 6-7\ \mu\text{m}$   $\mu S$  (Figure 3.6.a). On the other hand, comparing the experimental  $M$  with the theoretical light focusing capability  $l_1/l_2$ , as obtained from the simulations, resulted in a positive correlation with a Pearson's correlation coefficient of  $0.91$ , indicating that a better light focusing capability of a  $\mu S$  logically results in a higher magnification factor (Figure 3.6.b).



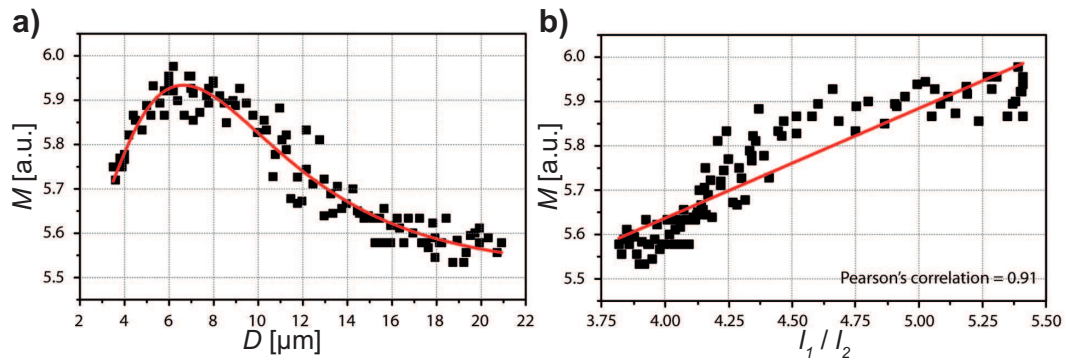


**Figure 3.6** – Analysis of the magnification factor. **a)** The dots represent the experimental magnification factor ( $M$ ) as a function of  $D$ , while the red solid line is a guide to the eye. **b)**  $M$  as a function of the light focusing capability  $l_1/l_2$  obtained from the simulations. The solid line represents a linear fitting curve with a Pearson's correlation coefficient of 0.91.

A remaining issue was, whether the light focusing capability of a  $\mu\text{S}$  has any impact on its super resolution imaging capabilities. For solving this question,  $LSP$ -s (chromium on glass substrate) with  $L=300$  nm and  $P=1200$  nm were imaged through the  $\mu\text{S}$ -s with different size by using the same optical microscope setup. As illustrated in Figure 3.7.a, the  $\mu\text{S}$  was positioned in the middle of two lines and due to the limitation factor of  $h$ , the magnified image only contained the interspacing at the center of the  $\mu\text{S}$  (darker zone in the image) and its neighbouring two lines (clearer zones in the image). Figures 3.7.b and 3.7.c show the microscopic

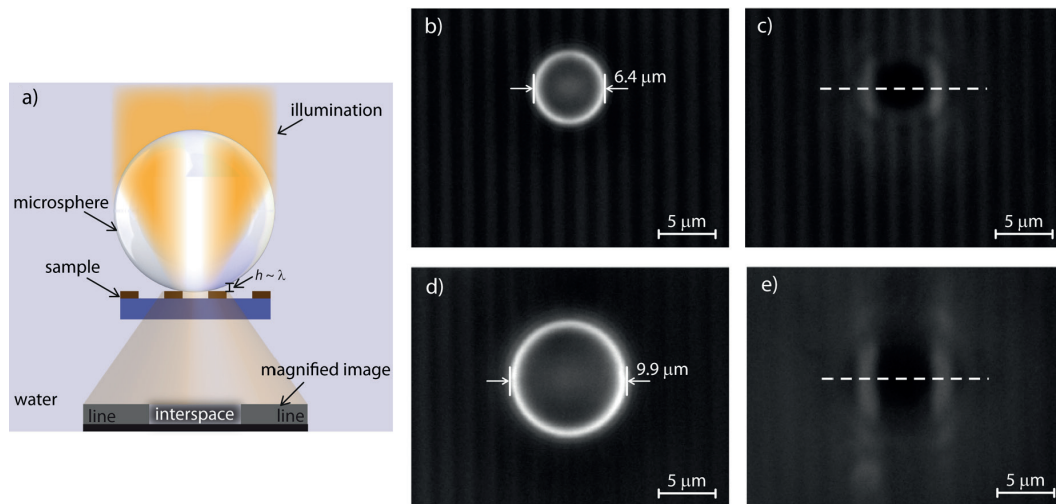


**Figure 3.7** – Experiments for the quantification of the resolution. **a)** A  $\mu\text{S}$  is positioned specifically in the middle of two lines of a dedicated test grating ( $LSP$  with  $L=300$  nm and  $P=1200$  nm) to characterize the sharpness of the line-space boundary in the virtual image. **b-e)** Optical microscopy images obtained by positioning  $\mu\text{S}$ -s on the  $LSP$  with sizes of **b),c)** 6.4  $\mu\text{m}$  and **d),e)** 9.9  $\mu\text{m}$ , respectively. The images of **b),d)** are focused on the  $\mu\text{S}$ ' center plane, while the corresponding images **c),e)** are focused on the virtual image plane. Each dashed line indicates where the intensity profile was taken that was fitted with the analytical  $PSF$  model.

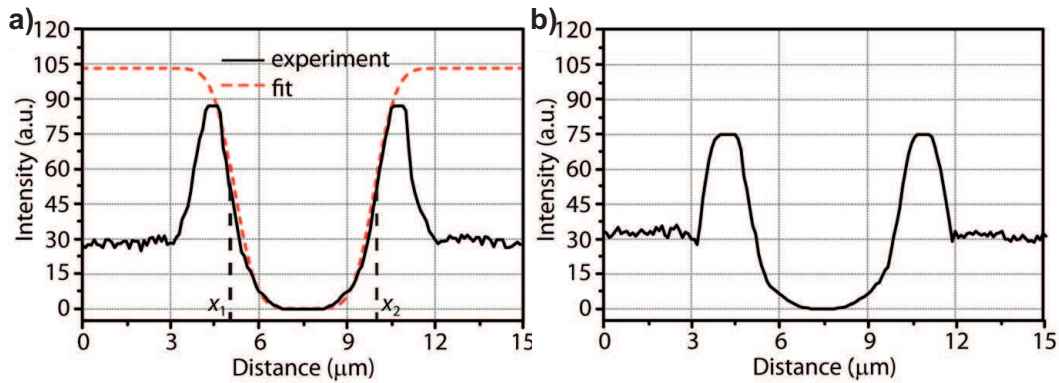


**Figure 3.8** – Measured data from the resolution quantification experiments. **a)** Intensity distribution along the dashed line in Figure 3.7.c with  $x_1$  and  $x_2$  the positions of the descending and ascending steps obtained from the fit using Equation 3.6. **b)** Intensity distribution along the dashed line in Figure 3.7.e.

images obtained by focusing on a  $D=6.4 \mu\text{m}$   $\mu\text{S}$  and on the image plane, respectively. The light intensity profile along the dashed line in Figure 3.7.c is shown in Figure 3.8.a. Moreover, similarly taken images obtained from a  $D=9.9 \mu\text{m}$   $\mu\text{S}$  are shown in Figures 3.7.d and 3.7.e, while the light intensity profile along the measurement line in the latter is shown in Figure 3.8.b. Comparison of Figure 3.8.a and 3.8.b determined clear differences on the peak intensities and on the intensity profiles.

These type of images were further analysed using an analytical *PSF* model to study the resolution in a quantitative way. The *PSF* is an important factor characterizing the mechanisms underlying the formation of an image in an optical system, defined as the response of the imaging system to a point object [148]–[150]. This *3D* function is characteristic of the imaging system and can have a rather complicated analytical expression, hence sometimes requiring simplifications or approximations to facilitate its use. However, the shape of the *PSF* is directly related to the resolution of the system, as the narrower the *PSF*, the better the resolution. The imaging process described here is based on the collimation of light that is incident on top of the  $\mu\text{S}$  into the *PNJ*. For detection of an object, the light is reflected back from the object into the detector, essentially following the same mirror-symmetric trajectory as during incidence. The width of the *PNJ* ( $l_2$ ) and more precisely the quantity  $l_1/l_2$  detailed in Figure 3.2 is a measure of the focusing capability of a  $\mu\text{S}$ . Indeed, the smaller  $l_2$  and the larger  $l_1/l_2$  is, the easier it will be for an initially evanescent wave, when it is reflected from the object, to be converted to a wave with higher spatial frequency that becomes propagating inside the  $\mu\text{S}$ . If higher spatial frequencies can be detected, this will result in a sharper image, hence in a better resolution and a narrower *PSF*. That is why the theoretical simulations of the *PNJ* profiles, provided for instance in Figure 3.2, are indicative of the diffraction processes in the optical system and can be useful to compare with the experimental *PSF*. Additionally, simulations hinted that the illumination profile partially describes the blurring introduced by the system and is at least indicative of the *PSF* in the absence of severe mismatches in the refractive indices [151]. As a consequence, these illumination profiles were used below to

establish assumptions on the overall *PSF*, and were justified *a posteriori*. Typically, the *PSF* can be approximated through models and numerical simulations. However, the purpose of this section is to find an experimental approach to evaluate the lateral resolution of the system through the *PSF* and to compare it to some of the results predicted by the simulations. In the case considered in this work, that is, where a plane is imaged, only the x-y profile of the *PSF* at the waist of the *PNJ* is relevant to the resulting image. Moreover, because of the cylindrical geometry of the problem, as shown in Figure 3.2, only the expression of the radial component at the waist is required to describe the *PSF* (Appendix A.1). Furthermore, only sections of the images located at the center of the  $\mu S$  were analysed. This guaranteed that distortions due to the spherical shape of the  $\mu S$  are limited, and that small translations along the x- and y-axes at the vicinity of the central axis of the system do not dramatically alter the image. This was supported experimentally by the images shown in Figures 3.5.d,f,h where the gratings are clearly resolved at the center of the  $\mu S$  and are parallel, hence ensuring that no dramatic radial distortion occurred. As a consequence, at the center of the  $\mu S$  the imaging device can be assumed to be largely shift independent in the x-y plane. Combined with the linearity of the system, this fact suggested that the image can be expected to be solely determined by the intensity profile of the *PSF* [152]. Furthermore, as shown by the shape of the illumination profiles discussed in the Appendix A.1, the shape of the *PNJ* is independent of phase shifts. As the final image is formed by the illumination light reflected by the object, one can assume that the whole system and therefore the *PSF* are not dependent on phase shifts. Briefly, it allowed to relate the recorded 2D image (*Im*) to the input object (*Ob*) through a convolution operation (denoted as  $*$ ) [153], [154]:

$$Im(x, y) \equiv (PSF * Ob)(x, y) \quad (3.2)$$

The *PSF* can be defined as the impulse response function of the system, that is, the image obtained from the imaging of a point. Mathematically, this impulse, or point, can be expressed as the Dirac function  $\delta$ , the function returning 0 for  $x \neq 0$  and  $y \neq 0$ , and whose integral is 1 over  $\mathbb{R}^2$ . More intuitively,  $\delta$  can be approximated as an infinitely high, infinitely sharp peak centered over  $(0, 0)$ , the function being equal to 0 anywhere else. Furthermore,  $\delta$  is the unit element for convolution, hence

$$PSF(x, y) = (PSF * \delta)(x, y) \quad (3.3)$$

Direct measurement of the *PSF* can be challenging, as obtaining a pure point as the object to image is impossible. It can be approximated by imaging a very small disk for instance, but the result can be distorted if the object is below the imaging capabilities of the device. A numerical simulation, as shown in Figure 3.2, or an exact analytical solution can be used, but this is not always available. Moreover, the purpose of this analysis is to confirm the results of the numerical simulation (Figure 3.4) with an experimental approach. To experimentally characterize the *PSF*, it has been suggested to image a step, corresponding to a Heavyside function  $H$  along one of the two dimensions of the image, here, for instance, along the x-axis. This is a more rigorous and elegant way to evaluate the *PSF* and also the reason why the

### Chapter 3. Principles governing micro-object-based imaging

---

grating nanostructure was used as sample in this work. Indeed,  $\delta$  is the derivative of  $H$  along the x-axis, and the convolution operation is stable through differentiation, leading to

$$PSF(x) = \frac{\partial}{\partial x} (PSF * H)(x) \quad (3.4)$$

It is commonly assumed that the  $PSF$  is accurately described with a  $2D$  Gaussian (see section 2.1), which can be reduced to one-dimension in the case of imaging a step along the x-axis. Even though an Airy function can be considered, as it describes the diffraction pattern generated by a small circular aperture on the xy-plane, numerical investigations showed that a Gaussian is also a very common fit in the xy-plane for the  $PSF$  of a confocal microscope [155]. To confirm the validity of using a Gaussian approximation in contrast to an Airy approximation, the intensity profiles at the waist along the x-axis for the simulations of the  $PNJ$  profiles shown in Figure 3.2 were fit with a Gaussian and an Airy function. In both cases, these fittings were found to be imperfect (Appendix A.1) but nevertheless resulted in comparably good fits ( $R^2 > 0.966$ ). As the use of a Gaussian facilitates considerably the calculations and the numerical analysis, this function was chosen to approximate the overall  $PSF$  of the system in the rest of this study.

Thanks to this approximation, the image could now be obtained by convoluting the step profile (the object) with a one-dimensional Gaussian (the  $PSF$ ) characterized by a standard deviation  $\sigma$  (Appendix A.1). By integrating Equation 3.4 along the x-axis, the image actually resulted in the integral of a Gaussian (the  $PSF$ ) and is by definition described by the error function  $f_{err}$

$$f_{err}(x) \equiv \frac{2}{\sqrt{\pi}} \int_0^x e^{-t^2} dt \quad (3.5)$$

By fitting the profile of the image with  $f_{err}$ , we could extract the  $\sigma$  associated with the  $PSF$ , which is directly associated with the lateral resolution of the imaging system.

Experimentally, the  $\mu S$  was sitting in the middle of two lines. As shown in Figures 3.7.c and 3.7.e, two stripes were observed for each  $\mu S$ , resulting in two opposite steps. In agreement with Equation 3.5, the obtained image profile should be described by the function  $f$

$$f(x) = \alpha \left( f_{c_{err}} \left( \frac{x - x_1}{\sigma' \sqrt{2}} \right) + f_{err} \left( \frac{x - x_2}{\sigma' \sqrt{2}} \right) \right) + constant \quad (3.6)$$

where  $f_{c_{err}}$  is the complementary error function,  $\alpha$  is a constant and  $x_1$  and  $x_2$  are the positions of the descending and ascending steps, respectively (shown in Figure 3.8.a), which together define the magnification of the image. The image standard deviation  $\sigma'$  was obtained from the fitting, and had to be divided by the amplification factor associated with the  $\mu S$  size (as shown in Figure 3.6.a) to obtain the actual  $\sigma$ . A description of a typical experimental image, along with the fitted  $f$ , is shown in Figure 3.8.a. From this fitting, the characteristic  $\sigma$  for each  $\mu S$  size could be computed and is presented in Figure 3.9.a. The other fitting parameters are discussed in Appendix A.1 and they support the analysis presented here with  $x_2 - x_1 \sim 900$  nm, which is in good agreement with the geometry of the sample, and

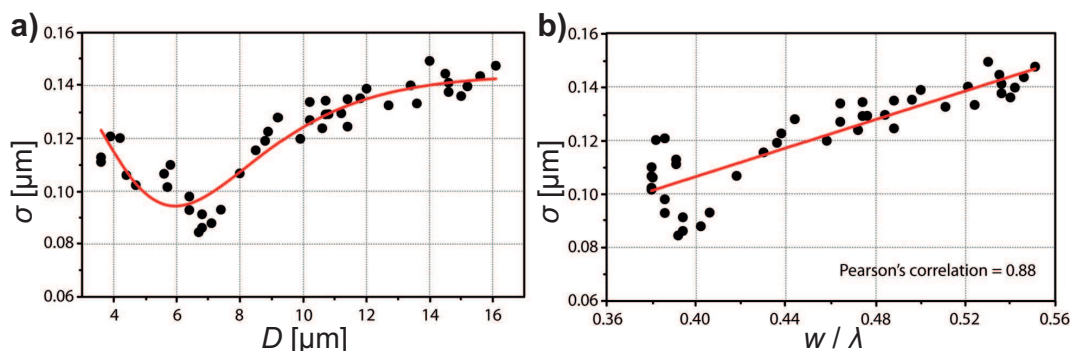


**Figure 3.9** – Results of the resolution quantification experiments. **a)** The actual image standard deviation  $\sigma$  that is obtained from the fit, related to the true resolution of the system, as a function of  $D$ . The dots are obtained from the fits with the analytical model, while the solid curve is a guide to the eye. **b)** The correlation between  $\sigma$  and the normalized waist of the  $PNJ$  ( $w/\lambda$ ). The solid line represents a linear fitting curve with a Pearson's correlation coefficient of 0.88.

$\alpha \sim 100$  for all the beads considered. In particular, the fact that the distance  $x_2 - x_1$  was correctly evaluated further validates the shift invariance assumption. If this was not the case, as this parameter was measured over a large part of the  $FoV$  appearing on the  $\mu S$ , a significant distortion would have occurred thus preventing the accurate measurement of the inter-grating distance. The best  $\sigma$  was obtained with  $D=6\mu\text{m}$   $\mu S$ -s and it was below 100 nm. The experimental  $\sigma$  was also in good agreement with the  $w$  values derived from the simulations. The actual  $\sigma$  fitted from the experimental data as a function of  $w/\lambda$  obtained from the simulations is plotted in Figure 3.9.b. A positive correlation with the Pearson's efficiency of 0.88 was obtained, indicating that the imaging resolution of the  $\mu S$  is clearly dependent on the waist of the  $PNJ$ . Additionally,  $w$  was defined at the  $FWHM$  of the  $PNJ$  along  $x$ , which in a Gaussian approximation is  $2\sqrt{2\ln(2)}\sigma \approx 2.355\sigma$ . As the simulated  $w$  was  $\sim 240$  nm (for  $\lambda=600$  nm) and the experimental  $\sigma$  was  $\sim 100$  nm, the correspondence between the simulation and the experimental analysis was excellent. This good agreement validated *a posteriori* the assumptions on the overall  $PSF$  shape drawn from considering the simulated  $PNJ$  profiles. It also supported the validity of the simulations, and that the resolution of the system is largely controlled by the illumination pattern, that is, the width of the waist of the  $PNJ$ .

In conclusion, we reported imaging of a sample's nano-features beyond the classical diffraction limit by using a conventional optical microscope in combination with a series of  $BTG$   $\mu S$ -s of different sizes. A  $FEM$  study on light propagation revealed the light focusing capability of a  $\mu S$  of a given size and the generation of the  $PNJ$ . By comparing the experimental imaging results with the numerical study, we found that the magnification factor obtained from the virtual images is highly correlated to the calculated light focusing capability of a  $\mu S$ . Moreover, we quantitatively studied the resolution of the  $\mu S$ -s of different sizes by analysing the images and fitting the results with a mathematical model based on the  $PSF$ . Our work demonstrated the intimate link of the super-resolution imaging mechanism of a dielectric  $\mu S$  with its light focusing capability and the development of the  $PNJ$ . Indeed, the combination of refractive and interferometric effects of the incident light produce the narrow-waist  $PNJ$  that exits the  $\mu S$ .

In the imaging mode of the  $\mu S$ , identical optical paths are used for generating the magnified image and, therefore, the degree of focusing of the incident light into a *PNJ* is closely related to the possibility of a  $\mu S$  to transform a high spatial frequency evanescent wave generated by the object into a propagating wave that becomes detectable in the far field. We believe that due to these physical insights, dielectric  $\mu S$ -s will be increasingly used in the future, providing a straightforward and robust tool to be integrated with a conventional microscope for super-resolution optical microscopy. This will allow affordable super-resolution imaging of a whole range of samples and biological objects, such as virus particles, labelled nucleic acids and molecules.

### 3.2 The reflected light pathway

As it was shown in section 2.3.1 and 3.1, for many years the *PNJ* was considered the main reason of the resolution increase, therefore extensive characterization of this illumination mode was done both by our research group and by the microscopy community. More recently, however, it has been proposed to revise and standardize the resolution claimed in  $\mu S$ -assisted microscopy and it was demonstrated that the experimentally observed resolution gains for big diameter  $\mu S$ -s ( $D > 20 \mu\text{m}$ ) cannot be explained solely by the creation of the *PNJ* [125]. Previous theoretical modelling suggested Mie resonances as potential source of resolution enhancement for wavelength-scale  $\mu S$ -s [119], but no experimental confirmation has been reported so far. For practical considerations, the attention was turned towards much larger  $\mu S$ -s ( $D > 20 \mu\text{m}$ ), because they provide a larger *FoV* and are easier to handle. For this reason and for their ability to improve the resolution of standard optical microscopes in a simple and affordable way, dielectric  $\mu S$ -s were used for a variety of applications as it was shown in section 2.3. However, because of the small ( $< 1 \mu\text{m}$ ) distance between the sample and the microsphere ( $h$ ) required for super-resolution imaging [125], [156], objects of different nature may require conditions that reduce the resolution power (*e.g.* use of a specific immersion medium for live-cell imaging). Therefore, to establish the best imaging conditions for incoherent microscopy, we (i) explored the illumination and the detection path through the  $\mu S$  to derive the theoretical resolution gain for different configurations, (ii) demonstrated its validity experimentally, and (iii) provided parameters for quantitative imaging system optimization.

To explore the contribution of the *PNJ* illumination, we studied its dependence on the optical contrast between the  $\mu S$  and the immersion medium. We used *FEM* numeric simulations (Appendix A.2) to calculate the *PNJ* generated by a  $D=40 \mu\text{m}$  *BTG*  $\mu S$  in either oil- or water-immersion medium (Figure 3.10.a). Both systems generated a *PNJ*, emerging at different distances from the shadow-side of the  $\mu S$ . We investigated the intensity profiles within  $1 \mu\text{m}$  from the  $\mu S$ , and found that they do not markedly differ in the two situations (Figure 3.10.b). Based on this finding, we extended our study and analysed different  $\mu S$  materials and sizes in the most common immersion media (Appendix A.2). We analysed the illumination generated by the  $\mu S$  in these conditions at two different distances ( $h_1=0.1 \mu\text{m}$  and  $h_2=1.0 \mu\text{m}$ ) from the shadow side of the  $\mu S$ . These positions corresponded to the location of the sample during the

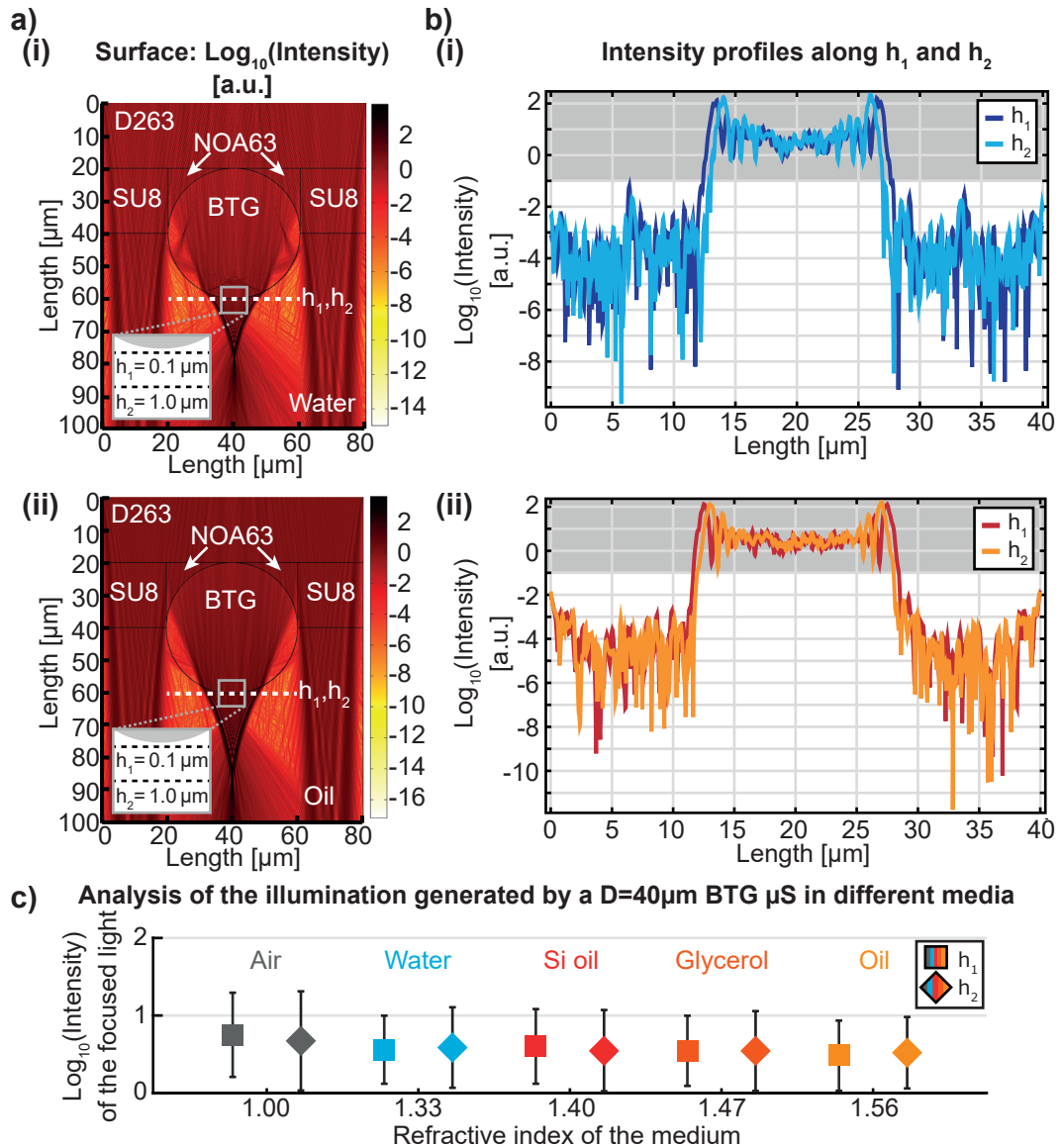


**Figure 3.10** – Analysis of the illumination profile in the imaging region of a  $\mu\text{S}$ . **a)** FEM simulation of the PNJ generated by a BTG  $\mu\text{S}$  in (i) water- and (ii) oil-immersion upon flat-field illumination from the top. The surrounding optical environment (SU8, D263 and NOA63) of the  $\mu\text{S}$  is modelled based on the experimental configuration, as detailed in Appendix A.2. **b)** Intensity profiles along the lines at  $h_1=0.1\mu\text{m}$  and  $h_2=1.0\mu\text{m}$  from the lower edge of the  $\mu\text{S}$  for (i) water- and (ii) oil-immersion. The grey-shaded regions indicate the focused light. **c)** Comparison of the focused light generated by the PNJ along  $h_1$  and  $h_2$  in different immersion media. Data are plotted as median  $\pm$  median absolute deviation (MAD).

imaging. Analysis of the intensity profiles showed that there is no significant difference in the region of interest (ROI), as shown by the numerical results in Figure 3.10.c.

To extend our study even further on the generated illumination, we investigated how the material and the size of the  $\mu\text{S}$  influence the intensity of the focused light. Simulations with

### Chapter 3. Principles governing micro-object-based imaging

soda-lime glass (*SLG*) and *BTG* were carried out for both  $D=20\ \mu\text{m}$  and  $D=40\ \mu\text{m}$   $\mu\text{S}$ -s. The intensity profiles were generated as described earlier. Measurements were made at the same distances as previously described and the numerical results are shown in Figure 3.11. In all cases, the calculated values for  $h_1$  and  $h_2$  are almost identical, which indicates that the illumination is robust in the imaging region, *i.e.* closer than  $1\ \mu\text{m}$  to the  $\mu\text{S}$ . Furthermore, the focused light intensity does not change significantly for *BTG*  $\mu\text{S}$ -s, which demonstrates that there is no size dependence in this case. As for *SLG*, a decreasing tendency is observable. This can be explained by the insufficient optical contrast, since  $n_{SLG}=1.50$ : for low *RI*-media, such as air and water, the optical contrast is still sufficient to generate the *PNJ*, and the intensity values are almost identical in the imaging region. However, as the contrast decreases, the focusing effect fades away. When the medium has almost the same *RI* (*e.g.* glycerol) as the  $\mu\text{S}$ , there is no focusing effect at all; therefore, the light intensity is not increased. If the *RI* of the media is further increased (*e.g.* oil), even deflection of the light can occur, which decreases the original intensity. This behaviour was observed independently from the size of the *SLG*  $\mu\text{S}$ . We conclude that if the optical contrast is high enough to create a *PNJ*, then the illumination in the imaging region is independent from the immersion medium.

To analyse the detection path from the sample to the microscope objective, we used an

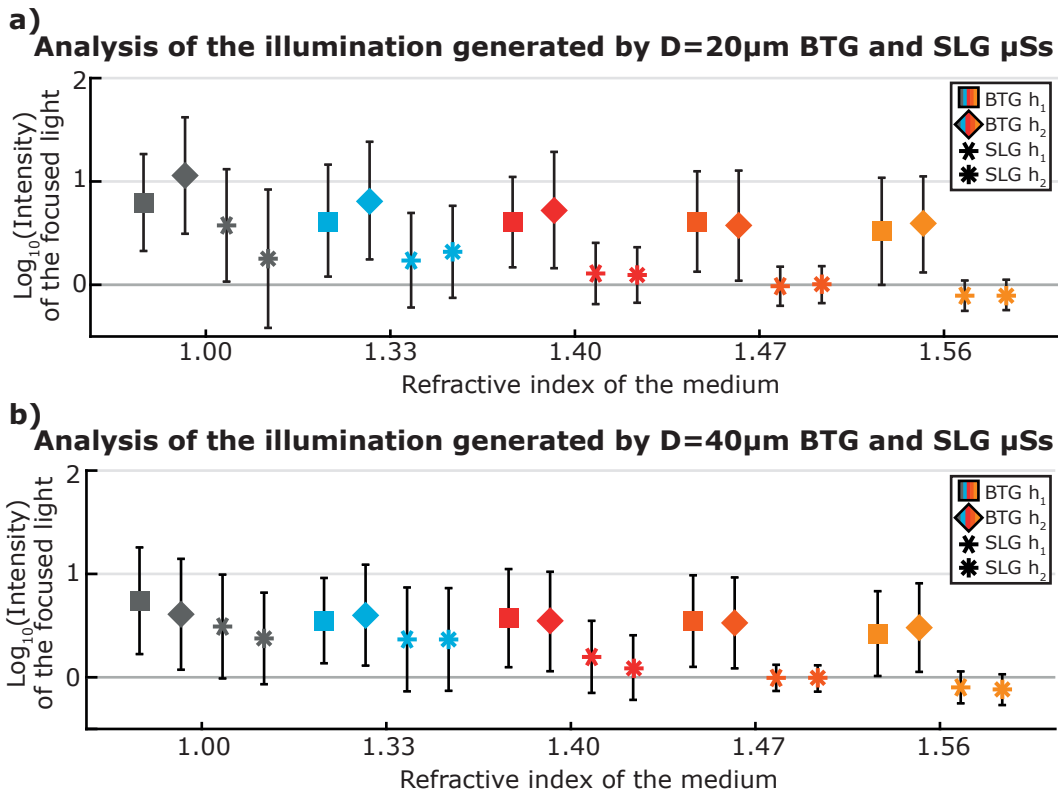


**Figure 3.11** – Analysis of the illumination for *BTG* and *SLG*  $\mu\text{S}$ -s with various diameters. **a), b)** Focused light intensity values for *BTG* and *SLG*  $\mu\text{S}$ -s with  $D=20\ \mu\text{m}$  and  $D=40\ \mu\text{m}$  are calculated with the same method as shown in Figure 3.10 and Appendix A.2. Data are plotted as median  $\pm$  *MAD*.



### 3.2. The reflected light pathway

analytical approach based on Fourier optics and ray tracing. Propagation of monochromatic light in homogeneous media can be described by the Helmholtz equation [147]:

$$(\nabla^2 + k^2)\Psi(r) = 0 \quad (3.7)$$

where  $\Psi(r)$  is the spatial part of the propagating field,  $k=(2\pi n_{medium})/\lambda$  is its wave number, with  $\lambda$  being its wavelength and  $n_{medium}$  the refractive index of the medium. The general solution of Equation 3.7 in linear coordinates can be written as

$$\Psi(x, y, z) = \int_{-\infty}^{+\infty} \int_{-\infty}^{+\infty} \hat{\Psi}_0(k_x, k_y) e^{i(k_x x + k_y y + k_z z)} dk_x dk_y \quad (3.8)$$

where  $k_x$ ,  $k_y$  and  $k_z$  are the component of the wave-vector ( $k = k_x x + k_y y + k_z z$ ), and  $\hat{\Psi}_0(k_x, k_y) = \int_{-\infty}^{+\infty} \int_{-\infty}^{+\infty} \Psi_0(x, y) e^{-i(k_x x + k_y y)} dx dy$  is the Fourier transform of the field at  $z=0$  (*i.e.* the object-plane).  $\hat{\Psi}_0(k_x, k_y)$  contains the spatial information about the object and is usually called angular spectrum [147]. With this approach, the spatial field solution can be interpreted as the sum of its plane wave components  $e^{i(k_x x + k_y y + k_z z)}$ , which are the eigenfunctions of the Helmholtz operator. Each of these plane waves carries some information about the spatial distribution of the object in the term  $\hat{\Psi}_0(k_x, k_y)$  and propagates at an angle  $\theta$  with respect to the  $z$ -axis. This angle is given by the standard definition of the wave vector components in spherical coordinates:

$$\begin{aligned} k_x &= k \sin\theta \cos\varphi \\ k_y &= k \sin\theta \sin\varphi \\ k_z &= k \cos\theta \end{aligned} \quad (3.9)$$

where  $\theta$  and  $\varphi$  are the polar and the azimuthal angle. The number of plane waves collected by the optical system determines the amount of spatial information retrieved about the original object, which explains why the maximum  $\theta_{obj}$  that can be collected by an objective (*i.e.* half of the acceptance angle) limits the spatial resolution of the optical system in accordance with the standard definition of Abbe's resolution (Equation 2.1). Methods to artificially increase the angular spectrum collected by the detection system are used in techniques such as I5M [157] and SIM [13].

Following this approach, we modelled the propagation of each individual wave originating from a point sample for a  $\mu S$  much larger than  $\lambda$  (Figure 3.12.a). Each wave propagates away from the sample at a certain angle with respect to the sample- $\mu S$  axis, then it enters the  $\mu S$  by refraction, propagates inside the  $\mu S$  and exits again by refraction. In this procedure, the  $\mu S$  can be interpreted as a non-linear operator that transforms an input angle  $\theta_{in}$  into an output angle  $\theta_{out}$ , both measured with respect to the optical axis. This operator depends on four parameters: (i) distance between the sample and the microsphere ( $h$ ), (ii) diameter of the  $\mu S$  ( $D$ ), (iii) refractive index of the microsphere ( $n_{sphere}$ ) and (iv) refractive index of the medium ( $n_{medium}$ ). By applying Snell's law to the refraction points for each ray, and linear propagation otherwise, we calculated the functional relation between  $\theta_{in}$  and  $\theta_{out}$  for a BTG

### Chapter 3. Principles governing micro-object-based imaging

$\mu S$  ( $D=40\ \mu\text{m}$ ,  $n_{\text{sphere}}=1.95$ ) immersed in oil ( $n_{\text{medium}}=1.56$ ) or in water ( $n_{\text{medium}}=1.33$ ), for  $0.1\ \mu\text{m} < h < 10\ \mu\text{m}$  (Figures 3.12.b and 3.12.c). The method for this calculation is detailed in Appendix A.2. The relation between  $\theta_{in}$  and  $\theta_{out}$  was very different for oil and water immersion. However, both situations led to a decrease of  $\theta_{out}$  compared to the absence of the  $\mu S$ . Parallel, the objective acceptance angles for an oil-immersion objective with  $NA=1.4$  and a water-immersion objective with  $NA=0.75$  are shown. The larger angles that are guided back to the objective by the  $\mu S$  generate an enhanced-resolution zone (*ERZ*), in which the amount of collected angular spectrum is increased. This translates into a net increase of the  $NA$  of the system (Figure 3.13.a), which results in a net gain for the lateral resolution as derived from Equation 2.1:

$$G = \frac{R_0}{R_{\mu S}} = \frac{n_{\text{medium}} \sin \theta_{\mu S}}{NA_{\text{obj}}} \quad (3.10)$$

where  $\theta_{\mu S}$  is the maximum  $\theta_{in}$  refracted by the  $\mu S$  that stays within the acceptance cone of the objective. For the axial resolution, which scales as  $NA^{-2}$ , the gain is even higher and corresponds to  $G^2$ . In Figure 3.13.b we show both lateral and axial resolution gains for the oil- and water-immersion objectives considered in Figures 3.12.b and 3.12.c. We find that the resolution gain is markedly different when using a  $\mu S$  in either water or oil medium, and that much more gain is expected theoretically when using the  $\mu S$  in water. Moreover, as the gain is uniform in this region, no very precise location of the sample is needed to get the same

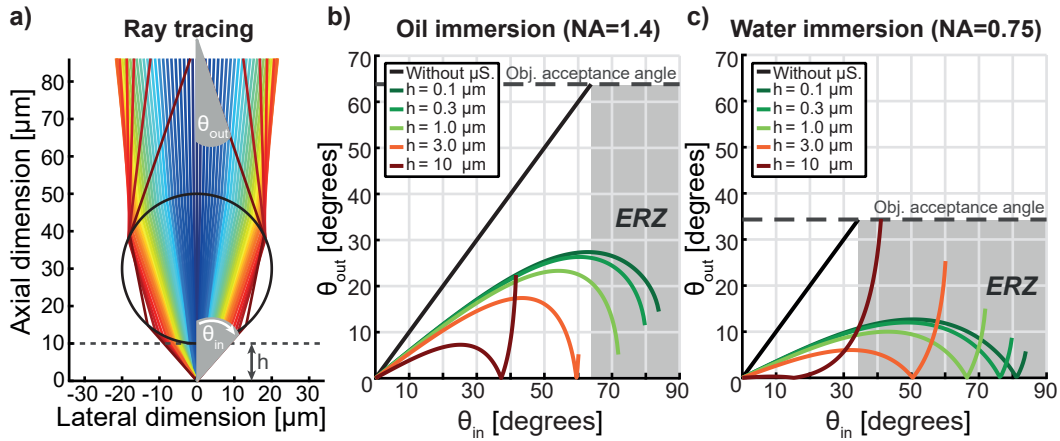


**Figure 3.12** – Calculation of the *ERZ* created by the  $\mu S$ . **a)** Rays emerge from a point sample (located at the origin), and propagate through a  $\mu S$  with  $n_{\text{sphere}}=1.95$  placed in a homogeneous medium ( $n_{\text{medium}}=1.56$ ) up to the microscope objective (not shown). The sample- $\mu S$  distance is marked with  $h$ ;  $\theta_{in}$  indicates the angle of a ray entering the  $\mu S$ , while  $\theta_{out}$  indicates the angle of the corresponding outgoing ray. The color gradient indicates different propagating rays. **b), c)** Relation between  $\theta_{in}$  and  $\theta_{out}$  for an oil- and a water-immersion objective, respectively, based on the model shown in a). Green curves indicate  $h$  distances for which the illumination of the sample through the  $\mu S$  is the most suitable thanks to the *PNJ*. The experimental angular acceptance of each objective is marked with a dashed line. The grey area shows the *ERZ*, where the  $\mu S$  mediates the collection of light coming from higher angles  $\theta_{in}$  compared to the objective alone.

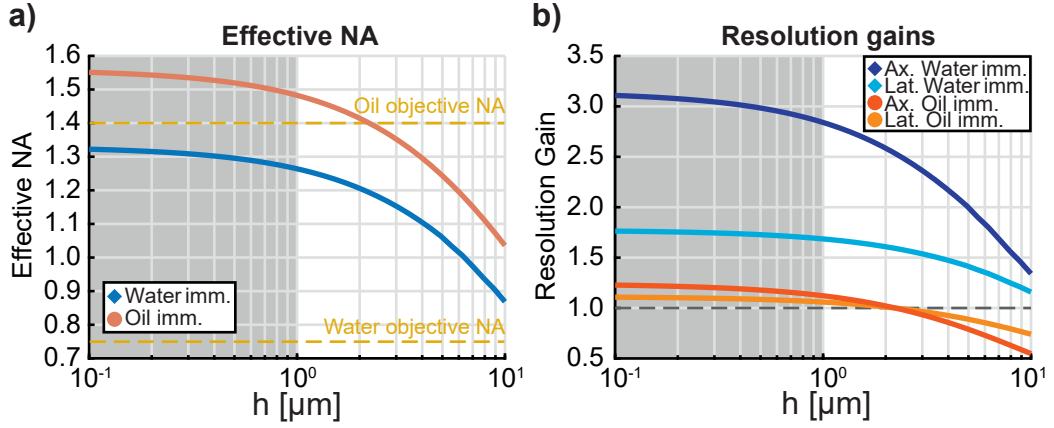


**Figure 3.13** – Quantitative estimation of the resolution gain in presence of the  $\mu\text{S}$ . **a)** Effective NA in the presence of the  $\mu\text{S}$  against  $h$ . A reasonable  $h$  value range was determined based on the configurations showed in Figure 3.10. The dashed lines indicates the nominal NA-s of the objectives without use of the  $\mu\text{S}$ . **b)** Lateral and axial resolution gains. The dashed line indicates the performance of the objectives in the absence of the  $\mu\text{S}$ . The grey areas in both a) and b) indicate the  $h$  distances for which the illumination of the sample through the  $\mu\text{S}$  is the most suitable thanks to the PNJ.

resolution enhancement. This guarantees the imaging robustness which is very useful in optical system design.

To verify the theoretical predictions, we compared the measured and calculated spatial frequency coverage by imaging *LSP*-s, which was shown as a suitable characterization of optical systems for both coherent [139] and incoherent [138] imaging. The spatial frequencies present in the object are partially filtered by the optical system, so that the contrast between the features in the object is attenuated in the image. In incoherent imaging, the intensity modulation in the object is transferred to an intensity modulation in the image by the *MTF* of the optical system, which is given by the modulus of the Fourier transform of the *PSF* [147]. In the case of microscope objectives, for which the *PSF* is the well-known Airy disk, the *MTF* is

$$MTF = \frac{2}{\pi}(f - \cos f \sin f) \quad (3.11)$$

where  $f = \arccos\left(\frac{\lambda}{2NA}u\right)$  is the normalized spatial frequency,  $u$  being the linear spatial frequency. In Figure 3.14.a, we calculated the *MTF* for the two objectives considered in Figure 3.12, in the presence and absence of a  $\mu\text{S}$ . The range of  $\lambda$  considered for this calculation was  $545 \pm 20$  nm, corresponding to the experimental band-pass filter placed behind the light source. Similarly, the *NA* considered in the presence of the  $\mu\text{S}$  was the one obtained for short sample- $\mu\text{S}$  distance (*i.e.* for the sample laying within the imaging region). The maximum spatial frequency that is predicted to be resolved by the objective (*i.e.*  $MTF(u) > 0$ ) is increased in the presence of the  $\mu\text{S}$  for both oil- and water-immersion. However, the water-immersion objective is expected to gain more than the oil-immersion objective. To illustrate the modulation enhancement in water-immersion, we show an *LSP* with  $P=360$  nm in the absence and

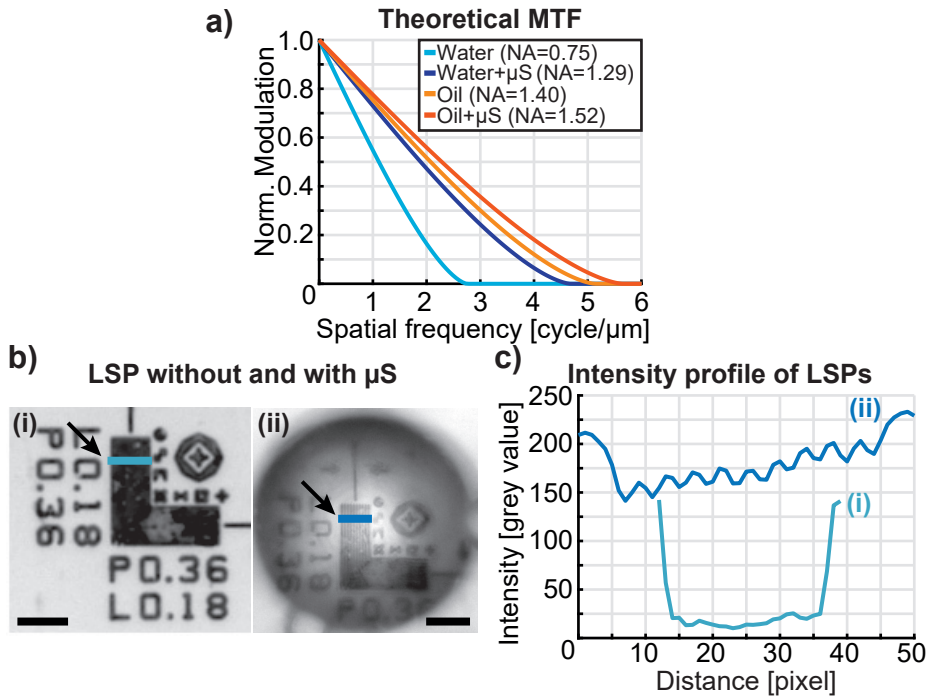


**Figure 3.14** – Experimental confirmation of the predictions for different configurations. **a)** *MTF* calculated at  $\lambda=545$  nm, for water- and oil-immersion objectives without and with use of a  $\mu$ S. The *NA* in the presence of the  $\mu$ S is derived from Figure 3.12.a, for  $h < 1$   $\mu$ m. **b)** Examples of the imaged *LSP-s* without (i) and with (ii) the  $\mu$ S, respectively. Scale bars 5  $\mu$ m. **c)** Intensity profiles along the lines *LSP-s* marked by the arrows in b).

presence of the  $\mu$ S in Figure 3.14.b, with their intensity profiles in Figure 3.14.c. The vertical shift between the intensity values is also explained by the higher amount of light collected in the presence of the  $\mu$ S, but the increased modulation capability is not direct consequence of this shift. The predictions were confirmed by the measurements on several *LSP-s* (detailed in Chapter 6), where the expected behaviour of the objective alone was confirmed, and the predicted spatial frequency coverage in the presence of the  $\mu$ S perfectly followed the predictions. To further explore the properties of the resolution gain, we calculated the relation between the input and the output angle for the most common immersion media (Figure 3.15.a). In order not to lose generality, we did not consider the optical glue and the supporting glass for these calculations, because they can be different in other implementations of the technique, as it was presented in section 2.3.2. On the same graph, we report the output  $NA_{out} = n_{medium}\theta_{out,max}$  for each condition, where  $\theta_{out,max}$  is the maximum output angle (*i.e.* the minimum acceptance angle needed for the objective to collect the entire spatial information). The lower  $NA_{out}$ , the larger the resolution gain that can be obtained. From air (lowest *RI*) to oil (highest *RI*) the behaviour changes in a non-monotonic way, since increasing  $n_{medium}$  does not always result in lowering  $NA_{out}$ . This demonstrates that the optimal resolution gain has a non-trivial dependence on the contrast between the refractive indices of the medium and the  $\mu$ S. To study this effect, we calculated  $\theta_{out,max}$  as a function of  $n_{medium}$  in the range 1-1.6 (Figure

3.15.b). A minimum is clearly visible for  $\theta_{out,max}$ , at which the resolution gain reaches a maximum. Finally, we studied this behaviour for several sizes of  $\mu S$ -s of two common glass types (Figure 3.15.c). We observed that the position of the maximum resolution gain shifts a lot when changing the  $\mu S$  material (*i.e.*  $n_{sphere}$ ), and slightly when varying the  $\mu S$  size ( $D$ ). This proves that the optical contrast is the primary source of the resolution enhancement and provides a quantitative design tool for optimization of  $\mu S$ -assisted imaging systems: for instance, when the sample requires no immersion, *SLG*  $\mu S$ -s give a higher gain; conversely, when studying living cells in water-based media, *BTG*  $\mu S$ -s are more suitable.

In conclusion, these results quantitatively describe the resolution gain mediated by the  $\mu S$  as a function of the physical parameters of the optical system, and provide predictions for several configurations of  $\mu S$  materials and immersion media, offering a method to optimize

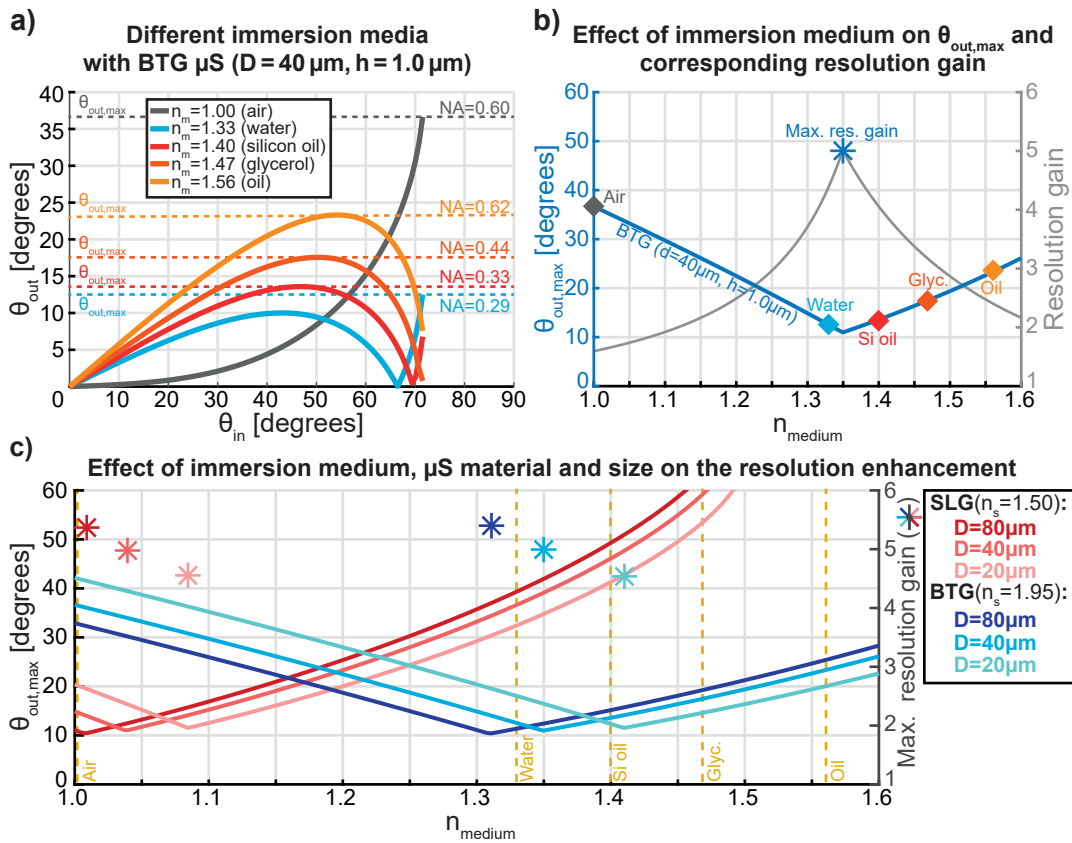


**Figure 3.15** – Effect of the optical contrast and the  $\mu S$  size on the resolution gain. **a)** Relation between  $\theta_{in}$  and  $\theta_{out}$  for the most common immersion media. Dashed lines indicate the maximum output angle ( $\theta_{out,max}$ ) and the corresponding minimum NA needed for the objective to collect the rays from all the input angles. **b)**  $\theta_{out,max}$  as a function of  $n_{medium}$  for the same  $\mu S$  as in a). The values corresponding to the five media from a) are marked with diamonds. The resolution gain for a given  $n_{medium}$  is shown on the secondary y-axis. The maximum value of the gain corresponds to the location of the minimum  $\theta_{out,max}$ , and is marked with an asterisk. **c)** Solid lines represents the  $\theta_{out,max}$  for *SLG* and *BTG*  $\mu S$ -s, for several  $D$ . Asterisks (\*) indicate the maximum resolution gain for the given combination of medium,  $\mu S$  material and diameter. Vertical dashed lines indicate the refractive indices of the most common immersion media.

### **Chapter 3. Principles governing micro-object-based imaging**

---

microscopy configuration for different application requirements based on  $\mu S$ -assisted imaging.

## 4 Microfabrication

*This chapter describes the development of a dielectric microsphere array chip that was used in our imaging system. In the first section, patterning methods are shown that can effectively immobilise microspheres in an array template. This is followed by the description of the different microfabricated prototypes. Description of various clean room techniques is also provided. Finally, the two-phase process (i.e. template fabrication and patterning) of the last version of our chip is shown.*

---

Section 4.1 was adapted from the following publication:

- **G. Huszka**, H. Yang, M. Cornaglia, and M. A.M. Gijs, “Patterning of melamine and SiO<sub>2</sub> microsphere lens arrays”, in MNE 2015 - the 41th International Conference on Micro and Nano Engineering, The Hague, The Netherlands, 2015.

*My contribution:* I fabricated the SiO<sub>2</sub> microsphere lens array, developed the patterning method, characterized its efficiency, wrote the manuscript and presented the results at the conference.

Parallel to the theoretical investigations, detailed in chapter 3, the experimental realization of a microsphere-based SRM system had begun. The main motivation of constructing such a setup was to enable a *FoV* with comparable area to a classical microscope objective, meanwhile preserving the super-resolving abilities of a  $\mu S$ . As it was shown in section 2.3, there are two possible directions of development to achieve these goals. Either multiple  $\mu S$ -s can be placed in the *FoV* of the microscope objective and therefore realize parallel imaging, or a scanning protocol must be established that allows translation of a single  $\mu S$  over the sample. We envisioned that with the help of microtechnology and smart system design the two can be combined, resulting in a scanning super-resolution optical microscope, where the scanning probe consists of an array of  $\mu S$ -s. Although, this approach seems more complicated at first sight, it promises multiple advantages over the traditional solutions. Implementing a scanning protocol would allow positioning of the  $\mu S$  to any desired location on the sample, overcoming the issue presented in many publications (section 2.3.1), namely, that only the part where the

$\mu S$  was initially placed could be imaged. On the other hand,  $40\times - 60\times$  microscope objectives provide a circular *FoV* with a diameter typically in the  $\sim 10^{-4}$  m range, depending on the magnification factor. Since the manufacturers claim aberration free image throughout this region, a reasonable approach would be to use as much of this area as possible (*e.g.* by imaging parallel with multiple  $\mu S$ -s) to facilitate the scanning process. A possible solution to achieve this would be the utilization of an array of  $\mu S$ -s that could either decrease the scanning time or increase the size of the imaged sample surface area. In order to realize the above described imaging method, a two-step practical approach was defined. First, a template chip had to be fabricated that allows  $\mu S$ -s to be placed at fixed and pre-determined positions. Then, a "connective" structure had to be made that attached this chip to the macro-components of a classical optical microscope. The development of the template chip will be detailed in this chapter, while the connecting elements, the overall system design, and the achieved results will be shown in chapter 5 and 6.

### 4.1 Microsphere array fabrication with self-assembly methods

In order to create an array of dielectric  $\mu S$ -s, a template chip had to be fabricated. This served as a macroscopic basis for fixing the  $\mu S$ -s, as its lateral dimensions were designed to be in the centimeter range. The realization of the templates was done in the clean-room of the Center of Micronanotechnology at École Polytechnique Fédérale de Lausanne. Here, ISO5 or ISO6 level of cleanliness was provided, depending on the process, which ensured high quality fabrication (*e.g.* photolithography, dry- and wet-etching). The patterning of the  $\mu S$ -s into the templates then was done in our laboratory.

Based on our results showed in section 3.1,  $\mu S$ -s that are smaller than  $10\mu m$  were in the focus of the experimental realization. Two chips were developed in parallel, where two different versatile patterning methods were implemented for creating the dielectric  $\mu S$  lens arrays. We patterned both melamine ( $D=3\mu m$ ) and  $SiO_2$  ( $D=5\mu m$ )  $\mu S$ -s in glass substrate-based polymer templates that were fabricated with standard clean-room procedures. The first proposed method used a  $3\mu m$  thick parylene-c film as template layer for accommodating the melamine  $\mu S$ -s and is shown in Figure 4.1.a. The substrate was realized by the following wafer-level processes. The back side of a fused silica wafer was coated with 200 nm indium tin oxide conductive layer. Subsequently,  $3\mu m$  parylene-c and 200 nm amorphous silicon was deposited on the front side. This was followed by a photolithography step that generated a mask for the etching of the top silicon layer. Based on this, the parylene-c layer could be etched and the template could be realized. The geometrical pattern of the template consisted of wells with  $P=40\mu m$  and a lateral shift of every second row with  $P/2$  distance as it is shown in Figure 4.1.c. The second method used positive photoresist as the template layer for the  $SiO_2$   $\mu S$ -s. The fabrication process was simpler here, as only one photolithography step was needed (Figure 4.1.d). Due to the different size of the  $\mu S$ -s, a  $5\mu m$  thin layer was deposited in a similar geometrical pattern as for the previous template (Figure 4.1.f).

Since the template could accommodate many  $\mu S$ -s, as its size was comparable to the *FoV*



#### 4.1. Microsphere array fabrication with self-assembly methods

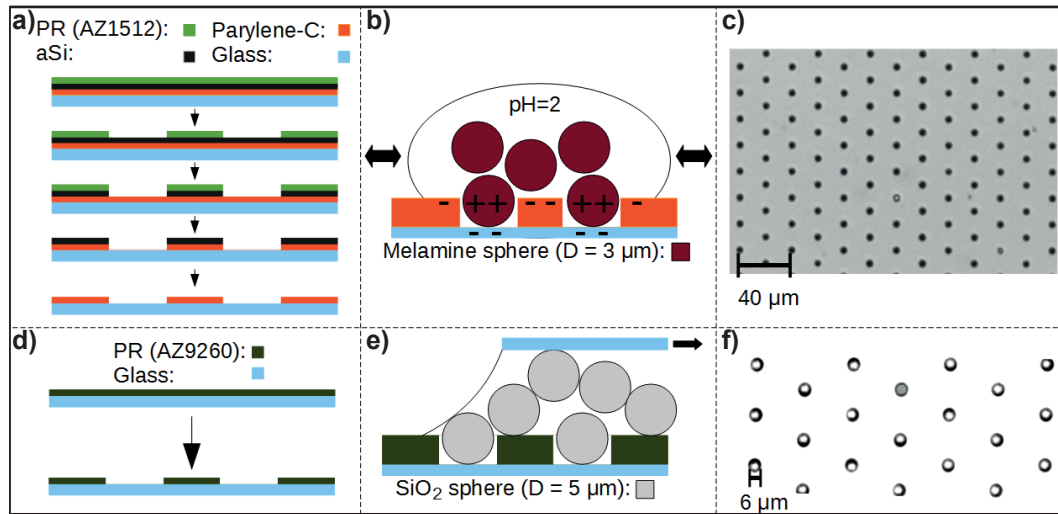


**Figure 4.1** – Summary of the self-assembly-based  $\mu S$ -array-chip fabrication. **a)** Fabrication process of the  $\mu S$  array template for melamine  $\mu S$ -s. **b)** Electrostatic patterning method of the melamine  $\mu S$ -s at low pH. **c)** Photograph of patterned melamine  $\mu S$ -s (filled wells are black dots). **e)** Fabrication process of the array template for  $SiO_2$   $\mu S$ -s. **f)** Patterning method used for  $SiO_2$   $\mu S$ -s based on a moving water meniscus. **g)** Photograph of patterned  $SiO_2$   $\mu S$ -s (filled wells are white dots with shadow).

of the objective, an effective method for patterning the  $\mu S$ -s had to be found. Our attention turned towards self-assembly techniques, because they fit for high-volume processes. From the many patterning possibilities (*e.g.* shape-matching, surface tension-based, capillary force-based) we opted for ones, which are simple, easy-to-implement, cost-effective and work in our desired size range. There was no need for special features such as dis- or re-assembling, active control or embedded advanced functions. Therefore, two passive methods were chosen. The melamine particles were placed in a droplet of buffer (a solution of hydrogen chloride in phosphate buffered saline) with pH=2, a condition for which their surface charge is positive. Then the droplet was moved on the surface of the template several times (Figure 4.1.b). The glass and the parylene-c had negative surface charge, which was highly enhancing the patterning efficiency. Subsequently the fabricated arrays were investigated under the microscope (Figure 4.1.c). As for the  $SiO_2$   $\mu S$ -s, the same buffer solution was used but in this case a droplet was placed on top of the template and it was swiped over it with a help of a standard microscope cover slide (Figure 4.1.e). As the droplet moved, the meniscus between the template surface and the cover slide exerted the patterning force and the process was repeated until a desired number of wells were filled (Figure 4.1.f).

To characterize the effectiveness of the two proposed methods, the template filling rate of the two processes was measured. Results showed that the pH of the buffer influences the efficiency of the first patterning method indeed (Figure 4.2.a). This essentially confirmed that the change in the surface charge, as induced by the low pH, highly increases the number of wells that are filled with melamine  $\mu S$ -s, while the same procedure does not significantly influence the patterning of the  $SiO_2$   $\mu S$ -s in their template. We also investigated how the number of cycles

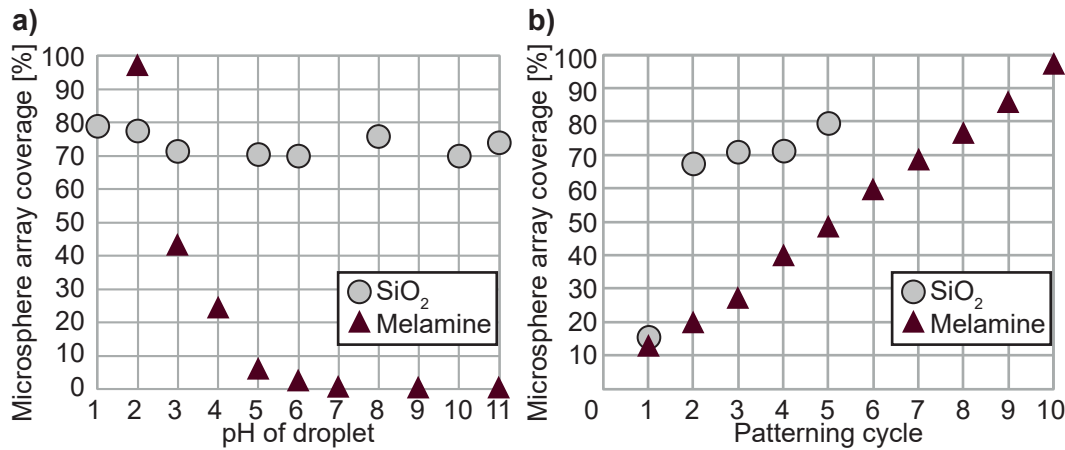


**Figure 4.2** – Comparison of the different patterning methods. **a)** Effect of the pH value of the droplet on the  $\mu S$  array coverage for both types of  $\mu S$ -s. **b)** Effect of the number of patterning cycles on the  $\mu S$  array coverage.

influenced the patterning efficiency for both methods (Figure 4.2.b). A cycle was defined by one passage of the droplet meniscus over the template area. We found, that the  $\mu S$  coverage increased in a linear way with the number of cycles in the case of the melamine particles, meanwhile for the  $SiO_2$   $\mu S$ -s, the swiping method reached high efficiency already after the second cycle. However, the final coverage in the case of the latter remained below 85%, while the melamine  $\mu S$  patterning had a yield over 95%. After patterning, we obtained stable  $\mu S$  arrays, probably due to electrostatic and van der Waals-type attractive forces between the  $\mu S$ -s and the templates.

Our work showed that patterning  $\mu S$ -s on templates can reach a high efficiency, even with simple methods. Furthermore, we demonstrated that besides the size, also the material and the environment of a  $\mu S$  have huge impact on the result of the patterning. Despite of these results, our fabrication protocol had to be modified, because practically these chips could not fit into the imaging setup. The major issue was the  $FoV$  that was extremely limited due to the small diameters of the  $\mu S$ -s. Even with high magnification microscope objectives, the mounted camera could only record a couple of useful pixels (*i.e.* the ones that contained the super-resolution image of the sample), which made image processing very difficult. Therefore, it was decided that despite of the weaker super-resolution capabilities, bigger diameter  $\mu S$ -s should be used.

## 4.2 Initial microsphere array fabrication on wafer level

The next generation  $\mu S$ -array chip had to fulfil two criteria: (i) its fabrication must be as simple as possible within the possibilities of microtechnology and (ii) it has to accommodate big diameter  $\mu S$ -s. We considered various  $\mu S$  diameters and materials based on our previous study (section 3.2) and finally chose  $D=40\ \mu m$  BTG  $\mu S$ -s (from Cospheric, USA). Our calculations showed that these are optimal for water-immersion imaging and at the same time they can be

## 4.2. Initial microsphere array fabrication on wafer level

used for oil-immersion applications. The main goal at this point became the demonstration of the maximum resolving power of our  $\mu S$ -based *SRM* method, therefore the system was first optimized for oil-immersion imaging. The motivation behind this decision was the superior imaging capabilities of the  $63\times$ ,  $NA=1.4$  objective (Carl Zeiss, Germany) that was used in our classical optical microscope (Axio Imager M2m, Carl Zeiss, Germany). On the other hand, this choice immediately introduced a big constrain on our design options, as this objective has a working distance of only 190 nm with cover glass correction up to 170 nm.

The first approach consisted of a silicon wafer that was micro-machined to accommodate the  $\mu S$ -s. Silicon was chosen over glass, because its Young's modulus is up to 100% higher and its fabrication, particularly, the etching of it, is way simpler in microtechnology. The concept of the template chip was to fabricate holes into the wafer that would serve as accommodation for the  $\mu S$ -s and enable observation through the wafer at the same time (steps 1-5 in Figure 4.3). For this, the front side of the wafer was coated with a positive photoresist that was used as a mask for the dry etching (steps 1-3). Deep reactive ion etching with the Bosch process was employed (step 4), because high aspect ratio was needed to achieve etching through the wafer. Practically, the etching process was stopped after  $150\mu m$ , and the back side of the wafer was ground until the openings appeared (step 5). This modification with respect

	Process description	Cross-section after process		Process description	Cross-section after process
01	Photoresist coating		08	Glass polishing	
02	Photo-lithography		09	UV tape protection on the back side	
03	Photoresist development and baking		10	Photoresist coating	
04	Deep reactive ion etching (Bosch process)		11	Photo-lithography	
05	Back side grinding and wafer cleaning		12	Photoresist development	
06	Anodic bonding		13	UV tape removal	
07	Glass wafer grinding		14	Dicing	

**Figure 4.3** – Process flow of the first glass-silicon-sandwich template chip. Color codes: grey - silicon; yellow - photoresist; blue - glass; purple - UV tape; black arrows - direction of UV light during exposure.

## Chapter 4. Microfabrication

to the standard process flow was needed due to restrictions on the etching tool. To prevent the wafer from falling apart, only limited areas were etched with this method, therefore, the surrounding unetched silicon could hold the individual chips together after dicing. Then, the  $\mu S$ -s were placed on the top side, in the etched holes. Keeping the diameter of the wells lower than  $D$  prevented the  $\mu S$ -s from descending below the surface. Finally, the chip was turned upside down, in a way that the  $\mu S$ -s could make direct contact with the sample. Despite of the conceptually nice method, none of the fabricated chips worked. During experiments, the sample was not observable through the chip, which indicated that the microscope light could not be efficiently transported through it.

The next step of development was to change the substrate to glass. To avoid complicated processes, the first design only consisted of a photoresist layer on a D263 type glass wafer. The former was patterned for the wells with photolithography, similarly to steps 1-3 in Figure 4.3, while the latter had only  $150\ \mu\text{m}$  thickness, which eliminated the need for grinding. However, as it turned out after multiple experiments, the handling of such a thin wafer is a non-trivial task, as breakage of the wafer happened continuously. To overcome this problem, reinforcing it with a silicon wafer was proposed. The attachment of the two was planned to be done by anodic bonding. Initial experiments showed, that the small mismatch between the thermal expansion coefficients of the two materials is big enough to cause cracks, which forced us to use borosilicate glass wafers. The issue with these was their thickness, as they were only available in  $500\ \mu\text{m}$ . To overcome this issue, the process flow had to be made more complex, but finally, a working prototype could be fabricated.

The developed process consisted of steps 1-14 shown in Figure 4.3. First, the silicon support was prepared as described earlier (steps 1-5). After the photoresist was removed and both the silicon and the glass wafer cleaned, they were attached by anodic bonding (step 6). This was followed by the grinding and polishing of the glass wafer (steps 7, 8). At this point a *UV*-tape was attached to the back side of the wafer (*i.e.* to the silicon; step 9). This was needed to prevent damages to the  $150\ \mu\text{m}$  thin glass "windows" during the following steps where the wafer was fixed in various machines by vacuum. The patterning of the wells into a photoresist layer, deposited on the glass was the next step in the process (steps 10-13). Finally, the wafer was diced (step 14) and the patterning of the  $\mu S$ -s could start. A photograph of the fabricated chip is shown in Figure 4.4. The main advantage of this design was that the  $\mu S$ -s could be

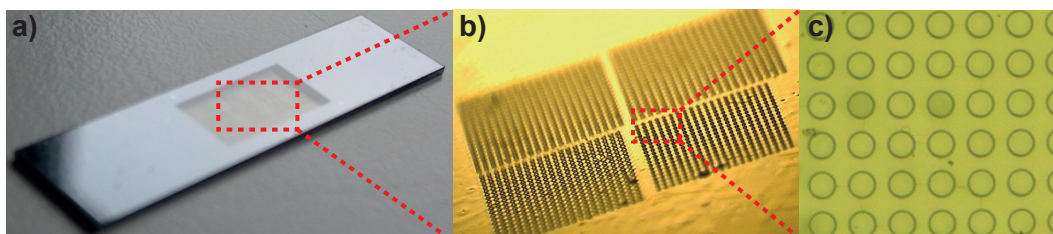


**Figure 4.4** – The glass-silicon template chip. **a)** Photograph of the chip. Dimensions:  $30\ \text{mm} \times 8\ \text{mm} \times 0.5\ \text{mm}$ . **b)** Detail of the central part of the chip, showing the array template in perspective. **c)** Detail of the chip from top view.

### 4.3. Chip for the single microsphere microsystem

---

ordered into an array that was located in the "window" of the chip. There, only the glass wafer was placed in the light path, therefore the sample could be freely observed and objectives with low working distance could be used. At the same time, the chip was robust enough that it could be fabricated with standard clean room procedures and also did not break easily during imaging experiments. Unfortunately, already the first tests pointed out a design error that hindered further studies. The issue was that unlike our non- or water-immersion objectives, the high  $NA$  oil-immersion objective had a very wide tip. Therefore, despite of the window, the objective could not approach the glass substrate, because it hit the silicon frame around it. This fact called for an urgent modification in the chip design. The observation window had to be enlarged. In order to reduce stress on the structure, the rectangular shape was changed to a circular one. The diameter of the new window was extended to 15 mm. With such a big observation area, only 8 chips could be placed on a 4 inch wafer. Despite of the updated geometry, the fabrication procedure was not flawless. Until step 6 in Figure 4.3, no problem occurred, but the grinding broke above 90% of the wafers. The unsupported glass area was simply too big to withstand the forces, applied on it by the process. However, with fine-tuned fabrication parameters, some of the wafers could be made, but typically only 2-4 windows out of 8 remained intact. Unfortunately, these wafers also could not be finished, because the second photolithography was not optimized for this complex wafer structure, therefore, the pattern could not be acceptably transferred. At this point, both the complexity and the cost of the fabrication was already above the expected level and because the first prototypes could not be made, this direction of the development was stopped.

In parallel, another approach was investigated, where a similar structure then presented in [130]–[133] was made. Here, a mold for casting the *PDMS* was fabricated on a silicon wafer with negative photoresist. The geometrical pattern consisted of an array of columns in the photoresist, which resulted in wells in the polymerized *PDMS* after casting. Then, the *BTG*  $\mu S$ -s could be patterned and fixed in these predefined positions. This fabrication procedure was simpler and yielded a higher throughput than the one for the glass-silicon chip, however a practical issue during the experimentation was raised. As it was pointed out in section 2.3, the main hindering factor with *PDMS*-based chips is the sticking. In our case, the sample was not damaged, because sturdy, *in silico* test objects were used, but the friction between the chip and the sample forbade scanning and image reconstruction. Due to these results, it was decided that despite of its long-term advantages (*e.g.* high-throughput fabrication, standardized processes with high repeatability), wafer-level fabrication will not be pursued, instead, chip-level processes will be implemented.

### 4.3 Chip for the single microsphere microsystem

Chip-level fabrication can be beneficial in many aspects, when considering small substrates rather than wafers. Due to the smaller surface and special tools, breakage is less frequent. No support has to be implemented, therefore only a single photolithography step is needed to fabricate the template chip. Furthermore, no dicing is needed, which reduces potential

damage during the process.

Initially the simplest possible solution was explored. In this approach, the aim was to fabricate a "zero"-dimensional array (*i.e.* fixing a single  $\mu S$ ). The substrate in this study was a  $22\text{ mm} \times 22\text{ mm} \times 0.15\text{ mm}$ , D 263 M borosilicate glass (Menzel-Gläser, Germany). A droplet of NOA 63 optical glue (Norland Products, USA) was placed on the top of it, into which the  $D=40\text{ }\mu\text{m}$  BTG  $\mu S$ -s were poured randomly. In order to enable imaging, the  $\mu S$  had to be in direct contact with the sample, therefore the thickness of the glue could not exceed  $D$ . As this condition was not fulfilled by placing a single droplet of NOA 63, two alternatives were developed. First, we explored if the glue can be diluted. Because its exact chemical components are not published by the manufacturer, commonly used chemicals (acetone, tetrahydrofuran and isopropanol) were tested. The two former showed promising results, as thinner layer could be achieved. In parallel, a second method was found, which consisted of swiping the undiluted glue over the surface of the substrate with another glass slide. Due to the viscosity of the NOA 63, a thin layer remained on the substrate after swiping that was still sufficient for further processing. This method did not require an extensive study on different dilution ratios, therefore it was chosen to be implemented in the fabrication protocol.

After the NOA 63 layer was deposited, the  $\mu S$ -s were poured on it randomly and consequently swiped with a secondary glass slide in order to ensure single-layer configuration. Finally, the chips were exposed to UV-light until the dose of  $4.5\text{ Joules/cm}^2$  was reached, in order to fix the glue and the position of the  $\mu S$ -s. Although this fabrication process was very simple and yet effective, it had many factors that slowed down the imaging experiments. Before imaging tests with the chip could begun, a search had to be done to find a  $\mu S$  and position it in the *FoV* of the microscope objective. Robustness of this construction was low, because  $\mu S$ -s were time-to-time released and left on the sample. Furthermore, fabrication repeatability was also low, because many steps were hand-made which decreased uniformity. Despite of these issues, successful experiments were carried out as it is shown in chapter 5 and further development took place.

### 4.4 Chip for the microsphere array microsystem

The next goal of the project was to improve the previously shown fabrication method by introducing a  $2D\ \mu S$ -array that would enable parallel imaging with multiple  $\mu S$ -s. Manufacturing of this new chip was done in two phases (steps 1-3 and 4-6 in Figure 4.5). The first one took place in the clean room, while the second was done in our laboratory. The fabrication started with creating a template chip using negative photoresist-based photolithography. The dimensions of the chip substrate was  $22 \times 22 \times 0.15\text{ mm}^3$  and it was made of D 263 M borosilicate glass (Menzel-Gläser, Germany). After oxygen plasma cleaning (step 1), it was coated with  $20\text{ }\mu\text{m}$  3025 type SU8 (MicroChem, USA; step 2). The glass-chromium mask used for the lithography consisted of an array of  $40\text{ }\mu\text{m}$  diameter wells with a pitch of  $60\text{ }\mu\text{m}$  (step 3). After development, the chip was transferred to our laboratory and the patterning of the  $\mu S$ -s began.

The second phase was an oxygen plasma treatment to modify the contact angle between the

#### 4.4. Chip for the microsphere array microsystem

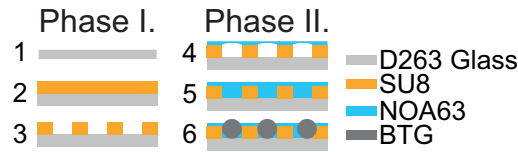


**Figure 4.5** – Schematic of the fabrication process of the  $\mu S$  array chip. 1: A cover glass chip is treated with oxygen plasma. 2: 20  $\mu m$  SU8 photoresist is spin-coated on the chip. 3: An array of microwells is patterned into the SU8 with photolithography. 4: A layer of NOA 63 optical glue is placed on the top, leading to air bubbles stuck into the microwells. 5: The air bubbles are removed with vacuum treatment. 6: BTG  $\mu S$ -s are patterned into the microwells and fixed by UV curing of the optical glue.

NOA 63 and the SU8 (step 4). Without this step, the 4  $\mu l$  droplet of the glue did not cover the array, but shrank into one spot. Before the vacuum treatment (step 5), which aimed to remove the stuck air bubbles, the chip was investigated under an optical microscope to check the full coverage of the array area. Typically, it was placed in the vacuum chamber for 20 minutes, but the time was increased on demand, based on the optical observations of the chip. This was followed by the initial random placement of the BTG  $\mu S$ -s. The patterning was then done by the swiping method presented already in section 4.1. In order to increase the final array coverage percentage to  $\sim 100\%$ , a manual adjustment with the help of a needle was applied as the final step of the patterning. Before the UV exposure, the excess amount of  $\mu S$ -s were removed to prevent them acting as spacers during the imaging. Later, the chip was exposed to a total dose of 4.5 Joules/cm<sup>2</sup> of UV-light, which was required for curing the NOA 63 glue (step 6). Finally, the chip was placed again in oxygen plasma for 3 minutes. This step ensured that the top of the  $\mu S$ -s were not covered with the glue. Photographs of the final chip are shown in Figure 4.6.a and 4.6.b.

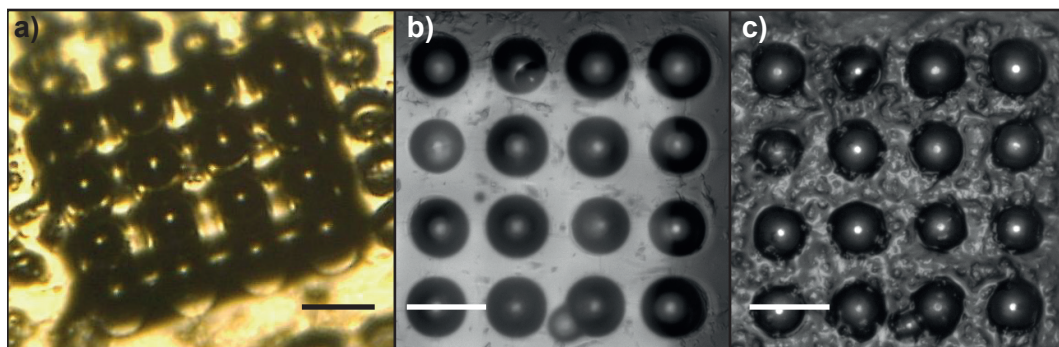


**Figure 4.6** – Photographs of the fabricated  $\mu S$  array chip from **a)** perspective and **b)** top view. **c)** Photograph of the same chip as in **b)** after the reliability experiment. Scale bars: 60  $\mu m$ .

To demonstrate the robustness of the new chip compared to the one shown in section 4.3, reliability experiments were conducted. These consisted of dipping the chip upside down 40 times into different immersion media (*i.e.* first into de-ionized water and then the experiment was repeated with immersion oil). As optical inspection confirmed, no  $\mu S$  was lost during the process, which proved that the  $\mu S$ -s are well fixed to the template (Figure 4.6.c). The results

## **Chapter 4. Microfabrication**

---

of the super-resolution imaging experiments, where this chip was employed, are detailed in chapter 6.



## 5 The single microsphere microsystem

*This chapter introduces the first microsphere-based, optical super-resolution imaging microsystem that was built. The first section describes the motivation behind the development, while it provides a brief review of the alternative microscopy techniques that were already established before. This is followed by the detailed description of the used materials and applied fabrication methods. Finally, the third section shows the achieved results and positions this imaging technique in the field of super-resolution microscopy by a comparison with other methods.*

---

This chapter was adapted from the following publications:

- **G. Huszka**, H. Yang, and M. A. M. Gijs, “Microsphere-based super-resolution scanning optical microscope”, *Optics Express*, vol. 25, no. 13, p. 15 079, 2017.  
*My contribution:* I built the imaging system, conducted the experiments and the numerical simulations, created the scanning and stitching algorithms, did the data analysis and wrote the manuscript.
- **G. Huszka**, H. Yang, and M. A. M. Gijs, “Dielectric microsphere-based optical system for super-resolution microscopy”, in *TRANSDUCERS 2017 - The 19th IEEE International Conference on Solid-State Sensors, Actuators and Microsystems*, Kaohsiung, Taiwan, 2017.  
*My contribution:* I fabricated the microchip, conducted the experiments, wrote the manuscript and presented the results at the conference.

### 5.1 Introduction

As it was shown in section 2.3, high- $RI$  dielectric  $\mu S$ -s positioned within the  $FoV$  of a microscope objective in a dielectric medium can focus the light into a so-called  $PNJ$ . A sample placed in such nanojet can be imaged by the objective with super-resolution. However, when imaging nanostructures on a substrate, the propagation distance of a light wave in the dielectric medium in between the substrate and the  $\mu S$  must be small enough to reveal the sample's

nanometric features. Therefore, only the central part of an image obtained through a  $\mu S$  shows super-resolution details, which are typically  $\sim 100$  nm using white light (peak at  $\lambda = 600$  nm). We have performed *FEM* simulations of the role of this critical distance in the super-resolution effect. Super-resolution imaging of a sample placed beneath the  $\mu S$  is only possible within a very restricted central area of  $\sim 10 \mu\text{m}^2$ , where the separation distance between the substrate and the  $\mu S$  surface is very small ( $\sim 1 \mu\text{m}$ ). To generate super-resolution images over larger areas of the sample, we have fixed a single  $\mu S$  on a frame attached to the microscope objective, which is automatically scanned over the sample in a step-by-step fashion. This generates a set of image tiles, which are subsequently stitched into a single super-resolution image of a sample area of up to  $\sim 10^4 \mu\text{m}^2$ . Scanning a standard optical microscope objective with  $\mu S$  therefore enables *SRM* over the complete field-of-view of the objective.

Classical optical microscopes are restricted in resolution by Abbe's diffraction limit, as waves carrying sub-diffraction details, which are present in the near-field, are evanescent and disappear in the far-field [147]. However, recent reports provided evidence of transmission of near-field information by placing directly on top of the sample a micro- or a nano-object (see section 2.3.1). As it was demonstrated, a drawback of these systems was the limited *FoV* that could not exceed the size of the applied micro- or nano-object placed on the sample. Another limiting factor was that, in these studies, the  $\mu S$ -s were placed randomly on the sample, which means that only a certain part of it could be imaged and the position could not be changed after the initial placement. On the other hand, a wide range of far-field techniques were developed that could achieve resolutions deeply below the diffraction limit (see section 2.1), but fluorescent labelling was necessary. Furthermore, their complexity induced rising instrumentation costs and in some cases acquisition time also became a relevant factor. An alternative for super-resolution imaging was provided by the near-field imaging techniques. Scanning tip-based microscopies, like *AFM* or *STM*, could image samples over micrometer ranges, meanwhile providing a resolution deeply below the optical diffraction limit [158]–[160]. A study showed that *AFM* can be combined with optical fluorescent imaging to have enhanced picture quality of biological samples [161]. Optical techniques, such as *PTM*, *NSOM*, *TENOM*, *PSTM* or *NORM* (see section 2.2), also performed very well in terms of super-resolution imaging. Others achieved super-resolution by replacing the point of an *AFM* tip with a so-called  $\mu S$  superlens, which could produce extended super-resolution images by scanning of the *AFM* head over the sample [144]. While benefiting from established *AFM*-positioning control schemes, these systems are less straightforward to operate, because of the intrinsic sensitivity of the detection principle on vibrations, which can hinder experimentation. Further techniques aiming to extend the *FoV* of  $\mu S$ -based imaging systems were presented in section 2.3.2, but their implementation was less robust, which prevented them from wide range applicability. A distinctive advantage of these established techniques is that the image processing is already implemented, meaning that the acquired data is processed automatically and shown to the user as a final picture. On the other hand, many image processing algorithms were recently developed and applied in various research projects [162]–[166]. It is possible to implement these in customized microscope setups, therefore, if the  $\mu S$  scanning principle could be combined in a robust way with observation through a normal optical microscope objective, this

would be of great value to microscopy, as such simple add-on tool would potentially upgrade any classical microscope to a super-resolution one.

## 5.2 Materials and methods

Our method, called microsphere-based super-resolution scanning optical microscopy (*MS-SOM*), combines the advantages of a classical easy-to-operate optical microscope with a surface scanning principle. The basis of our microscopy system is a dielectric  $\mu S$  with  $n_{sphere}=1.95$  that is placed on top of the sample and surrounded by a medium with  $n_{medium}=1.56$  (Figure 5.1.a). We have chosen these materials and the corresponding values based on our previous studies [129], [167]. A super-resolution image is created due to two factors (see section 3.1). First, the  $\mu S$  acts as a solid immersion lens and increases the *NA* of the system locally. Since the sample is placed within the focal length of this lens, it projects a virtual magnified image below the sample plane. The second factor is the development of the *PNJ*, which was defined already in section 2.3. While a dielectric  $\mu S$  is capable of creating super-resolution images, its *FoV* is

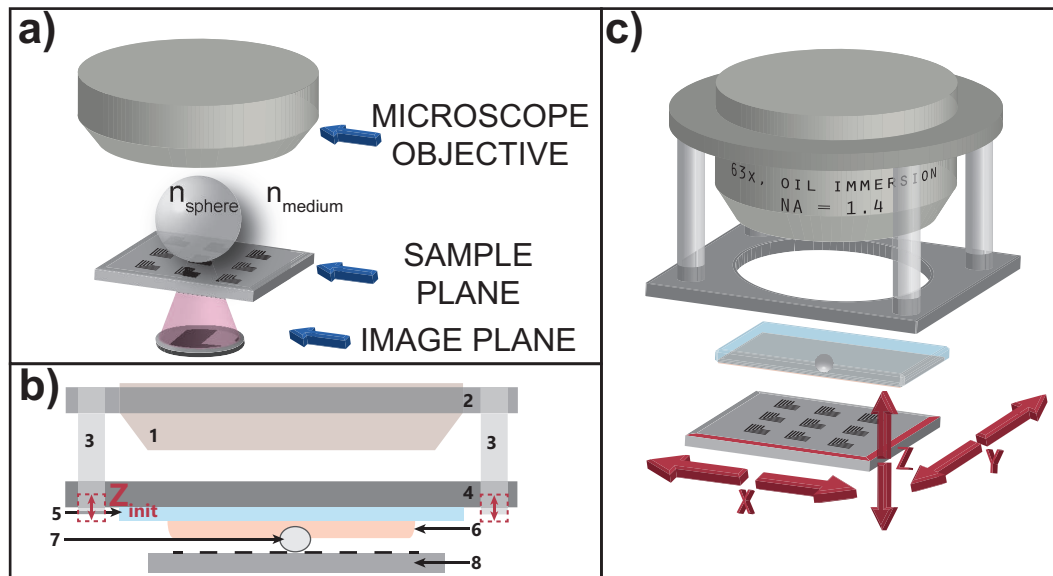


**Figure 5.1** – Principle of operation of the *MS-SOM*. **a)** A dielectric  $\mu S$  with  $n_{sphere}$  and situated in an optical medium with  $n_{medium}$  is placed on top of the sample and is observed by a classical optical microscope objective. This generates a virtual image below the sample plane, which shows super-resolution. **b)** Schematic cross-section of the experimental setup, allowing scanning of the sample with respect to the  $\mu S$ -objective system. 1: microscope objective; 2: fixation holder to the objective; 3: four metal rods are used for fixing element number 4, *i.e.* a metal frame with circular opening, to which a coverglass is glued (element number 5), to which a dielectric  $\mu S$  (element number 7), typically a *BTG*  $\mu S$  of 10-40  $\mu m$  diameter, is fixed via a thin layer of *NOA 63* glue (element number 6); 8: sample to be imaged, which is mounted on a motorized microscope stage. An initial vertical scan of the stage ( $Z_{init}$ ) is performed, during which the frame is translated with respect to the microscope objective by a frictional slide along the four rods, to find the optical image plane. **c)** 3D exploded view of the scanning system.

restricted by  $D$ . To overcome this limitation, we have first fixed  $D=40\ \mu\text{m}$  BTG  $\mu\text{S}$ -s (Cospheric, USA) on a  $150\ \mu\text{m}$ -thick glass microscope slide using NOA 63 glue (Norland Products, USA). This was done as it was described in section 4.3. After fabrication, the chip was attached to the microscope objective via a metal frame in a position, where a  $\mu\text{S}$  was in the center (Figure 5.1.b). The latter was connected to a fixation holder via four metal rods, by which the frame could slide with respect to the microscope objective. A motorized microscope stage carrying the sample could move independently from the fixed  $\mu\text{S}$ , in the x-, y- and z-directions.

A Zeiss Axio Imager M2m upright optical microscope equipped with HAL100 halogen light source, an AxioCam MRm camera and a  $63\times$ ,  $NA=1.4$  oil immersion objective with cover glass correction up until  $170\ \mu\text{m}$  thickness was used (all of them from Carl Zeiss, Germany). The initial step of the operation is positioning the sample within the focus of the microscope objective (Figure 5.1.c). This is followed by a search for the virtual image plane, which is below the sample and where the highest magnification and the biggest contrast is present. The process involves raising the stage step-by-step causing a frictional slide on the metal rods, thereby focusing the objective on lower-and-lower planes beneath the sample (z-axis). After finding the imaging plane, the movement of the stage is stopped and the obtained z-axis value is stored as initial value. The fully automated x-y scan starts from this point. Although the software provided by the manufacturer has the capability for automatic stitching of tiles, we could not utilize this function, as it only allows stitching together the full field-of-view tiles recorded by the mounted camera. Since we could only use a fraction of the area of a tile, namely the regions underneath a  $\mu\text{S}$ , where super-resolution occurs, a new procedure had to be developed. A custom algorithm, written in Visual Basic, which runs within the Zeiss AxioVision software, was created to control all stage movements and the camera. A single step in the scanning process involves first taking a picture through the microscope, after which the stage moves  $5\ \mu\text{m}$  down along the z-axis and makes one step along either the x- or the y-axis. Hereafter, the stage raises back over  $5\ \mu\text{m}$ , ready for taking the next picture. The extra lifting along the z-axis was implemented to avoid scratching the sample surface with the  $\mu\text{S}$  and to reduce the shear stress. Our software interface allows setting freely the scanning step size and choosing the area to be imaged; also it saves line-by-line the pictures for subsequent analysis.

### 5.3 Results and discussion

As imaging test structures, we used line patterns, like the ones shown in the insets of Figure 5.2.a and characterized by a line width  $L$  between  $0.13$  and  $0.18\ \mu\text{m}$  and a pitch  $P$  between  $0.26$  and  $0.36\ \mu\text{m}$ , as present on a MetroChip microscope calibration target (Pelco, USA). Before performing the super-resolution imaging experiments, various samples were imaged by the microscope objective without use of a  $\mu\text{S}$  (Figure 5.2.a inset and Figure 5.2.c). Theoretically, the resolution  $d$  of a classical microscope is determined by Abbe's diffraction limit:  $d = \lambda / (2 \times NA)$ . The halogen light source typically emits light in the  $400\ \text{nm} < \lambda < 700\ \text{nm}$  spectral range, with maximum peak irradiance at  $\lambda = 600\ \text{nm}$  (data obtained from Zeiss), at which a resolution  $d \sim 215\ \text{nm}$  is calculated. Experimentally, without use of a  $\mu\text{S}$ , a LSP with  $P=360\ \text{nm}$  could be

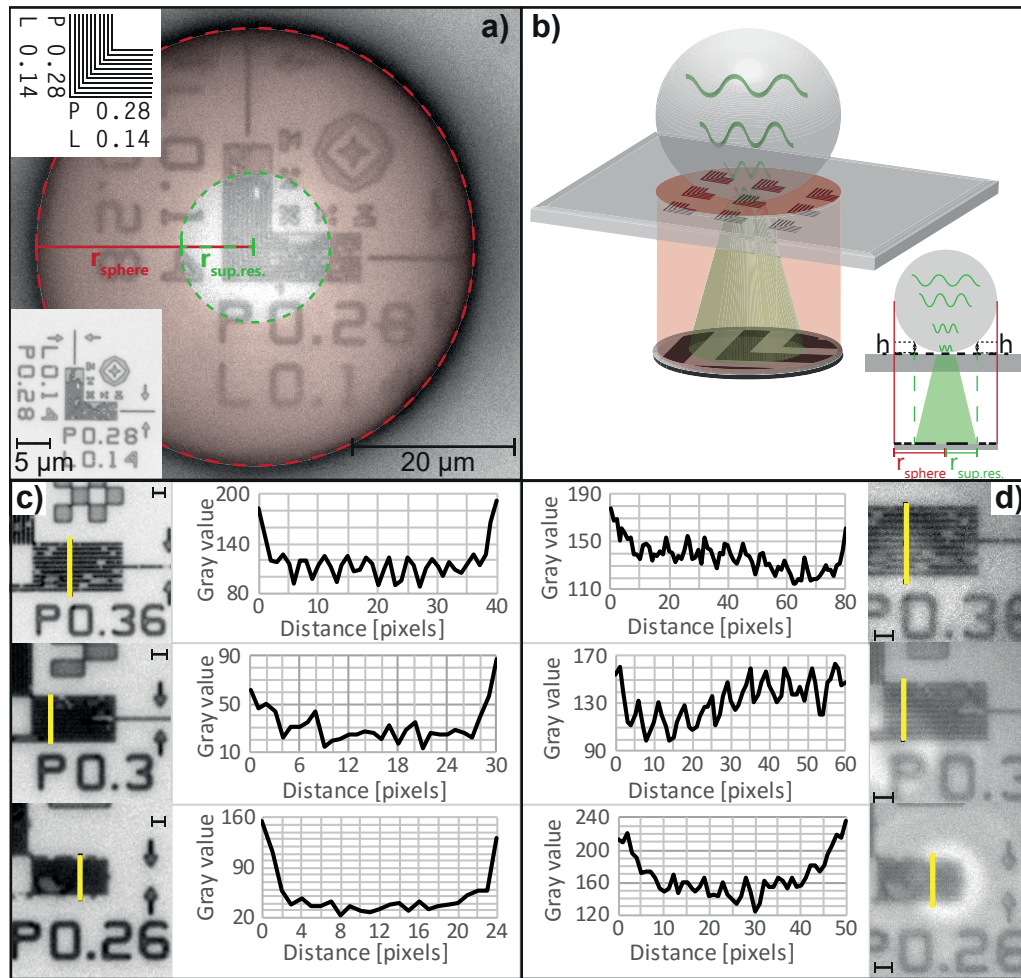


**Figure 5.2** – Image obtained after a single scan step and analysis of the super-resolution effect. **a)** Super-resolution imaging of the sample represented in the insets by positioning a  $D=40\ \mu\text{m}$  BTG  $\mu\text{S}$  on top of it, as observed by a regular microscope objective ( $63\times$ , oil-immersion,  $NA=1.4$ ). The dotted red circle indicates the total  $FoV$  of the  $\mu\text{S}$ , as defined by its radius  $r_{sphere}$ . The green dotted circle with radius  $r_{sup.res.}$  marks the area where super-resolution imaging occurs. Inset top left: Schematic of a typical LSP sample imaged in this study, with  $P=0.28\ \mu\text{m}$  and  $L=0.14\ \mu\text{m}$ . Inset bottom left: Sample imaged without the use of a  $\mu\text{S}$ . **b)** 3D and 2D (inset) schematics of the imaging by a  $\mu\text{S}$ . The light waves in the center of the  $\mu\text{S}$  (green) carry the super-resolution information;  $r_{sup.res.}$  implicitly defines the vertical distance  $h$  between sample and  $\mu\text{S}$  surface, below which super-resolution imaging is enabled. **c)** Samples with  $P=0.36\ \mu\text{m}$ ,  $0.3\ \mu\text{m}$ ,  $0.26\ \mu\text{m}$ , respectively, and a line:interspace ratio 1:1, as imaged with the same microscope objective as used in a) without the use of a  $\mu\text{S}$ . Gray-scale analysis along the marked yellow line is showed on the right of every image, respectively. The 11 down pointing spikes corresponding to the 11 lines of the samples can only be seen on the top picture, as they are not resolved in the middle and in the bottom. Scale bar:  $1\ \mu\text{m}$ . **d)** Improved imaging of the same samples as in c) by using a  $\mu\text{S}$  on.

imaged, while the one with  $P=300\ \text{nm}$  could not be resolved (Figure 5.2.c). This was confirmed by gray-scale analysis using ImageJ software. During acquisition of the image tiles, the camera was set to take the pictures with the highest possible contrast to make imaging of all tiles

comparable. Subsequently, the *ROI*-s were cropped from the pictures and the gray values within the *ROI*-s were analysed along a defined line (yellow line on the figures). When plotting these values, black color is marked with 0 and white with 255. As the sample had 11 dark lines, the plot should show 11 peaks pointing downwards. When placing a  $D=40\ \mu\text{m}$  *BTG*  $\mu\text{S}$  on the samples, the *LSP* could be clearly resolved (Figure 5.2.a and 5.2.d).

Interestingly, as discussed in chapter 2, imaging periodic nanometric line patterns with visible light tends to be a more challenging task, than imaging stand-alone objects [126], non- equal sized objects and spaces [112], [136], *Laser* light source [128], fluorescent samples [130]–[132] or any combination of these. Indeed, it is easy to realize that a signal coming from a stand-alone nanometric object can be much weaker and still be detectable, since it will have a bigger contrast with respect to the background than when imaging a periodic nanometric structure. As an example, a stand-alone  $L=100\ \text{nm}$  line was imaged from the same microscope calibration target as used earlier (Figure 5.3). The line is observable through the  $63\times$ ,  $NA=1.4$  oil-immersion objective using halogen light illumination, despite its width is below the diffraction limit. The same applies for periodic structures, where the gap between nanometric objects (particles or lines) is larger than the size of the particles or lines themselves. This phenomenon also can be exploited *vice versa*: having non-diffraction-limited objects combined with diffraction-limited gaps will be beneficial to the actual resolution of the system. Also applying a *Laser* light source highly increases the illumination power and therefore increases the reflected light's intensity. If the *Laser* is combined with a fluorescent sample, this further increases the lowest detectable signal, because in this case the nanometric sample acts as a virtual light source, and the background is almost fully dimmed. Therefore, to determine the exact resolution of our system, we imaged equally spaced *LSP*-s, despite of that fact, that this way our end-results did not show outstandingly low values, like the ones that can be found in literature. On the other hand, our characterization is based on a more robust definition and did not became sample-dependent.

The exploitable *FoV* for super-resolution was limited to the central part of the  $\mu\text{S}$  (Figure

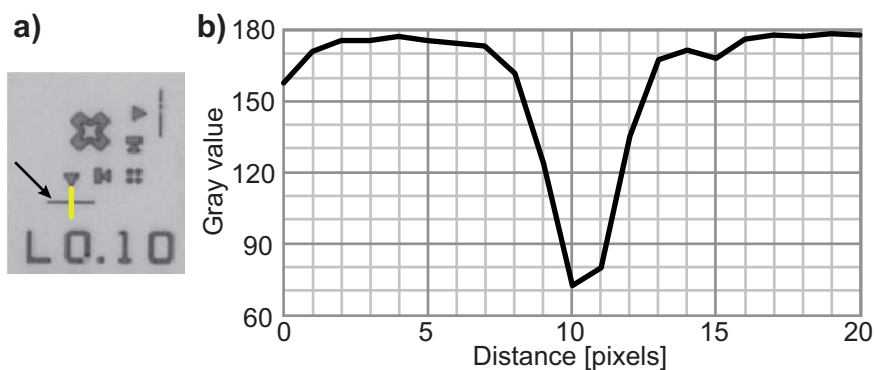


**Figure 5.3** – Photograph of a 100 nm-wide line from a microscope calibration target. **a)** The  $63\times$ ,  $NA=1.4$  oil-immersion objective could resolve the line in white-light illumination, despite of its sub-diffraction dimension. **b)** Analysis of the gray values along the yellow measurement line on a). The signal of the line (down-pointing peak) can be clearly distinguished.

5.2.a), marked by the radius  $r_{sup.res.}$ . During experiments it was observed, that the position  $r_{sup.res.}$  corresponds to a distance  $h$  between the sample and the  $\mu S$  of  $\sim 1 \mu m$ , which is a critical distance above which super-resolution imaging is no longer possible (Figure 5.2.b). Theoretically, Maxwell's wave equation applies in a medium with  $n_{medium}$

$$k^2 = k_x^2 + k_y^2 + k_z^2 = \left( \frac{2\pi n_{medium}}{\lambda} \right)^2 \quad (5.1)$$

with  $k_x$ ,  $k_y$  and  $k_z$  the spatial components of the wave number ( $k$ ), which correspond to a contrast variation in real space over a distance of  $\Delta x$ ,  $\Delta y$ ,  $\Delta z$ , respectively

$$k_x = \frac{2\pi}{\Delta x}, k_y = \frac{2\pi}{\Delta y}, k_z = \frac{2\pi}{\Delta z} \quad (5.2)$$

Considering there is a sub-diffraction feature along the x-axis in the object to be imaged, and that the object is linear along the y-axis, so that  $k_y$  is converging to 0, then the sub-diffraction feature will show an evanescent wave behaviour along the z-axis (*i.e.*  $k_z$  is imaginary). In this case, Equation 5.1 can be written as:

$$\Delta z = \frac{1}{\sqrt{\frac{1}{\Delta x^2} - \left( \frac{n_{medium}}{\lambda} \right)^2}} \quad (5.3)$$

with  $\Delta z$  the typical distance over which the wave vanishes in the z-direction. For example, when  $\lambda=600$  nm,  $\Delta x=280$  nm (corresponding to the structure at the left on Figure 5.2.a) resulting in  $\Delta z \sim 400$  nm. While this value is smaller than the experimental  $h$ , it is of the right order of magnitude. Also, we should realize that Equation 5.1 is valid for a homogeneous medium, while, in our case, the presence of high-*RI* materials, *i.e.* the *BTG* and the silicon, next to the thin layer of medium beneath the sphere can play a role. Additionally, the spectral range of the light source may be a relevant factor. To further investigate which parameters influence the  $h$  value, *FEM* simulations (COMSOL Multiphysics) of the light propagation from a multiple line source with wavelength of  $\lambda=650$  nm positioned on a silicon substrate ( $n_{silicon}=3.48$ ) through the *BTG*  $\mu S$  ( $n_{sphere}=1.95$ ) and surrounding dielectric medium ( $n_{medium}=1.56$ ) were carried out. A scalar equation was used to study transverse electric waves in a *2D* model,

$$\nabla \times (\nabla \times E) - k_0^2 \epsilon_r E = 0 \quad (5.4)$$

where  $k_0$  is the free-space wave number,  $\epsilon_r=(n-ik)^2$  is the relative permittivity, expressed with the *RI*  $n$  and its imaginary part  $k$ . In this model, the scattering boundary condition was used at all exterior boundaries, and the continuity boundary condition was used at all material interfaces. During meshing, the minimum element size was 10 nm, while the maximum element size of  $\lambda/4$  was set to obtain a precise solution. After the model was solved, the normalized electric field was plotted. Our study focused on the role of two major parameters, the width of the line pattern to be imaged ( $L$ ) and the closest distance between the sample and the  $\mu S$  ( $S_{offset}$ ).

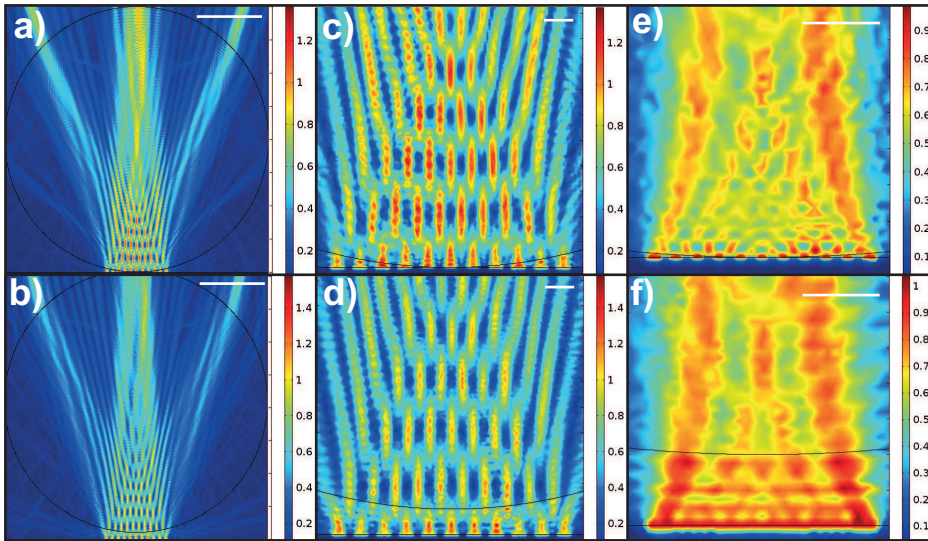


**Figure 5.4** – Simulated electric fields of light propagation originating from a line pattern sample placed at varying distances beneath a microsphere. **a), b)** A  $40\ \mu\text{m}$  BTG sphere is placed at 1 nm and 1000 nm distance, respectively, above a 450 nm wide line pattern. Scale bar  $10\ \mu\text{m}$ . **c), d)** Zoom on the region near the sample source of a) and b), respectively. Modulation of the electrical field can be clearly observed in both cases. Scale bar  $1\ \mu\text{m}$ . **e), f)** Zoom of the same region as in c) and d), but taking a 150 nm wide line pattern. While the modulation can be still observed in e), it is not any more present in f), indicating that a too large propagation distance for the light in the medium provokes loss of nanometric feature information. Scale bar  $1\ \mu\text{m}$ .

Figure 5.4.a and 5.4.c are simulations of a  $L=450\ \text{nm}$  and  $P=900\ \text{nm}$  LSP with  $S_{\text{offset}}=1\ \text{nm}$ , *i.e.* the  $\mu\text{S}$  is practically in contact with the substrate. Since, during an imaging experiment, the reflected light from a grating structure is investigated, we represent in the simulation a line of the grating as a light source. The simulations show the interference pattern between eleven line sources positioned at the bottom of the simulation area, propagating towards the microscope objective (not shown in this simulation). The modulation can be clearly observed, even if the distance increases to  $S_{\text{offset}}=1000\ \text{nm}$  (Figure 5.4.b and 5.4.d). Then we changed  $L$  to 150 nm, which is below the diffraction limit. Figure 5.4.e shows that the modulation was only present when  $S_{\text{offset}}=1\ \text{nm}$ . The simulation of the  $S_{\text{offset}}=1000\ \text{nm}$  shows that the modulation is lost (Figure 5.4.f), which agrees with Abbe's diffraction limit for resolving sub-diffraction features, *i.e.* the wave with spatial frequency of  $1/(300\ \text{nm})$  is non-propagating in the medium. To map how the value of the modulation changes as function of these two parameters, an extended electric field simulation study was carried out. The parameter  $L$  was varied between 120 nm and 450 nm with 1.3 times multiplication steps.  $S_{\text{offset}}$  was set to 1, 10, 100 and 1000 nm. All combinations of these parameters resulted in 24 different cases (Appendix A.3). For analysis, three lines for the evaluation of the normalized electrical field were introduced (Figure 5.5.a). The first, at  $Z_0$ , was placed on the light source. The second, at  $Z_1$ , was placed at a distance  $S_{\text{offset}}/2$ . The third, at  $Z_2$ , was placed at a distance  $S_{\text{offset}} \times (1.5 \pm \epsilon)$ , where  $\epsilon$  was such that the line was evaluating the first full wavefront within the  $\mu\text{S}$ . The normalized electrical field was plotted along the three lines (Figure 5.5.b) and these data were analysed afterwards by



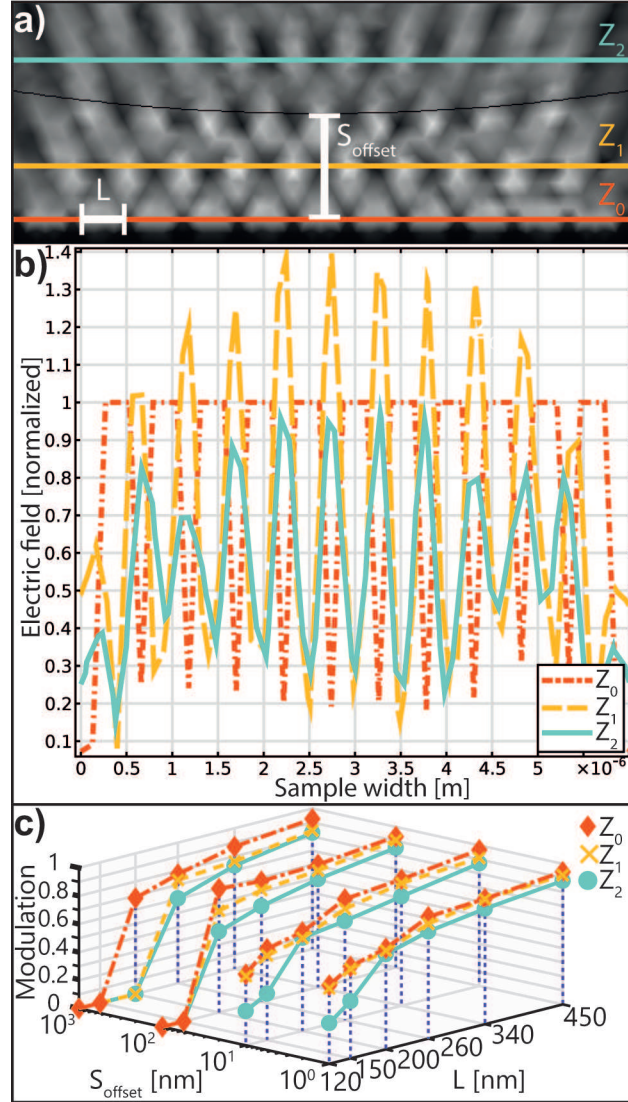


**Figure 5.5** – Analysis of the simulation results. **a)** Example of the three measurement lines that were used for evaluation of the modulation patterns in the electric field simulations.  $Z_0$  was placed at the light source,  $Z_1$  at the distance  $S_{\text{offset}}/2$  and  $Z_2$  at the distance  $S_{\text{offset}} \times (1.5 \pm \epsilon)$ , where  $\epsilon$  was chosen such that the line is evaluating the first full wavefront within the microsphere.  $L=260$  nm,  $S_{\text{offset}}=1000$  nm. **b)** Plot of the electrical field simulated in a) along the three measurement lines. **c)** Summary of the modulations that were calculated for a range  $10^0$  nm  $< S_{\text{offset}} < 10^3$  nm and  $120$  nm  $< L < 450$  nm, based on the electrical field calculations, like the one shown in b).

considering the averaged maximum and minimum normalized electrical fields that together define the modulation. The 72 final modulation values are summarized on Figure 5.5.c. The result shows that, for the smaller  $L$  values, the modulation is proportional to  $L$  and is even absent for the larger  $S_{\text{offset}}$ . For the larger  $L$  values, the modulation is maintained, *i.e.* the wave is fully propagating, whatever the value of  $S_{\text{offset}}$  is. These results show how the presence of a  $\mu S$  improves the imaging, as subdiffraction values of  $L$  have non-zero modulation values for smaller  $S_{\text{offset}}$  values, meaning that, when the  $\mu S$  is in close contact to the sample, imaging at a

sub-diffraction scale is possible.

Figure 5.2.a showed already that the  $FoV$  for super-resolution was limited to the central part of the  $\mu S$ , marked by the radius  $r_{sup.res.}$ . For each of the image tiles that was stored during the scanning process, our stitching algorithm exploited the central square comprised within the circle of radius  $r_{sup.res.}$  (Figure 5.6.a). This was possible, since the  $ROI$ -s are positioned exactly at the same place on all image tiles. Our algorithm created a new virtual canvas, to which the  $ROI$ -s were mapped, forming a mosaic image. To maximize the useful area per picture, the

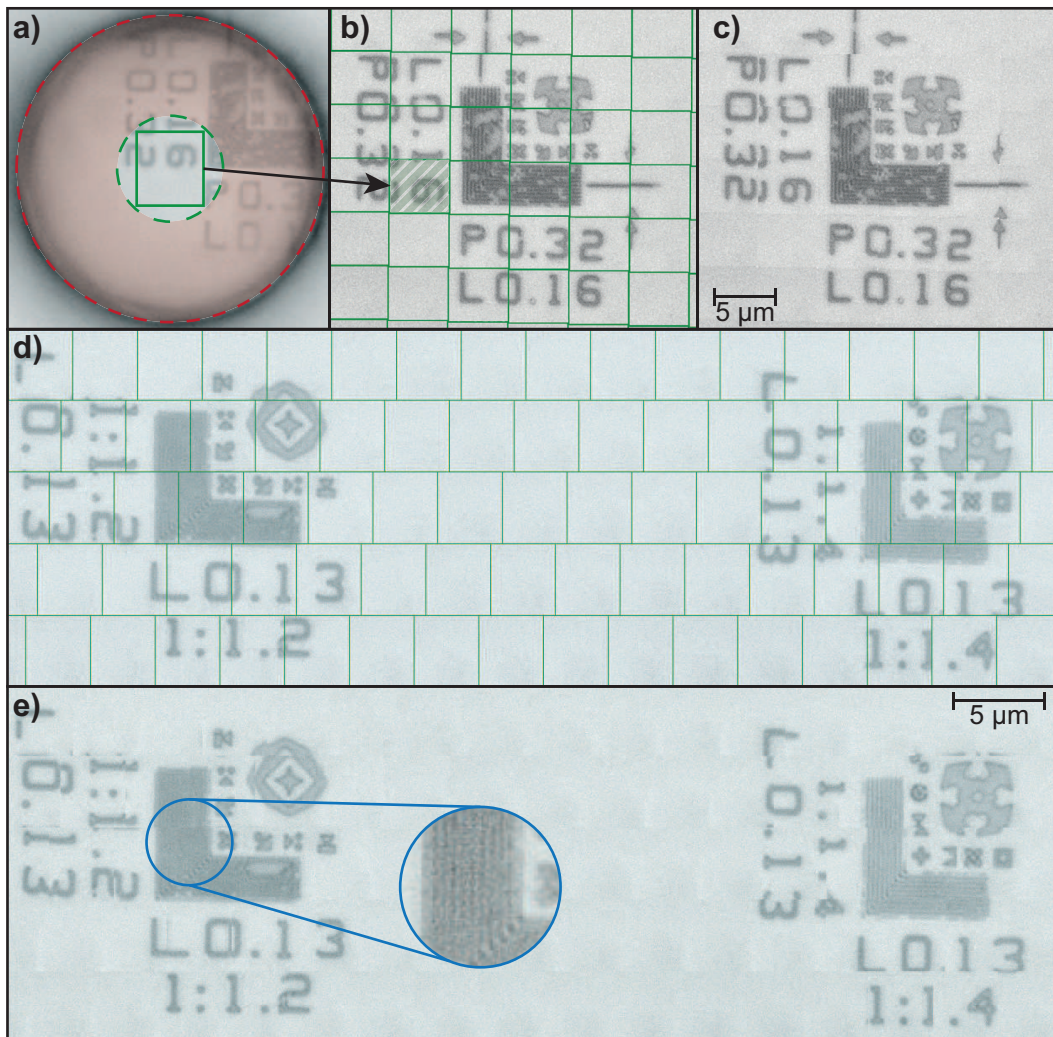


**Figure 5.6** – Scanning and image reconstruction. **a)** Image obtained after a single scan step. Only the area in the green central square that fits into the circle with radius  $r_{sup.res.}$  is used in the image reconstruction. **b)** Composed image obtained by stitching all square regions recorded during the scanning process. **c)** Same image as in **b)**, without indication of the tiles. **d)** Demonstration of the scanning super-resolution imaging of a larger sampling area, containing patterns with  $L=0.13 \mu m$  and width:interspacing ratio of 1:1.2 (left) and 1:1.4 (right), respectively. **e)** Same image as in **d)**, without indication of the tiles. The zoom in the blue circle shows that 130 nm lines with 156 nm interspacing can be resolved indeed.

overlap between the tiles was not implemented in the stitching algorithm, but in the scanning process itself. This approach was chosen because the pictures are not stitched after they are saved by the microscope-mounted camera, like in traditional mosaic imaging. Instead, only a central region of interest of a picture is used, namely exactly that where super-resolution occurs, *i.e.* in the center region of the  $\mu S$ . Since this area is relatively small compared to the  $FoV$  of the camera and even to  $D$ , every pixel is important. To not lose any, a  $5\ \mu\text{m}$  step size was used during the scanning (along both x- and y-axis) which resulted in an overlap that was monitored in the non-superresolution part of the image created by the  $\mu S$ . Since this part of the picture is cropped out from the final stitch, at the end it looks like an overlap-free stitching, though it is not strictly speaking. This way our program, which is written in Visual Basic and which runs independently from Zeiss AxioVison software, stitched the square tiles and enabled to reconstruct the big  $FoV$  image, with high magnification and with super-resolution. Figures 5.6.b and 5.6.c show a reconstructed image with and without showing the individual tiles, respectively. An advantage of the hybrid stitching presented above is that it is possible to adjust the stitching algorithm in a way that it can take into consideration a systematic error when scanning the frame over a large distance, for example when going back to the next line of the scan (Figures 5.6.d and 5.6.e). The total area imaged in Figure 5.6.e is  $\sim 2500\ \mu\text{m}^2$  and the scanning time was less than 1 minute.

To further demonstrate the imaging capabilities of our system, the surface of a Blu-ray disk was imaged. Figure 5.7.a shows a *SEM* picture of a single layer, 25 GB capacity Blu-ray disk with indication of typical feature sizes. The disk contains embossed concentric grooves with a pitch of 320 nm and data bits that have a minimum length of 150 nm [113]. To enable imaging these features, the  $100\ \mu\text{m}$ -thick protective film was removed from the disk, so that the sub-diffraction features could be in direct contact with the  $\mu S$ . After this step, the imaging process described before was started and super-resolution images were recorded (Figures 5.7.b and 5.7.c). Each tile had a brighter spot in the middle, the origin of which was the internal reflective layer of the Blu-ray disk, but this did not hinder the imaging. The result of the stitching operation of the scanned images is shown in Figure 5.7.d. For Figure 5.7.d(i), we found that

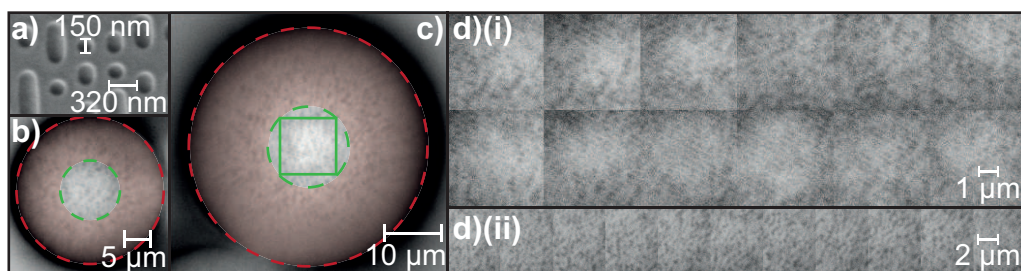


**Figure 5.7** – Scanning and image reconstruction of a Blu-ray disk surface. **a)** *SEM* picture of the surface of a Blu-ray disk with indication of the typical size of embossed features. **b)** Image obtained after a single scan step using a  $D=26\ \mu\text{m}$   $\mu S$ . For imaging, the  $100\ \mu\text{m}$  thick protective coating layer was removed from the disk. **c)** Image obtained after a single scan step using a  $D=40\ \mu\text{m}$   $\mu S$ . Only the area in the green central square will be used in the image reconstruction. **d)** (i and ii) Composed images obtained by stitching different square regions recorded during the scanning process.

the  $\mu S$  was slightly displaced with respect to the frame during scanning, due to friction forces on the glue, which caused a shadowing effect. However, our algorithm perfectly permitted to compensate for these small systematic position errors (except the dark-edge effect), resulting in a coherent composite image. For comparison, we conducted the same stitching with a seamless stitching method in ImageJ. Results showed that the other algorithm can mask the dark-edge error nicer, though not correct completely the shadowing effect. Therefore, it was concluded, that the scanning process has a much higher impact on the quality of the final image, than the chosen stitching algorithm.

In Table 5.1, we present an overview on the performance of existing super-resolution imaging techniques in comparison with our *MS-SOM* system. A classical optical microscope can be considered as the basic system, which is cost-effective, has a high *FoV*, but is diffraction-limited in resolution. One option to overcome this limit is going for far-field imaging techniques. They have an excellent lateral resolution performance, at the cost of increasing imaging time, using fluorescent samples and elevated instrumentation cost and complexity. On the other hand, near-field techniques can also achieve very high resolution, even in the sub-nanometer range, but their *FoV* is smaller and they are less robust than lens-based microscopes. The third possibility is the employment of micro- and nano-sized refractive structures that are cost-effective and fast in terms of imaging time. However, they are limited by a small *FoV*. The main advantage of our system is that it has all the good properties of a classical optical microscope (*FoV*, cost, imaging time), but it can produce images with super-resolution resolution. Our microscopy method therefore could demonstrate an alternative to the well-established far- and near-field techniques.

We introduced super-resolution scanning optical microscopy, using a transparent dielectric  $\mu S$  that was translated over a sample surface using a conventional microscope objective. By performing extensive *FEM* simulations of the light propagation within the sample/ $\mu S$ /medium system, we pointed out a critical separation distance between the sample and the  $\mu S$ , below which super-resolution imaging was enabled. Therefore, such imaging of a sample placed beneath the  $\mu S$  was only possible within a very restricted area of  $\sim 10 \mu\text{m}^2$  near the contact of the substrate and the  $\mu S$ . Combining the super-resolution imaging capability of a  $\mu S$  with customized scanning and image reconstruction algorithms allowed creating super-resolution images over the full *FoV* of the microscope objective. Our proof-of-concept device was tested on linear calibration samples with nanometric features. Sample areas in the  $\sim 10^4 \mu\text{m}^2$  range with features varying between 130 and 160 nm were imaged at a speed of 2 tiles/second. Compared to other techniques, our microscopy system allows super-resolution imaging in an affordable way, gaining almost 20% resolution over a classical optical microscope meanwhile benefiting from all of its advantages. Further improvements of this system will be detailed in the following chapter.

**Table 5.1** – Performance evaluation of super-resolution imaging systems.

Lateral resolution (LR): □=(LR&gt;300nm); □□=(300nm&gt;LR&gt;100nm); □□□=(100nm&gt;LR)

Size of imaged area (SA): ○=(SA<10<sup>2</sup>μm<sup>2</sup>); ○○=(10<sup>2</sup>μm<sup>2</sup><SA<10<sup>8</sup>μm<sup>2</sup>); ○○○=(10<sup>8</sup>μm<sup>2</sup><SA)

Est. cost of system (EC): \$=(EC&lt;50k USD); \$\$=(50k USD&lt;EC&lt;250k USD); \$\$\$=(250k USD&lt;EC)

Est. imaging time (ET): +=(ET&lt;1 min); ++=(1 min&lt;ET&lt;10 min); +++=(10 min&lt;ET).

	Name of imaging system	Reference	Lateral resolution	Size of imaged area	Estimated cost of system	Estimated imaging time
Far-field	Classical optical microscope	-	□	○○○	\$	+
	Confocal microscope	[168], [169]	□□	○○○	\$\$	++
	4Pi microscope	Section 2.1	□□	○○○	\$\$\$	++
	<i>STED</i>		□□□	○○	\$\$\$	++
	<i>SIM</i>		□□□	○○	\$\$	++
	<i>SMI</i>		□□□	○○	-	+
	<i>SMLM</i>		□□□	○○	\$\$	+++
Near-field	<i>AFM, STM</i>	[158]– [160], [170]	□□□	○○	\$\$	++
	Near-field super-resolution techniques	Section 2.2	□□□	○○	\$\$\$	++
Microobject-based	Fixed microobject-based microscopies	Section 2.3.1	□□	○	\$	+
	<i>MS-SOM</i>	-	□□	○○	\$	++



## 6 The microsphere array microsystem

*This chapter presents the improved version of the previously discussed single microsphere-based imaging system. The first part describes the improvements, then a detailed technical description of the used materials and methods is given. This is followed by the demonstration of the super-resolution capabilities in two immersion media and in different imaging modes. Finally, the robustness of this microscopy method is shown through an example of a big surface area imaging.*

---

This chapter was adapted from the following publications:

- **G. Huszka** and M. A. M. Gijs, “Turning a normal microscope into a super-resolution instrument using a scanning microlens array”, *Scientific Reports*, vol. 8, no. 1, 2018.  
*My contribution:* I built the new imaging system, fabricated the microsphere array chip, conducted the experiments, improved the scanning and stitching algorithms, did the data analysis and wrote the manuscript.
- **G. Huszka** and M. A. M. Gijs, “Custom adapter for extended field-of-view microsphere-based scanning superresolution microscopy”, in *MEMS 2018 - The 31st IEEE International Conference on Micro Electro Mechanical Systems*, Belfast, United Kingdom, 2018.  
*My contribution:* I developed the fabrication process, built the imaging system, conducted the experiments, analysed the data, wrote the manuscript and presented the results at the conference.

### 6.1 Introduction

The possibility of *FoV* extension of a  $\mu\text{S}$ -based imaging system by an automated scanning followed by image reconstruction was already proven in chapter 5. However, the presented *MS-SOM* suffered from three major issues: (i) the  $\mu\text{S}$  template chip fabrication had low repeatability; (ii) its fixation to the objective was not robust enough; (iii) the  $\mu\text{S}$ -s were fixed on the glass cover slide in random positions. These factors hindered experimentation and

prevented to show the true imaging potential of this technique. Therefore, the improvements made on the first concept aimed to overcome these difficulties to prove the more general applicability of this imaging system. As a first step, new template chips were designed that allowed exact positioning of the  $\mu S$ -s. As an added benefit, parallel imaging became possible, because the template fabrication technique enabled the creation of  $\mu S$ -arrays. Then, a new fixation system was implemented, in which the relative position between the template chip and the microscope objective could be controlled in a more precise way. This method also ensured a better contact between the sample and the  $\mu S$ -s that further enhanced the imaging quality. Meanwhile the first generation device was only operating in oil-immersion, water-immersion imaging was already demonstrated with the improved version. These findings opened up the possibility of large area super-resolution imaging both *in silico* and *in vivo*.

### 6.2 Materials and methods

The working principle of the improved imaging system is explained in Figure 6.1. As shown in Figure 6.1.a, if a dielectric  $\mu S$  with  $n_{sphere}$  is placed underneath a light microscope's objective and is surrounded by a medium with  $n_{medium}$ , a *PNJ* is created right under the  $\mu S$ . The position, shape and size of this *PNJ* is determined by (i) the wavelength of the illumination light (visible light in our study,  $400\text{ nm} < \lambda < 700\text{ nm}$ , with peak at  $\lambda=600\text{ nm}$ ), (ii) the shape of the micro-object (which is spherical in our case) and (iii) the ratio between the two refractive indices ( $n_{sphere}=1.95$  for the used *BTG*  $\mu S$ -s and  $n_{medium}=1.56$  for immersion oil, from Cospheric, USA and Sigma-Aldrich, Switzerland, respectively). These parameters must be tuned to generate a *PNJ* exiting exactly at the surface of the  $\mu S$ , to enable the best possible imaging resolution of diffraction-limited features of the sample. When a sample is placed just underneath the  $\mu S$  and the incident light is reflected back from the sample (Figure 6.1.b) the modulation pattern from the sample is transferred through the  $\mu S$ , towards the microscope objective. However, besides development of the *PNJ*, also the near-field interaction with the sample placed underneath the  $\mu S$  matters, so that the  $\mu S$ -based imaging resolution may become sample-dependent, as it was shown earlier in section 2.3. Therefore, in certain cases the super-resolution capability of a system can be only slightly better than the diffraction limit. Because of the geometrical optics properties of the  $\mu S$ , which acts as a lens, a virtual image will be projected about half- $D$  distance below the sample plane. This virtual image plane can be placed in the focus of the microscope objective. An image, recorded while observing this plane will contain information about the sub-diffraction features, therefore enables *SRM*. The major drawback of such an imaging is that the *FoV* is limited to size of the central part of the  $\mu S$ . To overcome this limitation we established a scanning mechanism, with which we could restore the *FoV* to the full size of the microscope objective.

Our revised setup consists of two major components as shown in Figure 6.2. The first is a metal frame, which is composed from 30 mm cage system parts (Thorlabs, Germany) including an SM1Z, z-axis translator that are fixed to the microscope objective (Figures 6.2.a and 6.2.b). An in-house designed and fabricated aluminium element is attached to the inside thread of



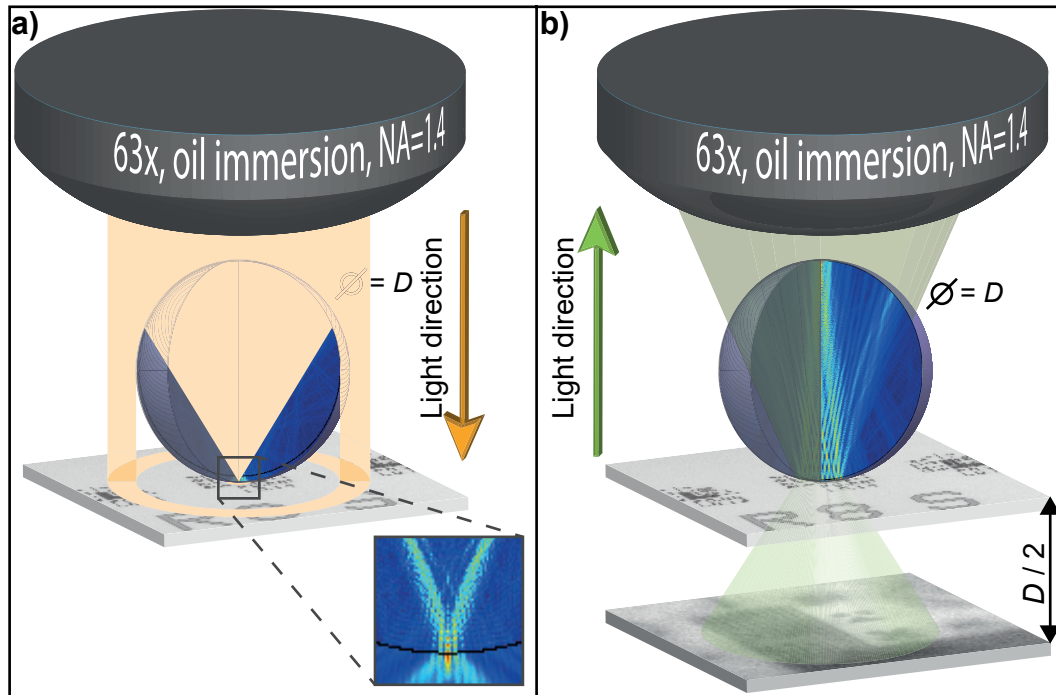


**Figure 6.1** – Operation principle of the improved imaging system. **a)** Excitation: light approaches through the microscope objective towards the dielectric  $\mu S$  with diameter  $D$ . In absence of an object to be imaged in the light path, the dielectric  $\mu S$  generates a *PNJ* on its shadow side, as is shown on the *FEM* simulation of the electric field in the inset. **b)** If an object is present underneath the  $\mu S$ , reflection occurs: the simulation shows reflection from a sample consisting of a modulated pattern of eleven lines and spaces with dimensions below the diffraction limit. The modulation is preserved and the near-field information of the diffraction-limited sample is propagated into the far-field within the  $\mu S$ . At the same time, the  $\mu S$  acts as a lens and generates a virtual image at  $D/2$  distance below the sample plane, as illustrated by the green cone.

the SM1Z translator (Figure 6.2.c), the aim of which is to fix a glass-based  $\mu S$  array chip onto the objective (Figure 6.2.d). The role of the  $z$ -axis translator between the objective revolver and the chip holder is to enable focus adjustment along the  $z$ -axis, as needed for positioning the chip in the right focal plane prior to imaging based on our findings already detailed in chapter 5. The second major component is the  $\mu S$ -array chip that was fabricated as described previously in section 4.4.

The imaged sample was a silicon-based microscope calibration target (MetroBoost, USA), which contained *LSP*-s (made from  $SiO_2$  – PolySi, respectively) with various pitch between 240 - 500 nm. The sample with the chip on top was imaged with an Axio Imager M2m upright optical microscope, equipped with HAL100 halogen light source (both from Carl Zeiss, Germany). A filter cube with a band-pass (524-565 nm) excitation filter and an 80T-20R beam splitter (both from AHE, Germany) was placed in the optical path for the resolution measurements. For the oil-immersion experiments, a 63 $\times$ ,  $NA=1.4$  objective (Carl Zeiss, Germany) was used. The images were captured with an AxioCam MRm (Carl Zeiss, Germany) that had 6.45  $\mu m \times 6.45 \mu m$  pixel size. This resulted in mapping 102 nm of the sample into 1 pixel. For

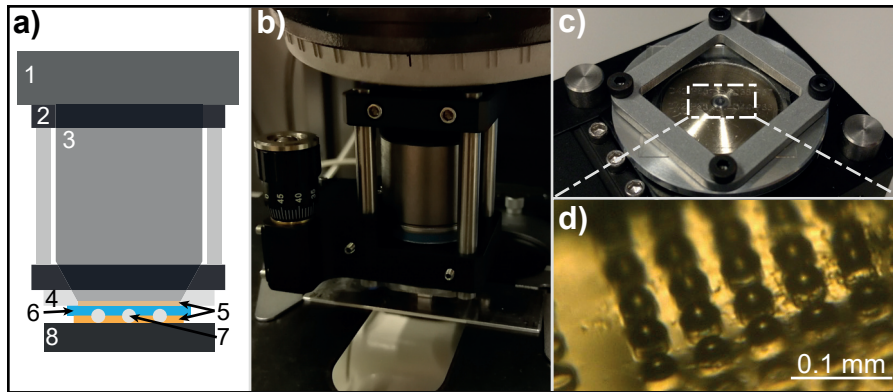


**Figure 6.2** – The improved imaging setup. **a)** Schematic of the optical microscope with our imaging setup attached. 1: Microscope revolver. 2: Optical cage (black) with spacers (metallic rods). 3: Microscope objective. 4: Aluminium adapter. 5: Immersion oil. 6: Chip template. 7: *BTG*  $\mu S$ . 8: Sample to be imaged. **b)** Photograph of the optical cage system and the z-axis translator. **c)** Photograph of the bottom part of the optical cage with a custom aluminium holder attached to the z-axis translator that clamps a glass  $\mu S$  array chip. **d)** Photograph of the fabricated  $\mu S$  array chip, showing that the  $\mu S$ -s emerge from the surface plane of the chip.

the water-immersion experiments, a  $40\times$ ,  $NA=0.75$  objective (Carl Zeiss, Germany) was used in combination with a DMK31BF03.H (TIS, Germany) camera that had  $4.65\ \mu\text{m} \times 4.65\ \mu\text{m}$  pixel size, which resulted in mapping  $116\ \text{nm}$  to 1 pixel. Note that, when present, the *BTG*  $\mu S$  introduces an extra  $\sim 2\times$  magnification to the system.

The microscope was equipped with a motorized microscope stage that was controlled by our in-house written algorithm. The scanning protocol was established as follows: after an initial focus setting along the z-axis, the microscope-attached camera took a picture, when focused on the virtual image plane of the sample. To make a single scanning step, the stage moved  $5\ \mu\text{m}$  downwards along the z-axis to prevent scratching the sample and took one step along either the x- or the y-axis, where the in-plane step-size was set by the user before the scanning. Finally, it moved back to the original z-axis position and was ready for taking the next picture. This scanning process was repeated until the pre-set sample area was fully scanned. Hereafter, the saved pictures were cropped to the *ROI* and subsequently stitched together to create a big *FoV*, super-resolution image. We implemented a stitching algorithm that overlapped the regions in the image that were just outside the *ROI*-s, to keep the useful amount of super-resolution pixels at maximum. To achieve that, we used the fact that the scanning went along a predefined path and that the useful area of a taken photograph was always at the same position, so that its size could be calculated in advance. Because of this, we did not have to use the conventional stitching algorithms, where the edges of the tiles are compared pixel-to-pixel for stitching. During experiments the oil-immersion objective limited the *FoV* to a  $2 \times 2$  array of  $\mu S$ -s, while the water-immersion allowed to observe  $3 \times 3$   $\mu S$ -s simultaneously. Therefore, we had up to four *ROI*-s per picture in the former case and up to nine in the latter one.

### 6.3 Results and discussion

In Figure 6.3.a, one can see a typical image captured from the virtual image plane. Technically, up to four  $\mu S$ -s could fit into the *FoV* of the camera, when the  $63\times$  objective was used. Practically, because of the size distribution of the  $\mu S$ -s and the dependence of the sensitivity of the detection principle on the distance between the sample and the microsphere ( $h$ ), we chose to use two  $\mu S$ -s for easy simultaneous imaging. In the center of the two  $\mu S$ -s (marked with the green dashed circles in Figure 6.3.a) super-resolution imaging is enabled. The yellow and the blue rectangles mark the *ROI* that will be extracted for the final image. During imaging, the  $\mu S$ -s have a fixed position on the pictures, while the sample is scanned (Figure 6.3.b). In Figure 6.3.c a composed image of the sample described in section 6.2 is shown. The calibration target shows L-shaped *LSP*-s with  $L=130$  nm, 140 nm and 150 nm, from the left to right, respectively. The patterns are repeated in every row; therefore, the patterns in row nine (marked as R9 S) are nominally the same as the ones in row eight (marked as R8 S). One can observe the individual tiles that were used for stitching (yellow and blue corresponds to the two  $\mu S$ -s) and

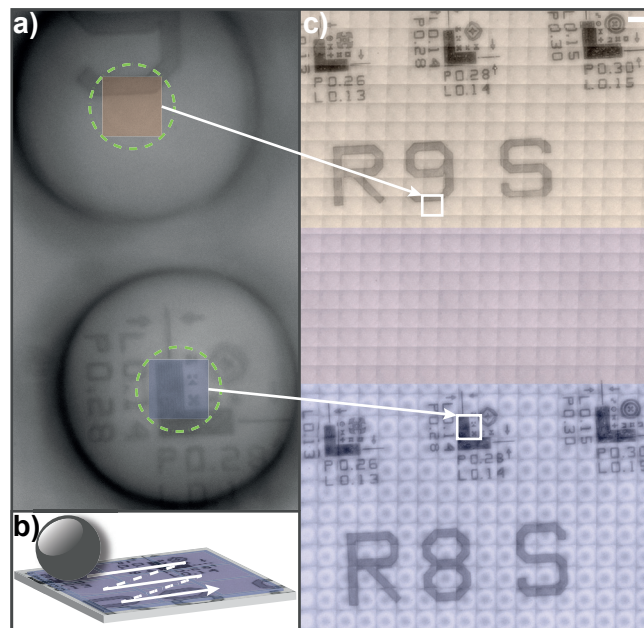


**Figure 6.3** – Demonstration of the  $\mu S$  scanning process. **a)** Two  $\mu S$ -s of the array that are in the *FoV* of the microscope-mounted camera generate virtual images of the sample. The central regions of the  $\mu S$ -generated images (marked with green circles) show super-resolution. At every step of the scanning process, the inside squares (marked with yellow for the first and with blue for the second  $\mu S$ , respectively) are retained for generating the final image. **b)** Schematics of the step-by-step scanning that is carried out using a motorized stage, controlled by an in-house developed scanning algorithm. **c)** Final image at the end of the process. First, individual tiles, two of which are indicated by the white squares, are extracted from the center of the  $\mu S$  images and are stitched together to form a mosaic image. Next, the thus-generated mosaic images of the individual  $\mu S$ -s, indicated by yellow and blue tiles, are combined. Since the pitch of the  $\mu S$  array is smaller than the scanned area, overlap between the yellow tiles from the first  $\mu S$  and blue tiles from the second  $\mu S$  occurs. Scale bar  $5\ \mu\text{m}$ .

the overlap between the two scanned areas. The reason for this overlap is the pre-set scanning parameters, as the step-size was set to  $5\ \mu\text{m}$  along both x- and y-axis, meanwhile the full scanned area was  $100 \times 100\ \mu\text{m}$ . Since the pitch distance of the  $\mu\text{S}$ -s is  $60\ \mu\text{m}$ , this resulted in a  $40\ \mu\text{m}$ -wide overlap area. Based on these results, it is possible to see the two major advantages of implementing scanning with multiple  $\mu\text{S}$ -s. With such a configuration, the scanning time could be reduced or the imaged area could be increased. The gain is proportional to the number of  $\mu\text{S}$ -s used during the process in both cases.

To determine the imaging performance of our system, first, we measured the modulation of *LSP*-s with different lateral dimensions in static imaging mode (*i.e.* without scanning). Figure 6.4.a is a typical example of an image of a  $P=280\ \text{nm}$ ,  $L=140\ \text{nm}$  *LSP*, showing that lines are better resolved towards the center of the  $\mu\text{S}$  and less sharp image is generated for increasing radial distance ( $r$ ). We quantified the imaging performance by measuring the variation of the pixel intensity along the seven dashed lines of a width of  $2\ \mu\text{m}$ , corresponding to 22 pixels. Hereby, we repositioned the *LSP* so that the complete range  $0 < r < 12\ \mu\text{m}$  could be studied. The extracted pixel gray values were normalized, taking as hundred percent the lighter region outside of the line pattern and zero percent the darkest pixel intensity of the micro-patterned structures. The peak-to-valley distances of the thus obtained curves were measured and marked as modulation. The graphs of Figure 6.4.b were constructed by placing *LSP*-s with

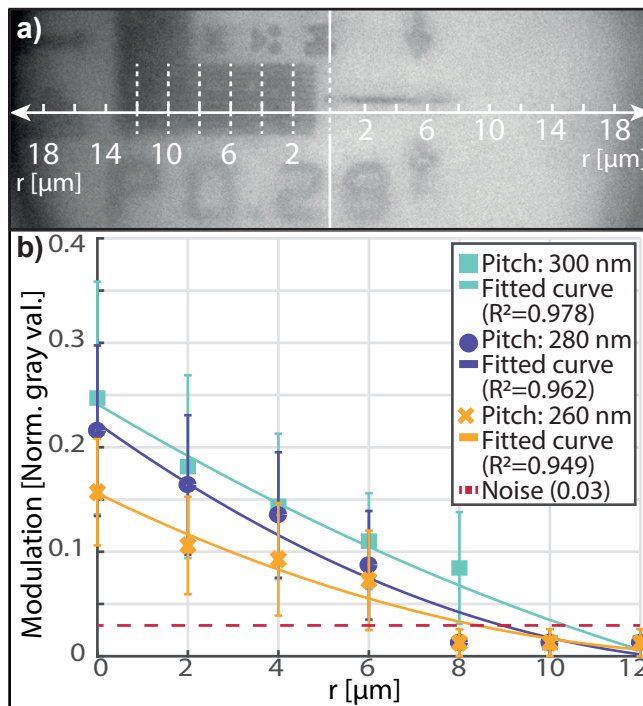


**Figure 6.4** – The dependency of the modulation on the radial distance. **a)** Micrograph of  $P=280\ \text{nm}$ ,  $L=140\ \text{nm}$  *LSP*, as imaged by a  $63\times$  oil-immersion objective through a single  $\mu\text{S}$ , showing that the modulation pattern is best resolved towards the center of the  $\mu\text{S}$  and is attenuated with increasing  $r$ . **b)** Measurement of the modulation as a function of  $r$  in the case of  $P=260\ \text{nm}$ ,  $280\ \text{nm}$  and  $300\ \text{nm}$ , respectively, along the dashed lines indicated in a).

$P=260$  nm, 280 nm and 300 nm, respectively, in the center of a single  $\mu S$ . Seven measurement lines were placed along the horizontal axis (shown on Figure 6.4.a) of the images, starting from the center with 2  $\mu m$  increments. The modulation rapidly decreases as  $h$  increases, in good agreement with our previous findings in chapter 5.

Based on these findings, we imaged various  $LSP$ -s in the  $240 \text{ nm} < P < 400 \text{ nm}$  range, positioned under the center of the  $\mu S$ . After acquisition, the images were stored as 8 bit grayscale pictures. To determine the modulation of the recorded signal, the average intensity values along a 5 pixel-wide line (crossing the  $LSP$ -s) were extracted, as demonstrated earlier in Figure 3.14.b and 3.14.c). The structure of 8 bit grayscale picture is constructed in a way that the value 255 belongs to a fully white pixel, meanwhile 0 marks a totally black one. Because of the material properties of the imaged sample, the background looked bright on the images and the lines were seen dark. Corresponding to that, when plotting the intensity profile, the signal looked like a step from a higher value to a lower one, around which the modulation was observable, followed by a step to the starting level (as shown earlier in Figure 3.14.c). The modulated region was analysed by detecting peaks and valleys and calculating all amplitudes ( $a$ ) from these values. Because of the structure of the sample, this meant 9-11 values (one per line), from which we calculated  $a' = \text{median}(\underline{a})$  and  $a'_{error} = \text{MAD}(\underline{a})$ , where  $\underline{a}$  is the vector of the amplitude values. Then the step ( $s$ ) was measured. Subsequently, the modulation ( $M$ ) was calculated as:

$$M = \frac{I_{max} - I_{min}}{I_{max} + I_{min}} = \frac{a'}{2s - a'} \quad (6.1)$$

To guarantee the same normalization of the modulation values as the theoretical  $MTF$ , which is always normalized at unity at zero spatial frequency, another area of the sample was imaged, where the same two materials had a common border but without any modulation pattern (*i.e.* with a null spatial frequency=0). This showed how the imaging system could map the maximum observable modulation ( $M_0$ ). From this measurement,  $M_0$  was calculated as:

$$M_0 = \frac{step - baseline}{step + baseline} \quad (6.2)$$

where *step* was the average grey value over 10 pixel in the  $SiO_2$  (to measure maximum dark value) and *baseline* was the same in PolySi (to measure maximum bright value). The final normalized modulation ( $M'$ ) that is shown in Figure 6.5 was derived as  $M' = M / M_0$ . The noise level modulation was calculated by applying the same methodology in 24 uniform regions (*i.e.* without the presence of any microstructured edge) for each immersion type, then averaged and normalized. Figures 6.5.a and 6.5.b show the results for oil- and water-immersion, respectively. The solid lines in the figures represent the theoretical  $MTF$  for  $\lambda=545$  nm, obtained from Figure 3.14.a, with the shaded bands marking the bandwidth ( $\pm 20$  nm) of the experimentally applied band-pass filter. The measured data points show excellent correspondence with the theoretically calculated values, which validates our model, already detailed in section 3.2. Results also confirm the resolution gain provided by the  $\mu S$ , with which our system could outperform the resolution of the standalone microscope objective in all measured cases.

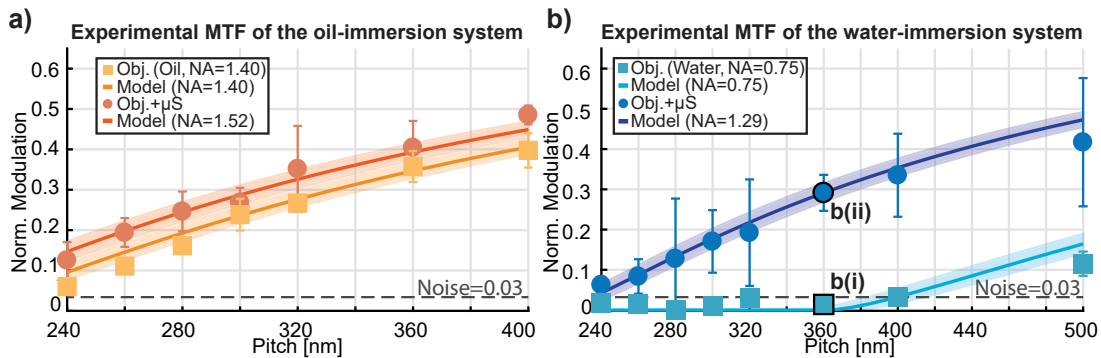


**Figure 6.5** – Resolution analysis of the oil- and the water-immersion system in static imaging mode. **a), b)** Experimental *MTF* for oil- and water-immersion, respectively, measured on Si-based *LSP-s* of several pitches. Data are shown as median  $\pm$  *MAD*. The solid lines with the shaded bands show the theoretical *MTF* for  $\lambda=545\pm 20$ nm, which corresponds to the band-pass filter of the microscope system. The dashed line marks the measured noise level of the imaging system.

To benchmark the performance of our microscopy method in dynamic imaging mode (*i.e.* with scanning and image reconstruction), we compared the composed picture to the image that was taken by the microscope camera without using a  $\mu S$  (Figure 6.6). In Figure 6.6.a, we see the *LSP-s* of row nine from the sample of Figure 6.3 in the upper part, and the *LSP-s* of row eight in the lower part. The white dashed rectangle shows a single *FoV* of the microscope mounted camera. To be able to make fair comparison with our composed image, we took two photographs from the microscope and stitched them together. In the insets, enlarged images of the *LSP-s* are shown, clearly indicating that the microscope cannot resolve features below the diffraction limit. To further support this statement, we drew five pixel-wide measurement lines on the taken photographs (blue lines correspond to patterns of row nine, while orange lines correspond to patterns of row eight), on which we evaluated the pixel gray values. We positioned these lines on exactly the same spot for every pattern, except for the 150 nm wide lines where they are shifted up by a few microns, because of a damaged region in the pattern of row eight. To exclude the shift caused by eventual different brightness of the light source, we normalized all pixel gray values, resulting in a modulation pattern as discussed already in Figure 6.4. One can observe that the down-pointing peaks are distinguishable on the most right side plot (evaluating the 150 nm wide lines), but that they disappear as the line width is decreased to 140 nm (center plot) and finally to 130 nm (left side plot).

In Figure 6.6.b we show the image of the same area, but in this case, the picture was created with our  $\mu S$  array. We applied yellow and blue colors on the picture to show which part of it was created by the first and which by the second  $\mu S$  in our array. The insets show enlarged stitched images of the *LSP-s*, with markings of the positions of our measurement lines. Just by eye observation, it is already clear that the lines, independently of their size, are more visible than in Figure 6.6.a. For evaluating the gray values along the measurement lines, we used the same method as described in the previous paragraph. On the plots in the center of Figure 6.6.b, one can observe that the peaks corresponding to the black lines on the sample are sharper and that the modulation amplitude is bigger. It is important to note, that the modulation did

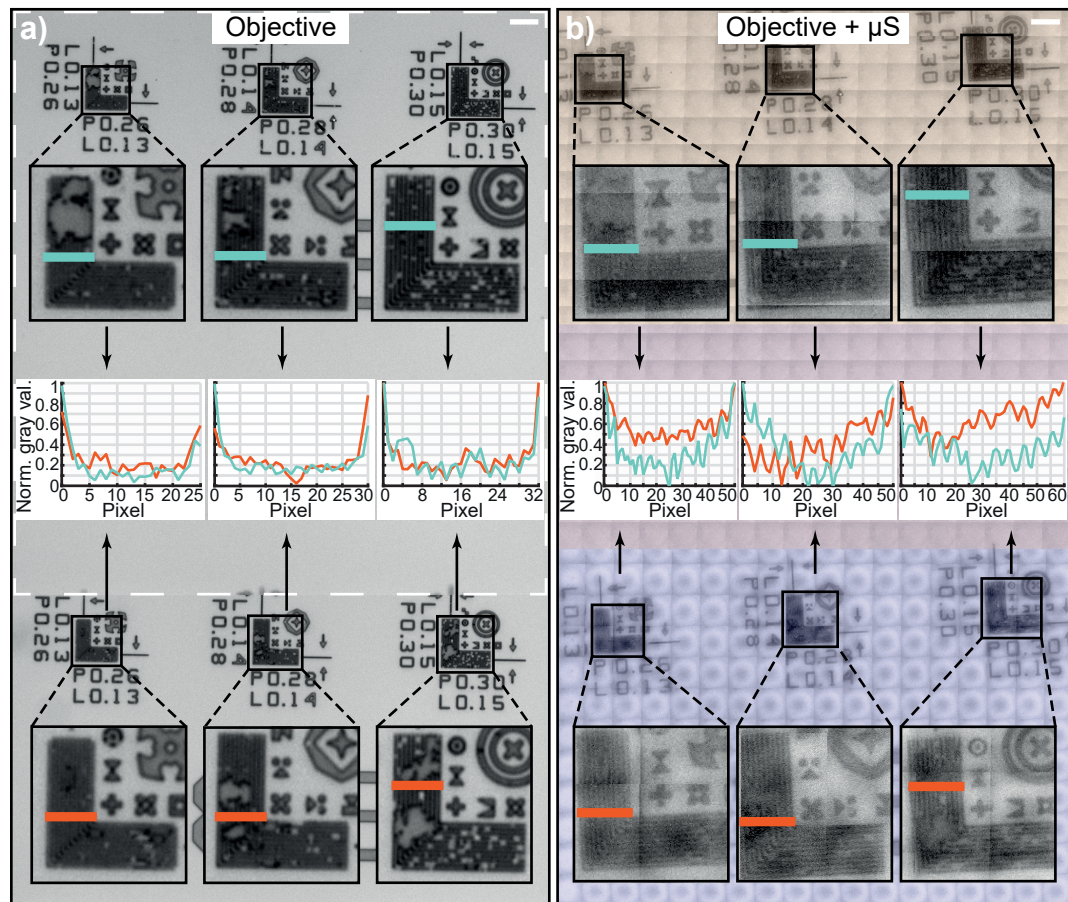


**Figure 6.6** – Resolution analysis of the oil-immersion imaging in dynamic mode. **a)** Picture of the sample taken via the 63 $\times$  oil-immersion microscope objective without use of the  $\mu S$  array. Since the *FoV* of the camera is smaller than the demonstrated scanned surface of the sample, two pictures were stitched together, one being marked by a white dashed rectangle. Nanostructures within the upper *FoV* are identical to the ones in the lower *FoV*, and are composed of  $L=130$  nm, 140 nm, and 150 nm *LSP*-s from the left to the right, respectively. Black squares are zooms on these patterns. The optical signals are evaluated along the five pixel-wide horizontal lines (blue for the upper part and orange for the lower part) and plotted in the center as normalized gray values (a black pixel generating zero signal and a white pixel generating signal one). One can observe that the  $L=150$  nm *LSP* is resolvable; meanwhile no modulation is observed for the *LSP*-s with  $L=130$  nm and 140 nm. **b)** Picture of the same sample as in a) and Figure 6.3.c, taken via the same microscope objective using the  $\mu S$  array. Yellow colored tiles were recorded by the first  $\mu S$ , and blue ones by the second  $\mu S$ . Insets show zooms on the recorded modulation patterns. Optical signals are evaluated along the same five pixel-wide lines as in a). Modulation plots in the center are generated with the same method as in a), showing that all *LSP*-s are resolvable. Scale bars 5  $\mu\text{m}$ .

not change significantly between the biggest ( $P=300$  nm) and the smallest ( $P=260$  nm) pitch, *i.e.* our imaging system could well resolve down to 260 nm in dynamic mode, using a halogen light source without filtering.

Finally, to demonstrate the robustness and full possibility of our imaging technique, we

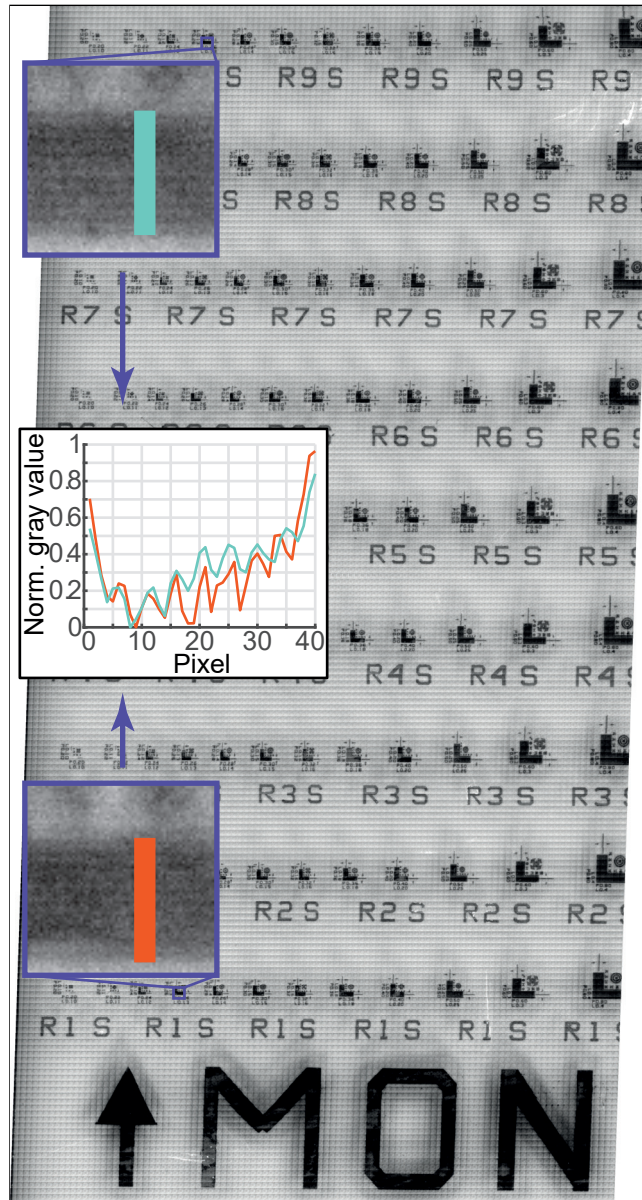


**Figure 6.7** – Demonstration of large area imaging with super-resolution. The sample area shown here is  $0.5 \text{ mm} \times 1.0 \text{ mm}$ . It was reconstructed from 20 301 individual pictures and its original file consists of  $\sim 175$  MPixels. Insets show that  $P=260 \text{ nm}$ ,  $L=130 \text{ nm}$  LSP-s remained resolvable over the whole scanned area.

show in Figure 6.7 a super-resolution imaging corresponding to a large surface area ( $0.5 \text{ mm} \times 1.0 \text{ mm}$ ). During scanning, 20 301 individual pictures were collected using our custom algorithm, resulting in  $\sim 60$  GB of raw data. Our stitching algorithm composed the final image that had  $\sim 175$  MPixel and  $\sim 530$  MB file size. One can observe that due to the shear stress generated during the scanning, a slight systematic tilt occurred on the picture, which was corrected by our image reconstruction algorithm. The shadow effect at the edge of the tiles



could not be compensated by our algorithm, therefore the quality of the stitching could be improved, *e.g.* by using seamless stitching in ImageJ, but it is important to note, that our solution completed the stitching  $\sim 100\times$  faster than the ImageJ algorithm. As the insets in Figure 6.7 show, the 260 nm lateral resolution was preserved over the total area of the scanned surface.

In this chapter, we demonstrated an advanced implementation of an optical microscopy super-resolution imaging technique, using an ordered array of dielectric  $\mu S$ -s. The imaging principle was explained to be related to the existence of a *PNJ* upon illumination of a  $\mu S$  (section 3.1) and the near-field interactions between the sample and the  $\mu S$  (section 3.2). We showed that it is possible to overcome the *FoV* limitations of previously published  $\mu S$ -based super-resolution imaging techniques by implementing a scanning and stitching process. Our simple but smart system achieved a  $P=240$  nm lateral resolution in static mode. Furthermore, in dynamic mode,  $P=260$  nm and simultaneously a much bigger total *FoV* than the one of the microscope-mounted camera was demonstrated. To show the robustness of the system, a surface scan of  $5 \times 10^5 \mu\text{m}^2$  was presented. However, we believe that even bigger areas can be imaged, since there are no intrinsic limits in our process. Later, the scanning system could eventually be optimized for mass production with the help of 3D printing, as this technique enables very flexible microfabrication of customized parts, as was shown earlier [146]. We therefore hope that our findings will help repositioning dielectric  $\mu S$ -based optical super-resolution microscopy beyond the proof-of-concept stage towards a fully operational real-life application.



## 7 Conclusion and outlook

In this dissertation, a novel super-resolution microscopy method was shown. The basis of this imaging system was micrometer-sized dielectric  $\mu S$ -s placed in the light path. These high  $RI$  objects modified the behaviour of the optical system and therefore enabled super-resolution. The phenomena governing the super-resolution imaging were investigated for both smaller and bigger than  $20\ \mu\text{m}$  diameter  $\mu S$ -s in chapter 3. It was found that the formation of the  $PNJ$  created by a  $\mu S$  significantly contributes to the super-resolving power of the imaging system for small diameter  $\mu S$ -s, while in the case of bigger diameter  $\mu S$ -s the near-field interactions between the sample and the  $\mu S$  play an important role. From these findings, the main influencing factors could have been extracted, therefore it was shown that the material and the diameter of the  $\mu S$  as well as the optical contrast (*i.e.* the ratio between the refractive index of the microsphere and the refractive index of the medium) are the key parameters that determine the performance of the  $\mu S$ -based super-resolution microscope. Parallel to this study, microfabrication techniques were explored as shown in chapter 4, in order to fabricate first a "zero-dimensional", then a  $2D$  ordered array of  $\mu S$ -s. The main challenge here laid in finding the balance between robustness of the chip containing these  $\mu S$ -s and the thickness of it, which was limited by the working distance of the microscope objective. Furthermore, two different techniques were presented that can facilitate the patterning of many  $\mu S$ -s into the template array in a simple but effective way by utilizing self-assembly methods. Based on these results, two types of chips were successfully fabricated. The first type was a wafer-level-made glass-silicon composite structure that was very robust but could only work with longer working distance objectives, while the second type had a cost-effective but smart design originating from a chip-level fabrication process that also allowed the final thickness of the chip to remain below  $190\ \mu\text{m}$ .

In the second part of this work, two microscopy systems were presented. The first generation, proof-of-concept device was shown in chapter 5. There, a single  $\mu S$  was fixed in the center of the  $FoV$  of a microscope objective via a metal cage. This attachment allowed to observe the sample with super-resolution, however, only in a limited part of the original  $FoV$ . To overcome this issue, a scanning and image reconstructing algorithm was implemented utilizing a motorized microscope stage. This way, the imaged area of the sample could be increased and finally,

## Chapter 7. Conclusion and outlook

a single, big *FoV* super-resolution image could be constructed. Later, this system was revised and upgraded as described in chapter 6. A new chip fabrication process allowed to create an ordered array of dielectric  $\mu S$ -s, which were later used for the imaging. This process consisted of standardized steps from which the artisanal manipulations were minimized compared to the previously introduced method, therefore we could increase the repeatability of the fabrication. A new design of the cage system was presented that allowed more stable contact between the chip and the optical microscope, which resulted in a great increase in the imaged sample surface area. Measurements on *in silico LSP*-s showed that this imaging system improved the resolution up to 20% and up to 40% for oil- and water-immersion, respectively, compared to the performance of the microscope objectives without the  $\mu S$ -s. Moreover, it increased the *FoV*  $\sim 1000$  times, compared to imaging methods, where static  $\mu S$ -s are employed. Based on the demonstrated results, this dissertation can be the basis of a future generalized *SRM* system that is easy-to-use and cost-effective. The first property is guaranteed by the high level of automation, enabled by the computer control of the image scanning and reconstruction, while the simple fabrication process and the possibility of implementing high throughput fabrication (*e.g.* 3D printing) ensure the second one.

Future developments of the system are envisioned both on the technical and on the application side. The optimization of the system for scanning with an array of  $\mu S$ -s could be done by adjusting the control algorithm, for which two ideas are provided in Figure 7.1. First, the scanning path could be modified to follow a meander-like pattern instead of the currently used zig-zag one. This would reduce the shear-stress between the sample and the  $\mu S$ -s and therefore eliminate the horizontal tilt present in Figure 6.7. The second idea aims to optimize the imaging process by reducing the scanning time. A possible way to do this, is to eliminate the overlap between imaged surface areas that were presented in Figure 6.3. For this, the scan

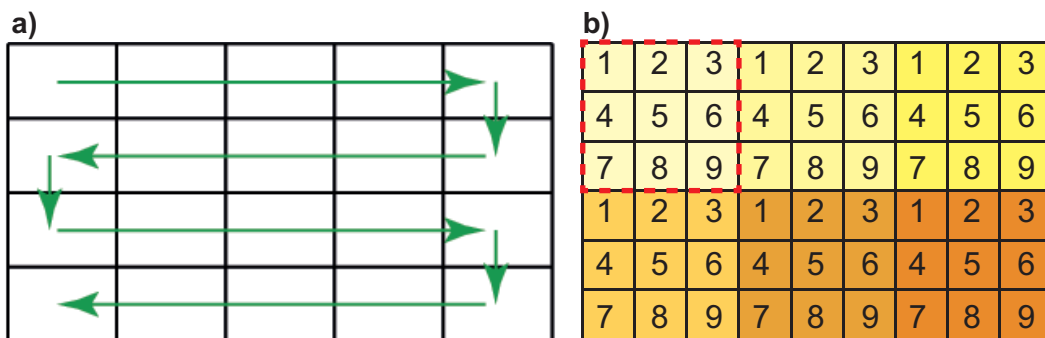


**Figure 7.1** – Future development plan of the scanning process. **a)** A meander-like scanning path can be introduced instead of the currently used zig-zag method in order to reduce shear stress between the sample and the  $\mu S$  array. **b)** Introduction of the *scan-cell*. When scanning with a  $3 \times 3$   $\mu S$  array, consisting  $\mu S$ -s from 1-9, the scan process stops when the pitch distance between the members of the array is reached in both x- and y-direction. The area mapped so far by the individual  $\mu S$ -s is composed from the yellow squares with numbers 1-9 and marked with red-dashed border. This is a single *scan-cell*. Then the array is moved over to a neighbouring sample area that was not imaged by any of the members of the array (area with darker tone of yellow). This is repeated until all of the surface area is imaged (all six tones on the graph).

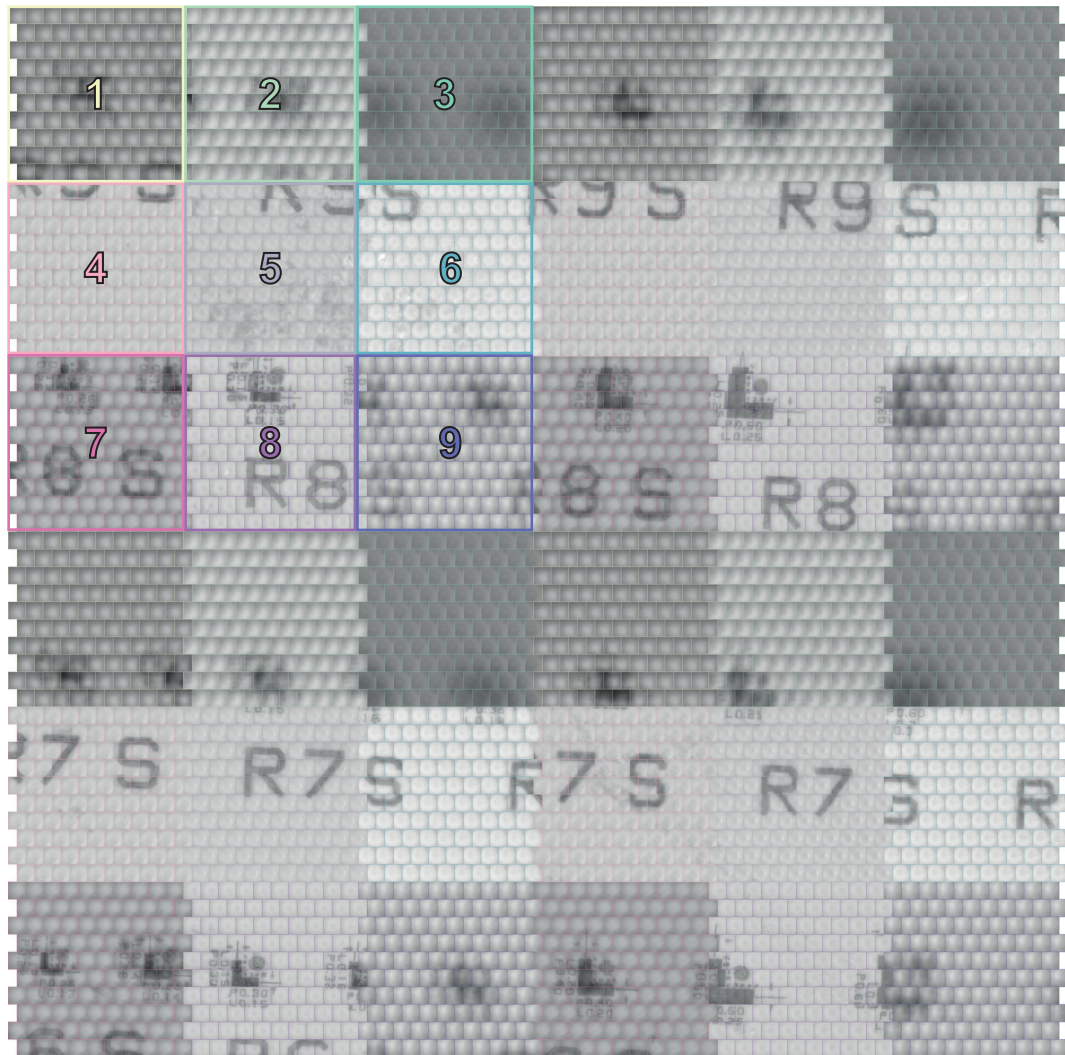


**Figure 7.2** – Demonstration of the new scanning technique. A  $3 \times 3$  array of  $\mu S$ -s (# 1-9) were scanned over a  $360 \mu\text{m} \times 360 \mu\text{m}$  surface area, forming  $2 \times 2$  *scan-cells*. One cell provides image over a  $180 \mu\text{m} \times 180 \mu\text{m}$  area. Each tile contributes with  $6 \mu\text{m} \times 6 \mu\text{m}$  imaged area and the ones with the same border color were produced by the same  $\mu S$ .

should stop once the pitch distance between the members of the array is reached in both x- and y-direction. The area that was covered during these steps can be called *scan-cell*. Then the array should move to a neighbouring area that was not scanned by any members of it, and start to image the next *scan-cell*. This can be repeated until the desired sample surface area is fully scanned. To enable this imaging mode, not just the scanning, but also the image reconstruction algorithm must be revised.

Initial experiments with  $D=40 \mu\text{m}$  BTG  $\mu S$ -s in water-immersion, using the same sample as in chapter 5 and 6 already showed that this method can be implemented successfully (Figure 7.2). However, they already raised new issues that have to be solved during the following development stage. Presented results show that from the  $3 \times 3$  array, not all  $\mu S$ -s could contribute

## Chapter 7. Conclusion and outlook

---

equally to the final image, as number 1-3 and 9 were out of focus. This might be caused by the non-uniformity of  $D$  or a fabrication error, when the  $\mu S$ -s were not correctly positioned in the template. The tilt presented in Figure 6.7 disappeared as anticipated, but another stress-related error occurred. However, this could be corrected already by the current version of our image reconstruction software.

On the application side, the potential circle of samples was increased by the improved setup, because imaging became possible in both oil- and water-immersion. The latter might raise a particular interest in the field of life sciences, as this is typically a crucial criteria in order to image *in vivo* samples. Our preliminary study showed that indeed, it is possible to image such samples both in fluorescent and bright-field mode, as we present in Figure 7.3. In Figure 7.3.a we show green fluorescent protein (*GFP*) expressing *E. coli* bacteria in water-immersion imaging, where the  $\mu S$ -generated magnified image made the individual bacteria visible. As we took photographs of the virtual image plane, only the areas below the  $\mu S$ -s show sharp pictures (marked by yellow dashed circles). In Figure 7.3.b, a *C. elegans* embryo was placed in a template (marked by yellow arrow), to fix its position and then it was observed through a  $\mu S$ . An enlarged image of a detail of the embryo became visible, potentially enabling the observation of special features of this specimen. To observe the whole embryo at once, imaging in dynamic mode would have been needed, however, at the current stage of development that was not available. The sole aim of these experiments was merely to illustrate the potential applications of our  $\mu S$ -based *SRM* system that eventually may become a widely available, simple microscope add-on, serving many researchers in the future.

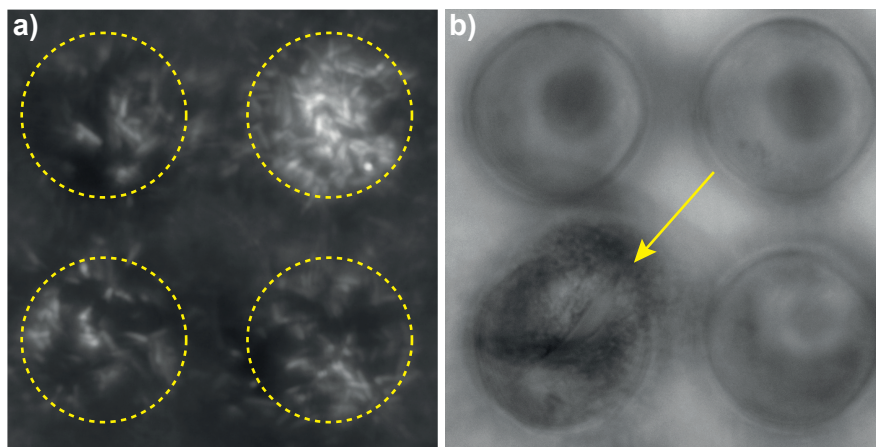


**Figure 7.3** – Demonstration of *in vivo* imaging. **a)** Fluorescent image of *GFP*-expressing *E. coli* bacteria through a  $2 \times 2$  array of  $D=40 \mu\text{m}$  *BTG*  $\mu S$ -s in water-immersion. Enlarged images can be observed simultaneously through all  $\mu S$ -s. Yellow dashed lines are guide to the eye. **b)** Bright-field photograph of a *C. elegans* embryo through a similar chip than in a). The embryo is located in the bottom left template position, marked by the yellow arrow.

# A Appendix

## A.1 Supplementary data for section 3.1

### Generation of the photonic nanojet

A *FEM* study of the electromagnetic wave propagation through a  $D=6\ \mu\text{m}$   $\mu\text{S}$  in water medium is shown in Figure A.1.1. For comparison, a light source with length half of  $D$  was placed on the left or right side of the  $\mu\text{S}$ , but far away from the front-surface of the  $\mu\text{S}$ . Most illumination light was refracted on the front-surface and refracted again when exiting from the rear-surface of the  $\mu\text{S}$ . Light sources placed above the left half (Figure A.1.1.a) and above the right half of the  $\mu\text{S}$  (Figure A.1.1.b), respectively, showed mirrored light intensity distributions. When a full light source, *i.e.* having the same width as the  $\mu\text{S}$ , was applied (Figures A.1.1.c and A.1.1.d), the wave-vector components  $k_{\parallel}$  originating from the left and right part locally eliminated each other by destructive interference, resulting in a *PNJ* that could maintain a highly confined transverse beam width and a *FWHM* that can be sub-wavelength. At the same time, the wave-vector components  $k_{\perp}$  were superimposed and the *PNJ* could extend more than  $\sim 2\lambda$  beyond the  $\mu\text{S}$  along the wave propagation direction. Therefore, the *PNJ* is a direct result of interference effects of the optical fields.

### Comparison between incoherent and coherent light source in the *FEM* study

In order to evaluate the influence of using an incoherent illumination source or a coherent light source for the numerical analysis results, we performed a *FEM* study on 11 models with light source at different positions to mimic the incoherent illumination. In these models, the  $D=6\ \mu\text{m}$   $\mu\text{S}$  was immersed in water, and an electromagnetic wave with wavelength of  $\lambda=600\ \text{nm}$  was applied on a boundary far away from the top-surface of the  $\mu\text{S}$ . The boundary in these 11 models was placed on a position with distance to the  $\mu\text{S}$ 's top-surface varying over a region  $(-\lambda/2, \lambda/2)$ . The boundary in the model shown in Figure 3.2.a in the manuscript was set as the original place on the vertical axis, *i.e.*  $y_0 = 0$ . Assuming that the distance between the boundary in the other 10 models and the one in Figure 3.2.a is  $\Delta y = y_n - y_0$ , where  $y_0$  is the

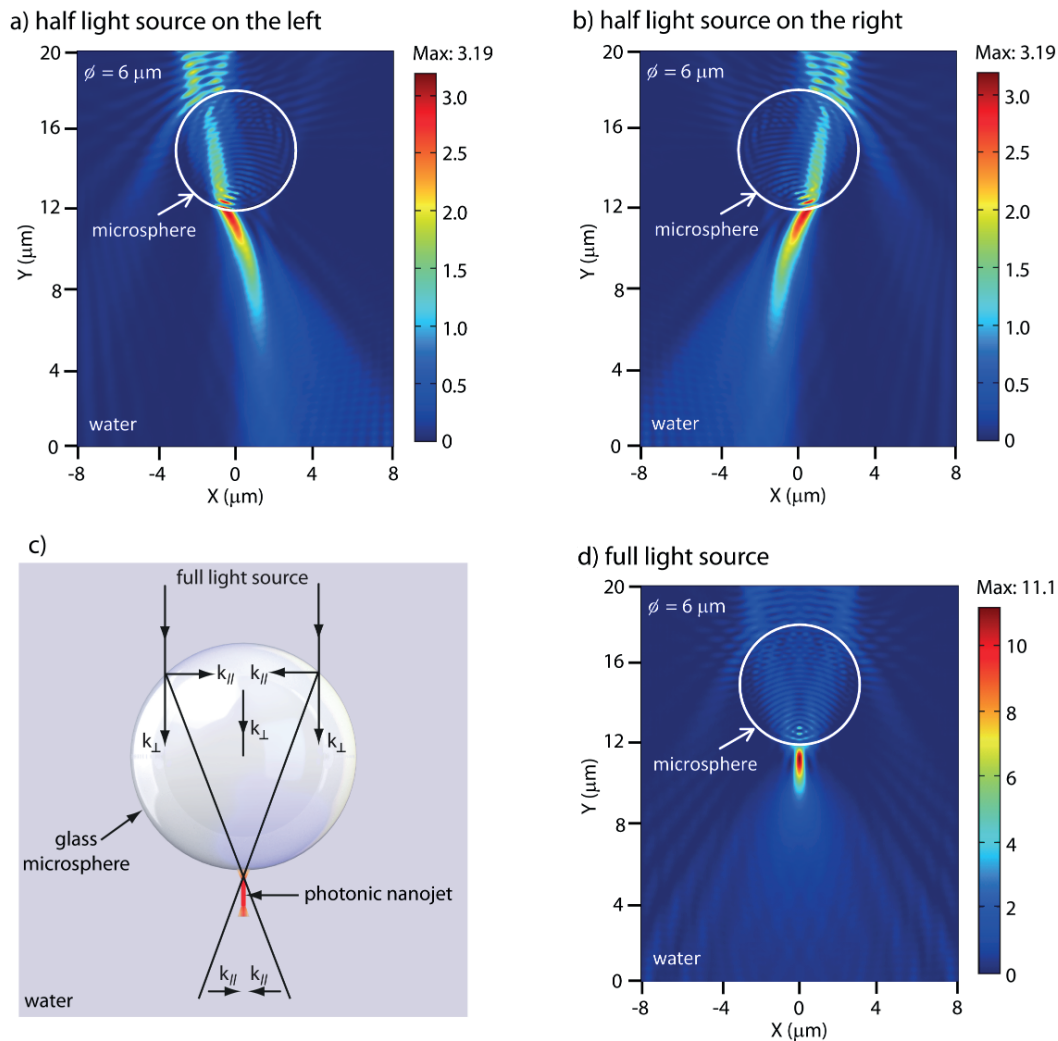


**Figure A.1.1** – Numerical study on *PNJ* generation. **a), b)** *FEM* simulation of the light propagation through a  $D=6 \mu\text{m}$  *BTG*  $\mu\text{S}$  in water. A light source with  $D/2$  width is placed on the left side a) and the right side b) of the  $\mu\text{S}$  but far away from its front-surface. **c)** Concept of the *PNJ* generation. When the  $\mu\text{S}$  is illuminated by a full light source, the left and right wave-vectors  $k_{||}$  are cancelling each other, while the  $k_{\perp}$  wave vectors are superimposed. Interference of the optical fields therefore can generate the *PNJ* with confined transverse beam width and extended longitudinal beam length. **d)** Same as a) and b) with a light source having the same width as  $D$ . A *PNJ* with sub-diffractive transverse beam width is generated indeed near the rear-surface of the  $\mu\text{S}$ .

reference position in the initial simulations shown in Figure 3.2 and  $y_n$  is the new reference position on the y-axis used in these phase shift simulations so that  $\Delta y = -31\lambda/64, -7\lambda/16, -\lambda/4, -3\lambda/32, -1\lambda/32, +\lambda/16, +5\lambda/32, +11\lambda/32, +15\lambda/32, +\lambda/2$ . These position shifts introduced a phase shift.

After all the 11 models were solved, the light intensity distributions obtained from each model were superimposed, and a figure indicating the *PNJ* under an incoherent-like illumination is therefore obtained, as shown in Figure A.1.2.a. As a comparison, the *FEM* simulation with



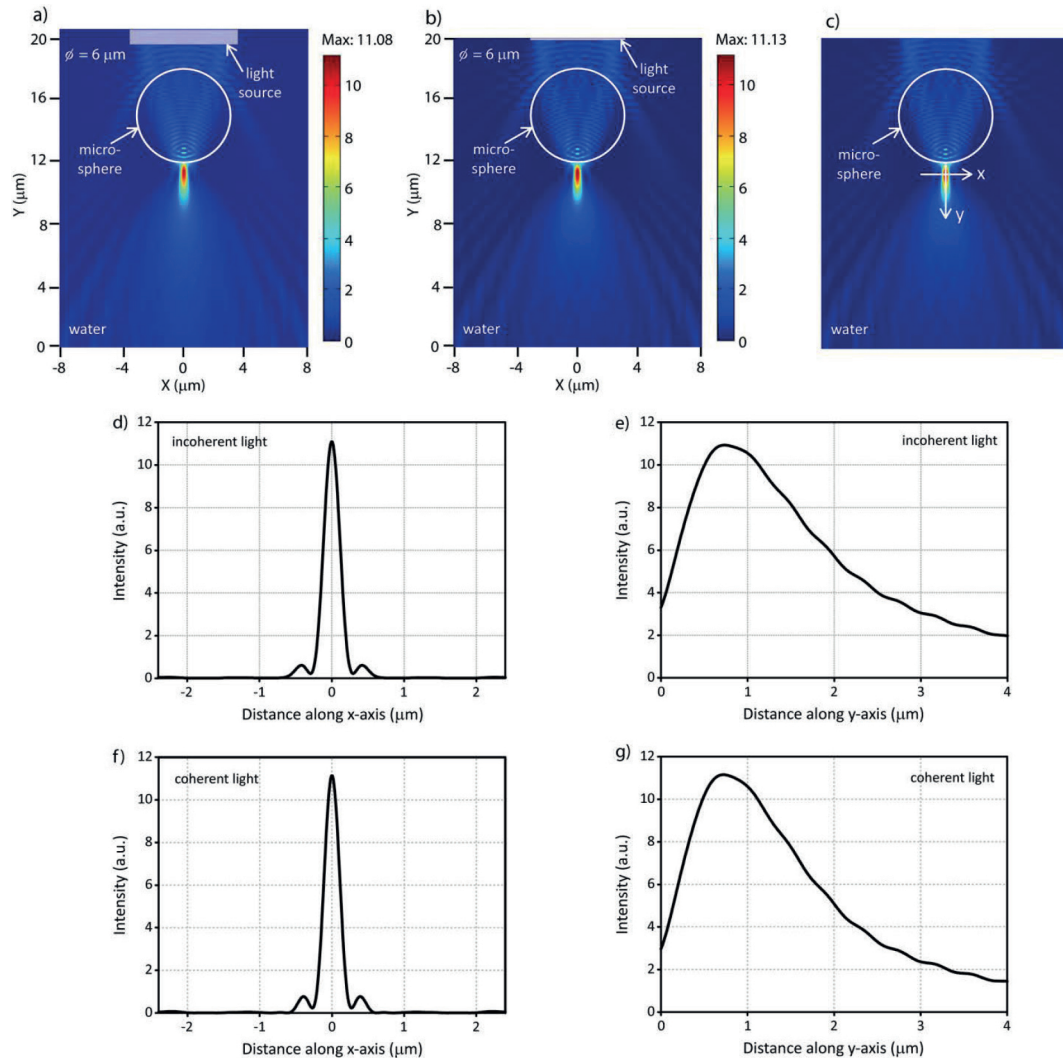


**Figure A.1.2** – Comparison of the *PNJ*-s generated by coherent and incoherent light sources. The light intensity distribution was simulated with the help of a *FEM* study in the vicinity of a  $D=6\ \mu\text{m}$   $\mu\text{S}$  that was placed in water and illuminated from the top. **a)** Simulation result obtained by superimposing 11 models with light sources at different positions along the vertical axis. The *PNJ* can be thought of as being generated under incoherent illumination. **b)** The model with a single light source, showing the *PNJ* generated by coherent illumination. **c)** Illustration of the coordinate system used to plot the intensity profiles. The x-axis is along the cross-section of the *PNJ* waist and its origin is located on the point with maximum intensity in the *PNJ*; the y-axis is along the vertical direction and its origin is located on the bottom surface of the  $\mu\text{S}$  where  $x=0$ . **d)**, **e)** The light distribution of the *PNJ*, as illuminated by an incoherent light source, along the x-axis **d)** and along the y-axis **e)**. **f)**, **g)** The light intensity profile of the *PNJ*, as illuminated by a coherent light source along the x-axis **f)** and along the y-axis **g)**.

a coherent illumination source is shown in Figure A.1.2.b. In Figure A.1.2.a, the intensity scale bar showing the light intensity was obtained by averaging the values from the 11 solved models. Moreover, we further compared the intensity distribution along the lateral and vertical direction of the *PNJ* in Figure A.1.2.a and A.1.2.b. As indicated in Figure A.1.2.c, the lateral

intensity distribution was obtained along the x-axis and its origin was put on the point with maximum intensity in the *PNJ*; the vertical intensity profile was plotted along the y-direction where  $x = 0$ , and the origin is at the bottom-surface of the  $\mu S$ . Figures A.1.2.d and A.1.2.e show the lateral and vertical intensity profiles that were obtained from the incoherent illumination source and Figures A.1.2.f and A.1.2.g show the profiles obtained from the coherent source. As illustrated in Figure A.1.2.d and A.1.2.f, the intensity profile along the *PNJ* waist did not significantly change when using an incoherent or a coherent light source in the *FEM* study, indicating that our simulation method can provide sufficient information to compare with the *PSF* obtained from the experimental results. Comparing Figure A.1.2.e and A.1.2.g, the intensity of the *PNJ* decays faster along the vertical axis under coherent light, this result however did not affect the resolution of the imaging system.

### Conversion of a near-field evanescent wave into a far-field propagating wave

From the Maxwell's equations, the wave vector equation for the light propagation in a  $\mu S$  with refractive index  $n_{sphere}$  can be expressed as it is shown in Equation 5.1. When the  $\mu S$  is simply used as a solid immersion lens, *i.e.* neglecting the eventual development of the *PNJ*, for an appropriate size and *RI* contrast, the resolution defined by the classical Abbe's diffraction limit is:

$$\Delta_{x-y} \approx \frac{\pi}{\sqrt{k_x^2 + k_y^2 + k_z^2}} = \frac{\lambda}{2n_{sphere}} \quad (\text{A.1.1})$$

Equation A.1.1 provides  $\lambda/3.8$  for a *BTG*  $\mu S$ , which indicates that the diffraction limit is lower in a medium with high *RI*. This was confirmed by our experimental study, as  $\sim\lambda/1.8 - \lambda/3.2$  was obtained for  $400 \text{ nm} < \lambda < 700 \text{ nm}$  (resolution of the microscope objective alone was  $\lambda/1.6$ ). The comparison of Equation A.1.1 suggests the origin of super-resolution: (i) the  $\mu S$  first acts as a solid immersion lens and provides local enhancement of the *RI* and a reduction of the effective wavelength, and (ii) the *PNJ*-related optical path, by which the near-field evanescent waves that carry the fine details of the sample are rapidly transformed into far-field propagating waves, the latter being easily collectable by the microscope.

### Effect of phase shift on Gaussian fittings

As the *PNJ* arises from wave interferences, both the phase and intensity of the signal should be considered. Here, and as described above, a family of simulated intensity profiles, where the light source is placed at different position along the y-axis, was obtained for a  $D=6 \mu\text{m}$   $\mu S$  (Figure A.1.3). The intensity profiles at the waist along x of these illumination patterns describing the *PNJ* profiles were obtained. Note that the vertical shifts  $\Delta y$  were chosen to minimize the risk of phase synchronization between the different simulations by ensuring that most of the  $\Delta y$  are not multiples of each other. From these profiles, it appears that the phase shift has little to no effect on the intensity profile at the waist.

In an attempt to quantify these variations, these curves were fit with a one-dimensional Gaussian function  $G$

$$G(x) = \alpha_G \exp\left(-\frac{x^2}{2\sigma^2}\right) \quad (\text{A.1.2})$$

where  $\alpha_G$  is a fitting constant. The validity of the Gaussian fitting is discussed below. As detailed in the main manuscript, the value of interest is the standard deviation  $\sigma$  which characterizes the quality of the image (labeled  $\sigma_{ill}$  for the illumination profile or  $PNJ$  profile considered here) and is proportional to the lateral resolution of the imaging system. The computed values for  $\sigma_{ill}$  for all the simulated  $PNJ$  profiles, as well as the approximation of an incoherent light source described earlier, are reported in Table A.1.1. As shown from these data, the variation of  $\sigma_{ill}$  is below the smallest mesh dimension ( $\sim 22$  nm) and can be considered as phase shift-independent. Furthermore, for all the cases considered, the Gaussian fitting was in good agreement with the simulated curves, as shown by the high coefficient of determination  $R^2$ .

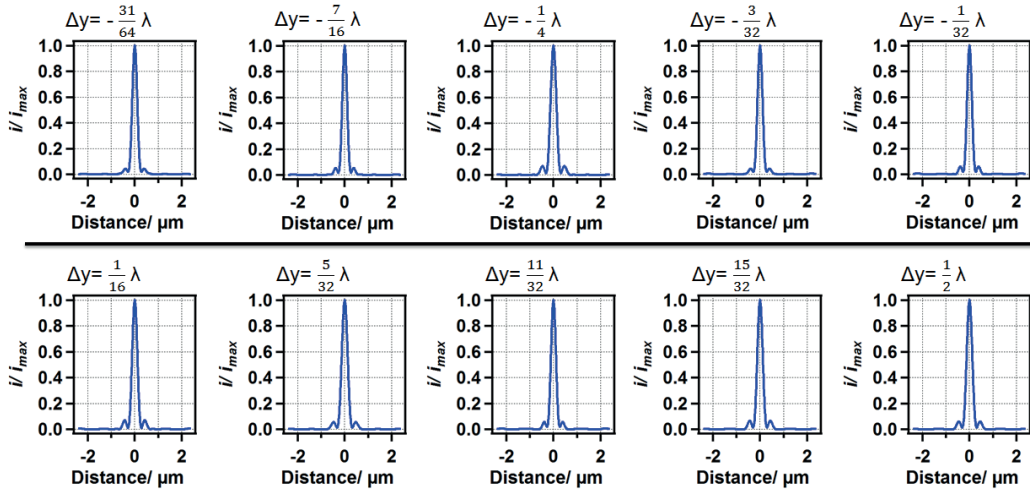


**Figure A.1.3** – Simulated intensity profiles at the waist of the  $PNJ$ , along the  $x$ -axis, for a  $D=6\ \mu\text{m}$   $\mu\text{S}$  and various  $\Delta y$ .

### Gaussian fittings against Airy patterns

Gaussian fittings are often used to simplify the  $PSF$ , especially in the  $xy$ -plane. Other functions can be suggested, such as the Airy pattern. This profile ( $A$ ) is generated by a wave diffracted through a circular aperture and has the following expression

$$A(x) = \beta \left( \frac{2J_1(\gamma x)}{x} \right)^2 \quad (\text{A.1.3})$$

where  $\beta$  and  $\gamma$  are constants and  $J_1$  is the Bessel function of the 1<sup>st</sup> kind of order 1. The  $PNJ$  profiles obtained from the simulations shown in Figure 3.2, for  $\mu\text{S}$ -s of different

## Appendix A. Appendix

**Table A.1.1** – Computed values for  $\sigma_{i||}$  obtained from the Gaussian fitting of the profiles shown in Figure A.1.3, with the coefficient of determination  $R^2$ . The results for the simulated incoherent light described earlier are shown in the column 'Sum'.

	$\Delta y = -\frac{31}{64}\lambda$	$\Delta y = -\frac{7}{16}\lambda$	$\Delta y = -\frac{1}{4}\lambda$	$\Delta y = -\frac{3}{32}\lambda$	$\Delta y = -\frac{1}{32}\lambda$	$\Delta y = 0$	
$\sigma_{i  } / \text{nm}$	102	99	116	102	99	100	
$R^2$	0.998	0.999	0.974	0.998	1.000	1.000	
	$\Delta y = \frac{1}{16}\lambda$	$\Delta y = \frac{5}{32}\lambda$	$\Delta y = \frac{11}{32}\lambda$	$\Delta y = \frac{15}{32}\lambda$	$\Delta y = \frac{1}{2}\lambda$	Sum	Average +/- SD
$\sigma_{i  } / \text{nm}$	105	118	100	108	113	106	$106 \pm 7$
$R^2$	0.996	0.968	1.000	0.992	0.983	0.996	$0.992 \pm 0.011$

diameters, were fit with a Gaussian and an Airy pattern (Figure A.1.4). As detailed in the main text, these curves were chosen, as they are indicative of the profile of the *PSF*. Overall, for both the Gaussian and Airy patterns, the fittings were imperfect. Even though the simulated *PNJ* profile shows a succession of rings, the intensity decays faster for the Airy pattern than for the simulation, hence leading to a poor fit on the additional rings. The observation of the *PNJ* profiles also revealed that the diffraction pattern generated in the *PNJ* is not trivial and does not admit an immediate analytical expression, such as a Gaussian profile or an Airy disk. For all the fittings,  $R^2$  was calculated and is shown in Figure A.1.4. For each of the  $\mu\text{S}$  geometries, the  $R^2$  was comparable for the Gaussian and the Airy pattern. As the Gaussian fitting is easier to derive and introduce in calculations, this expression was chosen to approximate the *PSF* in the calculations.

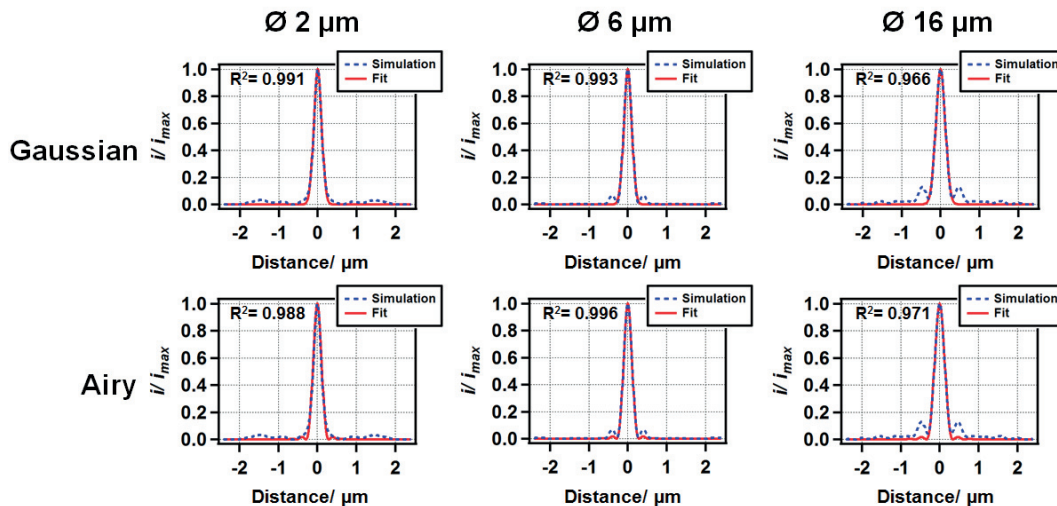


**Figure A.1.4** – Simulated *PNJ* profiles taken at the waist, along the x-axis, for  $D=2, 6$  and  $16 \mu\text{m}$   $\mu\text{S}$ -s obtained from the simulations shown in Figure 3.2. The traces were fit with a Gaussian (top) or an Airy pattern (bottom). The  $R^2$  of the fitting is shown in each panel.

### Fitting parameters of the line scans

Several parameters were extracted from the results presented in Figures 3.8 and 3.9 using Equation 3.6. The variations of  $\sigma$  are presented and discussed in the main text, and the results obtained for  $x_2-x_1$  and  $\alpha$  are shown here in Figures A.1.5.a and A.1.5.b, respectively.

In very good agreement with the sample imaged in this analysis,  $x_2-x_1$  was found to be close to 900 nm for all the observed  $\mu S$ -s. Indeed, the distance  $x_2-x_1$  between the centers of the two error functions should principally describe the distance between two consecutive gratings, which was 900 nm in our experiment. Please note that this parameter was here corrected to take into account the magnification. Similarly, the factor  $\alpha$  is merely an indication of the variation in intensity. Here,  $\alpha$  was found to be largely independent from  $D$ , thus indicating that this parameter did not introduce a bias in the fitting and that the maximal and minimal intensities in the different line-scans were all comparable, for all the  $\mu S$ -s considered. Overall, these considerations show that this fitting strategy matches the experimental conditions and validate the analysis on  $\sigma$  presented in the article.

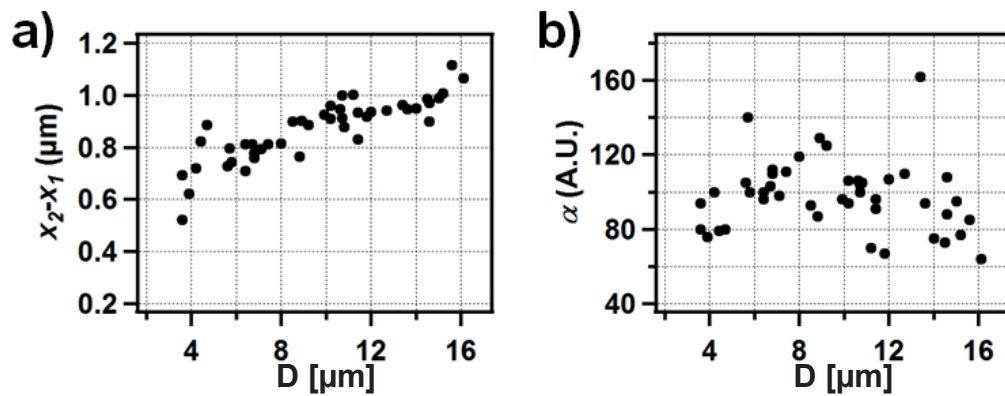


**Figure A.1.5** – Fitting parameters. The parameters **a)**  $x_2-x_1$  and **b)**  $\alpha$  obtained by fitting the experimental data with Equation 3.6, as detailed in the main article, are presented as functions of the diameter of the  $\mu S$ -s ( $D$ ).

## A.2 Supplementary data for section 3.2

### Calculations for comparing the photonic nanojet in water- and oil-immersion systems

To analyse the *PNJ*-s created by the water- and the oil-immersion system, *FEM* simulations were carried out in COMSOL Multiphysics software. Propagation of  $\lambda=545$  nm light (corresponding to the illumination setup) was modelled based on the configuration of the chip used for the experiments. The chip consisted of a D263 glass substrate ( $n_{D263}=1.525$ ) on which a *BTG*  $\mu S$  ( $n_{sphere}=1.950$ ) was placed between the SU8 ( $n_{SU8}=1.575$ ) side-walls. The cavities between the  $\mu S$  and the D263 were filled with *NOA 63* optical glue ( $n_{NOA63}=1.560$ ). The immersion medium was a changing parameter ( $n_{air}=1.000$ ,  $n_{water}=1.333$ ,  $n_{SiOil}=1.400$ ,  $n_{glycerol}=1.470$ , and  $n_{oil}=1.560$ ). The following scalar equation was used to study transverse electric waves in this two dimensional model:

$$\nabla \times (\nabla \times E) - k_0^2 \epsilon_r E = 0 \quad (\text{A.2.1})$$

where  $k_0$  is the free-space wave number,  $\epsilon_r=(n-ik)^2$  is the relative permittivity, expressed with the *RI*  $n$  and its imaginary part  $k$  and  $E$  is the electric field. In this model, the scattering boundary condition was used at all exterior boundaries, and the continuity boundary condition was used at all material interfaces. Practically, the model equalled to the one shown in section 3.1. During meshing, the minimum element size was 10 nm, while the maximum element size of  $\lambda/4$  was set to obtain a precise solution. After the model was solved, the normalized electric field was multiplied by its conjugate and the logarithmic of the intensity values were plotted (Figures 3.10, 3.11, A.2.1 and A.2.2).

### Finite element method simulations of the photonic nanojets

Based on the above described method, an extended *FEM* study was done to support the initial findings reported in section 3.2. In Figures A.2.1 and A.2.2, which completes Figure 3.10 in the thesis, the *BTG*  $\mu S$  is placed in different immersion media (left column in the figure). These media are the most commonly used in optical microscopy techniques. The surroundings of the  $\mu S$  is modelled based on the chip that was used for the experimental verification. We analysed the illumination generated by the  $\mu S$  at two different distances ( $h_1=0.1 \mu\text{m}$  and  $h_2=1.0 \mu\text{m}$ ) from the shadow side of the  $\mu S$  (right column in the figure). These positions correspond to the location of the sample during the imaging. Analysis of the intensity profiles show that there is no significant difference in the focused light region (shaded area on the plots). Numerical results of this analysis are shown in Figure 3.10.c.

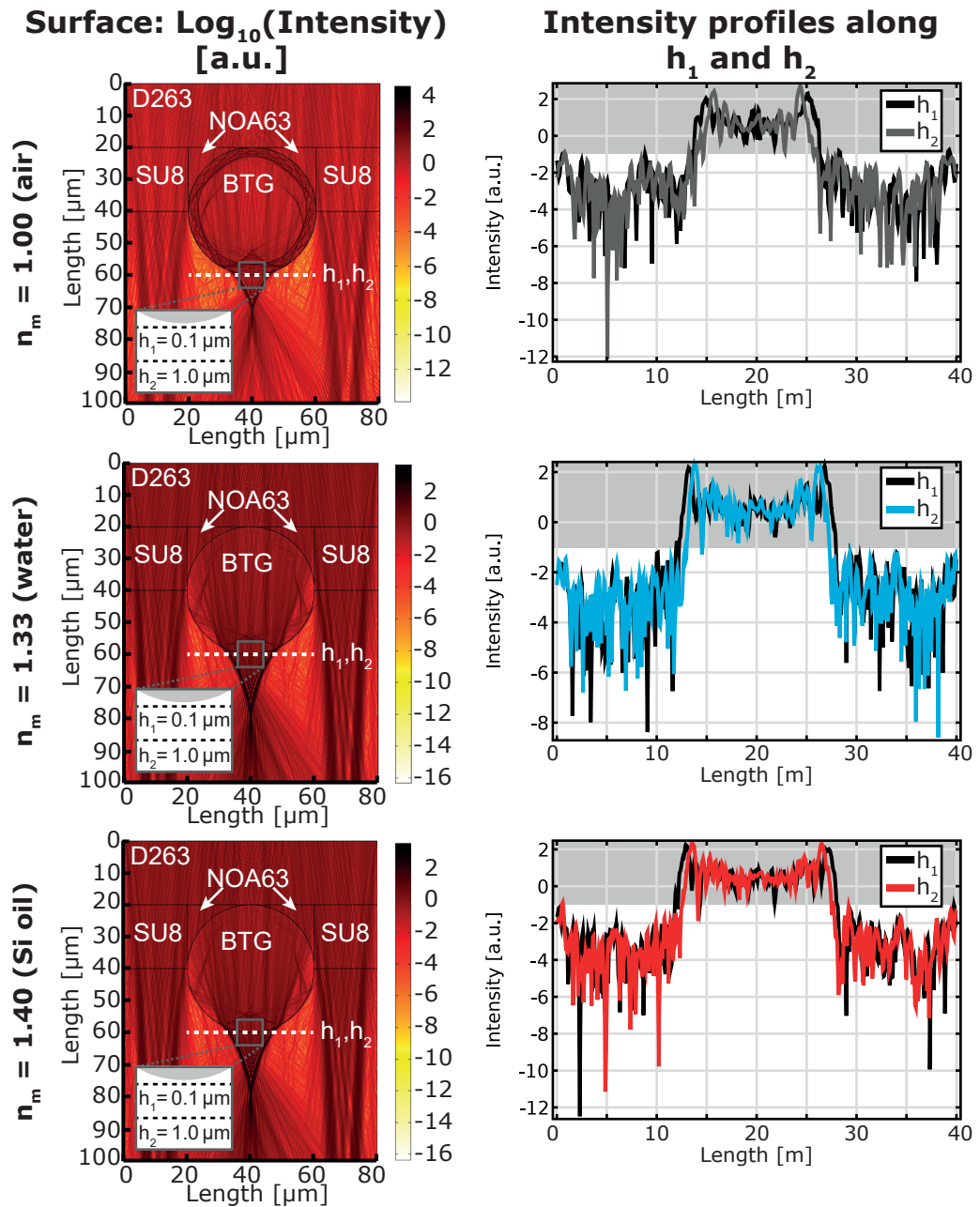


**Figure A.2.1** – Analysis of the illumination profile in the imaging region. *FEM* simulation of the *PNJ*-s generated by using different immersion media (left column) upon flat-field illumination from the top. Two measurement lines,  $h_1$  and  $h_2$  are located as shown in the insets. The corresponding intensity values along the two lines are shown on the plots (right column). Note, that here, the vertical axes have logarithmic scale. Figure continues on A.2.2.

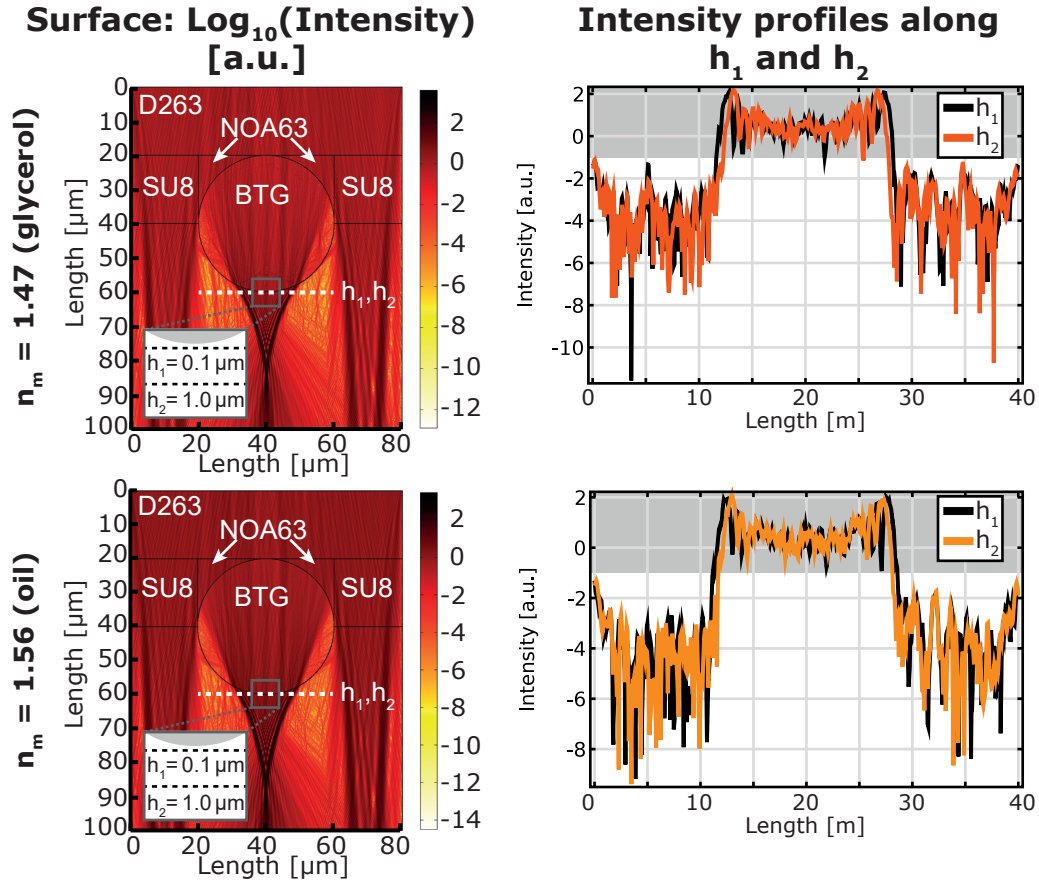


Figure A.2.2 – Analysis of the illumination profile in the imaging region II. Continued from Figure A.2.1.

### Analytical calculation of the light path through the microsphere

To quantitatively calculate the effect of the  $\mu S$  on the light cone rising from the sample, we used the property of cylindrical symmetry to reduce the calculation to a one-dimensional problem (Figure A.2.3). Each ray rising from the sample can be fully described by its starting polar angle  $\theta_{in}$  with respect to the sample- $\mu S$  axis. With the notation used in Figure A.2.3, Snell's law at the refraction points P1 and P2 imply

$$n_{medium} \sin \theta_1 = n_{sphere} \sin \theta'_1 \quad n_{sphere} \sin \theta_2 = n_{medium} \sin \theta'_2 \quad (\text{A.2.2})$$

Moreover, trigonometric properties imply

$$\theta_1 = \alpha + \theta_{in} \quad \theta'_2 = \gamma + \theta_{out} \quad \theta'_1 + \theta_2 + \beta = \pi \quad \alpha + \beta + \gamma = \pi \quad (\text{A.2.3})$$

Finally, simple geometry gives

$$x_1 = r \sin \alpha \quad z_1 = h + r(1 - \cos \alpha) \quad x_2 = r \sin \gamma \quad z_2 = h + r(1 - \cos \gamma) \quad (\text{A.2.4})$$



Equations A.2.2-A.2.4 were used to calculate  $\theta_{out}$  in the range of  $\theta_{in} \in \left[0; \arcsin\left(\frac{r}{r+h}\right)\right]$ , which corresponds to the angles that intercept the  $\mu S$ . In cases where the NOA 63 optical glue and the glass coverslip were taken into account, Snell's law and simple geometry gives

$$n_{NOA63} \sin \theta_{out} = n_{medium} \sin \theta'_{out} \quad (A.2.5)$$

where  $\theta'_{out}$  is the final output angle.

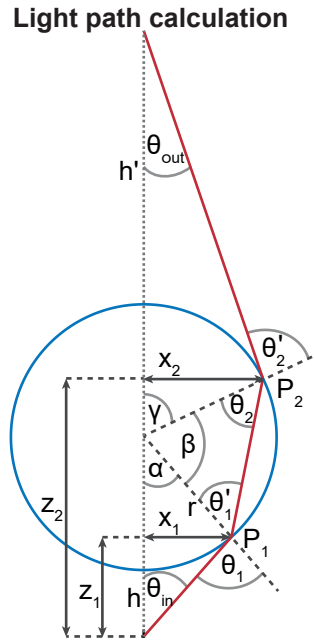
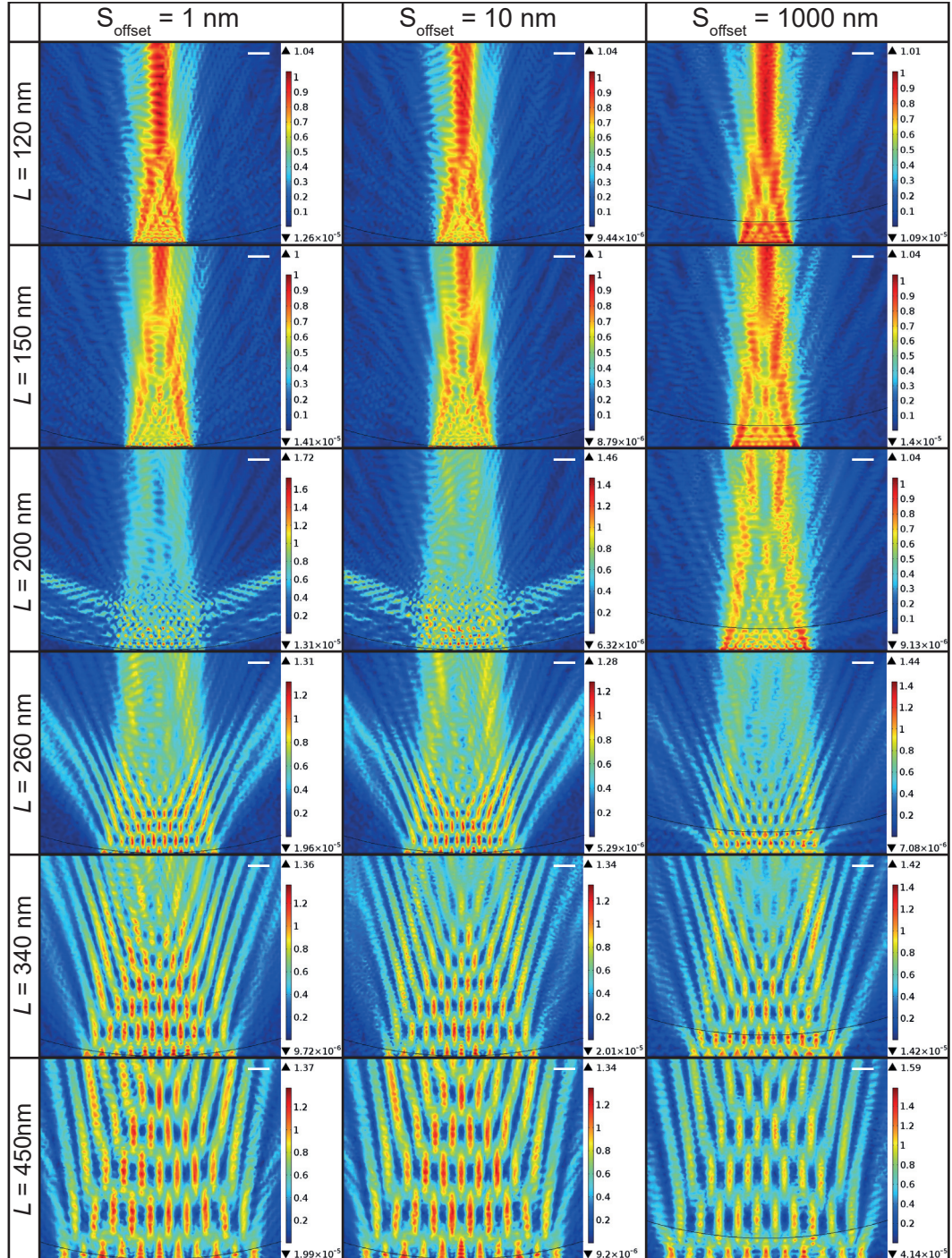


**Figure A.2.3** – Notation for light path calculation. The blue circle and the red line mark the  $\mu S$  and the ray path, respectively. The dotted vertical line shows the sample- $\mu S$  axis (*i.e.* the optical axis). The geometrical parameters are described in the text.

### A.3 Supplementary data for chapter 5

This section shows all the electric field simulation results from the study described in chapter 5. Multiple line patterns (*i.e.* LSP-s from side-view) with different line-width ( $L$ ) and different  $\mu S$  - sample distance ( $S_{offset}$ ) were evaluated by *FEM* simulations in the COMSOL Multiphysics software. Light propagation from the multiple line sources with wavelength of  $\lambda=650$  nm positioned on a silicon substrate ( $n_{silicon}=3.48$ ), through the BTG  $\mu S$  ( $n_{sphere}=1.95$ ) and surrounding dielectric medium ( $n_{medium}=1.56$ ) were carried out. Equation 5.4 was used to study transverse electric waves in a *2D* model, with scattering boundary condition at all exterior boundaries, and continuity boundary condition at all material interfaces. During meshing, the minimum element size was 10 nm, while the maximum element size of  $\lambda/4$  was set to obtain a precise solution. As the normalized electric fields show (Table A.3.1), smaller  $L$ -s and bigger  $S_{offset}$  distances can significantly reduce the modulation. Scale bars:  $10^{-6}$  m.

**Table A.3.1** – Electric field simulation results of multiple *LSP-s* with different line-widths (*L*) and different  $\mu S$  - sample distances ( $S_{offset}$ ). Smaller *L*-s and bigger  $S_{offset}$  distances significantly can reduce the modulation. Scale bar:  $10^{-6}$  m.



## A.4 Copyright licenses

This section contains copyright licenses for all materials that were adopted from already published works. The copyright permissions are grouped based on chapters as shown below.

### Chapter 2

- **Figure 2.1:** See the license granted for chapter 5.
  - **Figure 2.2:** License granted via RightsLink. License number: 4322380839218
  - **Figure 2.3:** See the license granted for chapter 5.
  - **Figure 2.4:** License granted via RightsLink. License number: 4322390244643  
Special remarks: "Reprinted by permission from Springer Nature: Springer Nature, Applied Physics B: Lasers and Optics, S.W. Hell and M. Kroug, "Ground-state-depletion fluorescence microscopy: a concept for breaking the diffraction resolution limit", Applied Physics B, vol. 60, no. 5, pp. 495–497, 1995. ©Springer-Verlag 1995"
  - **Figure 2.5:** License granted via RightsLink. License number: 4322390671951
  - **Figure 2.6:** License granted by the publisher in the following e-mail:  
From: "Wiley Global Permissions" <permissions@wiley.com>  
To: "Gergely Huszka" <gergely.huszka@epfl.ch>  
Subject: RE: NON RIGHTSLINK  
Date: Thu, 05 Apr 2018 15:21:00 +0200
- 

Dear Gergely,

Thank you for your email.

Permission is granted for you to use the material requested for your thesis/ dissertation subject to the usual acknowledgements (author, title of material, title of book/journal, ourselves as publisher) and on the understanding that you will reapply for permission if you wish to distribute or publish your thesis/ dissertation commercially.

You should also duplicate the copyright notice that appears in the Wiley publication in your use of the Material. Permission is granted solely for use in conjunction with the thesis, and the material may not be posted online separately.

Any third-party material is expressly excluded from this permission. If any material appears within the article with credit to another source, authorisation from that source must be obtained.

Many thanks,

Orla Davies  
Rights Assistant  
John Wiley & Sons Ltd

**WILEY**

- **Figure 2.7:** License granted via RightsLink. License number: 4322391466792
- **Figure 2.8:** License granted via RightsLink. License number: 4322400477835  
Special remarks: "Reprinted by permission from Springer Nature: Springer Nature, Nature Methods, M. J. Rust, M. Bates, and X. Zhuang, "Sub-diffraction-limit imaging by stochastic optical reconstruction microscopy (STORM)", Nature Methods, vol. 3, no. 10,

pp. 793–796, 2006. ©Nature Publishing Group 2006"

- **Figure 2.9:** See the license granted for chapter 5.
- **Figure 2.10:** License granted via RightsLink. License number: 4322400977431  
Special remarks: "Reprinted from B.Hecht, B. Sick,U. P.Wild, V.Deckert, R. Zenobi,O. J.Martin, andD.W. Pohl, "Scanning near-field optical microscopy with aperture probes: fundamentals and applications", The Journal of Chemical Physics, vol. 112, no. 18, pp. 7761–7774, 2000., with the permission of AIP publishing."
- **Figure 2.11:** License granted via RightsLink. License number: 4322410082880  
Special remarks: "Reproduced from N.Mauser and A. Hartschuh, "Tip-enhanced near-field optical microscopy", Chem. Soc. Rev., vol. 43, no. 4, pp. 1248–1262, 2014. with permission of The Royal Society of Chemistry."
- **Figure 2.12:** License granted via RightsLink. License number: 4322410262555  
Special remarks: "Reprinted from Y. V. Miklyaev, S. A. Asselborn, K. A. Zaytsev, and M. Y. Darscht, "Superresolution microscopy in far-field by near-field optical random mapping nanoscopy", Applied Physics Letters, vol. 105, no. 11, p. 113 103, 2014., with the permission of AIP publishing."
- **Figure 2.13:** See the license granted for chapter 5.
- **Figure 2.14:** See the license granted for chapter 5.
- **Figure 2.15:** License granted via RightsLink. License number: 4322410844489  
Special remarks: "Reprinted by permission from Springer Nature: Springer Nature, Nature Communications, Z.Wang,W. Guo, L. Li, B. Luk'yanchuk, A. Khan, Z. Liu, Z. Chen, and M. Hong, "Optical virtual imaging at 50 nm lateral resolution with a white-light nanoscope", Nature Communications, vol. 2, p. 218, 2011. ©Macmillan Publishers Limited 2011"
- **Figure 2.16:** See the license granted for chapter 5.
- **Figure 2.17:** License granted via RightsLink. License number: 4322420070224  
Special remarks: "Reprinted from A. Darafsheh, G. F.Walsh, L. Dal Negro, and V. N. Astratov, "Optical super-resolution by high-index liquid-immersed microspheres", Applied Physics Letters, vol. 101, no. 14, p. 141 128, 2012., with the permission of AIP publishing."
- **Figure 2.18:** License granted via RightsLink. License number: 4322420203850  
Special remarks: "Reprinted from A. Darafsheh, N. I. Limberopoulos, J. S. Derov, D. E.Walker, and V. N. Astratov, "Advantages of microsphere-assisted super-resolution imaging technique over solid immersion lens and confocal microscopies", Applied Physics Letters, vol. 104, no. 6, p. 061 117, 2014., with the permission of AIP publishing."
- **Figure 2.19:** License granted with special remark needed: "Adapted with permission from Y. Yan, L. Li, C. Feng,W.Guo, S. Lee, andM.Hong, "Microsphere-coupled scanning laser confocal nanoscope for sub-diffraction-limited imaging at 25 nm lateral resolution in the visible spectrum", ACS Nano, vol. 8, no. 2, pp. 1809–1816, 2014. ©2014 American Chemical Society."
- **Figure 2.20.a:** License granted via RightsLink. License number: 4322420733944  
Special remarks: "Reprinted by permission from Springer Nature: Springer Nature,

Nature Photonics, R. Horstmeyer, R. Heintzmann, G. Popescu, L. Waller, and C. Yang, "Standardizing the resolution claims for coherent microscopy", Nature Photonics, vol. 10, no. 2, pp. 68–71, 2016. ©Macmillan Publishers Limited 2016"

- **Figure 2.20.b:** See the license granted for chapter 5.
- **Figure 2.21:** License granted via RightsLink. License number: 4322420900491  
Special remarks: "Reprinted by permission from Springer Nature: Springer Nature, Scientific Reports, L. A. Krivitsky, J. J. Wang, Z. Wang, and B. Luk'yanchuk, "Locomotion of microspheres for super-resolution imaging", Scientific Reports, vol. 3, no. 1, 2013. ©Creative Commons Attribution-NonCommercial-ShareAlike 3.0 Unported license 2013."
- **Figure 2.22:** License granted via RightsLink. License number: 4322421066160  
Special remarks: "Reprinted by permission from Springer Nature: Springer Nature, Applied Physics A: Materials Science & Processing, B. Du, Y.-H. Ye, J. Hou, M. Guo, and T. Wang, "Sub-wavelength image stitching with removable microsphere-embedded thin film", Applied Physics A, vol. 122, no. 1, 2016. ©Springer-Verlag Berlin Heidelberg 2015"
- **Figure 2.23:** Distributed under Creative Commons CC BY
- **Figure 2.24:** Distributed under Creative Commons CC BY
- **Figure 2.25:** See the license granted for chapter 5.

### Chapter 3

- **Section 3.1:** Adapted with permission from H. Yang, R. Trouillon, G. Huszka, and M. A. M. Gijs, "Super-resolution imaging of a dielectric microsphere is governed by the waist of its photonic nanojet", Nano Letters, pp. 4862–4870, 2016. ©2016 American Chemical Society
- **Section 3.2:** submitted to Small

### Chapter 4

- Section 4.1: Conference contribution, credited at the beginning of chapter 4.

## Chapter 5

Permission regarding all material from The Optical Society was granted in the following e-mail:

From: pubscopyright <copyright@osa.org>  
 To: "Gergely Huszka" <gergely.huszka@epfl.ch>, pubscopyright <copyright@osa.org>  
 Subject: RE: permission to use figures in dissertation  
 Date: Fri, 13 Apr 2018 19:46:06 +0200

Dear Gergely Huszka,

Thank you for the additional information.

For your PhD dissertation, we have received the updated request for the use of the below figures:

Req #	Figure #	Journal	Vol.	Page
1	11	JOSA A	9	2159
2	1	OL	19	780
3	2	OL	19	780
4	3	AO	29	3741
5	2	OE	12	1214
6	3	OE	16	6930
7	5	OE	19	10206
8	12	OE	19	10206
9	5	AO	34	746
10	1	AO	56	3142

For the use of the above 10 figures:

OSA considers your requested use of its copyrighted material to be Fair Use under United States Copyright Law. It is requested that a complete citation of the original material be included in any publication.

For the use of material from the *Optics Express* article of which you are an author:

As long as the copyrighted material is included within the body, section or chapter, of the thesis, and is not posted separate from the thesis, OSA considers your requested use of its copyrighted materials to be permissible within the author rights granted in the Copyright Transfer Agreement submitted by the requester on acceptance for publication of his/her manuscript. If the entire article is being included, it is requested that the **Author Accepted (or preprint)** version be the version included within the thesis and that a complete citation of the original material be included in any publication. This permission assumes that the material was not reproduced from another source when published in the original publication.

The **Author Accepted** version is the preprint version of the article that was accepted for publication but not yet prepared and/or formatted by The Optical Society or its vendors.

Let me know if you have any questions.

Kind Regards,

Rebecca Robinson

Rebecca Robinson

April 13, 2018

Authorized Agent, The Optical Society

## Chapter 6

The article was distributed under Creative Commons CC BY license.





## Bibliography

- [1] W. J. Croft, *Under the Microscope: A Brief History of Microscopy*. World Scientific, 2006, 153 pp.
- [2] A. Kwan, J. Dudley, and E. Lantz, “Who really discovered snell’s law?”, *Physics World*, vol. 15, no. 4, p. 64, 2002.
- [3] “Double-confocal scanning microscope.”, EP0491289 (A1), CIB: G02B21/00; (IPC1-7): G02B21/00, 1992.
- [4] S. Hell and E. Stelzer, “Properties of a 4pi confocal fluorescence microscope”, *JOSA A*, vol. 9, no. 12, pp. 2159–2166, 1992.
- [5] S. Hell and E. H. K. Stelzer, “Fundamental improvement of resolution with a 4pi-confocal fluorescence microscope using two-photon excitation”, *Optics Communications*, vol. 93, no. 5, pp. 277–282, 1992.
- [6] S. W. Hell, S. Lindek, C. Cremer, and E. H. Stelzer, “Confocal microscopy with an increased detection aperture: type-b 4pi confocal microscopy”, *Optics letters*, vol. 19, no. 3, pp. 222–224, 1994.
- [7] S. W. Hell, “Improvement of lateral resolution in far-field fluorescence light microscopy by using two-photon excitation with offset beams”, *Optics communications*, vol. 106, no. 1, pp. 19–24, 1994.
- [8] S. W. Hell and J. Wichmann, “Breaking the diffraction resolution limit by stimulated emission: stimulated-emission-depletion fluorescence microscopy”, *Optics Letters*, vol. 19, no. 11, pp. 780–782, 1994.
- [9] S. Bretschneider, C. Eggeling, and S. W. Hell, “Breaking the diffraction barrier in fluorescence microscopy by optical shelving”, *Physical Review Letters*, vol. 98, no. 21, 2007.
- [10] (). The nobel prize in chemistry 2014, [Online]. Available: [https://www.nobelprize.org/nobel\\_prizes/chemistry/laureates/2014/](https://www.nobelprize.org/nobel_prizes/chemistry/laureates/2014/) (visited on 03/06/2018).
- [11] S. W. Hell and M. Kroug, “Ground-state-depletion fluorescence microscopy: a concept for breaking the diffraction resolution limit”, *Applied Physics B*, vol. 60, no. 5, pp. 495–497, 1995.

## Bibliography

---

- [12] E. Rittweger, D. Wildanger, and S. W. Hell, “Far-field fluorescence nanoscopy of diamond color centers by ground state depletion”, *EPL (Europhysics Letters)*, vol. 86, no. 1, p. 14 001, 2009.
- [13] M. G. Gustafsson, “Surpassing the lateral resolution limit by a factor of two using structured illumination microscopy”, *Journal of microscopy*, vol. 198, no. 2, pp. 82–87, 2000.
- [14] “Method and apparatus for three-dimensional microscopy with enhanced depth resolution”, US005671085A, 1995.
- [15] M. G. L. Gustafsson, “Nonlinear structured-illumination microscopy: wide-field fluorescence imaging with theoretically unlimited resolution”, *Proceedings of the National Academy of Sciences of the United States of America*, vol. 102, no. 37, pp. 13 081–13 086, 2005.
- [16] M. Hausmann, B. Schneider, J. Bradl, and C. G. Cremer, “High-precision distance microscopy of 3d nanostructures by a spatially modulated excitation fluorescence microscope”, in *Optical Biopsies and Microscopic Techniques II*, vol. 3197, International Society for Optics and Photonics, 1997, pp. 217–223.
- [17] B. Schneider, J. Bradl, I. Kirsten, M. Hausmann, and C. Cremer, “High precision localization of fluorescent targets in the nanometer range by spatially modulated excitation fluorescence microscopy”, *Fluorescence microscopy and fluorescent probes*, vol. 2, pp. 63–68, 1998.
- [18] B. Schneider, I. Upmann, I. Kirsten, J. Bradl, M. Hausmann, and C. Cremer, “A dual-laser, spatially modulated illumination fluorescence microscope”, *Microscopy and Analysis*, pp. 5–8, 1999.
- [19] B. Albrecht, A. V. Failla, A. Schweitzer, and C. Cremer, “Spatially modulated illumination microscopy allows axial distance resolution in the nanometer range”, *Applied optics*, vol. 41, no. 1, pp. 80–87, 2002.
- [20] H. Bornfleth, K. Sätzler, R. Eils, and C. Cremer, “High-precision distance measurements and volume-conserving segmentation of objects near and below the resolution limit in three-dimensional confocal fluorescence microscopy”, *Journal of Microscopy*, vol. 189, no. 2, pp. 118–136, 1997.
- [21] “Method and devices for measuring distances between object structures”, US6424421B1, 2002.
- [22] A. M. Van Oijen, J. Köhler, J. Schmidt, M. Müller, and G. J. Brakenhoff, “3-dimensional super-resolution by spectrally selective imaging”, *Chemical Physics Letters*, vol. 292, no. 1, pp. 183–187, 1998.
- [23] K. A. Lidke, B. Rieger, T. M. Jovin, and R. Heintzmann, “Superresolution by localization of quantum dots using blinking statistics”, *Optics Express*, vol. 13, no. 18, pp. 7052–7062, 2005.

- [24] E. Betzig, G. H. Patterson, and R. Sougrat, “Imaging intracellular fluorescent proteins at nanometer resolution”, *Science*, vol. 313, no. 5793, pp. 1642–1645, 2006.
- [25] S. T. Hess, T. P. Girirajan, and M. D. Mason, “Ultra-high resolution imaging by fluorescence photoactivation localization microscopy”, *Biophysical Journal*, vol. 91, no. 11, pp. 4258–4272, 2006.
- [26] S. T. Hess, T. J. Gould, M. V. Gudheti, S. A. Maas, K. D. Mills, and J. Zimmerberg, “Dynamic clustered distribution of hemagglutinin resolved at 40 nm in living cell membranes discriminates between raft theories”, *Proceedings of the National Academy of Sciences*, vol. 104, no. 44, pp. 17 370–17 375, 2007.
- [27] C. Geisler, A. Schönle, C. von Middendorff, H. Bock, C. Eggeling, A. Egner, and S. Hell, “Resolution of  $\lambda / 10$  in fluorescence microscopy using fast single molecule photo-switching”, *Applied Physics A*, vol. 88, no. 2, pp. 223–226, 2007.
- [28] M. J. Rust, M. Bates, and X. Zhuang, “Sub-diffraction-limit imaging by stochastic optical reconstruction microscopy (STORM)”, *Nature Methods*, vol. 3, no. 10, pp. 793–796, 2006.
- [29] M. Bates, T. R. Blosser, and X. Zhuang, “Short-range spectroscopic ruler based on a single-molecule optical switch”, *Physical Review Letters*, vol. 94, no. 10, 2005.
- [30] M. Heilemann, S. van de Linde, M. Schüttpelz, R. Kasper, B. Seefeldt, A. Mukherjee, P. Tinnefeld, and M. Sauer, “Subdiffraction-resolution fluorescence imaging with conventional fluorescent probes”, *Angewandte Chemie International Edition*, vol. 47, no. 33, pp. 6172–6176, 2008.
- [31] J. Fölling, M. Bossi, H. Bock, R. Medda, C. A. Wurm, B. Hein, S. Jakobs, C. Eggeling, and S. W. Hell, “Fluorescence nanoscopy by ground-state depletion and single-molecule return”, *Nature Methods*, vol. 5, no. 11, pp. 943–945, 2008.
- [32] D. Baddeley, I. D. Jayasinghe, C. Cremer, M. B. Cannell, and C. Soeller, “Light-induced dark states of organic fluochromes enable 30 nm resolution imaging in standard media”, *Biophysical Journal*, vol. 96, no. 2, pp. L22–L24, 2009.
- [33] T. Dertinger, R. Colyer, G. Iyer, S. Weiss, and J. Enderlein, “Fast, background-free, 3d super-resolution optical fluctuation imaging (SOFI)”, *Proceedings of the National Academy of Sciences*, vol. 106, no. 52, pp. 22 287–22 292, 2009.
- [34] T. Dertinger, R. Colyer, R. Vogel, J. Enderlein, and S. Weiss, “Achieving increased resolution and more pixels with superresolution optical fluctuation imaging (SOFI)”, *Optics express*, vol. 18, no. 18, pp. 18 875–18 885, 2010.
- [35] R. Kaufmann, P. Müller, M. Hausmann, and C. Cremer, “Imaging label-free intracellular structures by localisation microscopy”, *Micron*, vol. 42, no. 4, pp. 348–352, 2011.
- [36] I. Schoen, J. Ries, E. Klotzsch, H. Ewers, and V. Vogel, “Binding-activated localization microscopy of DNA structures”, *Nano Letters*, vol. 11, no. 9, pp. 4008–4011, 2011.

## Bibliography

---

- [37] S. Weisenburger, D. Boening, B. Schomburg, K. Giller, S. Becker, C. Griesinger, and V. Sandoghdar, “Cryogenic optical localization provides 3d protein structure data with angstrom resolution”, *Nature Methods*, vol. 14, no. 2, pp. 141–144, 2017.
- [38] G. BINNIG and H. ROHRER, “SCANNING TUNNELING MICROSCOPY”, *Surface Science*, no. 126, pp. 236–244, 1983.
- [39] G. Binnig and C. F. Quate, “Atomic force microscope”, *PHYSICAL REVIEW LETTERS*, vol. 56, no. 9, p. 5, 1986.
- [40] J. M. Guerra, “Photon tunneling microscopy”, *Applied Optics*, vol. 29, no. 26, pp. 3741–3752, 1990.
- [41] B. Hecht, B. Sick, U. P. Wild, V. Deckert, R. Zenobi, O. J. Martin, and D. W. Pohl, “Scanning near-field optical microscopy with aperture probes: fundamentals and applications”, *The Journal of Chemical Physics*, vol. 112, no. 18, pp. 7761–7774, 2000.
- [42] E. H. Synge, “A suggested method for extending microscopic resolution into the ultra-microscopic region”, *The London, Edinburgh, and Dublin Philosophical Magazine and Journal of Science*, vol. 6, no. 35, pp. 356–362, 1928.
- [43] D. W. Pohl, W. Denk, and M. Lanz, “Optical stethoscopy: image recording with resolution  $\lambda/20$ ”, *Applied Physics Letters*, vol. 44, no. 7, pp. 651–653, 1984.
- [44] A. Lewis, M. Isaacson, A. Harootunian, and A. Muray, “Development of a 500 Å spatial resolution light microscope: i. light is efficiently transmitted through  $\lambda/16$  diameter apertures”, *Ultramicroscopy*, vol. 13, no. 3, pp. 227–231, 1984.
- [45] A. Harootunian, E. Betzig, M. Isaacson, and A. Lewis, “Super-resolution fluorescence near-field scanning optical microscopy”, *Applied Physics Letters*, vol. 49, no. 11, pp. 674–676, 1986.
- [46] U. Dürig, D. W. Pohl, and F. Rohner, “Near-field optical-scanning microscopy”, *Journal of Applied Physics*, vol. 59, no. 10, pp. 3318–3327, 1986.
- [47] E. Betzig, M. Isaacson, and A. Lewis, “Collection mode near-field scanning optical microscopy”, *Applied Physics Letters*, vol. 51, no. 25, pp. 2088–2090, 1987.
- [48] H. Heinzelmann, B. Hecht, L. Novotny, and D. W. Pohl, “Forbidden light scanning near-field optical microscopy”, *Journal of Microscopy*, vol. 177, no. 2, pp. 115–118, 1995.
- [49] B. Hecht, H. Heinzelmann, and D. W. Pohl, “Combined aperture SNOM/PSTM: best of both worlds?”, *Ultramicroscopy*, vol. 57, no. 2, pp. 228–234, 1995.
- [50] U. C. Fischer and D. W. Pohl, “Observation of single-particle plasmons by near-field optical microscopy”, *Physical Review Letters*, vol. 62, no. 4, pp. 458–461, 1989.
- [51] F. Zenhausern, Y. Martin, and H. K. Wickramasinghe, “Scanning interferometric apertureless microscopy: optical imaging at 10 angstrom resolution”, *Science*, vol. 269, no. 5227, pp. 1083–1085, 1995.

- 
- [52] Y. Inouye and S. Kawata, "A scanning near-field optical microscope having scanning electron tunnelling microscope capability using a single metallic probe tip", *Journal of Microscopy*, vol. 178, no. 1, pp. 14–19, 1995.
- [53] P. Gleyzes, A. C. Boccara, and R. Bachelot, "Near field optical microscopy using a metallic vibrating tip", *Ultramicroscopy*, vol. 57, no. 2, pp. 318–322, 1995.
- [54] C. Girard, O. J. F. Martin, and A. Dereux, "Molecular lifetime changes induced by nanometer scale optical fields", *Physical Review Letters*, vol. 75, no. 17, pp. 3098–3101, 1995.
- [55] J. Koglin, U. Fischer, and H. Fuchs, "Scanning near-field optical microscopy with a tetrahedral tip at a resolution of 6 nm", *Journal of Biomedical Optics*, vol. 1, no. 1, pp. 75–79, 1996.
- [56] Sugiura, Kawata, and Okada, "Fluorescence imaging with a laser trapping scanning near-field optical microscope", *Journal of Microscopy*, vol. 194, no. 2, pp. 291–294, 1999.
- [57] B. Knoll and F. Keilmann, "Near-field probing of vibrational absorption for chemical microscopy", *Nature*, vol. 399, no. 6732, pp. 134–137, 1999.
- [58] D. Courjon, "Scanning tunneling optical microscopy", in *Scanning Tunneling Microscopy and Related Methods*, ser. NATO ASI Series, Springer, Dordrecht, 1990, pp. 497–505.
- [59] R. C. Reddick, R. J. Warmack, and T. L. Ferrell, "New form of scanning optical microscopy", *Physical Review B*, vol. 39, no. 1, pp. 767–770, 1989.
- [60] E. Betzig, J. K. Trautman, T. D. Harris, J. S. Weiner, and R. L. Kostelak, "Breaking the diffraction barrier: optical microscopy on a nanometric scale", *Science*, vol. 251, no. 5000, pp. 1468–1470, 1991.
- [61] G. A. Valaskovic, M. Holton, and G. H. Morrison, "Parameter control, characterization, and optimization in the fabrication of optical fiber near-field probes", *Applied Optics*, vol. 34, no. 7, pp. 1215–1228, 1995.
- [62] "Etch procedure for optical fibers", US4469554A, 1984.
- [63] P. Hoffmann, B. Dutoit, and R.-P. Salathé, "Comparison of mechanically drawn and protection layer chemically etched optical fiber tips", *Ultramicroscopy*, Selected Papers from the 3rd International Conference on Near-Field Optics and Related Techniques, vol. 61, no. 1, pp. 165–170, 1995.
- [64] P. Lambelet, A. Sayah, M. Pfeffer, C. Philipona, and F. Marquis-Weible, "Chemically etched fiber tips for near-field optical microscopy: a process for smoother tips", *Applied Optics*, vol. 37, no. 31, pp. 7289–7292, 1998.
- [65] H. A. Bethe, "Theory of diffraction by small holes", *Physical Review*, vol. 66, no. 7, pp. 163–182, 1944.
- [66] C. J. Bouwkamp, "On bethe's theory of diffraction by small holes", *Philips Research Reports*, vol. 5, pp. 321–332, 1950.

## Bibliography

---

- [67] J.-J. Greffet and R. Carminati, “Image formation in near-field optics”, *Progress in Surface Science*, vol. 56, no. 3, pp. 133–237, 1997.
- [68] O. J. F. Martin and N. B. Piller, “Electromagnetic scattering in polarizable backgrounds”, *Physical Review E*, vol. 58, no. 3, pp. 3909–3915, 1998.
- [69] C. Girard and A. Dereux, “Near-field optics theories”, *Reports on Progress in Physics*, vol. 59, no. 5, p. 657, 1996.
- [70] S. Jutamulia, M. Ohtsu, and T. Asakura, “Near-field optics: physics, devices, and information processing”, presented at the Near-Field Optics: Physics, Devices, and Information Processing, vol. 3791, 1999.
- [71] Martin, “3d simulations of the experimental signal measured in near-field optical microscopy”, *Journal of Microscopy*, vol. 194, no. 2, pp. 235–239, 1999.
- [72] A. Lewis, H. Taha, A. Strinkovski, A. Manevitch, A. Khatchatourians, R. Dekhter, and E. Ammann, “Near-field optics: from subwavelength illumination to nanometric shadowing”, *Nature Biotechnology*, vol. 21, no. 11, pp. 1378–1386, 2003.
- [73] J. Wessel, “Surface-enhanced optical microscopy”, *JOSA B*, vol. 2, no. 9, pp. 1538–1541, 1985.
- [74] R. Hillenbrand, T. Taubner, and F. Keilmann, “Phonon-enhanced light–matter interaction at the nanometre scale”, *Nature*, vol. 418, no. 6894, pp. 159–162, 2002.
- [75] F. Keilmann and R. Hillenbrand, “Near-field microscopy by elastic light scattering from a tip”, *Philosophical Transactions of the Royal Society of London A: Mathematical, Physical and Engineering Sciences*, vol. 362, no. 1817, pp. 787–805, 2004.
- [76] A. V. Zayats and V. Sandoghdar, “Apertureless scanning near-field second-harmonic microscopy”, *Optics Communications*, vol. 178, no. 1, pp. 245–249, 2000.
- [77] A. V. Zayats and I. I. Smolyaninov, “Near-field second-harmonic generation”, *Philosophical Transactions of the Royal Society of London A: Mathematical, Physical and Engineering Sciences*, vol. 362, no. 1817, pp. 843–860, 2004.
- [78] A. Bouhelier, M. Beversluis, A. Hartschuh, and L. Novotny, “Near-field second-harmonic generation induced by local field enhancement”, *Physical Review Letters*, vol. 90, no. 1, p. 013 903, 2003.
- [79] M. Danckwerts and L. Novotny, “Optical frequency mixing at coupled gold nanoparticles”, *Physical Review Letters*, vol. 98, no. 2, p. 026 104, 2007.
- [80] R. M. Stöckle, Y. D. Suh, V. Deckert, and R. Zenobi, “Nanoscale chemical analysis by tip-enhanced raman spectroscopy”, *Chemical Physics Letters*, vol. 318, no. 1, pp. 131–136, 2000.
- [81] N. Hayazawa, Y. Inouye, Z. Sekkat, and S. Kawata, “Near-field raman scattering enhanced by a metallized tip”, *Chemical Physics Letters*, vol. 335, no. 5, pp. 369–374, 2001.

- 
- [82] A. Hartschuh, E. J. Sánchez, X. S. Xie, and L. Novotny, “High-resolution near-field raman microscopy of single-walled carbon nanotubes”, *Physical Review Letters*, vol. 90, no. 9, p. 095 503, 2003.
- [83] L. Novotny, R. X. Bian, and X. S. Xie, “Theory of nanometric optical tweezers”, *Physical Review Letters*, vol. 79, no. 4, pp. 645–648, 1997.
- [84] M. I. Stockman, S. V. Faleev, and D. J. Bergman, “Coherent control of femtosecond energy localization in nanosystems”, *Physical Review Letters*, vol. 88, no. 6, p. 067 402, 2002.
- [85] T. Brixner, F. J. García de Abajo, J. Schneider, and W. Pfeiffer, “Nanoscopic ultrafast space-time-resolved spectroscopy”, *Physical Review Letters*, vol. 95, no. 9, p. 093 901, 2005.
- [86] M. I. Stockman, M. F. Kling, U. Kleineberg, and F. Krausz, “Attosecond nanoplasmonic-field microscope”, *Nature Photonics*, vol. 1, no. 9, pp. 539–544, 2007.
- [87] M. Aeschlimann, M. Bauer, D. Bayer, T. Brixner, F. J. García de Abajo, W. Pfeiffer, M. Rohmer, C. Spindler, and F. Steeb, “Adaptive subwavelength control of nano-optical fields”, *Nature*, vol. 446, no. 7133, pp. 301–304, 2007.
- [88] E. M. Purcell, “Spontaneous emission probabilities at radio frequencies”, in *Confined Electrons and Photons*, ser. NATO ASI Series, Springer, Boston, MA, 1995, pp. 839–839.
- [89] M. Thomas, J.-J. Greffet, R. Carminati, and J. R. Arias-Gonzalez, “Single-molecule spontaneous emission close to absorbing nanostructures”, *Applied Physics Letters*, vol. 85, no. 17, pp. 3863–3865, 2004.
- [90] A. Hartschuh, H. Qian, A. J. Meixner, N. Anderson, and L. Novotny, “Nanoscale optical imaging of excitons in single-walled carbon nanotubes”, *Nano Letters*, vol. 5, no. 11, pp. 2310–2313, 2005.
- [91] K. Aslan, I. Gryczynski, J. Malicka, E. Matveeva, J. R. Lakowicz, and C. D. Geddes, “Metal-enhanced fluorescence: an emerging tool in biotechnology”, *Current Opinion in Biotechnology*, Analytical biotechnology, vol. 16, no. 1, pp. 55–62, 2005.
- [92] A. Hartschuh, “Tip-enhanced near-field optical microscopy”, *Angewandte Chemie International Edition*, vol. 47, no. 43, pp. 8178–8191, 2008.
- [93] N. Mauser and A. Hartschuh, “Tip-enhanced near-field optical microscopy”, *Chem. Soc. Rev.*, vol. 43, no. 4, pp. 1248–1262, 2014.
- [94] O. Motoichi, “Progress of high-resolution photon scanning tunneling microscopy due to a nanometric fiber probe”, *Journal of Lightwave Technology*, vol. 13, no. 7, pp. 1200–1221, 1995.
- [95] Y. V. Miklyaev, S. A. Asselborn, K. A. Zaytsev, and M. Y. Darscht, “Superresolution microscopy in far-field by near-field optical random mapping nanoscopy”, *Applied Physics Letters*, vol. 105, no. 11, p. 113 103, 2014.

## Bibliography

---

- [96] Z. Chen, A. Taflove, and V. Backman, “Photonic nanojet enhancement of backscattering of light by nanoparticles: a potential novel visible-light ultramicroscopy technique”, *Optics express*, vol. 12, no. 7, pp. 1214–1220, 2004.
- [97] S. M. Mansfield and G. S. Kino, “Solid immersion microscope”, *Applied Physics Letters*, vol. 57, no. 24, p. 2615, 1990.
- [98] J. B. Pendry, “Negative refraction makes a perfect lens”, *Physical review letters*, vol. 85, no. 18, p. 3966, 2000.
- [99] X. Li, Z. Chen, A. Taflove, and V. Backman, “Optical analysis of nanoparticles via enhanced backscattering facilitated by 3-d photonic nanojets”, *Optics express*, vol. 13, no. 2, pp. 526–533, 2005.
- [100] S. Lecler, Y. Takakura, and P. Meyrueis, “Properties of a three-dimensional photonic jet”, *Optics letters*, vol. 30, no. 19, pp. 2641–2643, 2005.
- [101] A. V. Itagi and W. A. Challener, “Optics of photonic nanojets”, *JOSA A*, vol. 22, no. 12, pp. 2847–2858, 2005.
- [102] A. Devilez, B. Stout, N. Bonod, and E. Popov, “Spectral analysis of three-dimensional photonic jets”, *Optics Express*, vol. 16, no. 18, pp. 14 200–14 212, 2008.
- [103] Z. Chen, A. Taflove, X. Li, and V. Backman, “Superenhanced backscattering of light by nanoparticles”, *Optics letters*, vol. 31, no. 2, pp. 196–198, 2006.
- [104] P. Ferrand, J. Wenger, A. Devilez, M. Pianta, B. Stout, N. Bonod, E. Popov, H. Rigneault, *et al.*, “Direct imaging of photonic nanojets”, *Optics express*, vol. 16, no. 10, pp. 6930–6940, 2008.
- [105] A. Heifetz, S.-C. Kong, A. V. Sahakian, A. Taflove, and V. Backman, “Photonic nanojets”, *Journal of Computational and Theoretical Nanoscience*, vol. 6, no. 9, pp. 1979–1992, 2009.
- [106] A. Devilez, N. Bonod, J. Wenger, D. Gérard, B. Stout, H. Rigneault, and E. Popov, “Three-dimensional subwavelength confinement of light with dielectric microspheres”, *Optics Express*, vol. 17, no. 4, pp. 2089–2094, 2009.
- [107] Y. Geints, E. Panina, and A. Zemlyanov, “Control over parameters of photonic nanojets of dielectric microspheres”, *Optics Communications*, vol. 283, no. 23, pp. 4775–4781, 2010.
- [108] C. M. Ruiz and J. J. Simpson, “Detection of embedded ultra-subwavelength-thin dielectric features using elongated photonic nanojets”, *Optics express*, vol. 18, no. 16, pp. 16 805–16 812, 2010.
- [109] D. R. Mason, M. V. Jouravlev, and K. S. Kim, “Enhanced resolution beyond the abbe diffraction limit with wavelength-scale solid immersion lenses”, *Optics letters*, vol. 35, no. 12, pp. 2007–2009, 2010.



- 
- [110] J. Y. Lee, B. H. Hong, W. Y. Kim, S. K. Min, Y. Kim, M. V. Jouravlev, R. Bose, K. S. Kim, I.-C. Hwang, L. J. Kaufman, C. W. Wong, P. Kim, and K. S. Kim, “Near-field focusing and magnification through self-assembled nanoscale spherical lenses”, *Nature*, vol. 460, no. 7254, pp. 498–501, 2009.
- [111] J. J. Schwartz, S. Stavrakis, and S. R. Quake, “Colloidal lenses allow high-temperature single-molecule imaging and improve fluorophore photostability”, *Nature Nanotechnology*, vol. 5, no. 2, pp. 127–132, 2010.
- [112] Z. Wang, W. Guo, L. Li, B. Luk’yanchuk, A. Khan, Z. Liu, Z. Chen, and M. Hong, “Optical virtual imaging at 50 nm lateral resolution with a white-light nanoscope”, *Nature Communications*, vol. 2, p. 218, 2011.
- [113] T. R. Kumar and R. V. Krishnaiah, “Optical disk with blu-ray technology”, *arXiv preprint arXiv:1310.1551*, 2013.
- [114] M.-S. Kim, T. Scharf, S. Mühlig, C. Rockstuhl, and H. P. Herzig, “Engineering photonic nanojets”, *Optics express*, vol. 19, no. 11, pp. 10 206–10 220, 2011.
- [115] M.-S. Kim, T. Scharf, M. Brun, S. Olivier, S. Nicoletti, and H. P. Herzig, “Advanced optical characterization of micro solid immersion lens”, C. Gorecki, A. K. Asundi, and W. Osten, Eds., 2012, 84300E–84300E–10.
- [116] M.-S. Kim, T. Scharf, D. Nguyen, E. Keeler, S. Rydberg, W. Nakagawa, G. Osowiecki, R. Voelkel, and H. P. Herzig, “Light confinement effect of nonspherical nanoscale solid immersion lenses”, *Journal of Micro/Nanolithography, MEMS, and MOEMS*, vol. 12, no. 2, pp. 023 015–023 015, 2013.
- [117] D. Kang, C. Pang, S. M. Kim, H. S. Cho, H. S. Um, Y. W. Choi, and K. Y. Suh, “Shape-controllable microlens arrays via direct transfer of photocurable polymer droplets”, *Advanced Materials*, vol. 24, no. 13, pp. 1709–1715, 2012.
- [118] A. Darafsheh, G. F. Walsh, L. Dal Negro, and V. N. Astratov, “Optical super-resolution by high-index liquid-immersed microspheres”, *Applied Physics Letters*, vol. 101, no. 14, p. 141 128, 2012.
- [119] A. V. Maslov and V. N. Astratov, “Optical nanoscopy with contact mie-particles: resolution analysis”, *Applied Physics Letters*, vol. 110, no. 26, p. 261 107, 2017.
- [120] D. Grojo, N. Sandeau, L. Boarino, C. Constantinescu, N. De Leo, M. Laus, and K. Sparnacci, “Bessel-like photonic nanojets from core-shell sub-wavelength spheres”, *Optics Letters*, vol. 39, no. 13, p. 3989, 2014.
- [121] Y. Shen, L. V. Wang, and J.-T. Shen, “Ultralong photonic nanojet formed by a two-layer dielectric microsphere”, *Optics Letters*, vol. 39, no. 14, p. 4120, 2014.
- [122] G. Gu, R. Zhou, Z. Chen, H. Xu, G. Cai, Z. Cai, and M. Hong, “Super-long photonic nanojet generated from liquid-filled hollow microcylinder”, *Optics Letters*, vol. 40, no. 4, p. 625, 2015.
- [123] T. Jalali and D. Erni, “Highly confined photonic nanojet from elliptical particles”, *Journal of Modern Optics*, vol. 61, no. 13, pp. 1069–1076, 2014.

## Bibliography

---

- [124] R. Chen, J. Lin, P. Jin, M. Cada, and Y. Ma, “Photonic nanojets generated by rough surface micro-cylinders”, in *Electrical and Computer Engineering (CCECE), 2015 IEEE 28th Canadian Conference on*, IEEE, 2015, pp. 1393–1397.
- [125] B. S. Luk’yanchuk, R. Paniagua-Domínguez, I. Minin, O. Minin, and Z. Wang, “Refractive index less than two: photonic nanojets yesterday, today and tomorrow [invited]”, *Optical Materials Express*, vol. 7, no. 6, p. 1820, 2017.
- [126] S. Lee, L. Li, Y. Ben-Aryeh, Z. Wang, and W. Guo, “Overcoming the diffraction limit induced by microsphere optical nanoscopy”, *Journal of Optics*, vol. 15, no. 12, p. 125 710, 2013.
- [127] A. Darafsheh, N. I. Limberopoulos, J. S. Derov, D. E. Walker, and V. N. Astratov, “Advantages of microsphere-assisted super-resolution imaging technique over solid immersion lens and confocal microscopies”, *Applied Physics Letters*, vol. 104, no. 6, p. 061 117, 2014.
- [128] Y. Yan, L. Li, C. Feng, W. Guo, S. Lee, and M. Hong, “Microsphere-coupled scanning laser confocal nanoscope for sub-diffraction-limited imaging at 25 nm lateral resolution in the visible spectrum”, *ACS Nano*, vol. 8, no. 2, pp. 1809–1816, 2014.
- [129] H. Yang, N. Moullan, J. Auwerx, and M. A. M. Gijs, “Fluorescence imaging: super-resolution biological microscopy using virtual imaging by a microsphere nanoscope (small 9/2014)”, *Small*, vol. 10, no. 9, pp. 1876–1876, 2014.
- [130] A. Darafsheh, C. Guardiola, J. Finlay, A. Cárabe, and D. Nihalani, “Simple super-resolution biological imaging”, *SPIE Newsroom*, 2015.
- [131] A. Darafsheh, C. Guardiola, D. Nihalani, D. Lee, J. C. Finlay, and A. Cárabe, “Biological super-resolution imaging by using novel microsphere-embedded coverslips”, 2015, p. 933 705.
- [132] A. Darafsheh, C. Guardiola, A. Palovcak, J. C. Finlay, and A. Cárabe, “Optical super-resolution imaging by high-index microspheres embedded in elastomers”, *Optics Letters*, vol. 40, no. 1, p. 5, 2015.
- [133] B. Du, Y.-H. Ye, J. Hou, M. Guo, and T. Wang, “Sub-wavelength image stitching with removable microsphere-embedded thin film”, *Applied Physics A*, vol. 122, no. 1, 2016.
- [134] H. Yang and M. A. Gijs, “Optical microscopy using a glass microsphere for metrology of sub-wavelength nanostructures”, *Microelectronic Engineering*, vol. 143, pp. 86–90, 2015.
- [135] W. Fan, B. Yan, Z. Wang, and L. Wu, “Three-dimensional all-dielectric metamaterial solid immersion lens for subwavelength imaging at visible frequencies”, *Science Advances*, vol. 2, no. 8, e1600901–e1600901, 2016.
- [136] F. Wang, L. Liu, P. Yu, Z. Liu, H. Yu, Y. Wang, and W. J. Li, “Three-dimensional super-resolution morphology by near-field assisted white-light interferometry”, *Scientific Reports*, vol. 6, p. 24 703, 2016.

- 
- [137] V. N. Astratov, A. V. Maslov, K. W. Allen, N. Farahi, Y. Li, A. Brettin, N. I. Limberopoulos, D. E. Walker, A. M. Urbas, V. Liberman, and M. Rothschild, “Fundamental limits of super-resolution microscopy by dielectric microspheres and microfibers”, 2016, 97210K.
- [138] D. N. Sitter, J. S. Goddard, and R. K. Ferrell, “Method for the measurement of the modulation transfer function of sampled imaging systems from bar-target patterns”, *Applied optics*, vol. 34, no. 4, pp. 746–751, 1995.
- [139] R. Horstmeyer, R. Heintzmann, G. Popescu, L. Waller, and C. Yang, “Standardizing the resolution claims for coherent microscopy”, *Nature Photonics*, vol. 10, no. 2, pp. 68–71, 2016.
- [140] L. A. Krivitsky, J. J. Wang, Z. Wang, and B. Luk’yanchuk, “Locomotion of microspheres for super-resolution imaging”, *Scientific Reports*, vol. 3, no. 1, 2013.
- [141] Y. Li, Z. Shi, S. Shuai, and L. Wang, “Widefield scanning imaging with optical super-resolution”, *Journal of Modern Optics*, vol. 62, no. 14, pp. 1193–1197, 2015.
- [142] P. Ghenuche, J. de Torres, P. Ferrand, and J. Wenger, “Multi-focus parallel detection of fluorescent molecules at picomolar concentration with photonic nanojets arrays”, *Applied Physics Letters*, vol. 105, no. 13, p. 131 102, 2014.
- [143] J. Li, W. Liu, T. Li, I. Rozen, J. Zhao, B. Bahari, B. Kante, and J. Wang, “Swimming microrobot optical nanoscopy”, *Nano Letters*, vol. 16, no. 10, pp. 6604–6609, 2016.
- [144] F. Wang, L. Liu, H. Yu, Y. Wen, P. Yu, Z. Liu, Y. Wang, and W. J. Li, “Scanning superlens microscopy for non-invasive large field-of-view visible light nanoscale imaging”, *Nature Communications*, vol. 7, p. 13 748, 2016.
- [145] M. Duocastella, F. Tantussi, A. Haddadpour, R. P. Zaccaria, A. Jacassi, G. Veronis, A. Diaspro, and F. D. Angelis, “Combination of scanning probe technology with photonic nanojets”, *Scientific Reports*, vol. 7, no. 1, 2017.
- [146] B. Yan, Z. Wang, A. L. Parker, Y.-k. Lai, P. John Thomas, L. Yue, and J. N. Monks, “Superlensing microscope objective lens”, *Applied Optics*, vol. 56, no. 11, p. 3142, 2017.
- [147] J. W. Goodman, *Introduction to Fourier Optics*. Roberts and Company Publishers, 2005, 520 pp.
- [148] P. J. Shaw and D. J. Rawlins, “The point-spread function of a confocal microscope: its measurement and use in deconvolution of 3-d data”, *Journal of Microscopy*, vol. 163, no. 2, pp. 151–165, 1991.
- [149] M. J. Nasse and J. C. Woehl, “Realistic modeling of the illumination point spread function in confocal scanning optical microscopy”, *JOSA A*, vol. 27, no. 2, pp. 295–302, 2010.
- [150] L. Novotny and B. Hecht, *Principles of Nano-Optics*. Cambridge University Press, 2012, 583 pp.

## Bibliography

---

- [151] O. Haeberlé, M. Ammar, H. Furukawa, K. Tenjimbayashi, and P. Török, “Point spread function of optical microscopes imaging through stratified media”, *Optics Express*, vol. 11, no. 22, pp. 2964–2969, 2003.
- [152] I. T. Young, “Chapter 1 image fidelity: characterizing the imaging transfer function”, in *Methods in Cell Biology*, ser. Fluorescence Microscopy of Living Cells in Culture Part B. Quantitative Fluorescence Microscopy—Imaging and Spectroscopy, D. L. Taylor and Y.-L. Wang, Eds., vol. 30, Academic Press, 1989, pp. 1–45.
- [153] H. Knutsson and C. F. Westin, “Normalized and differential convolution”, in *Proceedings of IEEE Conference on Computer Vision and Pattern Recognition*, 1993, pp. 515–523.
- [154] X. Zhang, T. Kashti, D. Kella, T. Frank, D. Shaked, R. Ulichney, M. Fischer, and J. P. Allebach, “Measuring the modulation transfer function of image capture devices: what do the numbers really mean?”, in *Image Quality and System Performance IX*, vol. 8293, International Society for Optics and Photonics, 2012, p. 829 307.
- [155] B. Zhang, J. Zerubia, and J.-C. Olivo-Marin, “Gaussian approximations of fluorescence microscope point-spread function models”, *Applied Optics*, vol. 46, no. 10, pp. 1819–1829, 2007.
- [156] G. Huszka, H. Yang, and M. A. M. Gijs, “Microsphere-based super-resolution scanning optical microscope”, *Optics Express*, vol. 25, no. 13, p. 15 079, 2017.
- [157] M. G. Gustafsson, D. A. Agard, and J. W. Sedat, “I5m: 3d widefield light microscopy with better than 100nm axial resolution”, *Journal of microscopy*, vol. 195, no. 1, pp. 10–16, 1999.
- [158] S. Fukuda, T. Uchihashi, R. Iino, Y. Okazaki, M. Yoshida, K. Igarashi, and T. Ando, “High-speed atomic force microscope combined with single-molecule fluorescence microscope”, *Review of Scientific Instruments*, vol. 84, no. 7, p. 073 706, 2013.
- [159] P. Hapala, G. Kichin, C. Wagner, F. S. Tautz, R. Temirov, and P. Jelínek, “Mechanism of high-resolution STM/AFM imaging with functionalized tips”, *Physical Review B*, vol. 90, no. 8, p. 085 421, 2014.
- [160] T. Uchihashi, H. Watanabe, S. Fukuda, M. Shibata, and T. Ando, “Functional extension of high-speed AFM for wider biological applications”, *Ultramicroscopy*, vol. 160, pp. 182–196, 2016.
- [161] M. Cascione, V. de Matteis, R. Rinaldi, and S. Leporatti, “Atomic force microscopy combined with optical microscopy for cells investigation: AFM combined with optical microscopy”, *Microscopy Research and Technique*, 2016.
- [162] T. Xiang, G.-S. Xia, X. Bai, and L. Zhang, “Image stitching by line-guided local warping with global similarity constraint”, *arXiv preprint arXiv:1702.07935*, 2017.
- [163] L. Juan and G. Oubong, “SURF applied in panorama image stitching”, in *Image Processing Theory Tools and Applications (IPTA), 2010 2nd International Conference on*, IEEE, 2010, pp. 495–499.

- [164] J. Jia and C.-K. Tang, "Image stitching using structure deformation", *IEEE Transactions on Pattern Analysis and Machine Intelligence*, vol. 30, no. 4, pp. 617–631, 2008.
- [165] A. Zomet, A. Levin, S. Peleg, and Y. Weiss, "Seamless image stitching by minimizing false edges", *IEEE Transactions on Image Processing*, vol. 15, no. 4, pp. 969–977, 2006.
- [166] R. Szeliski and H.-Y. Shum, "Creating full view panoramic image mosaics and environment maps", in *Proceedings of the 24th annual conference on Computer graphics and interactive techniques*, ACM Press/Addison-Wesley Publishing Co., 1997, pp. 251–258.
- [167] H. Yang, R. Trouillon, G. Huszka, and M. A. M. Gijs, "Super-resolution imaging of a dielectric microsphere is governed by the waist of its photonic nanojet", *Nano Letters*, pp. 4862–4870, 2016.
- [168] X. Chen, Z. Zeng, H. Wang, and P. Xi, "Three-dimensional multimodal sub-diffraction imaging with spinning-disk confocal microscopy using blinking/fluctuating probes", *Nano Research*, vol. 8, no. 7, pp. 2251–2260, 2015.
- [169] J. Huff, "The airyscan detector from ZEISS: confocal imaging with improved signal-to-noise ratio and super-resolution", *Nature Methods*, vol. 12, no. 12, 2015.
- [170] B. Knoll and F. Keilmann, "Near-field probing of vibrational absorption for chemical microscopy", *Nature*, vol. 399, no. 6732, pp. 134–137, 1999.



# Acronyms

<i>μS</i>	microsphere
<i>2D</i>	two-dimensional
<i>3D</i>	three-dimensional
<i>AFM</i>	atomic force microscopy
<i>BALM</i>	binding-activated localization microscopy
<i>BTG</i>	barium titanate glass
<i>CCD</i>	charge-coupled device
<i>CFM</i>	confocal fluorescence microscopy
<i>CO<sub>2</sub></i>	carbon dioxide
<i>COLD</i>	cryogenic optical localization in 3D
<i>DNA</i>	deoxyribonucleic acid
<i>DSTORM</i>	direct STORM
<i>ERZ</i>	enhanced-resolution zone
<i>FDTD</i>	finite-difference time-domain
<i>FEM</i>	finite element method
<i>FPS</i>	frames per second
<i>FWHM</i>	full width at half-maximum
<i>FoV</i>	field-of-view
<i>GFP</i>	green fluorescent protein
<i>GSDIM</i>	ground state depletion microscopy followed by individual molecule return
<i>GSD</i>	ground-state-depletion
<i>HF</i>	hydrofluoric acid
<i>IPA</i>	isopropyl alcohol
<i>LED</i>	light emitting diode
<i>LSP</i>	lines-and-spaces pattern
<i>Laser</i>	light amplification by stimulated emission of radiation
<i>MAD</i>	median absolute deviation
<i>MS-SOM</i>	microsphere-based super-resolution scanning optical microscopy
<i>MTF</i>	modulation transfer function

## Acronyms

---

<i>NA</i>	numerical aperture
<i>NOA</i>	Norland Optical Adhesive
<i>NORM</i>	near-field optical random mapping
<i>NSOM</i>	near-field scanning optical microscopy
<i>ON</i>	(white-light) optical nanoscopy
<i>PALM / FPALM</i>	photoactivated localization microscopy / fluorescence photoactivation localization microscopy
<i>PALMIRA</i>	PALM with independently running acquisition
<i>PDMS</i>	poly(dimethylsiloxane)
<i>PNJ</i>	photonic nanojet
<i>PSF</i>	point spread function
<i>PSTM</i>	photon scanning tunneling microscopy
<i>PTM</i>	photon tunneling microscopy
<i>RI</i>	refractive index
<i>ROI</i>	region of interest
<i>RPM</i>	reversible photo-bleaching microscopy
<i>SEM</i>	scanning electron microscopy
<i>SIL</i>	solid immersion lens
<i>SIM</i>	structured illumination microscopy
<i>SLG</i>	soda-lime glass
<i>SMI</i>	spatially modulated illumination
<i>SMLM</i>	single molecule localization microscopy
<i>SMON</i>	swimming microrobot optical nanoscopy
<i>SNR</i>	signal-to-noise ratio
<i>SOFI</i>	super-resolution optical fluctuation imaging
<i>SPDM</i>	spectral precision distance / spectral position determination microscopy
<i>SRM</i>	super-resolution microscopy
<i>SSIM</i>	saturated structured illumination microscopy
<i>SSUM</i>	scanning superlens microscopy
<i>STED</i>	stimulated-emission-depletion
<i>STM</i>	scanning tunneling microscopy
<i>STOM</i>	scanning tunneling optical microscopy
<i>STORM</i>	stochastic optical reconstruction microscopy
<i>SiO<sub>2</sub></i>	silicon dioxide
<i>TENOM</i>	tip enhanced near-field optical microscopy
<i>TiO<sub>2</sub></i>	titanium dioxide
<i>UV</i>	ultraviolet



## Constants & Symbols

$\omega$	rad/s	angular frequency
$S_{offset}$	nm	closest distance between the sample and the microsphere
$D$	$\mu\text{m}$	diameter of the focusing curvature of the microobject / diameter of the microsphere
$d$	nm	diffraction limit
$h$	nm	distance between the sample and the microsphere
$E$	V/m	electric field
$\kappa$	S/m	electric conductivity
$I$	$\text{W}/\text{m}^2$	intensity of the light
$L$	nm	line width
$M$	-	magnification factor
$P$	nm	pitch
$r$	$\mu\text{m}$	radial distance
$\mu_r$	-	relative permeability
$\epsilon_r$	-	relative permittivity
$n_{medium}$	-	refractive index of the medium
$n_{sphere}$	-	refractive index of the microsphere
$\epsilon_0$	$\text{F}/\text{m}$	vacuum permittivity $\approx 8.854188 \times 10^{-12}$
$w$	nm	waist of the photonic nanojet ( <i>i.e.</i> the full width at half-maximum of the photonic nanojet laterally at the peak intensity axially)
$\lambda$	nm	wavelength of the light
$k$	1/m	wave number



# Gergely Huszka



**Sex:** Male

**Date of birth:** 18 April 1989

**Nationality:** Hungarian

**Address:** Avenue de Longemalle 26, 1020 Renens VD,  
Switzerland

**Phone:** +41 78 815 28 61

**E-mail:** gergory.huszka@gmail.com



Click or scan!



Click or scan!

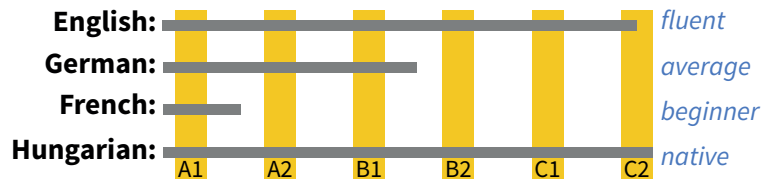
## Education

09. 2014 - Present **PhD in Microtechnology**  
Swiss Federal Institute of Technology (EPFL), Lausanne, Switzerland  
*Thesis:* Dielectric-sphere-based microsystem for optical super-resolution imaging
02. 2012 - 06.2014 **MSc in Info-Bionics Engineering**  
Pázmány Péter Catholic University (PPKE), Faculty of Information Technology, Budapest, Hungary  
*Thesis:* Implementation of a nucleic acid amplification method into microfluidic environment
09. 2012 - 06.2013 **MSc in Engineering (Bionics)**  
Tallinn University of Technology (TTÜ), Tallinn, Estonia  
*Thesis:* Development of a microfluidic platform for nucleic acid amplification tests
09. 2008 - 01.2012 **BSc in Molecular Bionics**  
Pázmány Péter Catholic University (PPKE), Faculty of Information Technology, Budapest, Hungary  
*Thesis:* Investigation on particle separation devices based on the Zweifach-Fung effect

## Work experience

09. 2014 - Present **Research Assistant**  
Swiss Federal Institute of Technology (EPFL), Lausanne, Switzerland  
*Tasks:*
- Development of a dielectric microsphere-based optical super-resolution microscope (hardware + software)
  - Teaching activities (theoretical + practical work)
  - Scientific writing in peer-reviewed journals
- Reference:* Prof. Martin A. M. GIJS
09. 2012 - 06.2013 **Trainee**  
Selfdiagnostics OÜ, Tallinn, Estonia  
*Tasks:*
- Development of a nucleic acid amplification test platform in microfluidic environment
- Reference:* Dr. Indrek TULP
09. 2010 - 06.2012 **Trainee**  
Hungarian Academy of Sciences, Institute of Technical Physics and Material Science, Budapest, Hungary  
*Tasks:*
- Application of analog microfluidics for particle separation
  - Development of Lab-on-a-Chip (LoC) devices
- Reference:* Dr. FÜRJES Péter

## Language skills



## Technical skills

- **Optics** Super-resolution microscopy, optical microscopy, scanning microscopy
- **Microtechnology** Microfluidics, Lab-on-a-Chip (LoC) technology
- **Microfabrication** Working experience in cleanroom environment (operator level)
- **Modelling software** MATLAB (data processing and analysis), COMSOL Multiphysics (finite element method simulations)
- **Programming languages** C++\*\*, Visual Basic\*\*, Javascript\*, HTML\*  
\*\*: advanced level, \*: beginner level
- **Editor software** MS Office, Libre Office, LATEX, Adobe Creative Suite (Illustrator, Indesign, Photoshop, Premiere Pro)

## Soft skills

- **Public appearance** Attended four international conferences, multiple teaching activities and demonstrations, on-line presence on YouTube and Twitch
- **Team work** Working experience in four research laboratories, being contact person between institutes
- **Creativity** Project management during master and doctoral studies, initiating new directions of development, graphical design of scientific posters, creating non-scientific short-films

## Personal highlights

- **Documents** Hungarian passport (free travel/move in EU), B residence permit in Switzerland, B category driving license
- **Hobbies** Indoor (gym, swimming) and outdoor (cycling, hiking) sports, reading sci-fi literature, photo- and video-editing

## List of publications

- **Journal papers**
  - Turning a normal microscope into a super-resolution instrument using a scanning microlens array  
Scientific Reports, Jan **2018**, DOI: 10.1038/s41598-017-19039-6
  - Microsphere-based super-resolution scanning optical microscope  
Optics Express, Jun **2017**, DOI: 10.1364/OE.25.015079
  - Super-Resolution imaging of a dielectric microsphere is governed by the waist of its photonic nanojet  
Nano Letters, Jul **2016**, DOI: 10.1021/acs.nanolett.6b01255
  - Performance characterization of micromachined particle separation system based on Zweifach–Fung effect  
Sensors and Actuators B Chemical, Feb **2012**, DOI: 10.1016/j.snb.2011.12.040
- **Conference posters**
  - Custom adapter for extended field-of-view microspherebased scanning superresolution microscopy, MEMS **2018**, Belfast, UK
  - Dielectric microsphere-based optical system for super-resolution microscopy, TRANSDUCERS **2017**, Kaohsiung, Taiwan
  - Patterning of melamine and SiO<sub>2</sub> microsphere lens arrays, MNE **2015**, The Hague, The Netherlands
  - Integrated microfluidic environment for solid-state nanopore sensors, EUROSENSORS **2012**, Krakow, Poland
  - Integrated microfluidic function for nanopore based biosensors, ICMAS **2012**, Budapest, Hungary

